Probing an ytterbium Bose-Einstein condensate using an ultranarrow optical line: Towards artificial gauge fields in optical lattices

Matthias Scholl

To cite this version:

Matthias Scholl. Probing an ytterbium Bose-Einstein condensate using an ultranarrow optical line: Towards artificial gauge fields in optical lattices. Quantum Physics [quant-ph]. UPMC Université Paris VI, 2014. English. NNT : . tel-01160837

HAL Id: tel-01160837
https://theses.hal.science/tel-01160837

Submitted on 8 Jun 2015

Laboratoire Kastler Brossel

École Normale Supérieure
Collège de France

THÈSE DE DOCTORAT
DE L'UNIVERSITÉ PIERRE ET MARIE CURIE

Spécialité: Physique quantique
École doctorale: «Physique en Île-de-France »

Présentée par:

Matthias Scholl

pour obtenir le grade de:
DOCTEUR DE L'UNIVERSITÉ PIERRE ET MARIE CURIE

Probing an ytterbium Bose-Einstein condensate using an ultranarrow optical line:

Towards artificial gauge fields in optical lattices

A soutenir le 19 décembre 2014
devant le jury composé de:

M. Thomas BOURDEL	Rapporteur
M. Henning MORITZ	Rapporteur
M. Yann LE COQ	Examinateur
M. Markus OBERTHALER	Examinateur
M. Jean DALIBARD	Directeur de thèse

Abstract

In this work I present the development of a new experiment to produce quantum degenerate gases of ytterbium. This project aims at realizing artificial gauge fields with ultracold atoms in optical lattices. Combining intense gauge fields with strong on-site interactions is expected to open a new area for ultracold quantum gases, where for instance the atomic analogs of fractional quantum Hall systems could be realized.

First I describe the experimental methods for the production of a Bose-Einstein condensate (BEC) of ^{174}Yb. This implies magneto-optical trapping on the $^1S_0 \leftrightarrow {}^3P_1$ intercombination transition and a transport of the atomic cloud in an optical dipole trap over a distance of 22 cm. Evaporative cooling in a crossed dipole trap results in the production of pure BECs of about 6×10^4 atoms.

The planned implementation of artificial gauge fields requires the coherent driving of the $^1S_0 \leftrightarrow {}^3P_0$ clock transition of ytterbium. For this purpose an ultrastable laser system at 578 nm, frequency locked to an ultralow expansion (ULE) cavity, has been realized. A precise determination of the temperature zero-crossing point of the ULE cavity allowed us to limit laser frequency drifts below 100 mHz/s. Spectroscopic measurements of the clock transition on a trapped and free falling BEC are presented, where typical linewidths in the kHz range are observed, limited by interatomic interactions.

Finally I present a detailed discussion of the methods to achieve artificial gauge fields in optical lattices and their possible experimental implementation. This includes a scheme to realize a bichromatic state-dependent optical superlattice in a doubly-resonant cavity.

Résumé

Je présente dans cette thèse le développement d'une nouvelle expérience destinée à produire des gaz quantiques d'atomes d'ytterbium. L'objectif de ce projet est de réaliser des champs de jauge artificiels sur des gaz d'atomes piégés dans des réseaux optiques. La combinaison de ces champs de jauge et des interactions entre atomes ouvre de nouvelles perspectives pour le domaine des gaz quantiques comme la réalisation d'états analogues à ceux apparaissant dans la physique de l'effet Hall quantique fractionnaire.

Tout d'abord, je présente les méthodes expérimentales développées pour produire un condensat de Bose-Einstein d'atomes (CBE) de ^{174}Yb. Je décris notamment la réalisation d'un piège magnéto-optique sur la raie d'intercombinaison $^1S_0 \leftrightarrow {}^3P_1$, le piégeage du nuage atomique dans un piège dipolaire et son transport sur une distance de 22 cm. Un condensat pur d'environ 6×10^4 est ensuite obtenu après évaporation dans un piège dipolaire croisé.

Les protocoles que nous souhaitons mettre en place pour réaliser des champs de jauge artificiels réquièrent le couplage cohérent du niveau fondamental $^1S_0$ et du niveau excité métastable $^3P_0$ sur la transition "horloge". Pour ce faire, nous avons développé un laser ultrastable à 578 nm asservi en fréquence sur une cavité de référence. En optimisant précisément la température de la cavité autour du point d'annulation de l'expansion thermique nous avons obtenu des dérives résiduelles en fréquence inférieures à 100 mHz/s. Nous avons réalisé une spectroscopie sur cette transition d'un CBE piégé ou en expansion et obtenu des largeurs de raies du l'ordre du kHz limitées par les interactions entre atomes.

Enfin, je présente en détail les protocoles pour réaliser des champs de jauge artificiels dans des réseaux optiques et leur éventuelle mise en pratique et notamment un schéma pour réaliser un réseau optique bichromatique dépendant de l'état interne des atomes dans une cavité doublement résonante.

Contents

Chapter 1

Introduction

The development of laser cooling and trapping techniques in the 80's has paved the way to a new range of temperatures achievable in a laboratory [1, 2, 3, 4] and was rewarded with the Nobel price in 1997 for Chu, Phillips and Cohen-Tannoudji. Based on these techniques it became possible to cool gaseous atomic clouds to temperatures well below 1 mK. This has enabled, together with the application of forced evaporative cooling, the first observations of Bose-Einstein condensation in 1995 [5, 6, 7]. This phenomenon had been predicted about 80 years earlier by Bose and Einstein based on statistical arguments. Its realization in a laboratory opened up the possibility to study quantum phenomena in a well-controlled environment on macroscopic length scales. In the first years the research was mainly focused on the properties of the Bose-Einstein condensate (BEC) itself. Among the greatest achievements are the observation of long range coherence in interference experiments [8], dark and bright solitons [9, 10, 11, 12], superfluidity via the creation of vortices [13] and atom lasing [14]. Few years later also fermionic gases were first brought to the quantum degenerate regime [15].

After gaining a profound understanding of the degenerate quantum matter itself, the research focus has moved in the last ten years towards the engineering of more complex quantum systems, where the quantum gases are a starting point rather than the main subject to investigate. The high control over the system parameters, for example the dimensionality [16] via the trapping potentials and the interaction strength via Feshbach resonances [17], enable thereby to simulate other quantum systems in a very clean and well-controlled environment. In particular interesting is the simulation of many-body phenomena [16]. One prominent example is the observation of the BEC-BCS crossover in two-component Fermi gases [18] and its link to the mechanism of Cooper pair formation, essential to understand superconductivity.

Another important example is provided by cold gases in optical lattices [19], where the atoms are subject to periodic potentials created by interfering laser beams. The analogy to electrons in a solid, that move in the periodic potential created by the ion crystal, allows to study many solid-state phenomena from a different point of view. The dynamic control over many system parameters like the lattice depth and geometry thereby enables to use probing techniques that cannot be used in condensed matter physics. This implies among others band mapping [20, 21], single site resolved imaging [22, 23, 24] and the measurement of on-site population statistics (for example via the doublon fraction [25]). Furthermore the possibility to engineer model Hamiltonians like the celebrated Bose-Hubbard and Fermi-Hubbard models allow to explore new physical phenomena, like the superfluid to Mott insulator transition for bosons [26] and fermions [25] or repulsively bound pairs [27].

1.1 Artificial gauge fields: State of the art

One feature that was missing for a long time in the toolbox of quantum simulation with cold atoms is the effect of orbital magnetism. Orbital magnetism is at the heart of many intriguing quantum effects like the integer and fractional quantum Hall effect in two-dimensional electron systems [28, 29, 30]. For atoms, the required Lorentz force does not naturally appear in the presence of an external magnetic field due to the charge neutrality. However, ways have been found to emulate equivalents of a Lorentz force for neutral atoms [31].

Simulation of orbital magnetism in the bulk

Pioneering work has involved the rapid rotation of the gas where the mathematical equivalence between the Coriolis and the Lorentz force is used. The appearance of vortices thereby signalized the transfer of angular momentum to the cloud [32]. To reach the limit of strong effective magnetic fields, required for the quantum Hall regime, the number of vortices needs to be on the same order as the number of particles. This is found to be technically challenging to realize in rotating gases since the achievable rotation speed is limited by the fact that centrifugal force needs to be compensated by the trapping potential [33, 34].

In a different approach artificial vector gauge potentials have been engineered using Raman transitions between internal atomic states, where a clever coupling of internal and external degrees of freedom is used. An atom following adiabatically the spatial variations of the Raman laser field acquires a phase that is analogue to the Aharonov-Bohm phase a charged particle picks up when moving in a magnetic field. Using this technique the formation of vortices [35], spin-orbit coupling [36] as well as a spin Hall effect [37] could be observed. However, the implementation using alkali atoms requires the Raman lasers to be close to resonance where strong spontaneous emission and associated cloud heating turn out to be problematic. This is a limiting factor and has for example inhibited the formation of an Abrikosov lattice of the vortices observed in [35].

Artificial gauge fields on a lattice

Schemes based on optical lattices seem more promising to reach the limit of strong magnetic fields and therefore the regime of strongly correlated states [38, 39, 40]. Within the framework of the so-called Peierls substitution, the key component to simulate orbital magnetism for neutral atoms on a lattice is the engineering of complex-valued tunneling matrix elements with a spatially dependent phase. This phase gets imprinted on the atomic wave function in a tunneling process, therefore coupling to atomic motion in the same way as the Aharonov-Bohm phase couples to electron motion. A gauge invariant quantitiy is the effective magnetic flux per unit cell that is determined by the sum of the phases a particle picks up on a round trip on a unit cell. Reaching the strong field limit means to achieve magnetic fluxes on the order of one flux quantum per unit cell. So far two different techniques have been implement to engineer gauge fields using complex valued tunneling matrix elements and have reached the strong field regime. Both techniques are based on a periodic driving of the lattice potential and will be briefly summarized in the following.

In the first technique the complex tunneling elements are induced by periodic shaking of the lattice potential, where the key to break the time-reversal symmetry is to apply an asymmetric periodic driving force. Transforming the dynamics into the moving frame and averaging over many driving periods, allows one to describe the dynamics by an effective Hamiltonian where complex tunneling matrix elements appear. This technique has been used in a two-dimensional triangular lattice [41], where a staggered magnetic flux with an alternating sign between the triangular lattice cells pointing upwards and those pointing downwards has been realized. This has enabled the simulation of an Ising-XY spin-model [42]. Recently also the realization of an effective magnetic flux in an hexagonal lattice configuration has been reported [43]. This realizes the so-called Haldane model [44] where a local staggered flux within each hexagonal unit cell is present, although the net magnetic flux per unit cell is zero.

The second technique is based on a lattice configuration where neighbouring lattice sites are shifted out of resonance by applying either an additional gradient or a superlattice potential. The tunneling is restored by resonantly coupling the neighbouring sites with a Bragg type transition using a pair of lasers propagating in different spatial directions. The small frequency detuning between the lasers leads to a running wave that modulates the lattice potential with a period given by the difference frequency. Also in this case the time averaging over many modulation periods leads to an effective Hamiltonian with complex valued tunneling matrix elements. With this technique a staggered [45, 46] as well as an homogeneous magnetic flux have been realized [47, 48], implementing the so-called Harper (or Hofstadter) model. In bosonic ladder geometries the occurrence of chiral edge currents could be observed [49] and recently the measurement of topological properties of Hofstadter bands has been reported [50].

The presented methods can be operated using far-off-resonant lasers only, overcoming the problems of spontaneous emission and associated heating in the case of the Raman coupling in the bulk case. However, one of the problems that both presented methods have in common is the fact that the frequency of the lattice modulation is usually in the kHz range. This is only about one order of magnitude above the typical tunneling time scale. In consequence the description using an effective Hamiltonian neglects effects where the fast, micro motion of the atoms couples to the averaged slow motion. Similar as in so-called rf-heating in ion traps [51], the coupling of the micro motion to the slow dynamics can lead in these schemes to heating, as also pointed out in [50]. In a recent work [52] this problem has been addressed from a theory point of view, where it is found that for the experimental parameters used in [50] substantial coupling to higher bands is expected.

A third technique, that has not been implemented yet, is based on laser-assisted tunneling in a state-dependent optical lattice potential [38]. This scheme assumes two long-lived internal atomic states that arrange in two spatially separated sublattices. The direct coherent coupling of the two involved internal states results in complex tunneling matrix elements, where the local phase of the laser is imprinted onto the atomic wave function. One could also view this scheme in the light of a periodic modulation of the lattice. However, in this case the modulation happens at optical frequencies where the approximation of an effective Hamiltonian is very well justified. Since furthermore only far-off-resonant laser light is involved, effects of heating are therefore expected to be negligible. In the most basic version of this scheme a staggered magnetic flux would be realized, but methods are available to achieve flux rectification using for example and optical superlattice configuration [39]. This is the method we plan to use in our experiment, which can be favourably implemented using atoms with two valence electrons, due to the existence of long-lived excited states in the spin-triplet manifold.

1.2 A novel experiment to study artificial gauge fields in optical lattices

The goal of this thesis work is the construction of an experimental apparatus for the study of artificial gauge fields in optical lattices. The atomic species we have chosen to implement this is ytterbium, that offers several advantageous properties. Firstly the metastable $^3\mathrm{P}_0$ state (with a lifetime larger than 10 s) is ideal for the implementation of the state-dependent optical lattice. The coherent coupling between the $^1\mathrm{S}_0$ ground and $^3\mathrm{P}_0$ metastable excited state can be achieved with visible light at 578 nm and has already been shown in several experiments [53, 54]. The required wavelengths to realize the desired state-dependent optical lattices are conveniently far from atomic resonances such that heating due to spontaneous emission is negligible (for details see chapter 5). Furthermore the possibility to have bosons (spin 0) and/or fermions (spin 1/2 and 5/2) in the same setup is a main advantage. Quantum degeneracy has already been shown for all stable isotopes and miscellaneous Bose-Bose, Bose-Fermi and Fermi-Fermi mixtures [55, 56, 57, 58]. Furthermore, elegant schemes for laser cooling are available including narrow line cooling on the $^1\mathrm{S}_0 \leftrightarrow {}^3\mathrm{P}_1$ intercombination line, where the Doppler temperature is as low as $4.5\,\mu$K.

The construction of the experiment comprises the implementation of laser cooling and trapping techniques and to achieve quantum degenerate gases of ytterbium. The key ingredient in this experiment is the laser system to coherently couple the $^1\mathrm{S}_0 \leftrightarrow {}^3\mathrm{P}_0$ transition. This laser system goes far beyond usual technology in quantum optics or atomic physics. The typically required laser linewidth is on the order of 10 Hz, which necessitates to build a laser system similar to the ones used as central components for optical atomic clocks [59]. Another challenge in the construction of the experiment is to handle the complexity arising from the large amount of different laser wavelengths. Directly used wavelengths in the experiment comprise (399, 532, 556, 578, 612, 760, 1070, 1224) nm, where additional wavelengths are needed for higher harmonic generation at (798, 1030, 1112, 1319) nm.

This new generation ultracold atoms experiment combines the techniques from complex quantum gases experiments with state of the art elements from metrology. The fusion of many-body physics with high precision metrology tools thereby enables to push the boundaries towards novel quantum many-body phenomena.

1.3 Thesis overview

The thesis is structured as follows:

Chapter 2 In this chapter the theory of optical lattices is reviewed and the process of laser-assisted tunneling in a state-dependent optical lattice is introduced from a theory point of view. Furthermore the basic concepts of orbital magnetism in quantum mechanics are briefly presented, comprising the Aharonov-Bohm phase. The Harper Hamiltonian is subsequently introduced and its properties briefly reviewed.

Chapter 3: The experimental setup and methods used for laser cooling and trapping of ytterbium are presented first. This is followed by the description and characterization of a transport of the atomic cloud in a mechanically displaced optical dipole trap. The results of evaporative cooling in a crossed dipole trap to achieve a BEC of ^{174}Yb are presented subsequently. The chapter terminates with some results on the adiabatic loading of the BEC into an optical lattice and the application of Kapitza-Dirac diffraction to calibrate the lattice depth.

Chapter 4: The first results of spectroscopic measurements on the $^1S_0 \leftrightarrow {}^3P_0$ clock transition are presented in this chapter. First some basic elements concerning the coupling of the clock transition for the bosonic isotopes and collisional properties of atoms in the $^3P_0$ are discussed. Then the ultra stable laser system is described and our method to calibrate its absolute frequency using a transition in molecular iodine as a frequency reference. In the subsequent sections the results of spectroscopic measurements on BEC of ^{174}Yb in a crossed dipole trap and during free fall are presented and the observed resonance widths are compared to values expected from theory models. Furthermore the frequency drifts of the reference cavity used to lock the laser to are characterized. Finally spectroscopic measurements after the hydrodynamic expansion of a BEC are presented that allow to calibrate the laser frequency with respect to the atomic resonance in a single measurement shot.

Chapter 5: In this chapter the details of the scheme to realize artificial gauge fields in optical lattices are presented first. A detailed discussion of the required conditions for the experimental implementation follows subsequently. In the last part the possible ways to realize the state-dependent superlattice potential are considered. This implies a study of experimental means to tune the relative phase between two retro-reflected optical lattices and possibilities to boost the achievable lattice depths for a given amount of laser power.

Chapter 6: Finally we terminate this thesis with a summary of the achieved results and an outlook into the near future of the experiment.

Chapter 2

Theory

This chapter is intended to set the theoretical basis for later following discussions. In a first part we will present the fundamental concepts of optical lattices, where the focus lies on the properties in the tight-binding regime. This limit of very deep lattice potentials is important to introduce since it is the relevant regime for the experiments we intend to realize. In a second part the theoretical basics of orbital magnetism in quantum mechanics are reviewed and the so-called Harper Hamiltonian is discussed. This is the most basic Hamiltonian that includes effects of orbital magnetism for atoms on a lattice and corresponds to the Hamiltonian we would like to implement experimentally.

2.1 Optical lattices

Optical lattices are an important tool in the field of ultracold atoms, since they enable one to create spatially periodic potentials for neutral atoms. This is in particular interesting to simulate the behaviour of electrons in a solid, where their properties are governed by the presence of a periodic potential created by the charged nuclei. The analogy between these two systems allows one to investigate solid state phenomena using cold atoms from a new perspective. The high experimental control over the periodic potential in the case of cold atoms enables to use measurement and preparation techniques that are not available in the condensed matter domain.

In this section the principle to create an optical lattice is presented as well as the basic theory of quantum particles moving in a periodic potential. Furthermore a theoretical description of so-called laser-assisted tunneling is introduced. All this will serve to set the theoretical background for later discussions concerning artificial gauge fields in optical lattices in chapter 5.

The discussions will be closely following [60] and [61].

2.1.1 Creating an optical lattice

In its simplest version an optical lattice consists of two counterpropagating laser beams with wavelength λ, wave vector $k = 2\pi/\lambda$ and equal intensities I_0 (see Figure 2.1). Assuming parallel polarizations of the two interfering beams, the resulting light intensity along the propagation axis x takes the form

$$I(x) = 4I_0 \cos^2(kx + \phi)\,. \tag{2.1}$$

The coordinate origin will be chosen in the following such that $\phi = 0$. If the wavelength λ is far detuned from any atomic resonance, the effect of the light field on the atom can be treated in form of a dipole potential (see [62] and Appendix A) that reads in general

$$V_{\mathrm{dip}}(\boldsymbol{r}) = -\frac{1}{2\epsilon_0 c}\mathrm{Re}[\alpha(\lambda)]I(\boldsymbol{r})\,. \tag{2.2}$$

Here $\mathrm{Re}[\alpha(\lambda)]$ denotes the real part of the complex atomic polarizability $\alpha(\lambda)$, c the speed of light and ϵ_0 the vacuum permittivity. In the following the case of red detuned light is assumed, $\mathrm{Re}[\alpha(\lambda)] > 0$, leading to an attractive periodic potential of the form

$$V_{\mathrm{lat}}(x) = -V_0 \cos^2(k_{\mathrm{lat}}x) = -V_0 \cos^2(\pi x/a)\,, \tag{2.3}$$

where $V_0 \geq 0$ is the lattice depth, $k_{\mathrm{lat}} \equiv \pi/a = k$ the lattice wave vector and $a = \lambda/2$ the lattice period.

In the more general case where the two interfering waves intersect with an angle θ with respect to each other, the lattice wave vector is modified to $k_{\mathrm{lat}} = k\sin(\theta/2)$ and thus the lattice period increased to $a = \lambda/[2\sin(\theta/2)]$, as sketched in Figure 2.1.

The natural energy scale that enters the system in the presence of an optical lattice is the recoil energy defined as $E_{\mathrm{R}} \equiv \hbar^2 k_{\mathrm{lat}}^2/2m$. This corresponds to the kinetic energy of a particle with mass m when moving with momentum $\hbar k_{\mathrm{lat}}$ and will be used in the upcoming discussions as the reference energy scale for the lattice depth and tunneling energies.

2.1.2 Bloch's theorem and band structure

In the following the problem of a particle with mass m, moving in a periodic potential along x direction is considered. To keep the formalism simple and demonstrative, only the one-dimensional case will be discussed. A generalization to more dimensions can be done for any Bravais lattice (see for example [63]). However, throughout this thesis only cubic lattices will be considered, where the potentials along the main axes separate and it is sufficient to treat one dimension at a time.

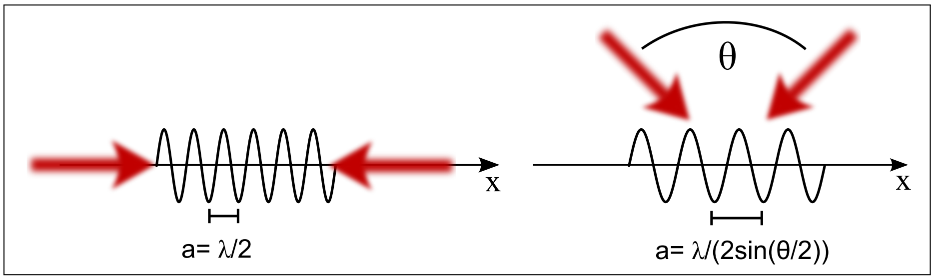

Figure 2.1: Sketch of the creation of an optical lattice. On the left hand side two counter propagating laser beams (red arrows) are considered forming a periodic potential of period $a = \lambda/2$. On the right hand side the two laser beams intersect at the angle of θ leading to a lattice constant of $a = \lambda/[2\sin(\theta/2)]$.

The Hamiltonian describing the system can be written in the form

$$\hat{H} = \frac{\hat{p}^2}{2m} + V(\hat{x}) , \tag{2.4}$$

where $\hat{p}$ is the momentum operator of the particle and $V(\hat{x}) = V(\hat{x} + a)$ is the periodic potential with period a. The eigenenergies $E_{n,q}$ and eigenstates $\psi_{n,q}$ of $\hat{H}$ are the solutions of the stationary Schrödinger equation

$$\hat{H}\psi_{n,q} = E_{n,q}\psi_{n,q} , \tag{2.5}$$

with periodic boundary conditions. The possible eigenenergies will occur in separated energy bands that are labelled in ascending order by the index n. The index q denotes the so-called quasi-momentum. According to Bloch's theorem the eigenfunctions take the form of a product of a plane wave and a function of periodicity a reading

$$\psi_{n,q}(x) = e^{iqx} u_{n,q}(x) , \tag{2.6}$$

with $u_{n,q}(x) = u_{n,q}(x + a)$. The eigenfunctions $\psi_{n,q}(x)$ themselves are not necessarily periodic with period a, but might differ by a phase factor from one lattice site[1] to another, that is determined by the quasi-momentum q. Since the phase difference is only defined up to 2π, the quasi-momentum q itself is only defined up to a multiple of $2\pi/a = 2k_{\text{lat}}$. This allows to restrict the values of q to the so-called first Brillouin zone, $-k_{\text{lat}} < q \leq k_{\text{lat}}$. The eigenfunctions $\psi_{n,q}(x)$ are usually called Bloch waves.

---

[1] The minima of the periodic potential will be called lattice sites in the following.

Numerical solution

We rewrite the potential from equation (2.3) without loss in generality in the form

$$V_{\mathrm{lat}}(x) = V_0 \sin^2(k_{\mathrm{lat}} x) \,, \quad V_0 > 0 \,. \tag{2.7}$$

Using the discrete periodicity of $V_{\mathrm{lat}}(x)$, the eigenfunctions (Bloch waves) for a given band index n can be developed as a Fourier series [60]

$$\psi_q(x) = \sum_{j\in\mathbb{Z}} C_j(q) e^{i(2jk_{\mathrm{lat}}+q)x}, \quad -k_{\mathrm{lat}} < q \leq k_{\mathrm{lat}} \,, \tag{2.8}$$

with expansion coefficients $C_j(q)$. Then the Schrödinger equation can be brought[2] to the form of a tridiagonal matrix equation [60] for the $C_j(q)$ given by

$$\boxed{\left[\left(2j + \frac{q}{k_{\mathrm{lat}}}\right)^2 + \frac{V_0}{2E_{\mathrm{R}}}\right] C_j - \frac{V_0}{4E_{\mathrm{R}}}(C_{j-1} + C_{j+1}) = \frac{E_q}{E_{\mathrm{R}}} C_j} \,. \tag{2.9}$$

The diagonalization of this, a priori, infinite dimensional matrix equation yields the eigenenergies E_q and the coefficients $C_j(q)$ of the eigenfunctions for a given pair of $(q/k_{\mathrm{lat}}, V_0/E_{\mathrm{R}})$. Since the coefficients C_j become very small for large j, one can truncate the summation in equation (2.8) in order to limit the dimension of the matrix to be diagonalized. Practically a limitation of $|j| \leq 20$ is reasonable for lattice depths up to $V_0/E_{\mathrm{R}} = 50$ (see [60]). For all numerical calculations based on equation (2.9) during this thesis, this choice of truncation is made. The numerically obtained eigenenergies for the first energy bands are shown in Figure 2.2 for several lattice depths.

2.1.3 Wannier functions and tight-binding approximation

The Bloch wave eigenfunctions $\psi_{n,q}(x)$, as introduced in the previous section, are in general functions that are delocalized over the whole lattice. However, in systems where local interactions are important, the physics becomes more clear when working with a basis of functions that are well localized around a given lattice site. Such a basis is realized by the so-called Wannier functions which are defined as a discrete Fourier transform of the Bloch wave functions

$$w_{n,j}(x) = \frac{1}{\sqrt{\mathcal{N}}} \sum_{q\in\,]-k_{\mathrm{lat}},k_{\mathrm{lat}}]} \psi_{n,q}(x)\, e^{-ijaq} \,. \tag{2.10}$$

---

[2] The potential $V_{\mathrm{lat}}(x)$ in equation 2.7 has only three non-vanishing Fourier terms, $V(x) = \sum_{l=0,\pm1} V_l \exp(2ilk_{\mathrm{lat}}x) = -V_0/2 + V_0[\exp(2ik_{\mathrm{lat}}x) + \exp(-2ik_{\mathrm{lat}}x)]$.

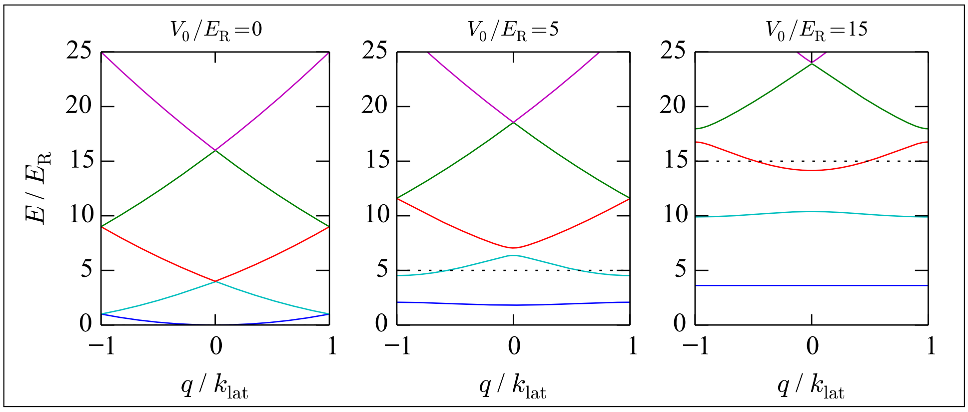

Figure 2.2: Dispersion relation of a particle in a periodic potential of the form $V(x) = V_0 \sin^2(k_{\text{lat}}x)$. Shown are the five lowest energy bands for three different potential depths. On the leftmost picture the case of $V_0 = 0$ is realized corresponding to a free particle. The dotted line indicates the depth of the potential V_0/E_R.

The label $j \in \mathbb{Z}$ now denotes the lattice site located at $x_j = ja$ and $\mathcal{N}$ is a normalization constant. It is to note that the Bloch waves $\psi_{n,q}$ are only defined up to a phase factor, which leaves an ambiguity for the definition of the Wannier functions. In the case of a one-dimensional potential with the symmetry $V(x) = V(-x)$, it has been shown in [64] that this phase factor can be chosen such that the Wannier functions are (i) real, (ii) symmetric or anti-symmetric with respect to $x = 0$ and (iii) fall off exponentially at large distances. Furthermore the Wannier functions build an orthonormal set of functions

$$\int w_{n,j}(x)\, w_{n',j'}(x)\, \mathrm{d}x = \delta_{n,n'}\delta_{j,j'}\,, \tag{2.11}$$

and for a given band index n they can be constructed from each other by a discrete translation

$$w_{n,j}(x) = w_{n,0}(x - ja)\,. \tag{2.12}$$

Therefore it is enough to know one Wannier function for each band in order to know the complete basis of functions. To illustrate that this new basis consists indeed of localized functions, some numerically computed Wannier functions for the potential (2.7) are shown in Figure 2.3. It is to note that the Wannier functions in the case of a very deep lattice $V_0 \gg E_R$ approach asymptotically the eigenfunctions of an harmonic oscillator potential given by $V_{\text{harm}} = m\omega^2x^2/2$, with angular trapping frequency $\omega = 2\sqrt{V_0 E_R}/\hbar$.

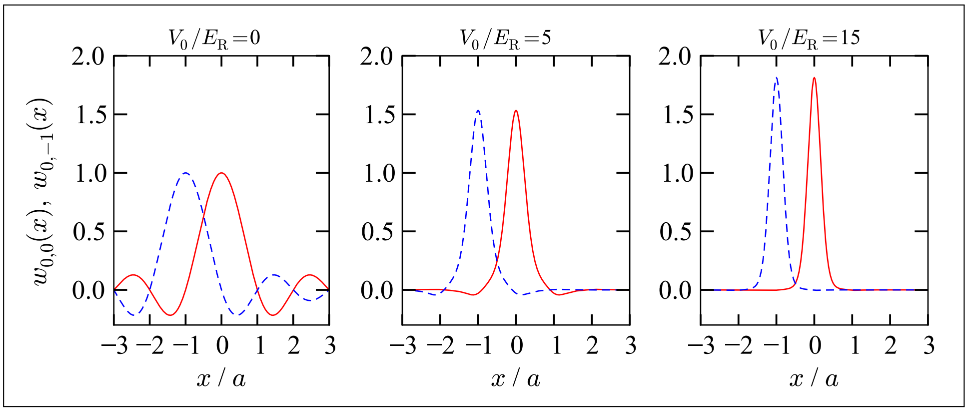

Figure 2.3: Wannier functions in the fundamental band for a periodic potential of the form $V(x) = V_0 \sin^2(k_{\text{lat}} x)$. Shown are the Wannier functions centered around the site $j = 0$ (red solid lines) and $j = -1$ (blue dashed lines) for different lattice depths V_0/E_{R}. As the lattice depth is increased, the Wannier functions become more and more localized and the contribution at adjacent sites diminishes. On the leftmost picture the case of a free particle is realized where the Wannier functions takes the form of a cardinal sine function.

The Hamiltonian (2.4) expressed in the new basis of the Wannier functions takes a non-diagonal form (as opposed to taking the Bloch wave basis) and reads in the language of second quantization

$$\hat{H} = \sum_{n,j,j'} J_n(j-j')\, \hat{a}^\dagger_{n,j} \hat{a}_{n,j'} \ , \tag{2.13}$$

where $\hat{a}^\dagger_{n,j}$ and $\hat{a}_{n,j}$ denote the creation and annihilation operators for a particle in state $w_{n,j}(x)$. This Hamiltonian describes the hopping of a particle from site j' to site j with an amplitude of $J_n(j-j')$. The hopping amplitude depends only on the band index n and the distance between the two considered sites and is defined as

$$J_n(j-j') = \int w^*_{n,j}(x) \left(-\frac{\hbar^2}{2m}\Delta + V(x) \right) w_{n,j'}(x)\, \mathrm{d}x\, . \tag{2.14}$$

Using the relation (2.10) this can be brought to the form

$$J_n(j-j') = \frac{1}{\mathcal{N}} \sum_{q\in]-k_{\text{lat}},k_{\text{lat}}]} E_{n,q}\, e^{i(j-j')\pi q/k_{\text{lat}}} \, , \tag{2.15}$$

with $\mathcal{N}$ a normalization constant. The tunneling energy $J_n(j-j')$ is thus nothing else than a (complex) weighted average (or Fourier transform) of all energy values of band n within the first Brillouin zone.

In the so-called tight-binding limit, where the lattice depth is large compared to the recoil energy $V_0/E_\mathrm{R} \gg 1$, the Wannier functions become well localized around each lattice site. As a consequence the hopping energies $J_n(j-j')$ for $|j-j'| > 1$ become very small compared to the nearest-neighbour tunneling energy $J_n(\pm 1)$. When restricting the dynamics to the lowest Bloch band $n = 0$ only, the Hamiltonian (2.13) can then be approximated to

$$\boxed{\hat{H} \approx -J \sum_{j\in\mathbb{Z}} \hat{a}^\dagger_{j+1}\hat{a}_j + h.c.}\,, \tag{2.16}$$

where $J = J_0(1)$ is the nearest-neighbour hopping energy (and "*h.c.*" is an abbreviation for the hermitian conjugate of the preceding term). This is the so-called tight-binding Hamiltonian for non-interacting particles. Within the tight-binding approximation the hopping energy J can be approximated by an analytic expression that reads [60]

$$\frac{J}{E_\mathrm{R}} \approx \frac{4}{\sqrt{\pi}} \left(\frac{V_0}{E_\mathrm{R}}\right)^{3/4} \exp\left[-2\left(\frac{V_0}{E_\mathrm{R}}\right)^{1/2}\right], \tag{2.17}$$

and falls off exponentially with $(V_0/E_\mathrm{R})^{1/2}$ for large V_0. The eigenenergies of the tight-binding Hamiltonian are given by [60]

$$E(q) = -2J\cos(aq) \tag{2.18}$$

and form the fundamental energy band of width[3] $4J$. Accordingly the width of the fundamental band also falls off exponentially with $(V_0/E_\mathrm{R})^{1/2}$ for large V_0. The width of higher lying Bloch bands is in general larger than the one of the fundamental band, as can be seen in the band structure images in Figure 2.2.

2.1.4 Interacting bosons and Bose-Hubbard model

The discussion for non-interacting particles from the previous section is here extended to the case of interacting particles, in particular bosons. The interatomic interactions are modeled in the pseudo-potential description where only contact interactions in the s-wave scattering regime are considered. The interaction Hamiltonian in three dimensions then can in general be written as [60]

$$\hat{H}_\mathrm{int} = \frac{g}{2}\int \hat{\Psi}^\dagger(\boldsymbol{r})\hat{\Psi}^\dagger(\boldsymbol{r})\hat{\Psi}(\boldsymbol{r})\hat{\Psi}(\boldsymbol{r})\mathrm{d}^3\boldsymbol{r}\,, \tag{2.19}$$

---

[3] For the case of a 2D square and 3D cubic lattice, the widths are $8J$ and $12J$, respectively.

where $g = 4\pi\hbar^2 a_\mathrm{s}/m$ quantifies the interaction strength via the s-wave scattering length a_s and $\hat{\Psi}(\boldsymbol{r})$ is the field operator annihilating a particle at position $\boldsymbol{r}$. When assuming the interaction energy to be small compared to the band gap, the description can be restricted to the fundamental Bloch band only. Then the field operator $\hat{\Psi}(\boldsymbol{r})$ can be developed in terms of annihilation operators $\hat{a}_j$,

$$\hat{\Psi}(\boldsymbol{r}) = \sum_j w_j(\boldsymbol{r})\,\hat{a}_j\,, \tag{2.20}$$

where the summation includes all possible lattice sites j and $w_j(\boldsymbol{r})$ are the three-dimensional Wannier functions in the fundamental Bloch band. By furthermore considering the lattice to be in the tight-binding regime, the overlap between neighbouring sites becomes small and the interaction energy of particles in Wannier functions located at different lattice sites is negligible. Keeping only interactions between particles at the same lattice site leads to the on-site interaction Hamiltonian

$$\hat{H}_\mathrm{int} \approx \frac{U}{2}\sum_j \hat{n}_j(\hat{n}_j - 1)\,. \tag{2.21}$$

Here $\hat{n}_j = \hat{a}_j^\dagger\,\hat{a}_j$ is the particle number operator at site j and U is the energy cost to bring two particles on the same lattice site, determined by

$$U = g\int w_0^4(\boldsymbol{r})\,\mathrm{d}^3\boldsymbol{r}\,. \tag{2.22}$$

For example in the case of spinless bosons in a three-dimensional square lattice the interaction energy can be calculated to be [60]

$$\frac{U}{E_\mathrm{R}} = \frac{g}{E_\mathrm{R}}\int w_0^4(x)\,w_0^4(y)\,w_0^4(z)\,\mathrm{d}^3\boldsymbol{r} \approx \sqrt{\frac{8}{\pi}}\,k\,a_\mathrm{s}\left(\frac{V_0}{E_\mathrm{R}}\right)^{3/4}\,, \tag{2.23}$$

where an harmonic approximation for the Wannier functions $w_0(x)$, $w_0(y)$ and $w_0(z)$ in the three axes of the cubic lattice is used.

The Hamiltonian combining nearest-neighbour tunneling and on-site interactions is called Bose-Hubbard Hamiltonian and reads

$$\boxed{\hat{H}_\mathrm{BH} \approx -J\sum_j \hat{a}_{j+1}^\dagger\hat{a}_j + h.c. + \frac{U}{2}\sum_j \hat{n}_j(\hat{n}_j - 1) + \sum_j \epsilon_j\hat{n}_j}\,. \tag{2.24}$$

The last term is added to account for possible external potentials that change the on-site energies by a local offset of ϵ_j. The system dynamics described by this model strongly depends on the ratio U/J of interaction energy to tunneling energy and on the mean particle density $\bar{n}$ in the lattice.

In the case where the tunneling energy dominates, $U/J \ll 1$, the system forms a superfluid and the density distribution in an external harmonic confinement is given by a Thomas-Fermi profile [65]. In the interaction-dominated case, $U/J \gg 1$, and the absence of an external confinement (ϵ_j = const), the system is in a superfluid phase for all J/U, except when the average number of particles per site $\bar{n}$ is integer. Then the ground state is a Mott-insulator, with exactly integer filling at each site. The transition between the two phases has been first observed in [26]. In three dimensions the transition appears according to mean-field theory at a critical value of $(U/J)_c \approx z\,5.8$ for $\bar{n} = 1$ [66] [16], where z denotes the number of nearest neighbours.

In the case where an external harmonic confinement is present and the central density $\bar{n}$ is larger than 1, both the superfluid and Mott-insulator phases can coexist in the same trap but in spatially separated regions. Due to the incompressibility of the Mott-insulator phase, the density distribution takes the form of a wedding-cake with plateaus corresponding to well-defined integer number of atoms per site (as directly observed in [24]). For further details the reader may consult for example [16] and the references therein.

2.1.5 Laser-assisted tunneling

In the so far discussed case of a particle in a periodic potential, tunneling between different lattice sites appears naturally. There exists however another class of tunneling processes, where the interaction with an external laser field induces the tunneling of the particles in the lattice. These processes, called laser-assisted tunneling, have for example been observed in configurations where neighbouring lattice sites are energetically shifted out of resonance by an additional external potential. The resonant coupling of neighbouring sites with two-photon Raman type transitions can then force an atom to change its lattice site (see for example [67], [48] and [45]). This direct coupling of the external degrees of freedom is one possibility to obtain laser-assisted tunneling.

In this section we introduce laser-assisted tunneling that is based on a laser driven change of the internal atomic state. For this a more complicated lattice configuration needs to be considered, where the potential felt by the atoms depends on their internal state. In such a state-dependent lattice a laser-induced change in internal atomic state can force an atom to change its lattice site. Interesting about the processes of laser-assisted tunneling in general is the fact that the laser phase gets imprinted on the atomic wavefunction, resulting in a complex valued tunneling amplitude. This allows one to engineer for example geometrical phases for atoms on a lattice, which is one essential ingredient to realize artificial gauge fields in optical lattices. The goal of this section is to derive a mathematical expression for the complex effective tunneling amplitude for the case of a simple two-level state-

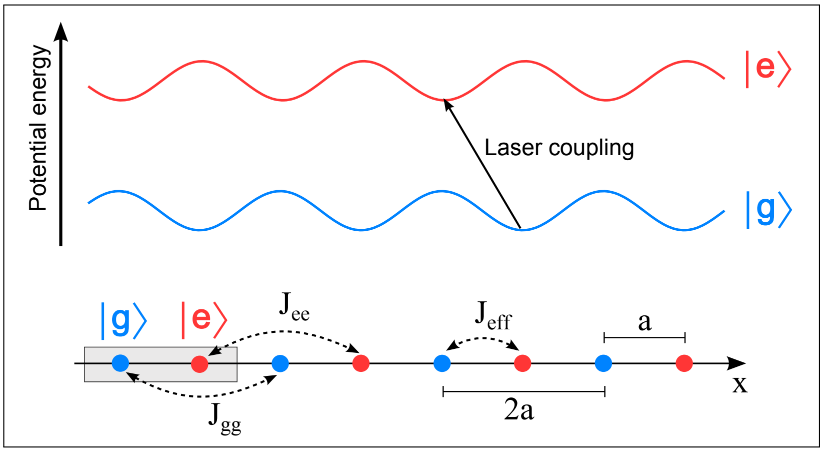

Figure 2.4: Sketch of the considered state-dependent optical lattice. The two internal atomic states $|g\rangle$ (blue circles) and $|e\rangle$ (red circles) arrange in two sublattices separated by a, where $2a$ is the common period of each sublattice. Such an arrangement can be created by a potential landscape as sketched in the upper half of the image. The possible tunneling processes within each sublattice are indicated by J_{gg} and J_{ee}, the laser-assisted tunneling between the two sublattices by J_{eff}.

dependent lattice, that will find direct application in the discussions in chapter 5.

The lattice configuration

In the following a state-dependent optical lattice along x direction is considered as sketched in Figure 2.4. In this lattice configuration two internal atomic states called $|g\rangle$ and $|e\rangle$ arrange in two distinct sublattices each having a lattice constant of $d_x = 2a$. The two sublattices are displaced along the x direction by half a lattice constant $d_x/2 = a$, leading to an alternating pattern of $|g\rangle$ and $|e\rangle$ states. It is to note that the unit cell, representing the repeating pattern of the lattice, contains in this case two atoms, like indicated as gray shaded in Figure 2.4.

The unit cells are in the following labelled by an index $j \in \mathbb{Z}$, such that atoms in $|g\rangle$ are located at positions $\boldsymbol{r}_j^g = 2ja\,\boldsymbol{e}_x$ and atoms in $|e\rangle$ at positions $\boldsymbol{r}_j^e = \boldsymbol{r}_j^g + \boldsymbol{a} = (2j+1)a\,\boldsymbol{e}_x$, where $\boldsymbol{e}_x$ is the unit vector along x. For both sublattices the tight-binding approximation is assumed to be valid and the discussion will be restricted to dynamics in the lowest Bloch band, $n = 0$. In anticipation of the later discussed cases, we assume the atoms in the perpendicular directions y and z also to be confined by separable lattice potentials in the tight-binding regime, that are identical for both states and will not be further specified here. This will in the following be absorbed into the notation of three-dimensional Wannier functions for the atoms in states $|g\rangle$ and $|e\rangle$ denoted by

$$\langle \boldsymbol{r}|w_j^g\rangle = w^g(\boldsymbol{r}-\boldsymbol{r}_j^g) \qquad = w_0^g(x-x_j^g)w_0(y)w_0(z) \tag{2.25}$$

$$\langle \boldsymbol{r}|w_j^e\rangle = w^e(\boldsymbol{r}-\boldsymbol{r}_j^g-\boldsymbol{a}) = w_0^e(x-x_j^g-a)w_0(y)w_0(z)\,, \tag{2.26}$$

where the transverse Wannier functions in the fundamental band $w_0(y)$ and $w_0(z)$ are assumed to be centered around $y = z = 0$.

Without any laser coupling between $|g\rangle$ and $|e\rangle$ the dynamics is governed by simple nearest-neighbour tunneling within each sublattice. The Hamiltonian for non-interacting particles in this case takes the form of two decoupled one-dimensional lattices given by

$$\hat{H}_0 = \sum_j J_{\mathrm{gg}}|g,w_j\rangle\langle g,w_{j+1}| + J_{\mathrm{ee}}|e,w_j\rangle\langle e,w_{j+1}| + h.c.\ , \tag{2.27}$$

with J_{gg} and J_{ee} being the tunneling energies for normal hopping within each sublattice and the short notation

$$|g,w_j\rangle = |w_j^g\rangle \otimes |g\rangle, \quad |e,w_j\rangle = |w_j^e\rangle \otimes |e\rangle\,. \tag{2.28}$$

Coupling the internal states with a laser

The situation becomes different when a coherent laser coupling between the two internal states is added. The interaction is then described by the operator [61]

$$\hat{V}_{\mathrm{coupling}} = \frac{\hbar\Omega_{\mathrm{Rabi}}}{2} e^{i\boldsymbol{k}\cdot\boldsymbol{r}} \otimes |g\rangle\langle e| + h.c.\ , \tag{2.29}$$

where Ω_{Rabi} is the free space Rabi frequency and $\boldsymbol{k}$ the wave vector of the coupling laser field. This operator can be expressed in the basis of Wannier functions by multiplying it from left and right with the completeness relation

$$\mathbb{1} = \Big(\sum_{j\in\mathbb{Z}} |w_j^g\rangle\langle w_j^g|\Big) \otimes |g\rangle\langle g| + \Big(\sum_{j'\in\mathbb{Z}} |w_{j'}^e\rangle\langle w_{j'}^e|\Big) \otimes |e\rangle\langle e|\,, \tag{2.30}$$

where $\mathbb{1}$ denotes the unity operator. Then it takes the form

$$\hat{V}_{\mathrm{coupling}} = \sum_{j,j'} \nu_{j,j'}|g,w_j\rangle\langle e,w_{j'}| + h.c.\ , \tag{2.31}$$

where it now describes tunneling processes of an atom in state $|e\rangle$ at site j' to state $|g\rangle$ at site j and vice versa with an effective tunneling energy of

$$\nu_{j,j'} = \frac{\hbar\Omega_{\mathrm{Rabi}}}{2}\langle w_j^g|e^{i\boldsymbol{k}\cdot\boldsymbol{r}}|w_{j'}^e\rangle\,. \tag{2.32}$$

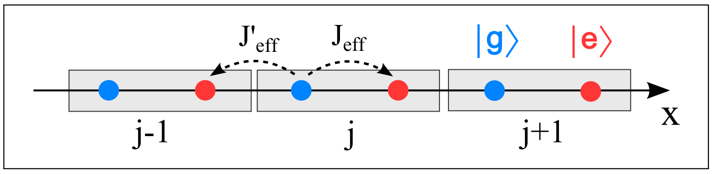

Figure 2.5: Sketch to illustrate the two possible laser-assisted tunneling directions from the same initial site. For tunneling within the same unit cell (gray shaded) the upper sign in equation 2.34 applies. Tunneling to the neighbouring unit cell requires using the lower sign.

These tunneling processes are called laser-assisted since the laser coupling enables the atoms to hop between the sites of the two sublattices, while also changing its internal state.

Within the tight-binding approximation the Wannier functions $|w_j^g\rangle$ and $|w_j^e\rangle$ can be considered as well localized such that only the overlap with nearest neighbours is important. Then the coupling operator can be simplified to

$$\boxed{\hat{V}_{\text{coupling}} \approx \sum_{\langle j,j'\rangle} J_{\text{eff}} |w_j^e\rangle\langle w_{j'}^g| + h.c.} \;, \tag{2.33}$$

where $\langle j, j'\rangle$ denotes the summation over nearest neighbours. The effective tunneling matrix element J_{eff} for nearest-neighbour laser-assisted tunneling is then in general given by the expression

$$\boxed{J_{\text{eff}} = \frac{\hbar\Omega_{\text{Rabi}}}{2}\, e^{i\boldsymbol{k}\cdot(\boldsymbol{r}_j^g \pm \boldsymbol{a}/2)} \int w_0^{e*}(\boldsymbol{r}' \mp \boldsymbol{a}/2)\, e^{i\boldsymbol{k}\cdot\boldsymbol{r}'}\, w_0^g(\boldsymbol{r}' \pm \boldsymbol{a}/2)\, \mathrm{d}^3\boldsymbol{r}'} \;. \tag{2.34}$$

The two different signs correspond to the possible transitions to the right hand side neighbour ($\boldsymbol{r}_j^g \to \boldsymbol{r}_j^e$, upper sign) and the left hand side neigbhour ($\boldsymbol{r}_j^g \to \boldsymbol{r}_{j-1}^e$, lower sign), as sketched in Figure 2.5.

The tunneling amplitude J_{eff} is in general a complex quantity and depends on the overlap integral of the Wannier functions of neighbouring $|g\rangle$ and $|e\rangle$ sites, weighted with a spatially dependent phase factor that describes the phase of the coupling laser field. The form of the coupling Hamiltonian 2.33 is similar to the one of a regular tight-binding model, where the effect to have internal states g and e becomes formally nothing more than an index on alternating lattice sites.

Explicit evaluation of J_{eff} for a square lattice

We next want to look a bit closer at the effective tunneling amplitude J_{eff} in the case of a three-dimensional square lattice as described above. The three-dimensional integration in expression (2.34) can then be decomposed as

$$J_{\text{eff}} = \frac{\hbar\Omega_{\text{Rabi}}}{2}\, e^{i\boldsymbol{k}\cdot(\boldsymbol{r}_j^g \pm \boldsymbol{a}/2)}\, \eta_x\, \eta_y\, \eta_z\,, \tag{2.35}$$

with the three integration factors

$$\eta_x = \int w_0^{e*}(x \mp a/2)\, e^{ik_x x}\, w_0^g(x \pm a/2)\, \mathrm{d}x\,, \tag{2.36}$$

$$\eta_y = \int |w_0(y)|^2 \cos(k_y y)\, \mathrm{d}y\,, \tag{2.37}$$

$$\eta_z = \int |w_0(z)|^2 \cos(k_z z)\, \mathrm{d}z\,, \tag{2.38}$$

and $\boldsymbol{k} = (k_x, k_y, k_z)$. It is to note that η_y and η_z are real quantities due to the mirror symmetry of $w_0(y)$ and $w_0(z)$ with respect to the coordinate origin. We will assume in the following for simplicity that the lattice potentials for $|g\rangle$ and $|e\rangle$ are equal, resulting in identical Wannier functions for the two states, $w_0^g(x) = w_0^e(x)$. Then also η_x is a real quantity and the effective matrix element J_{eff} can be decomposed as

$$J_{\text{eff}} = J_{\text{ge}} e^{i\phi}\,, \tag{2.39}$$

where the phase associated with the tunneling process $\phi = \boldsymbol{k}\cdot(\boldsymbol{r}_j^g \pm \boldsymbol{a}/2)$ is determined by the laser phase at the link location[4]. The amplitude $J_{\text{ge}} = \hbar\Omega_{\text{Rabi}}\, \eta_x\, \eta_y\, \eta_z/2$ is fixed by the vacuum Rabi frequency Ω_{Rabi} and the three integration factors.

A useful approximation for the integration factors can be made when assuming that $1/k_y$ and $1/k_z$ are large compared to the extension of the Wannier functions $w_0(y)$ and $w_0(z)$ (in anticipation of the later realized case), resulting in $\eta_y, \eta_z \approx 1$. A similar approximation can be done for η_x by assuming that the region of significant overlap between $w_0^{g*}(x \mp a/2)$ and $w_0^g(x \pm a/2)$ is small compared to $1/k_x$. Then η_x can be written as

$$\eta_x \approx \int w_0^{g*}(x \mp a/2)\, w_0^g(x \pm a/2)\, \mathrm{d}x\,. \tag{2.40}$$

In the following, numerical values for the integration factors are calculated in order to get the orders of magnitudes involved and to verify the presented approximations for the integration factors.

---

[4] It is to note that other choices for the origin of the integration variable are possible leading to a modified expression for ϕ: Different phase choices correspond to different gauge transformations. The present one is convenient due to its symmetry.

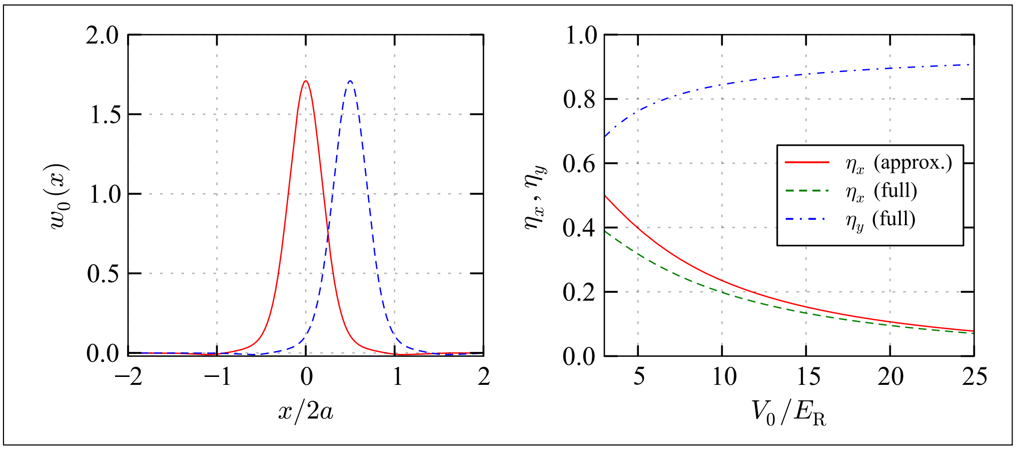

Figure 2.6: On the left hand side the numerically calculated Wannier functions for neighbouring $|g\rangle$ (red solid) and $|e\rangle$ (blue dashed) sites are shown for a lattice depth of $V_0/E_\mathrm{R} = 10$. It is to note that the lattice spacing of each sublattice is $2a$. On the right hand side the numerically calculated overlap integrals η_x and η_y are shown as a function of the depth of the corresponding lattice along x and y respectively. The calculations for η_x are based on the approximated form (2.40) (red solid) as well as on the full form (2.36) (green dashed), assuming equal potential depths for both states $|g\rangle$ and $|e\rangle$. For η_y the full form (2.37) is used and in all cases $k_x = k_y = |\boldsymbol{k}|$ is assumed as described in the text. All graphs are calculated on the same numerical grid consisting of 500 equidistant q-values distributed over the 1. Brillouin zone to calculate the Wannier functions and 800 equidistant real space points in the interval $[-8a, 8a]$ for the overlap calculations.

Important for this is to know the magnitude and the direction of the wave vector of the coupling laser field $\boldsymbol{k}$. In anticipation of the experimental situation, that will be presented in chapter 5, we leave an arbitrary direction for $\boldsymbol{k}$ but we fix its modulus to $|\boldsymbol{k}| = 2\pi/\lambda$ with $\lambda = 578\,\mathrm{nm}$. This value is used in the calculations as an upper limit for k_x and k_y. The numerically calculated overlap integrals are shown in Figure 2.6 as a function of the depth of the applied lattice in the according direction. Along the x direction the lattice depths are assumed to be equal for both states and the lattice spacing to be $2a = 306\,\mathrm{nm}$. Along the y direction we consider a lattice constant of 380 nm. The Wannier functions of two neighbouring $|g\rangle$ and $|e\rangle$ sites are also shown in Figure 2.6 for a lattice depth of $V_0/E_\mathrm{R} = 10$, to illustrate their finite overlap.

It can be seen that η_y takes values above 0.8 for lattices deeper than about $7\,E_\mathrm{R}$. In this range the approximation $\eta_y \approx 1$ (and similar for η_z) is an overestimation with an error of less than 20 %, that decreases with increasing lattice depths. For η_x the approximated form (2.40) also yields an overestimation of the full form (2.36) with a typical error below 20 % above 5 E_R, that also decreases with increasing lattice depth. The accuracies of the approximations are sufficient for later discussions, where we are mostly interested in finding the right orders of magnitudes.

The value of η_x for the typical range of lattice depths shown in Figure 2.6 is decreasing with increasing lattice depths and takes typical values in the range of 0.35 to about 0.1. This allows us to estimate the magnitude of the effective tunneling amplitude J_{ge} to be expected about one order of magnitude lower than the vacuum Rabi frequency Ω_Rabi.

2.1.6 2D lattice with harmonic confinements - conditions for unity filling

The scheme to implement artificial gauge fields in optical lattices (see chapter 5) implies to work with atoms in a two-dimensional optical lattice, where the motion in the third dimension is assumed to be frozen out. Due to the Gaussian envelopes of the laser beams that will be used to create the lattice potentials, residual harmonic confinements will be present on top of the lattice potentials. For reasons explained in section 5.2.3 it is favorable to work with a density corresponding to about one atom per lattice site. To reach this regime the number of atoms and the cloud size have upper limits that depend on the harmonic confinement and the atomic interaction strength. The goal of this section is to find mathematical expressions to estimate these two upper limits that become important in later discussions in section 5.2.

In the following a two-dimensional square lattice (in the x-y plane) of depth V_0 in the tight-binding regime is assumed, with a lattice spacing d and a tunneling energy J. On top of the lattice potential an additional radially symmetric harmonic confinement in the x-y plane of the form

$$V_\mathrm{harm} = \frac{1}{2} m\omega_\perp^2 r^2\,, \tag{2.41}$$

is considered, with $r = \sqrt{x^2+y^2}$ the radial coordinate and $\omega_\perp/2\pi$ the radial trapping frequency. In the z direction the system is assumed to be in the ground state of an harmonic oscillator with wavefunction $\zeta(z)$. The interaction energy for bosonic atoms in the pseudo-potential approximation [60] is then determined by

$$U = g\int |\zeta(z)|^4\,|w(x,y)|^4 \mathrm{d}^3\boldsymbol{r}\,, \tag{2.42}$$

where $g = 4\pi\hbar^2 a_\mathrm{s}/m$ is the interaction parameter with a_s the s-wave scattering length and $w(x,y)$ being the separable Wannier function in the fundamental band.

By approximating the Wannier functions with harmonic oscillator ground state wavefunctions in x and y direction the interaction energy calculates to

$$\frac{U}{E_{\mathrm{R}}} = \sqrt{\frac{8}{\pi}} \frac{a_{\mathrm{s}}}{a_z} \left(\frac{V_0}{E_{\mathrm{R}}} \right)^{1/2} , \tag{2.43}$$

with a_z the harmonic oscillator length in z direction.

Density profile in the superfluid regime

In the following the case of a superfluid will be considered ($U/J \ll (U/J)_c^{2D} = 0.0597$ in two dimensions for $\bar{n} = 1$ [68]). It has been shown in [65] that the atomic density coarse grained over many lattice sites has the form of a Thomas-Fermi profile given by

$$n(r) = \max \left[\frac{\mu - \frac{1}{2} m \omega_\perp^2 r^2}{U}, 0 \right] , \tag{2.44}$$

where μ is the chemical potential. It is to note that $n(r)$ is a smoothed density, normalized to the size of a unit cell $d \times d$, and thus corresponds to the average atom number per lattice site. Compared to a regular Thomas-Fermi profile for a BEC in a harmonic trap, the interaction energy has been rescaled by the one in the lattice, U. The Thomas-Fermi radius is determined by the condition $n(R) = 0$ that yields

$$R = \sqrt{\frac{2\mu}{m\omega_\perp^2}} . \tag{2.45}$$

The total number of atoms is given by

$$N = 2\pi \int_0^R \frac{n(r)}{d^2} r \, \mathrm{d}r = \frac{\pi \mu^2}{m \omega_\perp^2 d^2 U} . \tag{2.46}$$

In order to reach the regime of unity density in the center of the cloud, $n(0) \approx 1$, the chemical potential needs to be on the order of the interaction energy. This determines the cloud radius and atom number in the regime of unity filling to be

$$\boxed{R \approx \sqrt{\frac{2U}{m\omega_\perp^2}} , \quad N \approx \frac{\pi U}{m \omega_\perp^2 d^2} = \frac{\pi R^2}{2 d^2}} . \tag{2.47}$$

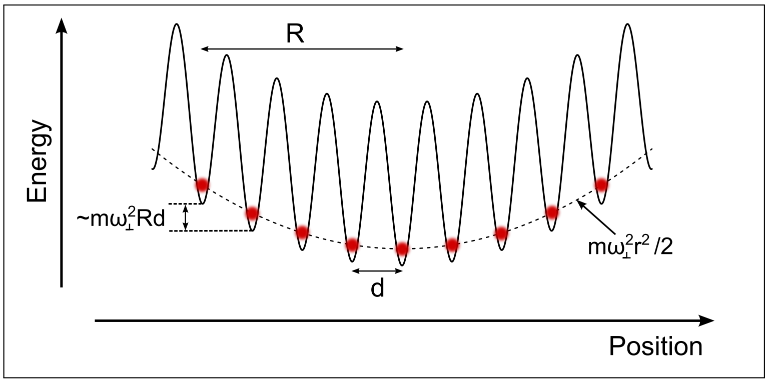

Figure 2.7: Illustration of the modification of the periodic lattice potential with spacing d in the presence of an additional harmonic confinement of the form $m\omega_\perp^2 r^2/2$.

Condition to maintain tunneling in the presence of a harmonic confinement

The presence of the harmonic confinement modifies the energies of the lattice sites as illustrated in Figure 2.7. The energy between neighboring sites is shifted which can lead to the suppression of tunneling if the energy shift becomes large compared to the tunneling energy. The energy shift between neighboring lattice sites is largest at the edge of the cloud where it is given by

$$\Delta E \approx m\omega_\perp^2 R d\,, \tag{2.48}$$

with R the radius of the cloud. To avoid the suppression of the basic tunneling one has to keep

$$m\omega_\perp^2 R d \leq J\,. \tag{2.49}$$

This imposes an upper limit on the harmonic trapping frequency for a given cloud radius R and tunneling energy J. With the expression for the cloud radius R in the case of unity filling, this condition transforms to

$$\boxed{2m\omega_\perp^2 d^2 \leq \frac{J^2}{U}}\,. \tag{2.50}$$

2.2 Orbital magnetism in quantum mechanics

The realization of artificial gauge fields using cold atoms is promising to explore quantum phenomena related to orbital magnetism like for example the quantum

Hall effect. The main idea is thereby to engineer the cold atom quantum system such that the resulting Hamiltonian emulates the physics connected to the phenomena one would like to study. The simplest model Hamiltonian comprising the physics related to the quantum Hall effect is the so-called Harper Hamiltonian. This Hamiltonian describes the physics of non-interacting particles on a 2D lattice in the tight-binding regime, subject to a homogeneous perpendicular magnetic field.

To introduce this Hamiltonian we first review in this section the main concept of orbital magnetism in quantum mechanics and the Aharonov-Bohm phase. Then the case of charged particles on a lattice is considered, where we derive the Harper Hamiltonian and discuss its properties.

2.2.1 Gauge transformation and Aharonov-Bohm phase

In quantum mechanics a particle with charge q and mass m, moving in a magnetic field $\boldsymbol{B}$ is described by the minimal coupling Hamiltonian

$$\hat{H} = \frac{[\hat{p} - q\boldsymbol{A}(\hat{\boldsymbol{r}})]^2}{2m}\,, \tag{2.51}$$

where $\hat{p}$ denotes the canonical momentum operator and $\boldsymbol{A}(\hat{\boldsymbol{r}})$ is the vector potential, connected to the considered magnetic field via

$$\boldsymbol{B} = \nabla \times \boldsymbol{A}\,. \tag{2.52}$$

As in classical electrodynamics, the choice of the vector potential leading to a given magnetic field is not unique. One can add the gradient of a function $\chi(\boldsymbol{r})$ to the vector potential, $\boldsymbol{A}(\boldsymbol{r}) \to \boldsymbol{A}'(\boldsymbol{r}) = \boldsymbol{A}(\boldsymbol{r}) + \nabla\chi(\boldsymbol{r})$, without changing the corresponding magnetic field. This defines a local transformation that is called gauge transformation in classical electrodynamics. In quantum mechanics a complete gauge transformation requires also modification of the wave function of the particle by a local phase factor and the full transformation has the form [61]

$$\boldsymbol{A}(\boldsymbol{r}) \to \quad \boldsymbol{A}'(\boldsymbol{r}) = \boldsymbol{A}(\boldsymbol{r}) + \nabla\chi(\boldsymbol{r})\,, \tag{2.53}$$

$$\psi(\boldsymbol{r},t) \to \quad \psi'(\boldsymbol{r},t) = e^{iq\chi(\boldsymbol{r})/\hbar}\psi(\boldsymbol{r},t)\,. \tag{2.54}$$

It is this combined local transformation that leaves the time-dependent Schrödinger equation invariant.

The fact that the choice of gauge for the vector potential influences the local phase of the particle wave function has been argued by Aharonov and Bohm [69] to be observable in interference experiments. In particular they proposed that a charged particle will pick up an additional phase when encircling an isolated magnetic flux line, without ever passing via a region of non-zero magnetic field. This effect has been observed in several experiments (for example [70], [71]) and has major consequences for our understanding of electromagnetism in the quantum world. It shows that the magnetic field alone does not contain the full information about an electromagnetic field in quantum mechanics and suggests that the vector potential in this sense is the more fundamental field to consider.

In a semi-classical picture the Aharonov-Bohm effect can be described by the effect that a particle moving from point $\boldsymbol{r}_1$ to $\boldsymbol{r}_2$ on a curve $\mathcal{C}$ in space, in the presence of a vector potential $\boldsymbol{A}(\boldsymbol{r})$, acquires a phase proportional to the line integral of the vector potential along the taken path given by

$$\phi(\boldsymbol{r}_1 \to \boldsymbol{r}_2) = \frac{q}{\hbar} \int_{\mathcal{C}} \boldsymbol{A}(\boldsymbol{r}) \cdot \mathrm{d}\boldsymbol{r} \,. \tag{2.55}$$

This phase is called Aharonov-Bohm phase and is picked up in addition to any dynamical (time-dependent) phase. It is independent of the time the particle needs to perform the trajectory and therefore a so-called geometrical phase. For a particle on a closed-loop trajectory $\mathcal{O}$, the phase is given by

$$\phi = \frac{q}{\hbar} \oint_{\mathcal{O}} \boldsymbol{A}(\boldsymbol{r}) \cdot \mathrm{d}\boldsymbol{r} = \frac{q}{\hbar} \iint_{\mathcal{A}} \boldsymbol{B} \cdot \mathrm{d}\boldsymbol{S} \,, \tag{2.56}$$

where $\mathcal{A}$ is a surface with boundary $\mathcal{O}$. The phase picked up by the wave function is therefore directly proportional to the magnetic flux $\Phi = \iint_{\mathcal{A}} \boldsymbol{B} \cdot \mathrm{d}\boldsymbol{S}$ through the area $\mathcal{A}$ defined by the closed loop $\mathcal{O}$.

2.2.2 Orbital magnetism on a lattice - the Harper Hamiltonian

After having briefly reviewed the concept of the Aharonov-Bohm phase in free space we turn here to the case where the quantum particles are confined by a periodic potential to well defined lattice sites. In particular interesting is the case where atoms move only in two dimensions, with a perpendicular magnetic field applied. This corresponds to a typical system where the quantum Hall effect appears.

The simplest case to consider are non-interacting particles with charge q on a two-dimensional square lattice (x-y plane). The lattice sites along x and y are in the following labeled with indices m and n in units of the lattice spacing d. When assuming to be in the tight-binding regime, the system is described by the Hamiltonian

$$\hat{H} = -J \sum_{m,n,\pm} \left(\hat{c}^\dagger_{m\pm1,n} \hat{c}_{m,n} + \hat{c}^\dagger_{m,n\pm1} \hat{c}_{m,n} \right) , \tag{2.57}$$

with $\hat{c}_{m,n}$ is the annihilation operator for a particle at site (m,n). The nearest-neighbour tunneling energy J is for simplicity chosen to be identical along x and y direction.

The goal is next to take the effect of a perpendicular homogeneous magnetic field $\boldsymbol{B} = B_0 \boldsymbol{e}_z$, described by the vector potential $\boldsymbol{A}(\boldsymbol{r})$. When assuming a weak magnetic field such that the coupling to higher bands can be neglected, this can be done by introducing effective tunneling matrix elements. For this, the Aharonov-Bohm phase along the semi-classical (direct line) tunneling trajectory from one site to another is taken into account, resulting in

$$J \to J \exp\left(-i\,\frac{q}{\hbar}\int_{\boldsymbol{r}_1}^{\boldsymbol{r}_2} \boldsymbol{A}(\boldsymbol{r}) \cdot \mathrm{d}\boldsymbol{r}\right) , \tag{2.58}$$

where $\boldsymbol{r}_1$ and $\boldsymbol{r}_2$ denote the position vectors of the two neigbhouring lattice sites involved. This is the so-called Peierls substitution[5]. The Hamiltonian after the substitution reads

$$\hat{H} = -J \sum_{m,n,\pm} e^{-i\frac{q}{\hbar}\int \boldsymbol{A}(\boldsymbol{r})\cdot \mathrm{d}\boldsymbol{r}}\, \hat{c}^{\dagger}_{m\pm1,n}\hat{c}_{m,n} + e^{i\frac{q}{\hbar}\int \boldsymbol{A}(\boldsymbol{r})\cdot \mathrm{d}\boldsymbol{r}}\hat{c}^{\dagger}_{m,n\pm1}\hat{c}_{m,n} \, , \tag{2.59}$$

where the phase factors in the tunneling matrix elements depend on the gauge chosen for the vector potential. When choosing the Landau gauge $\boldsymbol{A} = -B_z\, y\, \boldsymbol{e}_x$, for example, the phases for y direction tunneling vanish, leading to

$$\hat{H} = -J \sum_{m,n,\pm} e^{\pm i2\pi\alpha n}\, \hat{c}^{\dagger}_{m\pm1,n}\hat{c}_{m,n} + \hat{c}^{\dagger}_{m,n\pm1}\hat{c}_{m,n} \, , \tag{2.60}$$

where $\alpha = qBd^2/h = \Phi/\Phi_q$ denotes the magnetic flux through an elementary cell $\Phi = Bd^2$ in units of the quantum of flux for the considered charge $\Phi_q = h/q$. In the case of electrons this would correspond to the well known flux quantum of $\Phi_0 = h/e$. Equation (2.60) is the so-called Harper Hamiltonian. The lattice configuration described by this Hamiltonian is sketched in Figure 2.8, where the possible tunneling processes are illustrated.

It is to note that the exact form of the Harper Hamiltonian depends on the choice of gauge. By choosing for example the vector potential $\boldsymbol{A} = B_z\, x\, \boldsymbol{e}_y$ instead of the previously chosen one, the phases would only appear on the tunneling matrix elements along y direction. However, the relevant quantity that determines the

---

[5] The validity of this substitution leading to an effective Hamiltonian is discussed for example in [72], [73] and [74]. From the point of view of cold atoms, however, the validity is primarily not important since we directly engineer the Harper Hamiltonian (2.60) and are interested in studying the physics associated with it. The question of validity of the Peierls substitution becomes only important when trying to map the physics of the Harper Hamiltonian back to the case of electrons in a periodic potential with a real magnetic field.

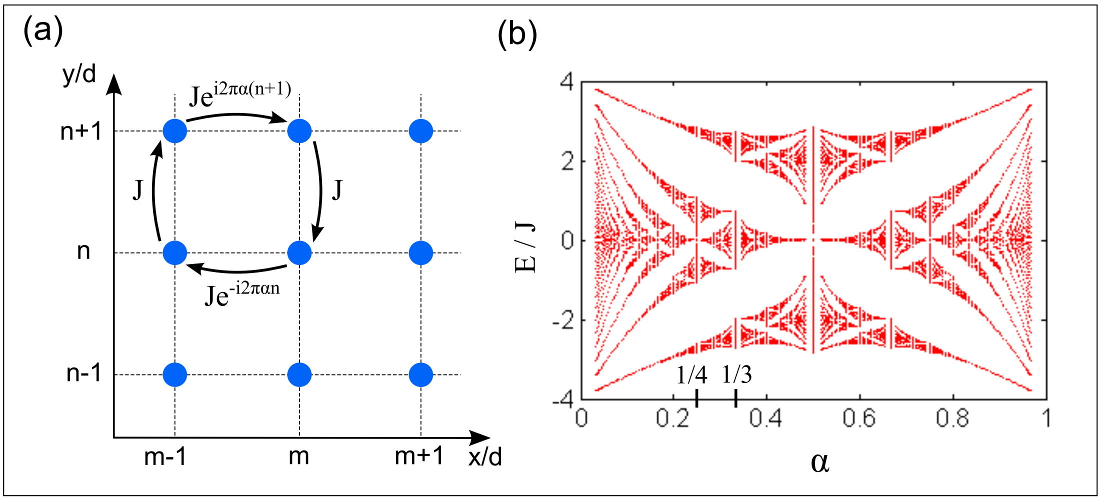

Figure 2.8: (a): Illustration of the lattice configuration of the Harper model. The tunneling matrix elements for a round trip on a unit cell are indicated. (b): Spectrum of the Harper Hamiltonian. Shown in red are the possible eigenenergies within the lowest Bloch band as a function of the normalized magnetic flux α.

physics is the magnetic flux per unit cell that is given by the sum of the phases on each link for a given unit cell of the lattice. By choosing another gauge one can redistribute the phases over the different links, but the sum of the phases on a unit cell will stay constant.

Spectrum of the Harper Hamiltonian

The energy spectrum of the Harper Hamiltonian is entirely characterized by the tunneling energy J and the normalized magnetic flux α. It has been studied by Hofstadter [75], who pointed out its remarkable self similar structure when plotted as an energy vs magnetic flux diagram as shown in Figure 2.8. It is clear that due to the ambiguity of 2π of the phase in the complex tunneling matrix elements, only values of α between 0 and 1 need to be considered. It can furthermore be seen that the spectrum is symmetric with respect to $\alpha = 0.5$, reflecting the fact that the spectrum is invariant under the inversion of the magnetic field direction.

Due to the chosen gauge, the Harper Hamiltonian in equation (2.60) obeys translational symmetry along x, whereas the translational symmetry along the y axis is broken. In the case where α is a rational number given by $\alpha = r/p$, with integer r and p, the translational symmetry along y is restored. The unit cell in this case has the size $d \times pd$ and has p sites per unit cell. Accordingly the fundamental Bloch band of width $8J$ splits into p subbands that are in general separated by energy gaps. This can be seen in the spectrum in Figure 2.8, where the special cases of $\alpha = 1/3$, $1/4$, are marked on the x axis.

It is to note that the magnetic field required to achieve a magnetic flux on the order of one flux quantum ($\alpha \sim 1$) is for a typical solid ($d \sim 0.5\,\mathrm{nm}$) on the order of $B = 10^4\,\mathrm{T}$. Such a strong magnetic field can so far not be realized in a laboratory. However, in the simulation of the Harper Hamiltonian (2.60) with cold atoms in optical lattices, values of α on the order of unity can be quite easily reached. The key for the simulation with cold atoms is thereby to engineer the complex tunneling matrix elements in (2.60) which will be further explained in chapter 5.

CHAPTER 3

Making a Bose-Einstein condensate of ytterbium atoms

The production of a Bose-Einstein condensate (BEC) is a mandatory step to obtain quantum gases in optical lattices: Producing an atomic cloud that is sufficiently cold to be loaded into the fundamental band of the lattice has so far not been demonstrated using laser cooling alone. In order to achieve a Bose-Einstein condensate of ^{174}Yb several steps are performed in this experiment. First an atomic beam of ytterbium is axially decelerated using the Zeeman slowing technique [76]. Then the atoms are captured in a magneto-optical trap (MOT) where they are laser-cooled close to the Doppler cooling limit. Afterwards the cloud is transferred to a single-beam optical dipole trap and is subsequently transported to another vacuum chamber. Finally the atoms are loaded into a crossed dipole trap where the temperature is further reduced using evaporative cooling to reach the BEC transition.

This chapter is devoted to the description of the details of all the above mentioned steps towards a BEC of ^{174}Yb that have been implemented and developed within this thesis work. First the basic electronic level structure of ytterbium is reviewed, followed by a brief description of the experimental control and the vacuum system used. Then the realization of the Zeeman slower and the magneto-optical trap are presented as well as a brief explanation of the absorption imaging technique. Subsequently the transport of the cold cloud in an optical dipole trap and the production of a BEC in a crossed dipole trap are discussed. The chapter terminates with some results on the adiabatic loading of a BEC into an optical lattice.

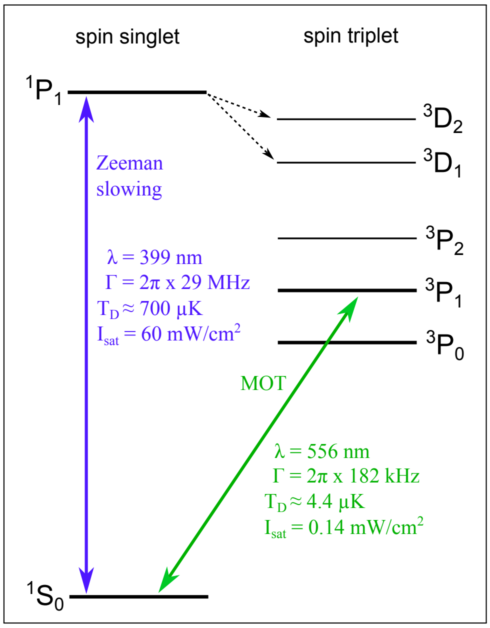

Figure 3.1: Schematic of the relevant lowest-lying electronic energy levels of ytterbium. The transitions used for laser cooling within this thesis are marked with coloured arrows. For those transitions the natural linewidth Γ, the transition wavelength λ, the Doppler temperature T_D and the saturation intensity I_sat are shown. The values are taken from [77] and [78].

3.1 Ytterbium level structure

To explain the laser cooling scheme realized in this experiment, the relevant electronic level structure of ytterbium will be briefly presented in the following. A more complete description of the properties of ytterbium and the lowest lying energy levels can be for example found in [78] and [79] and the references therein.

Ytterbium[1] is part of the Lanthanide series and has seven stable isotopes among which are five bosonic (^{168}Yb, ^{170}Yb, ^{172}Yb, ^{174}Yb, ^{176}Yb) and two fermionic ones (^{171}Yb, ^{173}Yb). The isotope used in this work is ^{174}Yb, which has the highest natural abundance of about 32 %. The electronic ground state configuration of ytterbium is $[\mathrm{Xe}]4f^{14}6s^2$ with two valence electrons closing the outer s-shell. Due to the presence of these two valence electrons, the energy spectrum splits into spin singlet and triplet states (see Figure 3.1) and the electronic level structure is

---

[1] It was first found in a mine near the village Ytterby in Sweden, where it takes its name from. Amusing is the fact that also the elements Terbium and Erbium were first found in this mine and their names were chosen by removing letters from ”ytterbium”.

quite similar to the one of alkaline earth atoms. The so-called "intercombination transitions" between the singlet and triplet manifolds are weakly allowed due to spin-orbit coupling[2]. The accordingly narrow linewidth of these lines is a feature that makes ytterbium interesting for applications like narrow line laser cooling, optical clocks and effective two level systems with negligible spontaneous emission rates. For laser cooling the interesting transitions are $^1\mathrm{S}_0 \leftrightarrow {}^1\mathrm{P}_1$ at about 399 nm and $^1\mathrm{S}_0 \leftrightarrow {}^3\mathrm{P}_1$ at about 556 nm with linewidths of $\Gamma_{399} \approx 2\pi \times 29\,\mathrm{MHz}$ and $\Gamma_{556} \approx 2\pi \times 182\,\mathrm{kHz}$, respectively.

The blue 399 nm transition is advantageous for Zeeman slowing due to its large linewidth and photon momentum. This transition however is not completely closed, since atoms in the $^1\mathrm{P}_1$ state can decay into the $^3\mathrm{D}_1$ and $^3\mathrm{D}_2$ states with a branching ratio that has a lower limit of about 10^{-7} [81]. The subsequent decay back to the $^1\mathrm{S}_0$ ground state via the $^3\mathrm{P}$ manifold can be quite slow since the $^3\mathrm{P}_2$ and $^3\mathrm{P}_0$ states have lifetimes of 12 s and > 20 s [78] respectively. This can lead to strong losses in the cooling cycle when operating a magneto-optical trap on the $^1\mathrm{S}_0 \leftrightarrow {}^1\mathrm{P}_1$ transition, as observed in [81]. For Zeeman slowing, however, where about $10^4 - 10^5$ photon absorption-reemission cycles are necessary for a complete deceleration of an atom, the depumping losses are have not been observed to be problematic.

The intercombination transition at 556 nm on the other hand is advantageous for magneto-optical trapping since the Doppler temperature is only about $T_\mathrm{D}^{556} \approx 4.4\,\mu\mathrm{K}$, due to its narrow linewidth. Having such a low Doppler temperature is important since sub-Doppler cooling mechanisms are not available for bosonic ytterbium due to the non-degenerate ground state. For the fermionic isotopes sub-Doppler cooling exists and has been observed in [82] for a MOT on the $^1\mathrm{S}_0 \leftrightarrow {}^1\mathrm{P}_1$ transition. Other particularities of a MOT on this transitions are further discussed in section 3.5.2.

3.2 Experimental control

Creating a Bose-Einstein condensate and performing subsequent experiments requires a real time electronic control system including synchronized digital and analog output channels. This is necessary since almost all steps during an experimental sequence are electronically controlled. This implies, amongst others, fast switching and pulsing of laser beams as well as ramping of laser frequencies and

---

[2] Without spin-orbit coupling the Russel-Saunders (or LS) coupling regime is realized. In this regime singlet-triplet transitions cannot occur, since the total spin quantum number cannot change. It is to note, however, that pure LS coupling does not strictly apply to atoms as heavy as ytterbium [80], although the usual convention is to use labels as in the LS coupling regime.

coil currents. Ideally the control system should be freely programmable and the experimental sequence be changeable from one run to another.

The control system used in this experiment is similar to the one described in [83] and [84]. Its electronic part is realized by a modular commercial real time control system that consists of a chassis[3] hosting exchangeable modules for digital and analog inputs and outputs as well as a module for the communication with a PC. In the current configuration[4], a total of 64 digital outputs, 27 analog outputs and miscellaneous digital and analog input channels are available. The values on the digital and analog outputs can be set with a time step resolution of $2\,\mu$s. Both digital and analog outputs are additionally buffered using opto-isolators (digital) and differential amplifiers (analog) within home-built circuits. The bandwidth of the analog outputs is several tens of kHz and the voltage range is $\pm 10\,$V, which is addressed in 12 bit or 16 bit resolution, depending on the output channel.

The programming and interfacing of the electronic control system with a PC is done using an open source experiment control program called Cicero[5] [84]. The program allows one to define an experimental sequence where each digital and analog channel can be freely programmed (within some maximum number of time steps). The programmed sequence is then uploaded to the real time system and can be executed repeatedly. Among the features of Cicero a particularly useful one is that predefined variables can be automatically changed from one run to another in order to perform parameter scanning and optimization. Equally useful are predefined communication protocols like RS232 and GPIB. A support to send TCP messages at the beginning of each sequence has been added by us in order to adapt to the present experimental needs. This is especially handy to send information about the current sequence to other PC systems in the network (for instance to the PC used for saving and analyzing images).

3.3 Vacuum system and atomic beam

In order to achieve Bose-Einstein condensation of a trapped atomic gas, an ultra-high vacuum (UHV) system is needed with a pressure at least as low as 10^{-10} mbar. This is mainly necessary to reduce collisions with the residual background gas (at room temperature) that would otherwise heat and deplete the atomic cloud very quickly.

---

[3] PXIe-1065, National Instruments.

[4] Currently used modules: PXIe-8370, PXI-6713 (x2), PXI-6733, PXI-6534, PXI-6535 and PXI-6363.

[5] This has been developed by Aviv Keshet, a former PhD student in the group of Wolfgang Ketterle at MIT and is used in many groups all over the world these days.

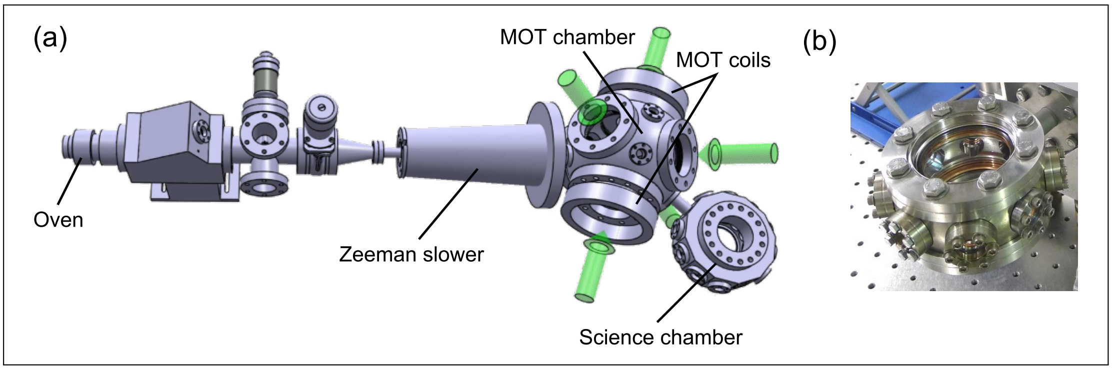

Figure 3.2: 3D Model of the vacuum system similar to the one used within this thesis (a). The green arrows indicate the direction of the six MOT beams. The science chamber in (a) is just an illustrative model, the one used within this thesis is shown in (b).

The vacuum system used in this experiment consists of three main sections in the following referred to as science chamber, MOT chamber and atomic beam section [see Figure 3.2 (a)]. The main idea of the chosen design is to spatially separate magneto-optical trapping and Zeeman slowing from the part where the actual experiments are carried out. This is required to ensure enough optical access to perform the planned experiments on artificial gauge fields in optical lattices.

MOT and science chamber

The science chamber used during this thesis[6] [see Figure 3.2 (b)] offers two CF63[7] connections in the vertical direction and eight CF16 connections in the horizontal plane used for the dipole trap and lattice beams as well as several imaging axis. One of the CF16 ports is used to attach a 2 l/s ion pump. The connection from the science chamber to the MOT chamber is realized via a CF16 tube. The MOT chamber itself is a commercially available model[8] having an outer diameter of about 18 cm. It offers eight CF16 ports that are partially used for the single beam dipole trap, the atomic beam arrival and the Zeeman slower beam. The four available CF63 and two CF100 ports are used for the six MOT beams and imaging. The pumping of this part is done by a 40 l/s ion pump and a NEG getter pump[9] that are connected using a CF63 T-shaped piece. The distance from the center of the

---

[6] It has been recently replaced by a different model that is more adapted to the experimental needs to realize artificial gauge fields.

[7] CF = conflat.

[8] 6.0” Spherical Square, MCF600-SphSq-F2E4A8 from Kimball Physics.

[9] Capacitorr D200, SAES Getters

MOT chamber to the center of the science chamber is about 22 cm. This is also the distance over which the atoms need to be transported.

Differential pumping and pressures

The atomic beam part hosts the ytterbium oven and is connected to the MOT chamber via two differential pumping stages. The first one consists of a CF40 blind flange of 2 cm thickness with a central bore hole of 4 mm diameter with a 20 l/s ion pump placed behind. The second one is a 30 cm long CF16 tube with an inner diameter of 10 mm, that is surrounded by the Zeeman slower and connects directly to the MOT chamber. Furthermore a linear valve is installed that allows one to isolate the MOT and science chamber from the atomic oven for potential maintenance or refilling of the oven. The volume right behind the atomic oven is pumped by two 20 l/s ion pumps. The distance from the oven exit to the center of the MOT is about 90 cm.

The pressures in the different parts are monitored using the calibrated ion pump currents. Having the oven switched off (on, at $T = 400\,^\circ\mathrm{C}$) they value to about 3×10^{-9} mbar (5×10^{-8} mbar) behind the exit of the atomic oven and about 3×10^{-10} mbar (5×10^{-10} mbar) in the MOT chamber. The pressure in the science chamber cannot be measured below 10^{-9} mbar due to the limitation on the measurable current in the 2 l/s ion pump. Its pressure however is expected to be similar to the one in the MOT chamber, since similar lifetimes have been measured in both chambers. These pressure values are achieved without a bake out of the vacuum system.

It is to note that all ion pumps used in the setup are shielded by a Mu-metal housing to minimize the influence of the pump magnetic fields on the MOT quadrupole field. This is important since the MOT magnetic field gradients are relatively small (~ 1 Gauss/cm).

Oven design

In order to create an atomic beam, a reasonable vapor pressure for the considered atomic species needs to be reached. For ytterbium, this implies to work at temperatures on the order of 400 °C which is realized in an oven that consists of a simple stainless steel reservoir with ytterbium chunks placed inside. A copper tube of $L = 10$ cm length and $d = 2$ mm inner diameter is screwed to the oven in order to collimate the exiting atomic beam. The heating of the oven is performed by two heating collars[10] and an additional heating tape wrapped around. Those are configured such that the temperature of the collimation tube is always kept about 10 °C above the oven temperature. This prevents clogging of the tube due

---

[10] Bought from Acim Jouanin.

to adsorption of ytterbium on its walls, which has been observed to be an issue when the tube is not specifically heated. To inhibit the rest of the vacuum chamber from heating up as well, the connecting CF40 flange of the oven is in thermal contact with a water cooled copper pipe. This allows us to have temperatures of 40 °C about ten centimeters away from the oven.

Atomic beam

The properties of the atomic beam that exits the oven are mainly determined by its temperature T and the geometry of the collimation tube placed at its exit. The atomic velocities $\boldsymbol{v}$ of the vapour inside the oven volume are distributed according to the Maxwell-Boltzmann law

$$f(\boldsymbol{v}) = \left(\frac{m}{2\pi k_\mathrm{B}T}\right)^{3/2} e^{-mv^2/2k_\mathrm{B}T}\,, \tag{3.1}$$

where m is the mass of an atom and k_B the Boltzmann constant. The collimation tube of length L and radius R effectively acts as a velocity filter for the atoms leaving the oven. When neglecting gravity, only atoms with a ratio of axial to transverse velocity of $v_\mathrm{ax}/v_\perp \lesssim L/2R$ can leave the oven without hitting the collimation tube wall. This filtering forms an atomic beam with a theoretical full beam divergence angle that approximates to $\theta_\mathrm{div} \approx R/L \approx 0.6\,^\circ$ for the present parameters. The longitudinal velocity distribution after the velocity filtering is calculated as

$$f(v_\mathrm{ax})_\mathrm{beam} = \sqrt{\frac{m}{2\pi k_\mathrm{B}T}}\, e^{-mv_\mathrm{ax}^2/2k_\mathrm{B}T}\left[1 - \exp\left(\frac{-mv_\mathrm{ax}^2 4R^2}{2k_\mathrm{B}TL^2}\right)\right]. \tag{3.2}$$

In the present case of a very long and thin collimation tube ($L \gg R$), this expression is well approximated by

$$f(v_\mathrm{ax})_\mathrm{beam} \approx \frac{R^2}{L^2}\, 4\pi \left(\frac{m}{2\pi k_\mathrm{B}T}\right)^{3/2} v_\mathrm{ax}^2\, e^{-mv_\mathrm{ax}^2/2k_\mathrm{B}T}\,. \tag{3.3}$$

The most probable velocity of this distribution is $\sqrt{2k_\mathrm{B}T/m}$ and the root mean square velocity is $\sqrt{3k_\mathrm{B}T/m}$. The distribution is shown in Figure 3.3 for our experimental parameters.

3.4 Zeeman slower

In order to capture atoms from the atomic beam into the magneto-optical trap, the velocity of the atoms needs to be brought below the capture velocity of the MOT

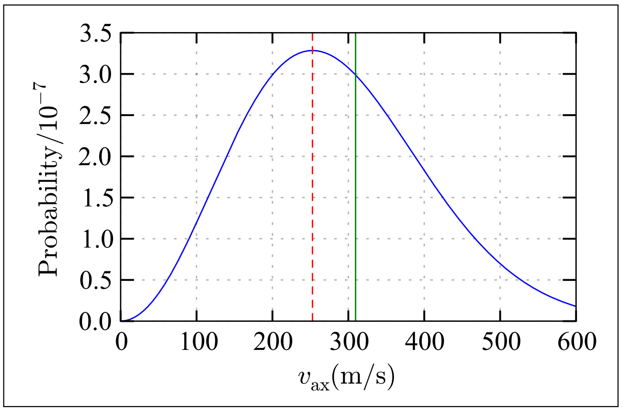

Figure 3.3: Calculated axial velocity distribution of the atomic beam according to equation (3.2). The curve is plotted for a temperature of $T = 400\,°\mathrm{C}$ and a collimation tube of length $L = 10\,\mathrm{cm}$ and radius $R = 1\,\mathrm{mm}$. The most probable velocity $\sqrt{2k_{\mathrm{B}}T/m}$ is at about 250 m/s (red dashed vertical line) whereas the root mean square $\sqrt{3k_{\mathrm{B}}T/m}$ is at about 310 m/s (green solid vertical line).

which is in our case expected to be on the order of $v_{\mathrm{c}} \sim 5\,\mathrm{m/s}$ (see [85] and section 3.5.2). However most of the atoms in the atomic beam have an axial velocity much larger than v_{c}, according to the discussion in the previous section. To increase the number of atoms within the capture range of the MOT the atomic beam is axially decelerated using the Zeeman slowing technique with a laser resonant with the $^1\mathrm{S}_0 \leftrightarrow {}^1\mathrm{P}_1$ transition.

3.4.1 Working principle

The Zeeman slowing technique is based on the radiation force of a resonant laser beam on an atom. When choosing this laser beam to be counter propagating with respect to the atomic beam direction, axial deceleration can be achieved. Having the laser in resonance with an atomic transition, the acceleration for an atom with mass m is given by [86]

$$a = \frac{\Gamma}{2}\frac{\hbar k}{m}\frac{s}{s+1}\,, \tag{3.4}$$

with Γ the natural linewidth of the atomic transition, $\hbar k$ the photon momentum of the resonant light and $s = I/I_{\mathrm{sat}}$ the saturation parameter given by the ratio of laser intensity to saturation intensity. In the case of a constant uniform deceleration of a, the velocity of an atom along the propagation axis z evolves like

$$v(z) = v_0\sqrt{1 - \frac{z}{z_0}}\,, \tag{3.5}$$

where v_0 is the initial velocity and $z_0 = v_0^2/2a$ is the distance needed to stop the atom. Due to the Doppler shift, the frequency detuning $\delta/2\pi$ of the light with respect to resonance of the moving atom depends on the axial velocity and therefore on the position z via

$$\delta(z) = \omega_\mathrm{L} - \omega_0 + kv(z)\,, \tag{3.6}$$

where $\omega_\mathrm{L}/2\pi$ denotes the laser frequency and $\omega_0/2\pi$ the atomic resonance frequency for an atom at rest. In order to keep the light force on the atoms maximal, the resonance condition $\delta(z) = 0$ needs to be fulfilled along the total distance of deceleration. This can be achieved by adding a spatially varying magnetic field that compensates the Doppler shift via the Zeeman effect. For the case of an atomic resonance from state g to e with total angular momenta $J_g = 0 \rightarrow J_e = 1$ (like the ${}^1\mathrm{S}_0 \leftrightarrow {}^1\mathrm{P}_1$ transition in ytterbium) that is driven by circularly polarized light, the ideal magnetic field profile arising from the conditions $\delta(z) = 0$ and constant deceleration calculates to

$$B_\mathrm{ideal}(z) = -\frac{\hbar(\omega_\mathrm{L} - \omega_0)}{\mu} - B'\sqrt{1 - \frac{z}{z_0}}\,, \tag{3.7}$$

with $B' = \hbar k v_0/\mu$ and $\mu = g_e M_e \mu_\mathrm{B}$, where $g_e = 1.035$ [87] is the Landé g-factor of the excited state, $M_e = \pm 1$ the magnetic quantum number and μ_B the Bohr magneton.

The first term in equation (3.7) describes a magnetic field offset that determines the frequency detuning of the Zeeman light with respect to atom at rest, $\delta_{v=0} = \omega_\mathrm{L} - \omega_0$. The second term is the spatially varying magnetic field part that ensures the resonance condition for the atoms during deceleration which can be chosen to be either increasing or decreasing along the propagation direction of the atom. The circular polarization of the counter propagating beam has to be adapted accordingly.

On the contrary to the case of alkali atoms, depumping losses at a magnetic field zero crossing, where atoms could exit the cycling transition, are very small (see section 3.1). This allows one to operate the Zeeman slower with a magnetic field zero crossing along the deceleration distance, without the need for additional repumping light. Such a configuration is advantageous since it reduces the peak amplitude of the required magnetic field.

3.4.2 Laser system at 399 nm

To create the 399 nm light needed for Zeeman slowing on the ${}^1\mathrm{S}_0 \leftrightarrow {}^1\mathrm{P}_1$ transition, the technique of frequency doubling is used. The source for the laser light at the fundamental wavelength of 798 nm is a commercial tapered amplifier system[11] providing an output power of about 500 mW. This light is frequency doubled in a ppKTP[12] non-linear crystal of 1 cm length at a quasi-phase matching temperature of about 75 °C. Since the maximum doubling efficiency in a single pass configuration would only be on the order of several percent, the crystal is placed in an enhancement cavity with a finesse of about 60. The achieved maximum output power when locking the cavity is on the order of 100 mW.

The waist in the crystal is chosen to be on the order of 200 μm which is quite far from the theoretical optimum for the Boyd-Kleinman factor of 23 μm to achieve the highest doubling efficiency. The reason is that strong thermal effects in the ppKTP crystal have been observed, similar to the ones reported for example in [88]. These effects lead to local heating of the crystal due to an enhanced absorption of infrared light in the presence of frequency-doubled blue light. This influences locally the refractive index of the crystal and therefore the effective cavity length in a non-linear way. Experimentally this can be observed as highly asymmetric cavity peaks when scanning the cavity resonances slow enough ($\sim$ 50 ms), as shown in Figure 3.4. In one scanning direction the peak looks almost like an orthogonal triangle. The steep fall-off on one of the wings lead to difficulties in achieving a stable cavity locking. To circumvent this problem, the intensity in the crystal has been lowered by increasing the waist and thus reducing the thermal effects. This results in a reduced output power but the achieved power on the order of 100 mW is found to be sufficient for our experimental needs.

Frequency locking using a hollow cathode lamp

To frequency lock the Zeeman laser a saturated absorption spectroscopy is performed. To create an ytterbium vapor with a reasonably high density, an ytterbium hollow cathode lamp (HCL) is used. A HCL consists of a glass cell filled with a nobel buffer gas in which a discharge between an anode and an ytterbium coated cathode is driven. The buffer gas ions created in the discharge are accelerated towards the cathode where they sputter off ytterbium atoms from the surface. The local vapour density of ytterbium is high enough to perform spectroscopy. This is in particular interesting as a low cost and simple to set up alternative to the construction of a heat pipe which can be quite involved (see section 3.5.3). For the model used in this experiment[13] the achievable level of relative absorption at 399 nm is on the order of 20 % at the nominal discharge current of 10 mA. Absorptions above 90 % have been observed when running the lamp close to its maximum

---

[11] Toptica TA-Pro.

[12] Periodically poled potassium titanyl phosphate.

[13] Model used here: 50 mm HCL, Heraeus.

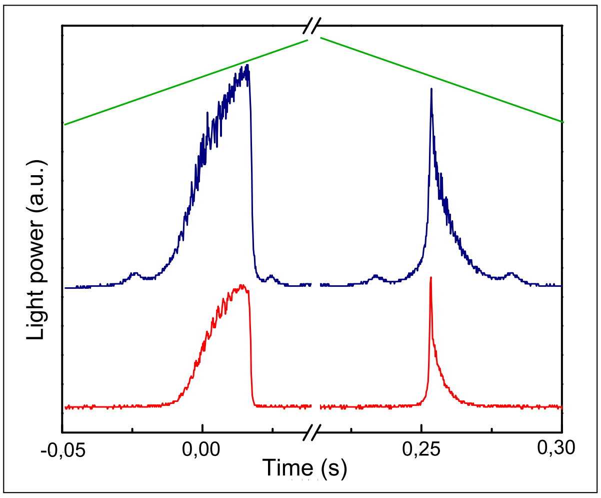

Figure 3.4: Observation of thermal effects in the ppKTP crystal. Shown is the light power leaking the doubling cavity for the infrared light (red curve) and the frequency doubled blue light (blue curve), when scanning the cavity length with a piezoelectric actuator. The shown cavity resonance is scanned with increasing and decreasing cavity length, as indicated by the green lines.

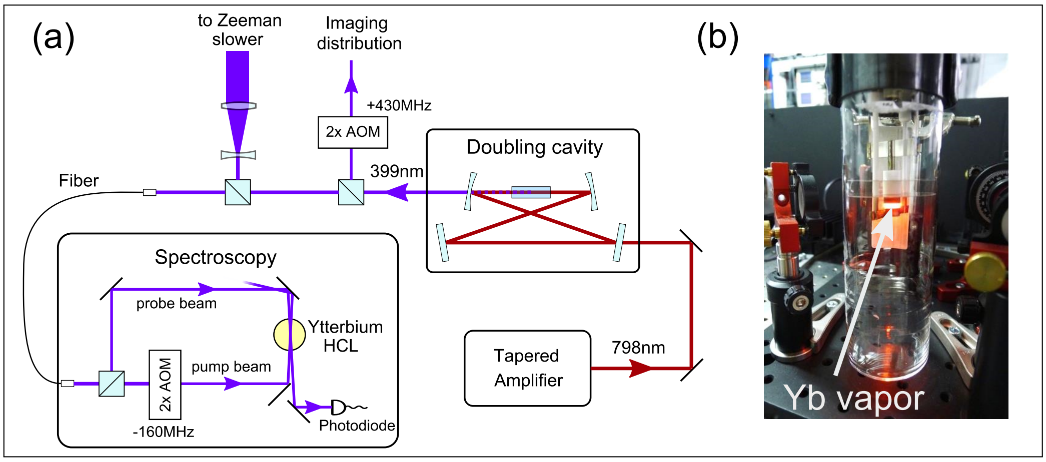

Figure 3.5: (a): Optical setup of the 399 nm laser used for Zeeman slowing and imaging. (b): Photo of the hollow cathode lamp used to perform saturated absorption spectroscopy. The orange fluorescence of the collisionally excited buffer gas and ytterbium atoms indicates the region of high vapour density.

current. However a trade off between signal strength and lamp lifetime has to be found[14].

The setup for the saturated absorption spectroscopy is sketched in Figure 3.5. The laser is locked to the ^{176}Yb line that is 509 MHz red detuned [79] with respect to the ^{174}Yb transition. The fact that the pump beam frequency is shifted with respect to the probe beam by -160 MHz, leaves the pump beam in the locked state with a detuning of +80 MHz with respect to the ^{176}Yb line. This results in a total detuning of the Zeeman beam of about -429 MHz with respect to the ^{174}Yb transition.

3.4.3 Experimental realization and optimization

Zeeman slower configuration

The Zeeman slower has been designed[15] for a constant maximum deceleration of $a_{\text{design}} = \eta\, a_{\text{max}}$. The safety parameter $\eta \leq 1$ is intended to account for experimental imperfections leading to possible deviations from the theoretical maximum acceleration of $a_{\text{max}} = \hbar k \Gamma / 2m$. In the present case the safety parameter is chosen to be $\eta = 0.4$ which determines the length of the Zeeman slower to be 24 cm. The maximum slowed velocity per design is $v_{\text{max}} = 311$ m/s, which is comparable to the root mean square velocity in Figure 3.3. The final velocity is optimized to be well below 10 m/s.

The magnetic field of the Zeeman slower is created by two separate layers of coils. The first one has a constant number of windings along the slower length and is intended to produce an homogeneous offset field. This offset field corresponds to the first term in equation (3.7) and will determine the detuning of the Zeeman beam with respect to an atom at rest. The second coil has a spatially varying number of windings to create the needed field gradient according to the second term in equation (3.7). The magnetic field produced by the two coils has been measured experimentally and is compared to the simulated and ideal field in Figure 3.6. The field configuration shown in this figure is close to the final one found in the experimental optimization. To compensate for the small remaining magnetic field at the MOT position, an additional compensation coil is placed at the end of the Zeeman slower. For heat dissipation purposes, the gradient and offset coils are placed between two layers of water-cooled copper tubes. The distance from the end of the Zeeman slower to the MOT is about 13 cm.

---

[14] It has been observed that the transmission of the glass cell reduces over time due to some material deposit on the walls. It dropped from about 80 % at the beginning to 50 % after 3 months and to 17 % after 10 months of operation.

[15] Details about the design and theoretical simulations will be presented in the upcoming PhD thesis of Alexandre Dareau.

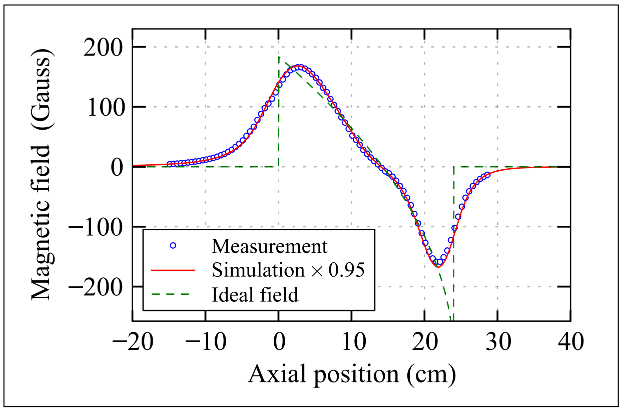

Figure 3.6: Magnetic field produced by Zeeman gradient and offset coil along the axis of the Zeeman slower. The blue circles are the measured field values for a current of 9.2 A in both gradient and offset coil. The red curve corresponds to the simulated field for the used coil configuration which is in accordance with the real field up to a scaling factor of 0.95. The green dashed line shows the form of the ideal magnetic field from equation 3.7.

The frequency detuning of the counter propagating Zeeman laser beam is fixed at $\delta_{v=0} \approx -15 \times \Gamma_{399} \simeq -2\pi \times 430\,\text{MHz}$ with respect to an atom at rest. In this way, the circularly polarized Zeeman light is not in resonance with the atoms in the MOT. The Zeeman beam has a $1/e^2$ diameter of about 8 mm at the entrance of the MOT chamber and is focussed to approximately match the divergence of the atomic beam.

Experimental optimization

The main optimization of the Zeeman slower consists in adapting the magnetic field gradient and offset to have the largest fraction of atoms following a constantly slowed velocity trajectory. This also depends on the maximum scattering rate imposed by the intensity of the Zeeman beam.

Experimentally the optimization of the Zeeman slower coil currents is performed by maximizing the number of atoms in the MOT for a fixed loading time. The detuning of the Zeeman beam is kept constant at -15$\times\Gamma_{399}$ during the full optimization. Due to the relatively small gradient of the MOT magnetic field ($\sim$ 1 Gauss/cm), the MOT position is influenced by changes in the magnetic field of the Zeeman slower. To ensure the same loading conditions for all measurements, the current in the compensation coil has been adapted to keep the MOT at the same position. An example optimization curve is shown in Figure 3.7.

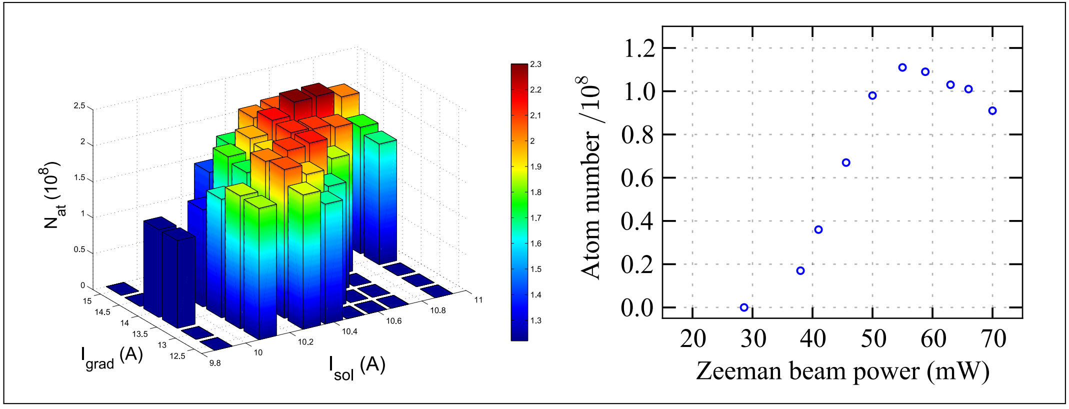

Figure 3.7: Example data of the optimization of the Zeeman slower parameters. On the left-hand side a 2D-optimization of the Zeeman offset and gradient coil currents on the MOT atom number is shown. The optimum is found to be at $I_{\text{grad}} = 14.5\,\text{A}$ and $I_{\text{offset}} = 10.6\,\text{A}$ with a total number of captured atoms of $N_{\text{atoms}} = 2.3 \times 10^8$ after 15 s loading. On the right-hand side the atom number in the MOT is shown as a function of the applied Zeeman beam power, keeping all other parameters fixed.

The power in the Zeeman beam has been scanned for a fixed set of Zeeman coil parameters. Some example optimization data is shown in Figure 3.7. It can be seen that there is an optimum value for the Zeeman power and that too much power leads to a reduced MOT loading. This is expected to be due to an increase in light force at higher powers that pushes the atoms that arrive from the Zeeman slower back towards the latter before they can reach the MOT capture region. Here the optimum is found for about 55 mW which corresponds to a saturation parameter on the order of $s = I/I_{\text{sat}} \approx 3$ at the position of the MOT.

3.5 Magneto-optical trap

The realization of the magneto-optical trap on the ${}^1\text{S}_0 \leftrightarrow {}^3\text{P}_1$ transition is presented in this section. First some general considerations of a MOT on this transition are presented followed by the experimental implementation and optimization.

3.5.1 Working principle

A magneto-optical trap (MOT) is a combination of an optical molasses and a quadrupole magnetic field. The optical molasses thereby consists of three orthogonal pairs of counter propagating laser beams that are slightly red detuned with respect to an atomic transition. The molasses is used to cool the atoms via a velocity dependent light force. In a semi-classical description this light force takes the role of a damping term in the equations of motion for an atom [86]. The quadrupole magnetic field allows us to add a position dependence on the radiative force that is used to create an effective confinement for the atomic cloud. In the semi-classical picture this corresponds to a restoring force for the atoms towards the region of zero magnetic field. For the following discussion two characteristic quantities of a MOT are important, namely the lowest achievable temperature and the capture velocity.

The capture velocity of a MOT denotes the limit velocity above which an incident atom cannot be trapped. This velocity is mainly determined by the maximum number of photons the atom can scatter within the interaction volume with the MOT and the associated photon recoil momentum. A precise quantification of the capture velocity is in general not easy and requires numerical simulations. However an optimistic estimation can be given by assuming the maximum possible radiation force acting constantly on the atom within the crossing volume of the MOT beams. When approximating the diameter of the crossing volume by twice the MOT beam waist $2w_0$, the capture velocity calculates to

$$v_\mathrm{c} \simeq \sqrt{2w_0 \hbar k \Gamma / m}\,, \tag{3.8}$$

where Γ denotes the natural linewidth of the MOT transition. This estimation gives an upper limit on the capture velocity in the sense that the required magnetic field profile to keep the atoms in resonance during deceleration would be that of a Zeeman slower (see equation 3.7). In reality however the quadrupole field will have a constant field gradient and the real capture velocity is therefore expected to be a fraction of this estimation. The main techniques to approach the ideal case consist in enlarging the effective frequency spectrum of the cooling light such that the resonance condition is fulfilled for a larger range of atomic velocities during deceleration. This can be achieved by adding frequency sidebands to the MOT light or by working in a high saturation broadening regime. The latter also slightly increases the effective interaction volume between MOT beams and atoms.

The temperature of the atoms in a MOT is determined by an equilibrium of the laser cooling effect and heating caused by the diffusion of the atomic momentum associated with the spontaneous emission during the cooling cycles. The resulting minimum equilibrium temperature in a single atom picture is called the Doppler temperature and is given by [86]

$$T_\mathrm{D} = \frac{\hbar\Gamma}{2k_\mathrm{B}}\,. \tag{3.9}$$

In order to reach this temperature the MOT light intensity has to be small compared to the saturation intensity, $I \ll I_{\mathrm{sat}}$. However, this limit temperature can be beaten by means of sub-Doppler cooling mechanisms [3] [4]. It is furthermore to note that for the typical atom numbers in our experiment the density in the MOT is at a level where effects of multi-photon scattering become important and the single atom picture breaks down [89]. Therefore we do not expect to reach the Doppler limit experimentally.

3.5.2 Particularities of a MOT on the $^1\mathrm{S}_0 \leftrightarrow {}^3\mathrm{P}_1$ transition.

The ytterbium MOT in this experiment is performed on the $^1\mathrm{S}_0 \leftrightarrow {}^3\mathrm{P}_1$ transition and is directly loaded from the Zeeman slower. The natural linewidth of the used transition $\Gamma_{556} = 2\pi \times 182\,\mathrm{kHz}$ is quite small compared to transitions usually used in alkali atoms with Γ on the order of at least several MHz [90]. One major consequence is that the Doppler temperature is only about $T_{\mathrm{D}} \simeq 4.5\,\mu\mathrm{K}$ which allows one to easily reach sufficiently low temperatures for efficient loading in optical dipole traps. This feature is especially important since no sub-Doppler cooling mechanism is available for bosonic ytterbium atoms. This results from the fact that for bosonic ytterbium there is only one single non-degenerate ground state. This, on the other hand, has the advantage that no repumping light is needed, compared to the case of alkali atoms.

The difficulty in realizing a MOT on this narrow transition lies in the intrinsically reduced capture velocity according to the estimated $\propto \sqrt{\Gamma}$ scaling in equation (3.8). In alkalis typical capture velocities are on the order of several tens of m/s [91] whereas for ytterbium an upper limit estimation using equation (3.8) yields about 10 m/s, assuming a MOT beam diameter of $2w_0 \approx 3\,\mathrm{cm}$. Consequently this necessitates the use of large MOT beams and potentially the use of frequency sidebands or strong saturation broadening to reach reasonable capture velocities as well as a careful design of the Zeeman slower. Furthermore the fact that the scattering rate is small requires also smaller MOT magnetic field gradients as compared to alkalis which increases the sensitivity to magnetic stray fields. Typically gradients are on the order 1 G/cm.

3.5.3 Laser system at 556 nm

The light for magneto-optical trapping at 556 nm is created using second harmonic generation of a fiber laser[16] emitting at 1112 nm with an output power of 2 W. The frequency doubling is carried out in a ppSLT non-linear crystal of 2 cm length. To

---

[16] Orange One, Menlo Systems.

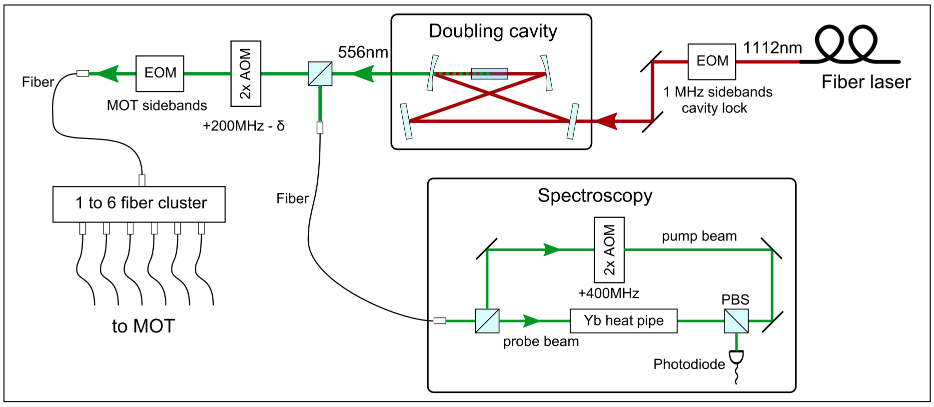

Figure 3.8: Simplified sketch of the optical setup used for the MOT light system. The electro-optical modulator (EOM) directly after the 1112 nm laser is used to create the locking signal for the doubling cavity lock. The EOM before the cavity is used to add sidebands with negligible amplitude for cavity locking. Legend: 2xAOM: AOM in double passage, PBS: polarizing beam splitter cube.

enhance the doubling efficiency with respect to a single pass configuration the crystal is placed in a bow-tie type enhancement cavity with a finesse of about 50. The waist in the crystal is about 45 μm and the maximum observed green power at the output of the doubling cavity on the order of 900 mW.

The laser setup is sketched in Figure 3.8. The frequency doubled light for the MOT passes via an AOM in double pass and an electro-optical modulator (EOM) before being coupled into a single mode fiber. The AOM allows us to control the frequency detuning and the power of the MOT light, whereas the EOM allows us to add frequency sidebands. The light arriving in the single mode fiber is sent to a commercial fiber cluster system[17] that distributes it into six output fibers with equal powers. These independent fiber outputs are then used to create the circularly polarized MOT beams.

Frequency locking scheme and spectroscopy on a heat pipe

Saturated absorption spectroscopy is used to frequency lock the green laser. Using a hollow cathode lamp as a vapor source, like for the 399 nm laser, is not an option since a much higher vapor density would be needed due to the two orders of magnitude smaller linewidth of the 556 nm transition. Instead a heat pipe is

---

[17] Schäfter + Kirchhoff.

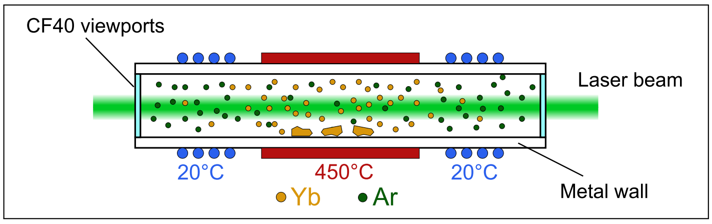

Figure 3.9: Sketch of the heat pipe used for saturated absorption spectroscopy on the 556 nm transition of ytterbium. The total length of the metal tube is about 40 cm and the heated region spans about 10 cm.

used to create the needed vapor pressure of ytterbium[18]. The heat pipe consists of an evacuated stainless steel tube with ytterbium chunks placed inside that are heated to about 450 °C (see Figure 3.9). In order to keep the ytterbium atoms from reaching the glass viewports and coating them, the tube walls next to the windows are cooled to room temperature. In addition a partial pressure of 0.1 mbar of Argon is injected into the cell such that the diffusion of ytterbium atoms is in a hydrodynamic regime. This ensures that ytterbium atoms moving towards the windows thermalize quickly and condense on the cold walls before reaching the windows.

The saturated absorption spectroscopy lines obtained with this heat pipe have a residual width of about 1 MHz which is probably limited by collisions with the Argon buffer gas. The laser is locked to the ^{174}Yb line, whereas the pump and probe beam are frequency shifted with respect to each other (similar to the case of the blue locking setup). The probe beam in the locked state is detuned by -200 MHz with respect to the ^{174}Yb. The remaining +200 MHz towards the ytterbium resonance (minus the MOT detuning) are bridged with the AOM in the main beam.

3.5.4 MOT configuration and experimental optimization

The MOT beams are circularly polarized and are collimated to a $1/e^2$-radius of about 1.5 cm. Typically the power per MOT beam is on the order of 20-30 mW leading to a saturation parameter per beam of about $s = I/I_{\text{sat}} \simeq 50$ in the beam center. The quadrupole magnetic field is created by two coils in (close to) anti-Helmholtz configuration that are designed to reach gradients in the MOT center of up to about 8 G/cm (16 G/cm) in the weak (strong) axis of the quadrupole field.

---

[18] At a later stage the heat pipe will be replaced with an iodine spectroscopy cell which is much easier to handle. The laser will then be locked to an iodine line that is about 1 GHz shifted from the green ^{174}Yb resonance.

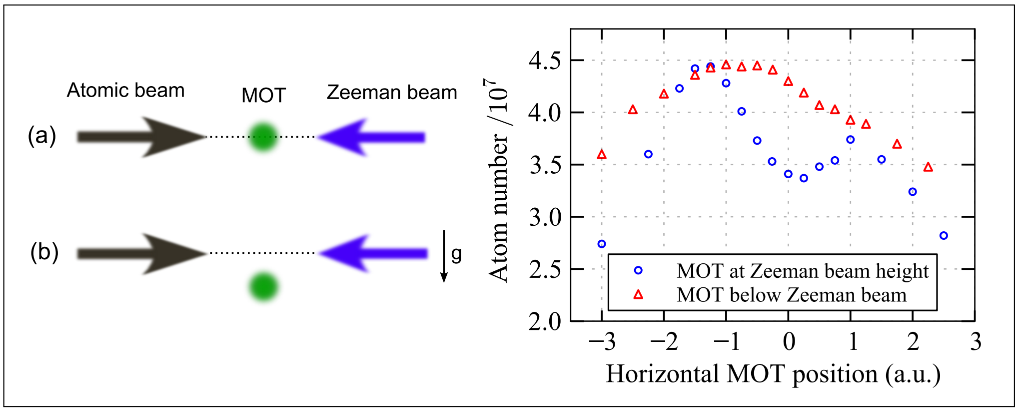

Figure 3.10: Effect of the Zeeman light pressure on the MOT loading. On the left-hand side the two considered loading situations are sketched, (a) having the MOT at the same height as the Zeeman beam, (b) loading slightly below the Zeeman beam. On the right-hand side the atom number in the MOT after 10 s loading is shown as function of the horizontal MOT position, for the two considered vertical MOT positions.

To be able to compensate for residual magnetic fields at the MOT position several compensation coils, producing homogeneous offset fields, are installed around the chamber. The lifetime of the atoms in the MOT is about 15 s.

Effect of Zeeman beam on the MOT loading

Even though the Zeeman beam is about $15\times\Gamma_{399}$ detuned from the 399 nm resonance a non negligible effect of radiation pressure on the atoms in the MOT is observed. This can be seen in the data shown in Figure 3.10 where the MOT loading is measured as a function of the horizontal MOT position. The measurement is carried out for two different vertical MOT positions, one at the same height as the Zeeman beam and one slightly below. The influence of the Zeeman light pressure on the MOT loading can be clearly seen as a spatially resolved dip in the blue data set. To circumvent this problem the MOT is loaded slightly below the Zeeman beam. The shown data suggest that the off-centered loading does not influence the basic loading rate that would be attained without the light pressure of the Zeeman beam. The MOT is shifted up to the center of the chamber after the loading is finished and the Zeeman light beam blocked.

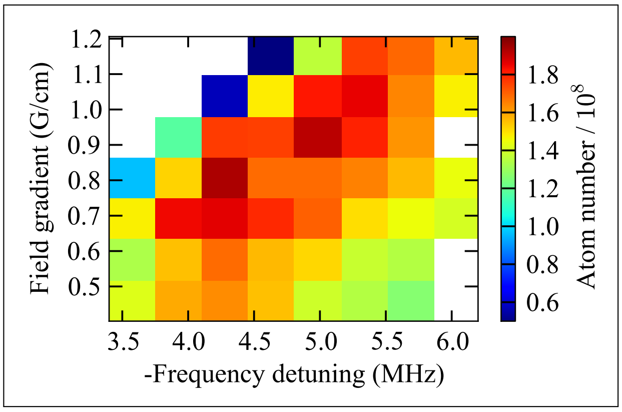

Figure 3.11: 2D optimization data of MOT detuning and magnetic field gradient. Shown the is atom number in the MOT after 10 s loading in color scale as a function of the MOT detuning and the magnetic field gradient in the weak axis of the quadrupole field. Unmeasured points are marked in white.

Optimization of MOT loading

The loading rate of the MOT for a given flux and velocity distribution of the incoming atomic beam is mainly determined by the capture velocity of the MOT. To optimize the capture velocity the best combination of MOT gradient and frequency detuning has to be found. Example data of a 2D scan of the MOT beam detuning and gradient is shown in Figure 3.11. It can be seen that a quite broad optimum for the frequency detuning ranging from about -4 MHz to -5.5 MHz is found where similar loading performance is observed, as long as the field gradient is adapted accordingly. This might be connected to the fact that the transition is highly power-broadened ($\Gamma_{\text{eff}} = \sqrt{1+6s} \times \Gamma_{556} \approx 2\pi \times 3.1\,\text{MHz}$, assuming the saturation effect of single MOT beam) and is therefore quite insensitive to detuning changes on the order of the broadened linewidth.

The chosen working point is at a detuning of about $\delta_{\text{MOT}} \simeq -27 \times \Gamma_{556} \simeq -2\pi \times 5\,\text{MHz}$ and a magnetic field gradient of 0.9 G/cm in the weak axis of the quadrupole field. Intuitively the optimum combination is expected close to the point where the Doppler shift of the incoming atoms at the border of the MOT is compensated by the Zeeman effect and the MOT beam detuning. With the found optimum parameters this condition is fulfilled for atoms with an axial velocity of about 4.5 m/s.

Effect of frequency sidebands

With the goal to increase the effective capture velocity of the MOT, frequency sidebands are added to the MOT light. It is to note that the frequency sidebands will not increase the upper limit on the capture velocity that is estimated in equation (3.8). They will rather help to approach this limit by providing a broader range of frequencies such that more atomic velocity classes can be addressed during the deceleration within the MOT.

Experimentally the frequency sidebands are created by phase modulation of the MOT light using an EOM. The resonance frequency of the EOM is fixed at 1.8 MHz, which determines the spacing of the added sidebands. The modulation amplitude controls the power ratio between the carrier and the sidebands and the number of sidebands with considerable power. After a full optimization iteration of the modulation amplitude and all MOT and Zeeman parameters, an increase in atom number in the MOT of about a factor of 2 is observed (under otherwise equal conditions). The optimal detuning and gradient values for the case with sidebands are found to be $\delta_{\mathrm{MOT}} \simeq -30 \times \Gamma_{556} \simeq -2\pi \times 5.8\,\mathrm{MHz}$ and $0.7\,\mathrm{G/cm}$ respectively.

The fact that the addition of the sidebands doesn't show a dramatic increase in atom number could be explained with the fact that the capture velocity might be already at a reasonable level thanks to the beforehand mentioned strong power broadening of the transition. This is coherent with the observations in similar ytterbium experiments in Munich and Hamburg. In the Munich experiment similar power levels of the MOT beams are available and the effect of sidebands is also found to be marginal. However in the Hamburg experiment, working with much less power in the MOT beams, sidebands are found to be crucial to obtain reasonable MOT loading.

MOT temperature

The settings that are found to optimize the MOT loading are not necessarily the best ones to achieve low temperatures. Therefore after finishing MOT loading, we attempt to cool the cloud as much as possible by optimizing the MOT detuning and reducing the MOT beam power. The coldest achieved temperature is $T = 9.7(5)\,\mu\mathrm{K}$ (see data in Figure 3.12), which is about a factor of two above the Doppler temperature of $T_{\mathrm{D}} \approx 4.5\,\mu\mathrm{K}$. However it is not expected that the Doppler temperature can be reached since the condition for the intensity to be much smaller than the saturation intensity cannot be fulfilled without loosing the atoms due to gravity. Furthermore in the regime of experimentally realized densities, multiple-photon scattering effects become important where the minimum achievable temperature is expected to be higher than T_{D}, which is the limit temperature in a single atom picture.

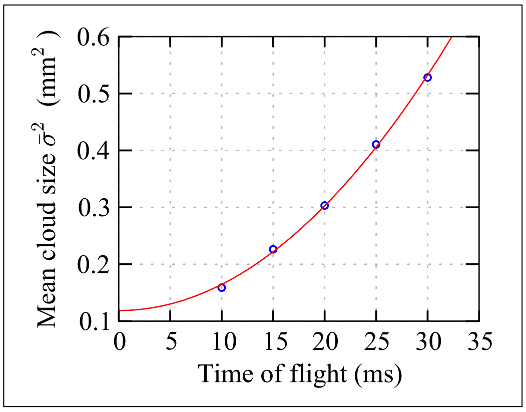

Figure 3.12: Temperature measurement of the MOT after cooling stage. The square of the mean cloud size $\bar{\sigma}(t) = [\sigma_x(t) + \sigma_y(t)]/2$ (blue circles) is shown for different time-of-flight durations, where $\sigma_{x,y}$ are the Gaussian RMS widths along the main system axis. The temperature is extracted from the cloud size evolution by a fit with equation (3.10) (red solid line), where the temperature and initial cloud size act as free fit parameters.

The temperature has been determined in a series of time-of-flight images where the evolution of the cloud size is measured as a function of the free expansion time. When assuming the initial density distribution of the thermal cloud to be Gaussian with RMS widths of $\sigma_{i,0}$, $i = x, y, z$, in a free, ballistic expansion the distribution stays Gaussian and the RMS width evolves like [92]

$$\sigma_i^2(t) = \sigma_{i,0}^2 + \frac{k_\mathrm{B}T}{m}t^2\,, \tag{3.10}$$

where t denotes the duration of free expansion and T the initial cloud temperature.

The reported temperature is achieved after switching off the sidebands and performing a compressed MOT with a field gradient of about 6.7 G/cm in the weak quadrupole axis. This is necessary to increase the confinement since otherwise the atoms cannot be held against gravity when working with reduced MOT beam powers. The optimum frequency detuning for cooling is found to be around $\delta_\mathrm{MOT} = -2\pi \times 1.2\,\mathrm{MHz}$. In theory the Doppler temperature of $4.5\,\mu\mathrm{K}$ is expected to be obtained at $\delta_\mathrm{MOT} = -\Gamma_{556}/2 \simeq -2\pi \times 90\,\mathrm{kHz}$. It is to note that more than 50 % percent of the atoms are lost during this cooling stage resulting in a final trapped atom number of about 7×10^7.

3.6 Absorption imaging

The method to detect the cold atomic cloud throughout this thesis is the commonly used absorption imaging. In this technique a resonant laser beam is sent onto the atoms and the shadow cast by the atomic cloud is imaged onto a charged coupled device (CCD) camera. When the intensity of this probe beam is small compared to the saturation intensity I_{sat} of the atomic resonance, the absorption of the probe beam is proportional to the atomic density. Then the transverse intensity profile after passing through the atomic cloud is determined by the Lambert-Beer law

$$I_1(x,y) = I_0(x,y) \exp\left(-\sigma_0 \int n(x,y,z)\,\mathrm{d}z\right) , \tag{3.11}$$

with $I_0(x,y)$ the initial transverse intensity profile and with $\sigma_0 = 3\lambda^2/2\pi$ the resonant atom-photon scattering cross section for $I_0 \ll I_{\mathrm{sat}}$, with λ the resonance wavelength. From this expression the line-integrated density can be derived as

$$\tilde{n}(x,y) = \int n(x,y,z)\,\mathrm{d}z = -\frac{1}{\sigma_0} \ln\left[\frac{I_1(x,y)}{I_0(x,y)}\right] = \frac{D}{\sigma_0} , \tag{3.12}$$

where $D = -\ln[I_1(x,y)/I_0(x,y)]$ is the optical density of the cloud. Experimentally the line-integrated density of the cloud can therefore be determined by measuring $I_1(x,y)$ (with atoms) and $I_0(x,y)$ (without atoms) using a CCD camera. To image the plane of the atomic cloud to the CCD camera two lens imaging systems are used that allow to choose the image magnification at the CCD camera via the ratio of the focal lengths.

When imaging the cloud directly in the trap, essentially all the probe light is absorbed due to the high density of the cold atomic cloud (typically $D \gtrsim 5$ in-situ). In this case noise dominates the absorption signal and reliable measurements are not possible. This is usually avoided by performing the measurements after time-of-flight. For this the trapping potential is switched off several milliseconds before imaging and the cloud expands according to its initial momentum distribution resulting in a reduced density. By this method, depending on the time-of-flight duration, the density in momentum space can be measured and information about the cloud temperature and atom number extracted.

The absorption imaging throughout this thesis work is done on the 399 nm transition of ytterbium. To keep perturbations of the resonant probe light on the measured density distribution small, the probe beam is send in a short pulse with typically tens of microseconds duration. Probe lasers and imaging systems are installed on several axis, in order to allow us to choose the probe direction according to the experimental needs.

3.7 Optical transport of a thermal cloud

To bring the laser cooled atomic cloud from the MOT chamber to the science chamber, a transport over a distance of about 22 cm is necessary. Common ways to perform such a transport are in mechanically moved optical [93], [94] or magnetic traps as well as in static configurations using traveling optical lattices [95], spatial chaining of magnetic traps [20] or focus tunable lenses [96]. Since ^{174}Yb in its ground state is not magnetically sensitive, the only way to trap and transport it is by optical means. Therefore the transport in this experiment is carried out in an optical dipole trap where the focus of the trapping beam is moved from one chamber to the other using a mechanical translation stage. Similar as in optical tweezers, the atoms are forced to follow the potential minimum and can therefore be moved through space. The transport is executed with a thermal cloud at a temperature of about 80 μK.

In the following, first the theoretical basics of an optical dipole trap are set followed by some models to describe the physics of the optical transport. Afterwards the experimental realization and loading of the dipole trap is presented as well as experimental data on the transport optimization.

3.7.1 Dipole potential and Gaussian beams

The optical dipole trap used in this experiment is created by a far-off-resonant Gaussian laser beam. For a radially symmetric Gaussian beam propagating along the z axis the intensity can be written in the form

$$I(r,z) = \frac{2P_0}{\pi w^2(z)} e^{-2r^2/w^2(z)}\,, \tag{3.13}$$

where r is the radial coordinate, P_0 the total power and $w(z)$ the $1/e^2$ beam radius given by

$$w(z) = w_0\sqrt{1+\frac{(z-z_0)^2}{z_\mathrm{R}^2}}\,. \tag{3.14}$$

Here w_0 denotes the beam waist defined as the $1/e^2$ radius at the focus position $z = z_0$. The Rayleigh length z_R characterizes the axial extension of the focus region and is connected to the waist w_0 and the wavelength λ via

$$z_\mathrm{R} = \frac{\pi w_0^2}{\lambda}\,. \tag{3.15}$$

The dipole trap potential created by this laser beam is proportional to the light intensity (see Appendix A) and takes the form

$$U_\mathrm{dip}(r,z) = -\frac{U_0}{1+\frac{(z-z_0)^2}{z_\mathrm{R}^2}}\, e^{-2r^2/w^2(z)}\,, \tag{3.16}$$

where $U_0 > 0$ denotes the trap depth. Close to the minimum of the trapping potential the harmonic approximation is valid, where the potential reads

$$U_{\mathrm{dip}}(r,z) \approx -U_0 + \frac{1}{2}m(\omega_{\mathrm{rad}}^2 r^2 + \omega_{\mathrm{ax}}^2 z^2)\,, \tag{3.17}$$

with the radial and axial angular trapping frequencies ω_{rad} and ω_{ax} determined by

$$\omega_{\mathrm{rad}} = \sqrt{\frac{4U_0}{mw_0^2}}\,, \quad \omega_{\mathrm{ax}} = \sqrt{\frac{2U_0}{mz_{\mathrm{R}}^2}}\,. \tag{3.18}$$

This approximation will be often used in the following.

3.7.2 Transport theory models

To describe the physics of the optical transport from a theoretical point of view, two main models are presented here that are intended to clarify possible heating and atom loss mechanisms. The focus thereby lies on effects that are intrinsic to the transport itself and not due to technical imperfections like heating due to pointing fluctuations of the dipole trap beam during transport. The first one is a simple model for the center of mass motion of the cloud in a moving harmonic potential. This model allows one to estimate the excitation energy transferred to the cloud during motion and to identify the regime of adiabatic transport. The second one is intended to model the modification of the trapping potential under the influence of the finite acceleration during transport. The induced effective reduction of the trap depth can lead to atom spilling which I try to estimate quantitatively. Both models are based on ideas presented in [97].

The non-adiabatic transport model

One of the simplest models to describe the transport of a cold cloud is to consider the center of mass motion using classical Newtonian equations of motion. For this the optical potential along the transport axis z will be considered to be harmonic in the following with an angular trapping frequency of ω_z. During transport, the harmonic potential is subjected to a time dependent acceleration $a(t)$ leading to an equation of motion for the center of mass position z given by

$$\ddot{z}(t) + \omega_z^2 z(t) = a(t)\,. \tag{3.19}$$

Assuming the boundary conditions $z(0) = \dot{z}(0) = 0$, the solution of this equation reads [97]

$$z(t) = \frac{1}{\omega_z}\int_0^{\mathrm{t}} \sin[\omega_z(t-t')]\, a(t')\,\mathrm{d}t'\,. \tag{3.20}$$

When considering a finite transport time T_t with $a(t<0)=a(t>T_\mathrm{t})=0$, the solution after the end of the transport can be expressed [97] as

$$z(t>T_\mathrm{t}) = \frac{|\mathcal{F}[a(t')]\,(\omega_z)|}{\omega_z}\sin(\omega_z t+\phi)\,, \tag{3.21}$$

where $\mathcal{F}[a(t')]\,(\omega_z)=\int_{-\infty}^{\infty}a(t')e^{-i\omega_z t'}\mathrm{d}t'$ denotes the Fourier transform of the time dependent acceleration profile $a(t')$ at angular frequency ω_z. Using the identity $\mathcal{F}[f^{(n)}(t)]\,(\omega_z)=(i\omega_z)^n\mathcal{F}[f(t)]\,(\omega_z)$ this result can be simplified to

$$\boxed{z(t>T_\mathrm{t}) = |\mathcal{F}[v(t')]\,(\omega_z)|\ \sin(\omega_z t+\phi)}\,. \tag{3.22}$$

The interpretation of this equation is that at the end of the transport the center of mass in general performs oscillations at the trap frequency. These oscillations are excited during the transport and their amplitude is determined by the spectral contribution of the velocity profile $v(t)$ at the angular trap frequency ω_z.

To estimate the oscillation amplitude the precise velocity profile needs to be considered. For the profile used in this experiment (see section 3.7.3) the oscillation amplitude can be analytically calculated to be [97]

$$\boxed{|\mathcal{F}[v(t)]\,(\omega_z)| = d\,\cos^2\left(\frac{\omega_z T_\mathrm{t}}{16}\right)\left|\cos\left(\frac{\omega_z T_\mathrm{t}}{8}\right)\right|\,\mathrm{sinc}^4\left(\frac{\omega_z T_\mathrm{t}}{16}\right)}\,. \tag{3.23}$$

This expression scales linearly with the transport distance d and its dependence on the transport time T_t is shown in Figure 3.13.

In the case of a transport in the non-adiabatic regime ($T_\mathrm{t}\sim T_\mathrm{osc}=2\pi/\omega_z$), the oscillation amplitudes are in general quite large and on the order of the transport distance d. However there are optimal transport cases appearing at integer multiples of twice the oscillation period ($T_\mathrm{t}=n\cdot 4\pi/\omega_z$, with positive integer n) where the oscillation amplitudes fall down to zero. Physically these points corresponds to the special case where the excitation during motion is compensated during deceleration such that the center of mass is at rest at the end of the motion profile. In literature this effect is denoted as "shortcut to adiabaticity" and has been observed experimentally in BEC transport experiments [93]. The regime of adiabatic transport can be identified for $T_\mathrm{t}\gg 2\pi/\omega_z$, where the strong initial exponential decay of the envelope of the oscillation amplitudes with the transport distance gets reduced. In this regime, typical oscillation amplitudes are on the order or below $d\times 10^{-4}$.

When staying within the harmonic approximation, the excess energy associated with a given oscillation amplitude can be calculated as

$$\Delta E = \frac{1}{2}m\omega_z^2 z_\mathrm{max}^2\,, \tag{3.24}$$

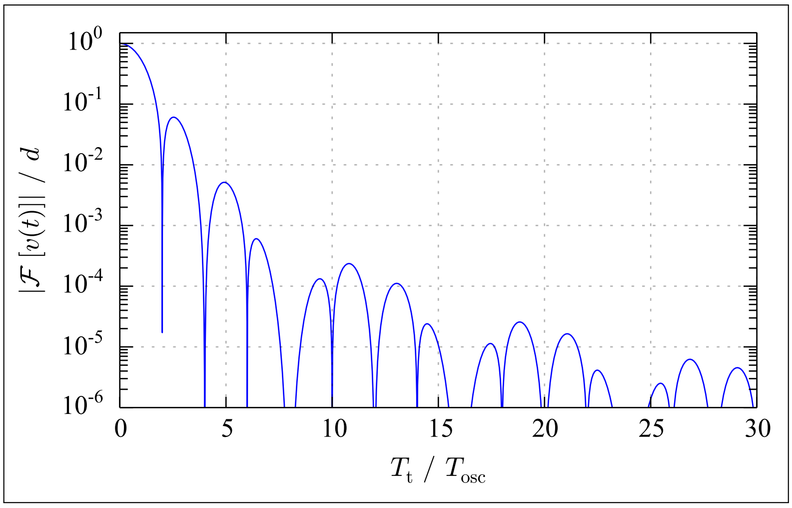

Figure 3.13: The oscillation amplitude after transport is shown in log scale as a function of the transport time T_t. The transport time is shown in units of the oscillation period $T_\mathrm{osc} = 2\pi/\omega_z$ and the oscillation amplitude in units of the transport distance d.

with $z_\mathrm{max} = |\mathcal{F}[v(t)]\,(\omega_z)|$. It is proportional to the square of the oscillation amplitude and therefore also to the square of the transport distance. In the experiment, this excitation energy will sooner or later transform into cloud heating due to rethermalization and trap anharmonicities, where the expected temperature increase can be estimated as $\Delta T \simeq \Delta E/k_\mathrm{B}$.

The validity of this model is quite limited since it neglects experimentally important effects of anharmonicities of the trapping potential and subsequent possible rethermalization of the cloud during transport. Furthermore it neglects the fact that the trapping potential has a finite depth. However this description allows us to estimate an order of magnitude of the expected heating due to induced cloud excitations, which will be done in section 3.7.5.

Acceleration-induced losses

The model described in the previous section assumes a harmonic confinement that has in principle an infinite potential depth. However the fact that the real dipole trap potential has a finite depth has major consequences for the transport. Under

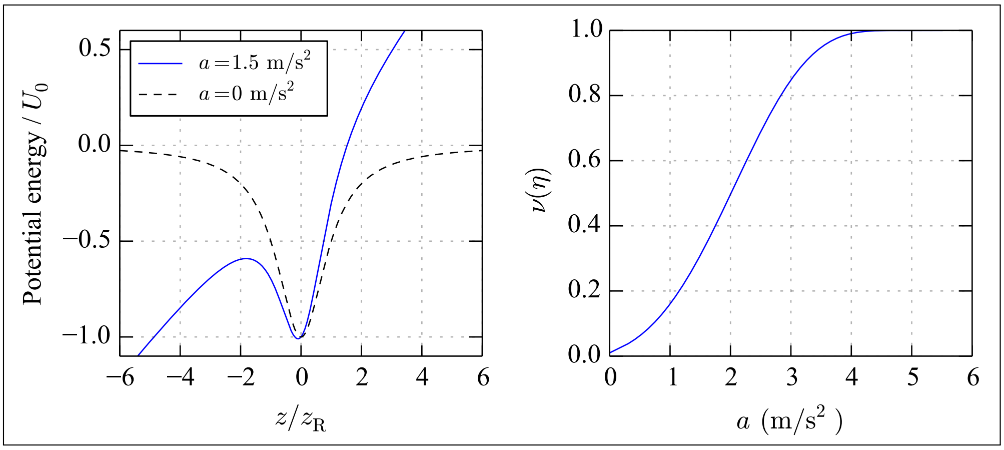

Figure 3.14: Effect of a constant acceleration on the dipole trap potential and the accordingly expected atom loss. The on-axis dipole trap potential from equation (3.25) is shown on the left-hand side in presence and absence of an acceleration, for the parameters ($U_0 = 680\,\mu$K, $z_R = 4.2\,$mm). On the right-hand side the fraction of atoms $\nu(\eta = U_{\text{eff}}/k_\text{B}T)$ with an energy higher than the effective trap depth is shown as a function of the applied acceleration. Here the experimental parameters $U_0 = 680\,\mu$K, $z_R = 4.2\,$mm and $T = 80\,\mu$K are used.

the presence of an acceleration a along the transport axis z, the full dipole trap potential in the moving frame is static and given by

$$U_{\text{dip,acc}}(r,z) = -\frac{U_0}{1+\frac{z^2}{z_\text{R}^2}}\,e^{-2r^2/w^2(z)} + maz\,, \tag{3.25}$$

where m is the mass of the considered atom. The influence of the linear acceleration potential on the bare dipole trap potential becomes important when $maz_\text{R} \gtrsim U_0$. Then the resulting potential takes an highly asymmetric form as shown in Figure 3.14 for some typical experimental parameters. It can be seen that the trapping potential gets opened to one side and that the effective trap depth is reduced. This can lead to atom spilling during transport and can be a limiting factor for the fastest achievable transport speed.

To estimate the amount of atom loss due to the finite acceleration one can assume in a simple model that all particles in the thermal cloud with an energy larger than the effective trap depth U_eff will be lost. To get some numerical estimates the energy distribution of the thermal cloud needs to be known. Assuming the atomic cloud at temperature T in a three dimensional harmonic confinement, the fraction of particles with an energy above the effective trap depth is given by [98]

$$\nu(\eta) = \frac{2 + 2\eta + \eta^2}{2e^\eta}\,, \tag{3.26}$$

with $\eta = U_\mathrm{eff}/k_\mathrm{B}T$. Typically η is on the order of 10 for a cloud that is well thermalized within a given potential depth. Assuming $k_\mathrm{B}T \simeq U_0/10$ as the initial cloud temperature, the fraction of atoms with an energy above the effective trap depth for a given acceleration can be calculated. The result is shown in Figure 3.14 for the present experimental trap parameters. It can be seen that strong atom loss is expected for accelerations above $2\,\mathrm{m/s^2}$ which will determine the fastest possible transport time.

It is however to note that the effective trap depth for a given acceleration depends strongly on the Rayleigh length z_R and therefore on the axial trap frequency. By choosing a strong enough axial confinement the effect of acceleration-induced losses can be limited to ensure reasonably short transport times (see upcoming experimental data). It is also to note that a constant acceleration can be present when the trapping beam is not perfectly horizontal. Depending on the resulting angle this might also statically influence the effective trap depth. In our experiment this angle is below $0.5\,^\circ$ due to the geometry of the setup.

3.7.3 Experimental setup and transport profile

Optical setup

The optical setup used for the transport is shown in Figure 3.15. The single beam dipole trap is created by a (longitudinally multimode) fiber laser[19] emitting at $\lambda = 1070\,\mathrm{nm}$ with an output power of $50\,\mathrm{W}$. The power arriving at the atoms is about $45\,\mathrm{W}$ where the beam is focused to a waist of about $38\,\mu\mathrm{m}$. Between the last focusing lens and the vacuum chamber a mechanical translation stage[20] is placed with a mirror combination mounted on top to reflect the incoming dipole trap beam. By moving the translation stage, the path length between the last lens and the vacuum chamber can be dynamically changed. Accordingly the position of the dipole trap focus along the beam propagation axis can be moved, to realize the transport of the atoms. With the chosen setup the transport distance is given by twice the travel distance of the stage. To ensure enough space to place the translation stage used for the transport, the last focusing lens is chosen to have a relatively long focal length of $f = 800\,\mathrm{mm}$. To achieve the desired waist at the atoms the incident beam is therefore first enlarged to a diameter of about $3\,\mathrm{cm}$.

---

[19] YLR-50-LP-AC-Y12, IPG Photonics.

[20] XMS160 from Newport with XPS controller.

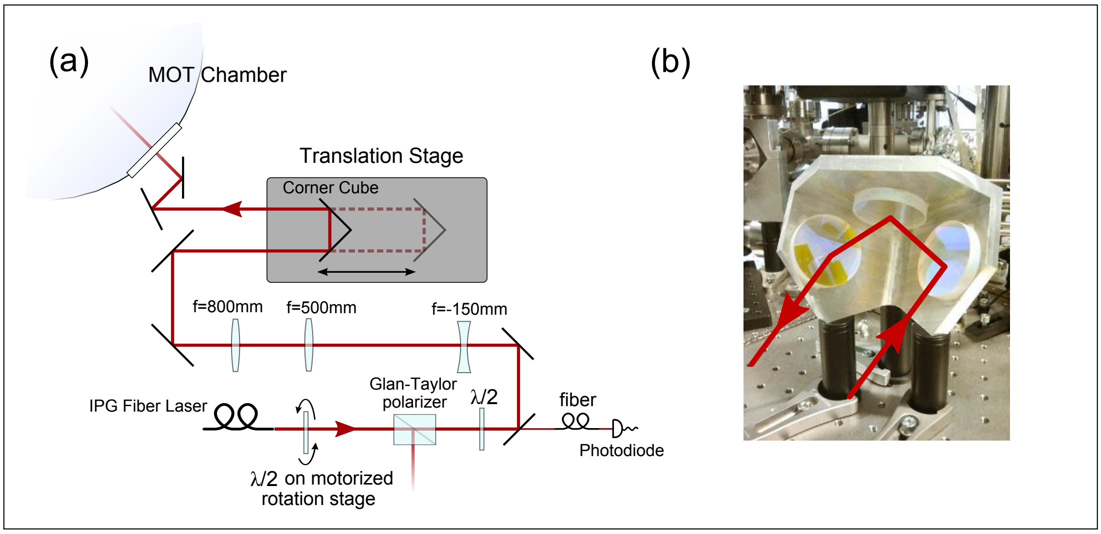

Figure 3.15: Optical setup to transport the atomic cloud in a single beam dipole trap. A sketch of the optical arrangement is shown on the left-hand side (a). On the right-hand side (b) a photo of the corner cube reflector is shown used to reflect the incoming beam off the translation stage. The red arrowed lines illustrate the trajectory of an incoming beam within the corner cube reflector.

In order to successfully perform the transport of the atomic cloud, it is important to limit heating effects during motion. Those can be caused by fluctuations of the transverse dipole trap position induced by vibrations and off-axis movement of the mechanical translation stage [99]. The element that couples the vibrations and off-axis motion to the dipole trap position is the reflecting device on the translation stage. The choice of this device is important and can significantly reduce the coupling (for details see Appendix C.). In this experiment a so-called ”corner cube reflector” is used as shown in Figure 3.15. It consists of three mirrors placed on mutually orthogonal planes that mimic the reflection of the beam in the corner of a cube. In this configuration the position and angle of the reflected dipole trap beam is intrinsically insensitive to rotations of the corner cube reflector. Using this device the sensitivity to vibrations and off-axis motion can be drastically reduced compared to using just a single mirror (see Appendix C).

The remaining parts shown in the optical setup in Figure 3.15 concern the ramping and stabilization of the dipole trap power that is explained in section 3.8.1.

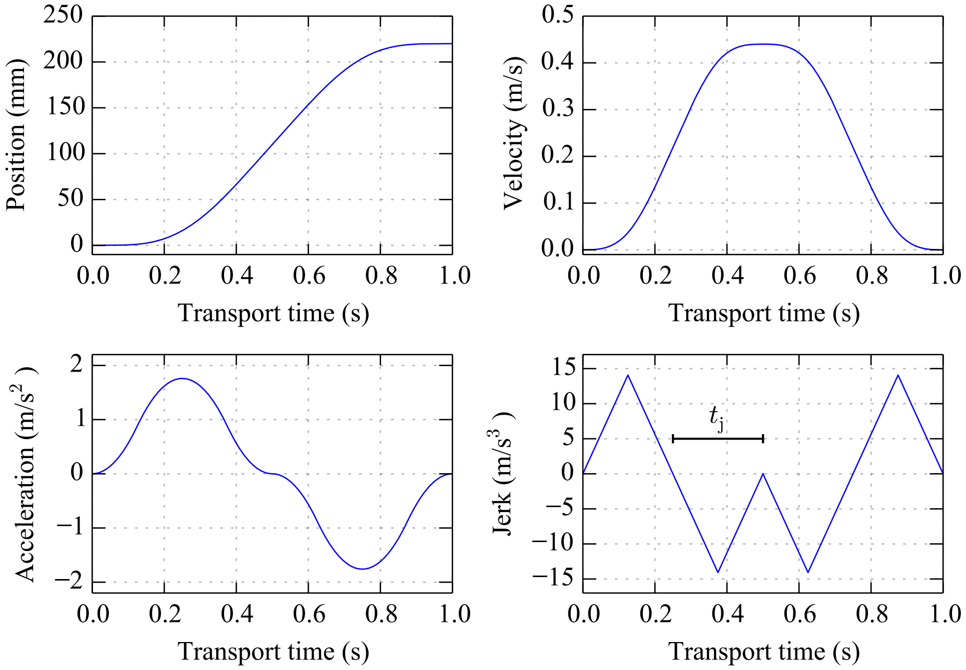

Figure 3.16: Motion profile for the choice of the jerk time $t_\mathrm{j} = T_t/4$. Shown are the position, velocity, acceleration and jerk as a function of time for a travel distance $d = 22\,\mathrm{cm}$ and travel time $T_t = 1\,\mathrm{s}$. The jerk time is defined as the length of the jerk triangles as indicated in the lower right graph.

Transport motion profile

The motion profile describing the axial trap position $z_\mathrm{trap}(t)$ as a function of time determines the properties of the transport. In order to keep vibration amplitudes on the translation stage low, a sufficiently smooth profile should be chosen. In this experiment, a predefined motion profile provided by the translation stage controller[21] is used. For this profile the position trajectory $z_\mathrm{trap}(t)$ is a piecewise-defined 4th order polynomial. Accordingly the velocity (acceleration, jerk) is a 3rd (2nd, 1st) order piecewise-defined polynomial. Typical curves for the position, velocity, acceleration and jerk during motion can be seen in Figure 3.16, for an example transport duration of $T_t = 1\,\mathrm{s}$. The characteristic quantities of this motion profile are the transport distance d, the transport time T_t, the peak acceleration a_max, the peak velocity v_max and the jerk time t_j, defined as the duration of the jerk triangles as illustrated in Figure 3.16.

---

[21] The used motion profile on the XPS controller from Newport is referred to as ”SGamma”.

To limit the number of parameters to optimize experimentally, the jerk time is always set to the longest possible, namely $t_\mathrm{j} = T_t/4$. This choice is reasonable since for a given transport time T_t it minimizes the maximum jerk and therefore the time spend at the peak acceleration a_max, ensuring a maximum of smoothness during motion. The remaining free parameters within this choice are the travel distance d and the transport time T_t. The peak acceleration and velocity are uniquely calculated from d and T_t via the relations

$$a_\mathrm{max} = \frac{8\,d}{T_t^2}\,, \quad v_\mathrm{max} = \frac{2\,d}{T_t}\,. \tag{3.27}$$

Since d is pre-determined by the dimensions of the optical setup, T_t is the only free parameter to experimentally optimize the transport.

3.7.4 Dipole trap loading and characterization

Dipole trap loading sequence

Before transporting the atoms they have to be loaded from the MOT into the single beam dipole trap. This is achieved using the experimental sequence as sketched in Figure 3.17. After MOT loading of about 15 s, the frequency sidebands are turned off while the MOT frequency detuning is adapted to compensate for the change in light force. Next the MOT position is shifted up from the loading position below the Zeeman beam to the center of the chamber using the vertical compensation coil. In this stage we also compress the MOT by an increasing the magnetic field gradient. Subsequently the dipole trap is switched on and the MOT atoms are cooled into the trap by lowering the MOT light power and approaching the frequency detuning closer to resonance. The parameters for timings and ramping values, as indicated in Figure 3.17, are empirically optimized until satisfactory results were achieved.

After this sequence, about 2×10^7 atoms are loaded into the optical dipole trap which corresponds to about 10 % overall transfer efficiency from the MOT after 15 s loading. The temperature of the transferred cloud after about 1 s of plain evaporation is about 70 μK.

Dipole trap characterization

Important for the transport considerations is to know the axial trap frequency since it determines the sensitivity to acceleration-induced losses and the conditions to be in the adiabatic transport regime. It is measured by monitoring the sloshing motion of the cloud after an axial excitation using the translation stage. The resulting evolution of the cloud center position is shown in Figure 3.18. The radial

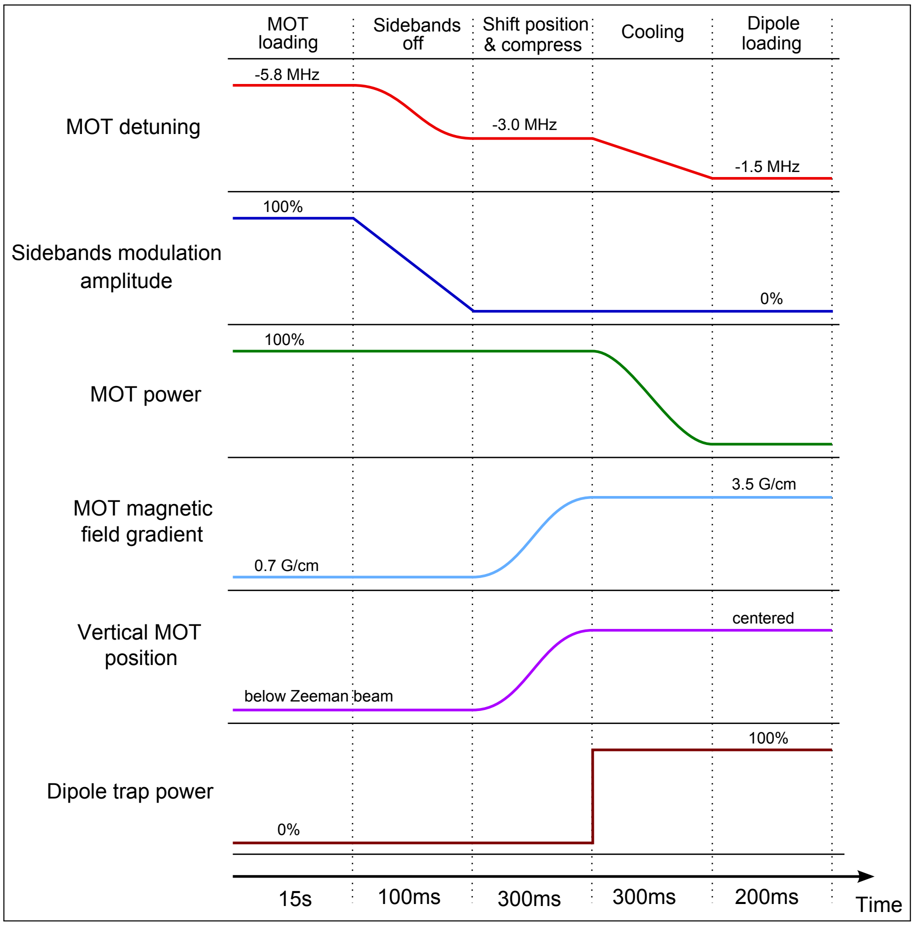

Figure 3.17: Typical experimental sequence for MOT loading and subsequent transfer to the single beam optical dipole trap.

trap frequency has been measured by means of parametric heating [100] where the dipole trap power is sinusoidally modulated. The resulting measured trapping frequencies are $\omega_{\text{ax}}/2\pi = 9.5(3)\,\text{Hz}$ and $\omega_{\text{rad}}/2\pi = 1.45(20)\,\text{kHz}$. For an incident power of 45 W, those two results are in accordance with a waist of the dipole trap beam of $w_0 \approx 38\,\mu\text{m}$ resulting in a theoretically expected trap depth of about $680\,\mu\text{K}$.

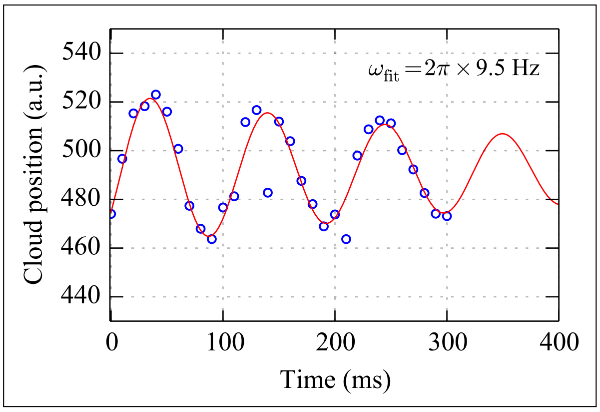

Figure 3.18: Measurement of the axial trap frequency $\omega_z/2\pi$ of the dipole trap at 1070 nm. The axial center of mass position of the cloud is shown as a function of waiting time after an excitation (blue circles). The excitation is done by a sudden small displacement of the trap position using the mechanical translation stage. The red curve is a fit using a damped sine oscillation.

3.7.5 Experimental transport optimization and comparison with theory models

The two trap configurations used for transport

The transport of the cold cloud has been carried out in two different dipole trap configurations. In the beginning a configuration with relatively small trap frequencies of about $\omega_{\mathrm{ax}}/2\pi \approx 2.2\,\mathrm{Hz}$ and $\omega_{\mathrm{rad}}/2\pi \approx 590\,\mathrm{Hz}$ was used corresponding to a trap depth of about $260\,\mu\mathrm{K}$. However the resulting cloud density and elastic scattering rate after transport were found to be unfavourable for subsequent evaporative cooling and loading of a crossed dipole trap. In a second step the trap as described in the previous section was installed, providing much better initial conditions. We have investigated the transport for these two configurations and will make a quantitative comparison between the two in this section. This will allow to identify the important parameters to ensure ideal transport conditions. The two configurations will be referred to as "old" ($\omega_{\mathrm{ax}}/2\pi \approx 2.2\,\mathrm{Hz}$) and "new" ($\omega_{\mathrm{ax}}/2\pi \approx 9.5\,\mathrm{Hz}$) configurations in the following.

In order to quantify the transport efficiency, an important effect is the finite lifetime of the cloud in the dipole trap. This has been measured in the MOT chamber for the old trap configuration and the resulting data is shown in Figure 3.19. In the first 100 ms a quite strong atom loss is found which is probably due to the relaxation of the cloud from a non-equilibrium distribution directly after loading into the dipole trap [101]. After that, an exponential decay with a time

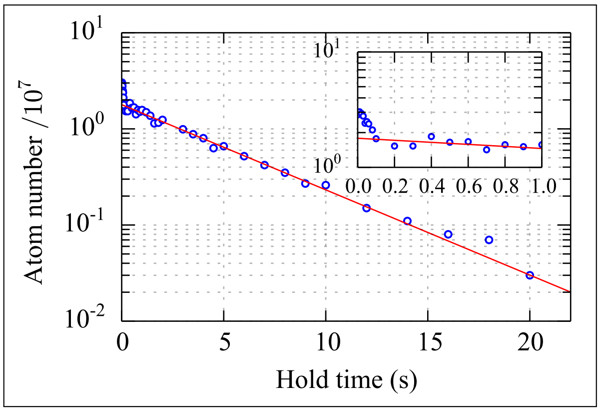

Figure 3.19: Lifetime measurement of the atomic cloud in the dipole trap. The atom number in the dipole trap is measured as a function of hold time. The red curve is an exponential fit to the data from 0.2 to 20 s hold time with a fitted time constant of $\tau_{\text{lifetime}} = 4.9(1)\,\text{s}$.

constant of about $\tau_{\text{lifetime}} \simeq 4.9\,\text{s}$ is found down to at least 20 s of hold time. Since the measured lifetime is on the same order as the transport duration, the evaluation of the real transport efficiency needs to be corrected to account for "background" losses.

Experimental transport data

Experimentally the transport is carried out over a distance of $d = 22\,\text{cm}$ using the motion profile as described in section 3.7.3. Within the explained choice of profile parameters, the total transport time T_t is the only free parameter to optimize experimentally. For the two trap configurations the relative atom number measured after transport is shown in Figure 3.20 as a function of the total transport time T_t. For each of the three shown data sets an atom number reference point is measured after a certain waiting time[22] in the MOT chamber without performing any transport. The relative atom numbers shown in Figure 3.20 are the measured atom numbers normalized to the initial atom number $N(t = 0)$ that is extrapolated for each data set using its reference point and the lifetime calibration, under the assumption that the lifetime is equal in both trap configurations.

---

[22] The additional waiting time is used in order to remove effects due to the non-equilibrium distribution of the atoms after the laser cooling into the dipole trap. After about 150 ms the density distribution in the dipole trap has relaxed into thermal equilibrium (as suggested by the data in Figure 3.19). The reference atom number points are: red circles: 1.1×10^7 after 2 s, red triangles: 1.2×10^7 after 1 s, blue squares: 1.8×10^7 after 2.4 s.

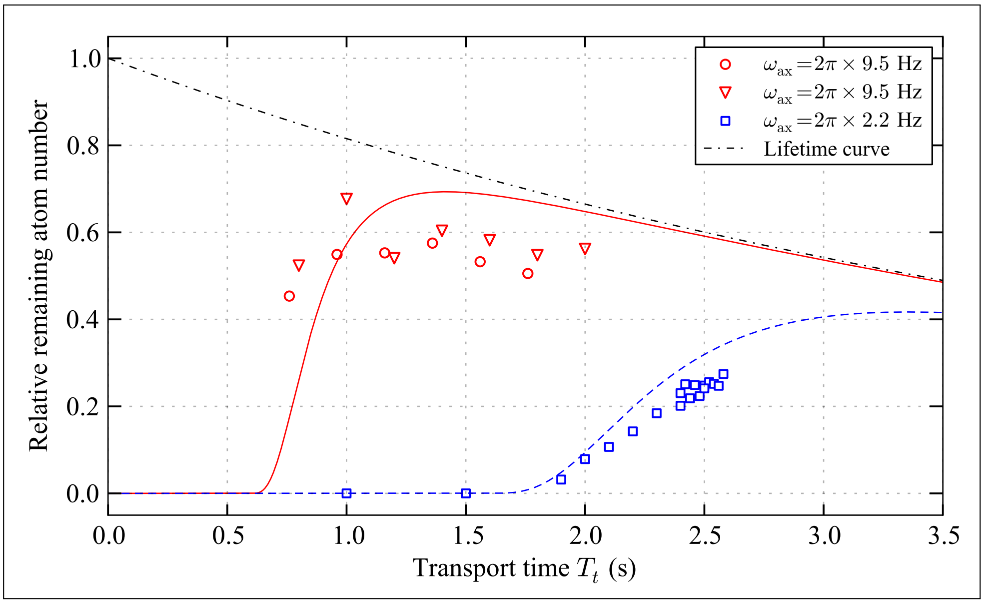

Figure 3.20: Characterization of the optical transport. Shown is the remaining fraction of atoms as a function of the transport time T_t for the two considered trap configurations with axial trap frequencies of 9.5 Hz (red circles and triangles) and 2.2 Hz (blue squares). The red triangles and circles correspond to two independent measurement series taken half a year apart. The red solid and blue dashed lines are theory curves based on equation (3.29), taking acceleration-induced losses and the finite cloud lifetime for the two configurations into account. The lifetime limitation itself is shown as the black dash-dot line.

From the bare data, it can be seen that with the old trap configuration reasonable transport efficiencies can only be reached for transport times longer than about 2 s. However, even at still acceptable transport times of about 2.5 s, the achieved efficiency does not exceed about 30 % overall (50 % when correcting for the lifetime). With the new trap configuration, however, the transport can be executed much faster: At about 1 s transport time overall efficiencies on the order of 60 % are reached (80 % when correcting for the lifetime). Even down to the speed limitation of the translation stage ($T_t = 0.74$ s) reasonable efficiencies are observed.

The total atom number in the trap after a 1 s transport in the new configuration values to about 1×10^7 atoms at a temperature of about 70 μK. It is to note that the same temperature is measured for the cloud when simply waiting 1 s in the MOT chamber without performing a transport. No signs of sloshing motion of the

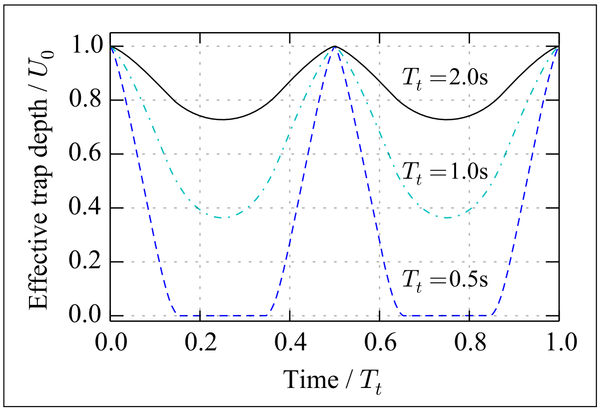

Figure 3.21: The effective trap depth as a function of time is shown under the influence of the time dependent acceleration during transport. The shown graphs are calculated for the trap configuration with $\omega_{\mathrm{ax}}/2\pi = 9.5\,\mathrm{Hz}$, according to the acceleration profile type as shown in Figure 3.16. The curves show the case of transport times of 2 s (black solid), 1 s (cyan dashed-dot) and 0.5 s (blue dashed).

cloud after transport have been observed, which shows that there is no significant heating of the cloud during transport.

Comparison with theory models

To understand the significant difference in atom loss during transport for the two trap configurations, we now apply the models as presented in section 3.7.2. First, the model of acceleration-induced losses is applied, where it has been shown that the effect of a finite acceleration influences the effective trap depth during transport. In Figure 3.21 the typical evolution of the trap depth as a function of time during the transport is shown for the new trap configuration.

The shown curves indicate that the modification of the potential depth at fast transport times cannot be neglected. To quantify the acceleration-induced losses that come along with this, it is assumed that all atoms with an energy higher than the minimum effective trap depth during transport are lost. This very simplified view results in a model function of the remaining fraction of atoms of

$$\frac{N(T_t)}{N(0)} = 1 - \nu\left(\frac{U_{\mathrm{eff,min}}}{k_{\mathrm{B}}T}\right) , \tag{3.28}$$

where $U_{\mathrm{eff,min}}$ denotes the effective trap depth at the peak acceleration that is given in equation (3.27) and $\nu(U_{\mathrm{eff,min}}/k_{\mathrm{B}}T)$ quantifies the fraction of atoms with an energy higher than the effective trap depth assuming an energy distribution of a harmonically trapped cloud, as defined in equation (3.26). To complete the model function the maximum reachable atom number due to the lifetime limitation is empirically taken into account leading to

$$\frac{N(T_t)}{N(0)} = \left[1 - \nu\left(\frac{U_{\mathrm{eff,min}}}{k_{\mathrm{B}}T}\right)\right] \times e^{-t/\tau}\,. \tag{3.29}$$

This function is plotted in Figure 3.20 as theory curves using the parameters of the two trap configurations and assuming fixed cloud temperatures of $T = 80\,\mu$K and $T = 30\,\mu$K during transport for the new and the old configuration respectively. These temperatures are mean values that are chosen with respect to the initial and final measured temperatures.

The theory curves of this very simplified model explain the qualitative difference between the two transport configurations. The limitation in terms of transport speed due to acceleration-induced losses becomes apparent for the old configuration. In the new configuration where the axial confinement is further increased, the sensitivity to acceleration-induced losses is reduced and allows one to use much faster transport times. Quantitatively the model functions allows us to some extent to estimate the threshold where acceleration-induced losses become important, though they are not able to reproduce the exact behaviour of the experimental data. This could be due to uncertainties in the trap characterizations and measured cloud temperatures. Furthermore, for a full quantitative description it is expected that effects of rethermalization and evaporation during transport due to the time dependent potential depth might become important. Also the effect that the trapping potential in presence of an acceleration is only opened to one side might suggest that effects of atom recapturing in the periods of rising trap depth might also play a role. For this also the time scale for an atom to leave the trapping volume needs to be taken into account.

For completeness also the non-adiabatic transport model is applied to the present case, that allows one to estimate effects of center of mass excitations due to the axial displacement of the trap minimum. In harmonic approximation of the trapping potential, the excitation energy can be estimated using equation (3.24). The resulting expected heating of the cloud is plotted in Figure 3.22 for the two trap configurations. It can be seen that for the new configuration the energy deposition is expected to be below 100 nK for all possible transport times ($T_t > 0.74\,$s). This is completely negligible with respect to the cloud temperature of about $70\,\mu$K after transport and is in accordance with the observed absence of heating and sloshing. However it is to note that this effect is independent of the initial cloud temperature and might become important when trying to transport a BEC under the same trapping conditions.

For the old trap configuration an energy deposition on the order of several μK is expected in the range of transport times between 2 s and 2.5 s. This is still small

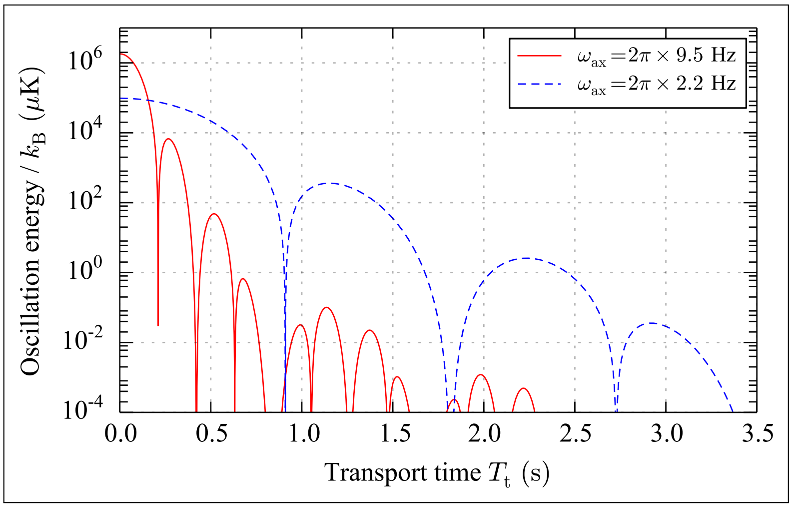

Figure 3.22: Center of mass oscillation energy after transport according to equation (3.24). The oscillation energy in temperature units is shown as a function of transport time for the two considered trap configurations.

compared to the cloud temperature of about 30 μK and is not expected to play a big role. This is also supported by the fact that the atom loss is already reasonably well described by acceleration-induced losses.

In conclusion one can derive from this discussion that a sufficiently strong axial confinement is the main factor to achieve an efficient and fast transport of an atomic cloud, reducing both acceleration-induced losses and facilitating the conditions for adiabaticity with respect to the axial trapping frequency.

3.8 Evaporative cooling to BEC in a crossed dipole trap

After the optical transport the phase-space density (PSD) in the center of the atomic cloud is on the order of 10^{-4}. To reach Bose-Einstein condensation the phase-space density needs to be increased to the critical value of about 2.6. In order to achieve this, the temperature (density) of the cloud needs to be further reduced (increased) which is done using the technique of evaporative cooling. In this technique, the high energy atoms in the tail of the thermal distribution are continuously removed, leaving the remaining cloud at a lower temperature after rethermalization takes place. Experimentally this can be achieved by gradually lowering the depth of the trap at a speed that allows the cloud to stay in thermal equilibrium. The efficiency and speed of evaporative cooling depends strongly on the elastic scattering rate which determines the time scale for rethermalization of the cloud. In the single beam dipole trap, it is on the order of hundreds of Hz when operating at the full trap depth. However, during evaporation the trap depth is reduced by lowering the laser power which also diminishes the trapping frequencies, thus the density and elastic scattering rate. Towards the end of the evaporation this can result in quite low elastic scattering rates such that the cooling gets very inefficient. To avoid this problem, the evaporative cooling is performed in a crossed dipole trap where much higher trapping frequencies and therefore elastic scattering rates are achieved. The experimental realization of the crossed dipole trap and subsequent evaporation to a BEC is presented in the following sections.

3.8.1 Experimental realization of the crossed dipole trap

Trap configuration

The crossed dipole trap consists of two radially symmetric focused laser beams that are intersecting in the horizontal plane at an angle of 90 °. The first one is the 1070 nm dipole trap beam that is also used to transport the atomic cloud as described in the previous section. The second dipole trap beam is at a wavelength of 532 nm provided by a Verdi laser system with a maximum used power of 1.2 W. The radial trapping frequency at the maximum power is measured to be $\omega_r/2\pi = 1.35(10)\,\mathrm{kHz}$ which corresponds to a waist of about $19\,\mu$m. From this the axial trap frequency can be estimated to be about $\omega_{\mathrm{ax}}/2\pi = 9\,\mathrm{Hz}$ and the trap depth to be on the order of $130\,\mu$K.

Control and stabilization of laser powers

The laser powers of the two dipole trap arms are individually controlled. For the 532 nm beam the power control is realized using an acousto-optical modulator where the provided radio-frequency power determines the amount of light diffraction into the dipole trap beam. The desired light power is set according to a previously performed calibration curve and no active stabilization is performed at this point.

For the 1070 nm beam a combination of two independent ways to control the dipole trap power is used. The first one consists of an analog control input on the fiber laser itself that allows us to tune the output power via the current of the pump diode. This allows for tuning between 10 % and 100 % of the nominal power with a bandwidth of about 10 kHz. The second way uses a $\lambda/2$-waveplate mounted

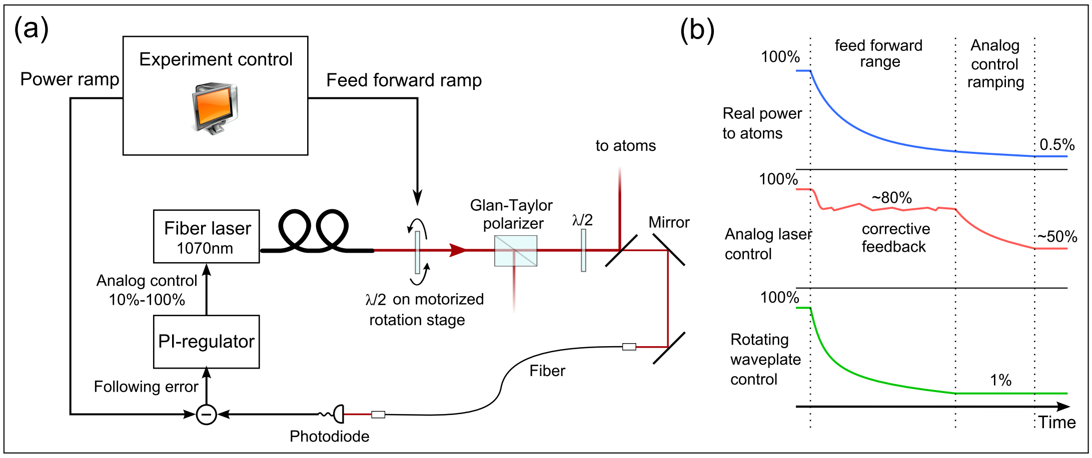

Figure 3.23: A sketch of the power ramping and stabilization scheme of the 1070 nm dipole trap is shown in (a). The contributions of the feed-forward and the analog laser control during a typical power ramp is shown in part (b). For ramps beyond the range of the feed-forward control, the analog control automatically takes over the ramping part.

on a motorized rotation stage[23] with a high power polarizer[24] placed behind. The rotation angle θ of the $\lambda/2$-waveplate controls the beam polarization and therefore the amount of transmitted light on the polarizer according to a $\cos^2(\theta)$ law (also called Malus's law). The maximum extinction ratio achievable on the polarizer is about 1:130, limited by the purity of the laser polarization. Together the two ways allow for a power control with a dynamic range of about a factor 1000, which is enough for the evaporation ramps used in this experiment[25].

The setup for the closed loop power control operation is sketched in Figure 3.23. To monitor the real dipole trap power the light leaking on a mirror is sent to a photodiode. The photodiode signal is compared to an analog command voltage provided by the experimental control that defines the current power level to be attained. The difference signal is zeroed with the help of a PI[26]-regulator that feeds back to the analog input control of the fiber laser. This closed loop operation allows for rapid power control with a dynamic range of a factor of 10.

---

[23] DRTM-40, OWIS.

[24] GL15-C26, Thorlabs

[25] The reachable extinction ratio on the polarizer could be increased to over 1:1000 by cleaning the polarization first with another polarizer before the rotating $\lambda/2$-waveplate. This however comes with an additional power loss of about 5 % and an increased sensitivity to thermal lensing effects and has not been installed.

[26] Proportional integral.

To get the full needed dynamic range, the main ramping for evaporation is performed by the motorized rotation stage that is provided with a pre-calculated feed-forward signal from the experimental control. The closed loop feedback to the fiber laser input therefore only needs to perform corrections to the ramp performed by the rotation stage. The feed-forward signal is calculated by the experimental control such that the analog input control operates around 80 % of the maximum power to ensure a reasonable dynamic range for corrections. Operating too close to the 10 % lower limit results in an increased relative intensity noise and is therefore avoided. For fast switch-off of the laser power a digital switching input on the fiber laser is used that allows us to disable the laser output within about 10 μs.

Compared to the usually used AOM control [102] of the optical power this system has several advantages. Firstly, the amount of power loss when using an AOM in first order diffraction is typically on the order of 15 % − 20 %, whereas on the polarizer only 5 % are not usable. Secondly, an efficient diffraction on the AOM usually requires a beam radius on the order of 500 μm where especially at high powers (tens of Watts) thermal lensing effects can be problematic and lead to pointing instabilities [102]. The typical beam radius in the polarizer however can be ten times larger and thermal effects are therefore drastically reduced. Thirdly the AOM diffraction usually comes with a degradation of the transverse mode profile which is not present in the polarizer case. The main disadvantage with respect to the AOM solution is the limited control bandwidth. This however is not an issue for dipole trap ramping as long as no sub-millisecond pulsing or a strong intensity noise suppression are required.

The feed-forward control

The motorized rotation stage itself works in an independent closed loop position control mode whose working principle is sketched in Figure 3.24. The rotation stage is equipped with an optical rotary encoder and a Hall reference sensor that allows us to track the absolute rotation angle in real time with a discrete step resolution of 0.06 °. For this the digital rotary encoder signals are processed by an Arduino Uno microcontroller to extract the current position information that is subsequently converted to an analog voltage proportional to the angle of the stage. This voltage is then compared to the desired feed-forward signal provided from the experimental control. A commercial analog PI-regulator with an integrated power stage then feeds back to the motor current to zero the following error. The high maximum rotation speed of the chosen motor model (3600 °/s) allows for a full scale power ramp in less than 100 ms. This ensures sufficient bandwidth to follow the rapid power changes in the beginning of the exponential ramps.

However the system performance using the commercial analog control unit was not satisfactory in the sense that the full regulation precision of the rotary encoder

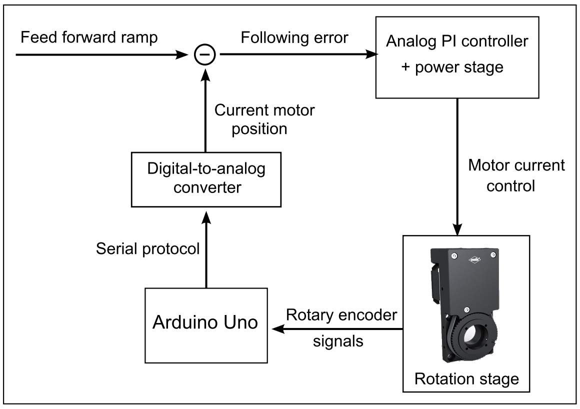

Figure 3.24: Working principle of the closed loop rotation stage position control within the feed-forward branch of the dipole trap power control.

could not be reached in closed loop mode. For this reason a second generation controller has been developed within this thesis work, based on a fully digital control system using an Arduino DUE microcontroller. This system implements a general purpose digital PID controller that rules out an analog control systems in many features, especially in flexibility and customizability. Technical details about this new generation controller can be found in Appendix B.

3.8.2 Evaporation ramp optimization

Power ramping sequence

The evaporative cooling is experimentally performed in two steps. During the first step the power of the 1070 nm trap is reduced while the 532 nm trap is kept at constant maximum power. This step serves to roughly equilibrate the potential depths of the two traps (that initially differ by about a factor of five) in order to gather a maximum of atoms in the crossed region. In the second step, the two trap beam powers are reduced with identical ramps such that the trap depth ratio between the two stays constant. This choice is mainly made to reduce the number of free parameters to optimize. The ramp forms for both steps are chosen to be simple exponentials given by

$$P_{1070}(t) = \begin{cases} P_{0,1070}\, e^{-t/\tau_1} & \text{for} \quad 0 \leq t \leq T_1 \\ P_{\text{interm}}\, e^{-t/\tau_2} & \text{for} \quad T_1 < t \leq T_1 + T_2 \end{cases}, \tag{3.30}$$

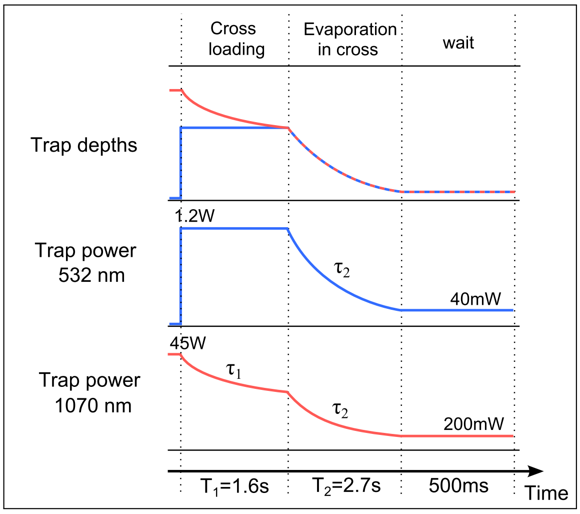

Figure 3.25: Schematic of the power ramping sequence used for evaporative cooling to BEC. The cooling is performed in two stages of duration T_1 and T_2 followed by 500 ms hold time to ensure thermalization of the cloud.

$$P_{532}(t) = \begin{cases} P_{0,532} & \text{for} \quad 0 \leq t \leq T_1 \\ P_{0,532}\, e^{-t/\tau_2} & \text{for} \quad T_1 < t \leq T_1 + T_2 \end{cases}, \tag{3.31}$$

where T_1 and T_2 denote the durations of the first and second evaporation stage respectively, $P_{0,1070}$ and $P_{0,532}$ the initial trap powers and P_{interm} the 1070 nm power after the first stage. This typical ramping scheme to reach a BEC is illustrated in Figure 3.25.

With this choice of ramp forms the free parameters to be optimized experimentally are the two time constants τ_1 and τ_2 as well as the initial power in the 532 nm trap $P_{0,532}$ and the intermediate equilibration power of the 1070 nm part P_{interm}. The two stages have been optimized independently and an optimized BEC atom number has been found for $\tau_1 = \tau_2 = 800\,\text{ms}$, $P_{0,532} = 1.2\,\text{W}$ and $P_{\text{interm}} = 0.11 \times P_{1070,0}$, leading to a total evaporation time of $T_1 + T_2 \approx 4.3\,\text{s}$.

Evolution of cold cloud parameters

The evolution of the cold cloud parameters during the evaporation sequence has been measured experimentally. The important quantities to consider are the atom number N, the cloud temperature T, the phase-space density ρ_{PSD}, the elastic scattering rate Γ_{el} and the atom loss rate due to inelastic three-body collisions.

The atom number as well as the cloud temperature are extracted from the cloud density distribution that is measured after time-of-flight (TOF). The phase-space density, elastic collision rate and inelastic three-body loss decay rate are determined in the center of the thermal cloud in harmonic approximation of the trapping potentials. The phase-space density is then given by [103]

$$\rho_{\mathrm{PSD}} = \frac{\hbar^3 \bar{\omega}^3 N}{k_{\mathrm{B}}^3 T^3}\,, \tag{3.32}$$

where $\bar{\omega} = (\omega_x \omega_y \omega_z)^{1/3}$ denotes the geometrical mean of the angular trapping frequencies. The elastic collision rate in harmonic approximation reads [103]

$$\Gamma_{\mathrm{el}} = \frac{m \bar{\omega}^3 \sigma N}{2\pi^2 k_{\mathrm{B}} T}\,, \tag{3.33}$$

with $\sigma = 8\pi a_{\mathrm{s}}^2$ the scattering cross section that is determined by the s-wave scattering length a_{s}. The effect of three-body losses is in general described by a rate equation [104]

$$\frac{\mathrm{d}N}{\mathrm{d}t} = -K_3 \int n^3(\boldsymbol{r}, t)\, \mathrm{d}^3\boldsymbol{r}\,, \tag{3.34}$$

with K_3 the three-body loss coefficient for thermal atoms. This can be rewritten in the form

$$\frac{\mathrm{d}N}{\mathrm{d}t} = -K_3 \, \langle n(\boldsymbol{r})^2 \rangle \, N \equiv -\Gamma_{3-\mathrm{body}}(N)\, N\,, \tag{3.35}$$

with $\langle n(\boldsymbol{r})^2 \rangle = \int n(\boldsymbol{r}) n^2(\boldsymbol{r}) \mathrm{d}^3\boldsymbol{r}/N$, representing the mean of the squared density. The coefficient $\Gamma_{3-\mathrm{body}}(N)$ then quantifies the instantaneous decay rate that can be estimated by

$$\Gamma_{3-\mathrm{body}} = K_3 \, \langle n(\boldsymbol{r})^2 \rangle \sim K_3\, n(0)^2 = K_3\, \bar{\omega}^6 N^2 \left(\frac{m}{2\pi k_{\mathrm{B}} T} \right)^3\,, \tag{3.36}$$

where $n(0)$ is the density in the center of the cloud. The values for the three-body loss coefficient and the s-wave scattering length for ^{174}Yb were measured in [57] and value to $K_3 = 4.2 \times 10^{-29}\,\mathrm{cm}^6/\mathrm{s}$ and $a_{\mathrm{s}} = 5.55\,\mathrm{nm}$. The trapping frequencies for each point in time are calculated according to the $\sqrt{P}$ scaling with the trap beam power P, starting from the measured values at maximum power. The resulting experimental data is shown in Figure 3.26.

It is to note that during the evaporation cycle two regimes have to be distinguished. In the beginning the evaporation mainly takes place in the 1070 nm trap and no increased density in the crossed region is measured. In this part the atom number and temperature is measured for the full cloud and the trapping frequency calculations take only the 1070 nm trap into account. Those data points are shown as blue triangles. After about 1.5 s a reasonably large fraction of atoms is loaded into the crossed region of the two dipole traps. Starting from this point the atom

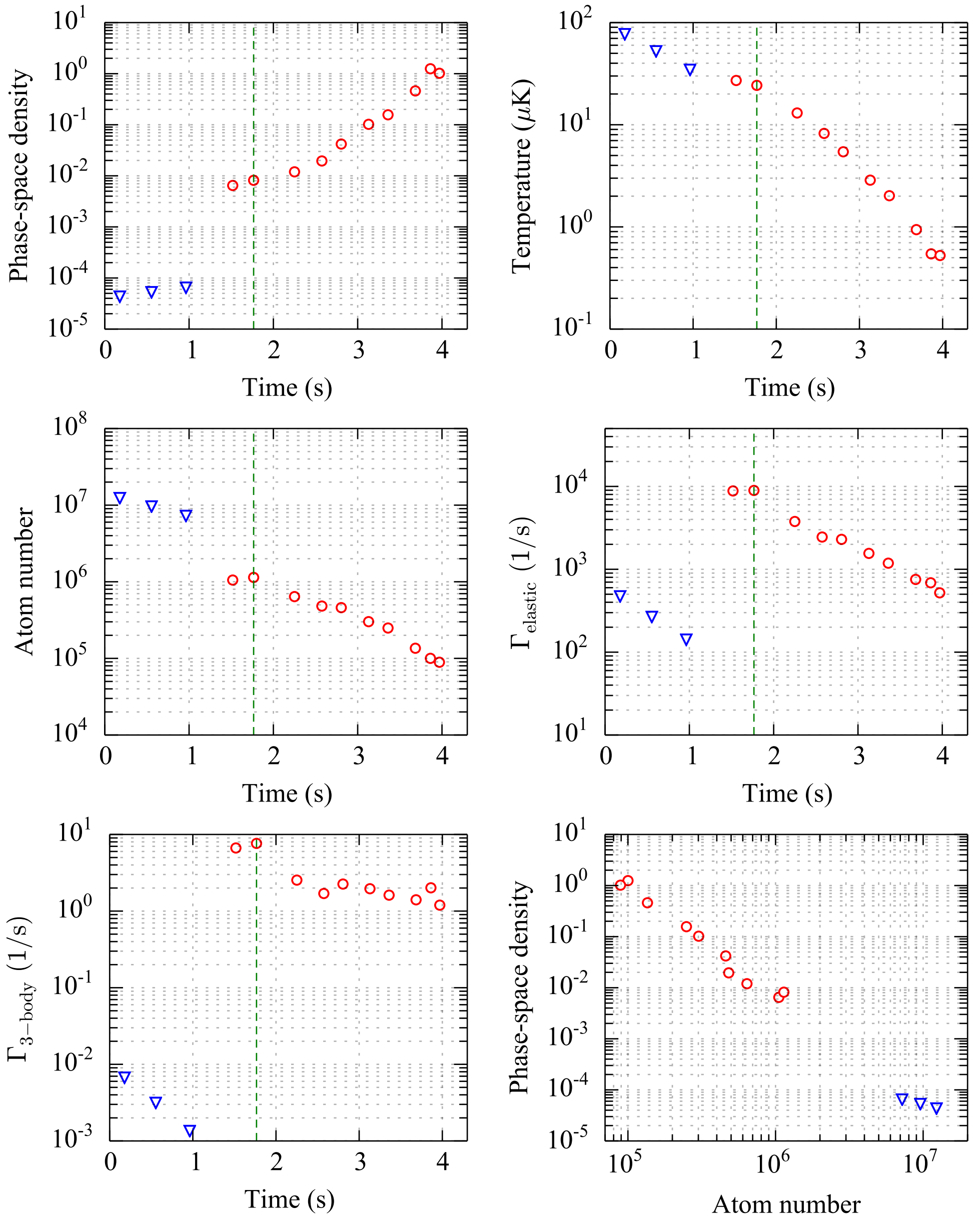

Figure 3.26: Example data of the evolution of the cold cloud properties during evaporative cooling. The blue triangles correspond to data at the beginning of the evaporation where the atoms are still mainly in the 1070 nm trap and the potential of the 532 nm trap is neglected. For the red circle data points the atoms located in the crossed region are considered together with the combined trapping potential. The green dashed line indicates the beginning of the second evaporation stage from where on both dipole trap powers are ramped.

number and temperature is measured only for the fraction of atoms located in the crossed region and both trapping potentials are considered for the trap frequency calculations. Those points are shown as red circles.

In the first part the phase space density increases marginally but the elastic scattering rate is high enough to effectively load atoms into the crossed region. Once a reasonable fraction is loaded into the cross, the phase space density is strongly increased due a the strong enhancement in trapping frequency and therefore central density. At the end of evaporation stage 1, where the trap depths are roughly equilibrated, the trapping frequencies value to $(\omega_x, \omega_y, \omega_z)/2\pi \simeq (0.48, 1.43, 1.35)\,\mathrm{kHz}$, where x and z denote the propagation axis of the 532 nm trap and 1070 nm trap respectively. The central density at this point is about $4 \times 10^{14}/\mathrm{cm}^3$ leading to a quite large elastic scattering that allows for a rapid evaporative cooling in the following to a PSD on the order of unity within a total time of about 4 s. However along with the high density comes a non negligible effect of three-body losses with a decay rate of $\Gamma_{3-\mathrm{body}} \gtrsim 1\,\mathrm{s}^{-1}$ for the current configuration of trap parameters. It is therefore expected that the atom loss during evaporation could be diminished by increasing the beam waists of one of the two dipole trap beams to reduce the central density further.

3.8.3 BEC transition and atom number stability

Observing the BEC transition

The phase transition from a thermal gas to a BEC occurs when the cloud temperature is brought below the critical temperature T_c. For a non-interacting bosonic gas in the thermodynamic limit $N \to \infty$ it is given by [105]

$$T_\mathrm{c} = 0.94\,\frac{\hbar\bar{\omega}N^{1/3}}{k_\mathrm{B}}\,. \tag{3.37}$$

Experimentally the phase transition has been observed as the transformation of the density distribution after time-of-flight from a thermal profile described by a Bose function to a peaking condensate wave function described by an integrated Thomas-Fermi profile [92]. The observation of this transformation is shown in the data in Figure 3.27.

Close below the transition temperature the thermal and BEC phase are in coexistence which can be observed as a so-called bimodal momentum distribution where the condensate atoms appear as a characteristic peak above the background of the thermal atoms. In this case, the column density (integrated along the

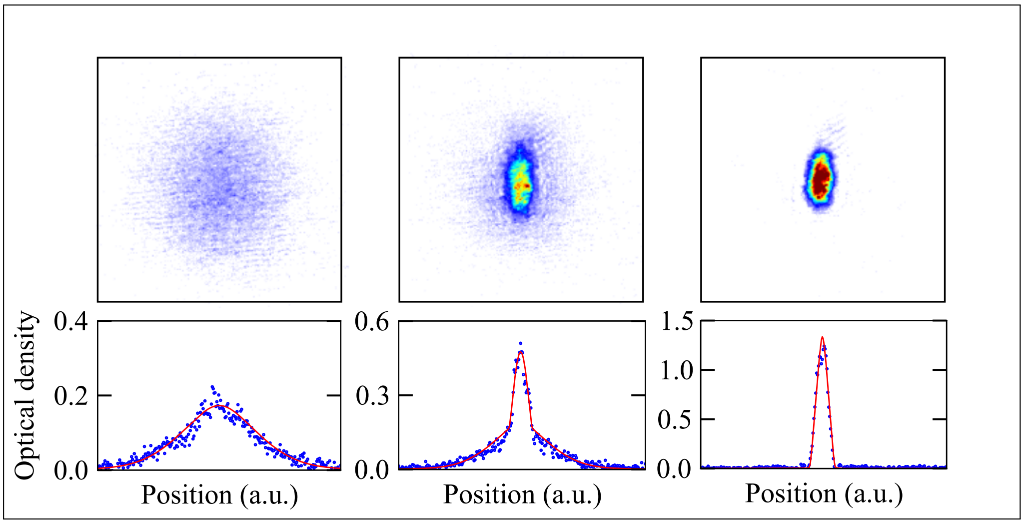

Figure 3.27: Observation of the thermal cloud to BEC transition in time-of-flight absorption images. The upper images are measurements of density distribution after time-of-flight that reflect the momentum distribution of the cloud in false color. The lower plots show a horizontal cut of the density distribution through the center of the cloud (blue dots) and the according cut of the 2D fit of equation 3.39. From left to right the temperature of the cloud decreases.

imaging direction z) measured after time-of-flight can be described by the sum of the thermal and condensate part given by [92]

$$\tilde{n}(x,y) = \tilde{n}_{\mathrm{c}}(0)\left[\max\left(0, 1-\frac{x^2}{\sigma_{x,c}^2}-\frac{y^2}{\sigma_{y,c}^2}\right)\right]^{3/2} \tag{3.38}$$

$$+\,\tilde{n}_{\mathrm{th}}(0)\, g_2\left(\exp\left[-\frac{x^2}{\sigma_{x,th}^2}-\frac{y^2}{\sigma_{y,th}^2}\right]\right) \tag{3.39}$$

where $\tilde{n}_{\mathrm{c}}(0)$ and $\tilde{n}_{\mathrm{th}}(0)$ denote the central line densities of the condensate and thermal part respectively, $\sigma_{x/y,c/th}$ describe the transverse extensions and $g_j(z) = \sum_i z^i/i^j$ denotes the Bose function. A fit of this distribution to the measured density profile allows one to determine the cloud temperature T from the size of the thermal component and the number of atoms in the condensed state N_0 (for details see [83], [106]). The fraction of condensed to total number of atoms N_0/N is in theory described by [105]

$$\frac{N_0}{N} = 1-\left(\frac{T}{T_{\mathrm{c}}}\right)^3, \tag{3.40}$$

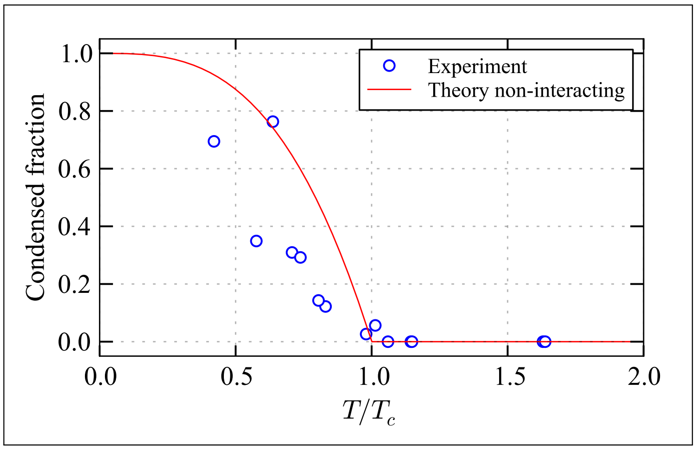

Figure 3.28: The condensed fraction as a function of cloud temperature in units of the critical temperature T_c is shown. The experimental data is shown as blue circles where for each measurement point a new reference transition temperature T_c is calculated according to the current trap frequency and atom number. The red solid line shows a theory curve for non-interacting particles according to equation (3.40).

when assuming non-interacting bosons in the thermodynamic limit in a harmonic trap.

Experimentally the condensed fraction has been measured as a function of the cloud temperature as shown in Figure 3.28. The measured transition temperature of about $T_\mathrm{c}^\mathrm{exp} = 570(40)\,\mathrm{nK}$ is in accordance with the one expected from equation (3.37) for the non-interacting case, that calculates to $T_\mathrm{c} = 580(30)\,\mathrm{nK}$. The theory of the condensed fraction for non-interacting bosons describes the qualitative behaviour of the data. Quantitatively however the data does not match the theory very well, that systematically overestimates the condensed fraction. This however is expected, since interaction effects are known to play an important role and result in general in a lower transition temperature as well as a lower condensed fraction for a given temperature (see for example [105]). Other possible explanations could be errors in the determination of the trap frequencies that are scaled down from the measured ones at full trap beam powers. Small errors in the power calibration curves might have a large influence especially for the 532 nm beam that is not actively stabilized.

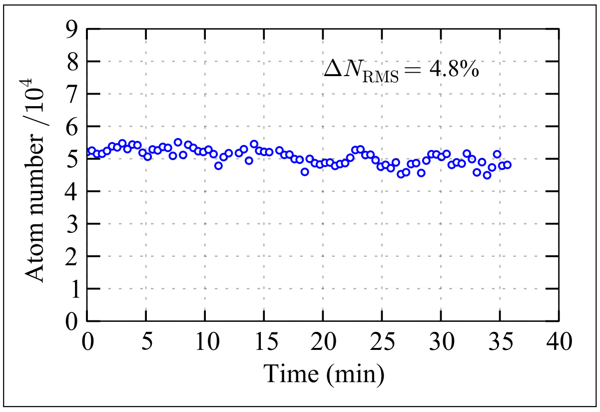

Figure 3.29: Atom number stability measurement for repeatedly produced BECs with a condensed fraction above 80 %. The number of atoms in the BEC is shown for 82 consecutive runs with a total duration of about 35 min.

BEC atom number stability

The typical achieved atom numbers in a pure BEC ($N_0/N > 80\,\%$) is about 5×10^4. The trapping frequencies at this point are about $(\omega_x, \omega_y, \omega_z) \simeq 2\pi \times (100, 275, 250)\,\mathrm{Hz}$. The full experimental cycle to produce a BEC with this atom number has a duration of about 22 s. However experimentally the reproducibility of the BEC is as important as the size one is able to achieve. An example measurement of the atom number fluctuations in this experiment is shown in Figure 3.29 for a series of 82 consecutive BEC productions with identical sequences. The observed RMS atom number fluctuations ΔN_{RMS} are below 5 % for the full set and below 3 % for the first 40 runs.

3.9 Loading a BEC into an optical lattice

It is important for the planned experiments to be able to load the atomic cloud into the fundamental band of an optical lattice and to keep the cloud sufficiently cold on the timescale of typical experiments (tens to hundreds of milliseconds). In this section some characterization measurements of the adiabatic loading and the heating in the lattice are presented for the case of a one-dimensional optical lattice. Furthermore it is important later on to be able to calibrate the depth of the applied optical lattice. This is done using the method of Kapitza-Dirac diffraction where also experimental results are presented.

3.9.1 Experimental characterization of adiabatic loading and heating in a lattice

The typical procedure to load atoms into the fundamental band of an optical lattice is to start by the production of a pure BEC with negligible thermal fraction and to subsequently ramp up the power of the optical lattice. It is important to avoid excitations during ramp up that will lead to heating of the cloud after equilibration in the final lattice configuration. To ensure this the lattice ramp up has to be slow enough, where in general two intrinsic time scales of the system determine the conditions for adiabaticity. The first one is the time scale associated with the population of higher bands during loading which is usually on the order of the inverse recoil frequency [107], typically about tens to hundreds of microseconds. To verify adiabaticity with respect to the band population the methods presented in [108] can be used. The second time scale to consider is the relaxation of the BEC into the many-body ground state of the lattice. Basically this corresponds to the time scale the atoms need to redistribute into the equilibrium density distribution over the full lattice geometry which is determined by the tunneling energy and the trapping frequencies of the external confinement. The typical order of magnitude for this is tens to hundreds of milliseconds [109] and is in general the more constraining time scale to ensure adiabaticity.

In the following the loading of a one-dimensional retro-reflected optical lattice in vertical direction at a wavelength of 760 nm is considered with a lattice depth of $U_0/E_\mathrm{R} \simeq 11$. The radial trapping frequency of the lattice potential is calculated to be about $\omega_\mathrm{r}^\mathrm{latt} \approx 2\pi \times 17\,\mathrm{Hz}$.

Adiabatic loading

To characterize the adiabaticity of the lattice loading with respect to the many-body ground state, the heating of the cloud when ramping up and down the lattice is measured. This is realized using a partially condensed cloud, whose condensed fraction is highly sensitive to changes in cloud temperature. For the measurements the ramps for loading and unloading the lattice are chosen to be complementary cubic splines with equal durations. Between ramping up and down a hold time of 300 ms duration is added to allow for possible excitations to transform into cloud heating. The measured condensed fraction after this sequence is then compared to the one obtained when no lattice beam is applied after the same total duration. In both cases the full dipole trap potentials are maintained during the lattice sequence. The resulting data is shown in Figure 3.30.

It can be seen that a steady state regime of the condensed fraction is reached for ramping times above about 25 ms where heating seems to be no longer decreased by longer ramp times. This suggests that the loading can be considered as adiabatic

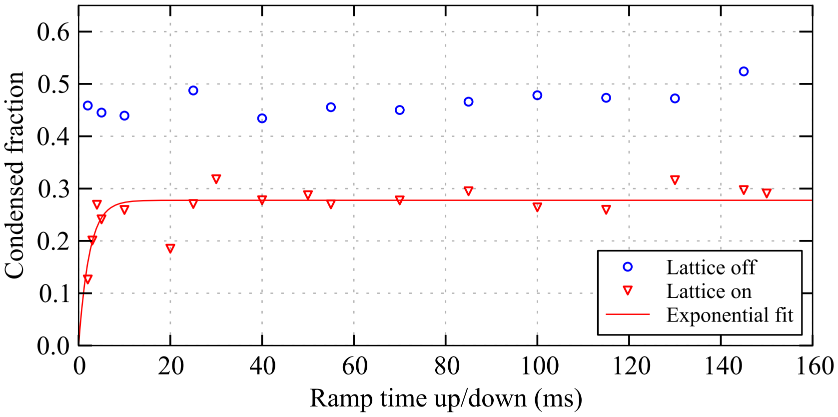

Figure 3.30: Measurement of the condensed fraction of the cloud as a function of the ramp time used for loading and unloading (with equal ramp time) the lattice. Between the ramping up and down the cloud is held in the lattice for 300 ms. The measurement is performed with the lattice beams activated (red triangles) and for comparison the same sequence without any applied lattice beam (blue circles). The red solid line is an exponential fit to the data with the lattice switched on, that mainly serves as a guide to the eye.

above 25 ms. The fact that the condensed fraction is systematically reduced with respect to the case of no lattice loading suggests that nevertheless there is heating in the lattice within the 300 ms hold time. The corresponding measured increase in temperature is about 50 to 100 nK. This increase is expected to be not caused by excitations due to a non-adiabatic loading, but more due to technical reasons as will be discussed in the next section.

Heating in the lattice

Next the heating in the lattice is characterized assuming that the lattice loading is performed adiabatically. For this the ramp up and down duration is chosen to be 25 ms and the heating of the cloud measured after a variable hold time in the lattice. Again this is performed with a partially condensed cloud with the goal to measure the time evolution of the cloud temperature and condensed fraction. The resulting data is shown in Figure 3.31.

Without applying the optical lattice it can be seen that the atom number as well as the temperature drops over time which suggests that there is still evaporative cooling ongoing. At the same time the condensed fraction rises marginally in the first second which supports this statement. For hold times longer than about a

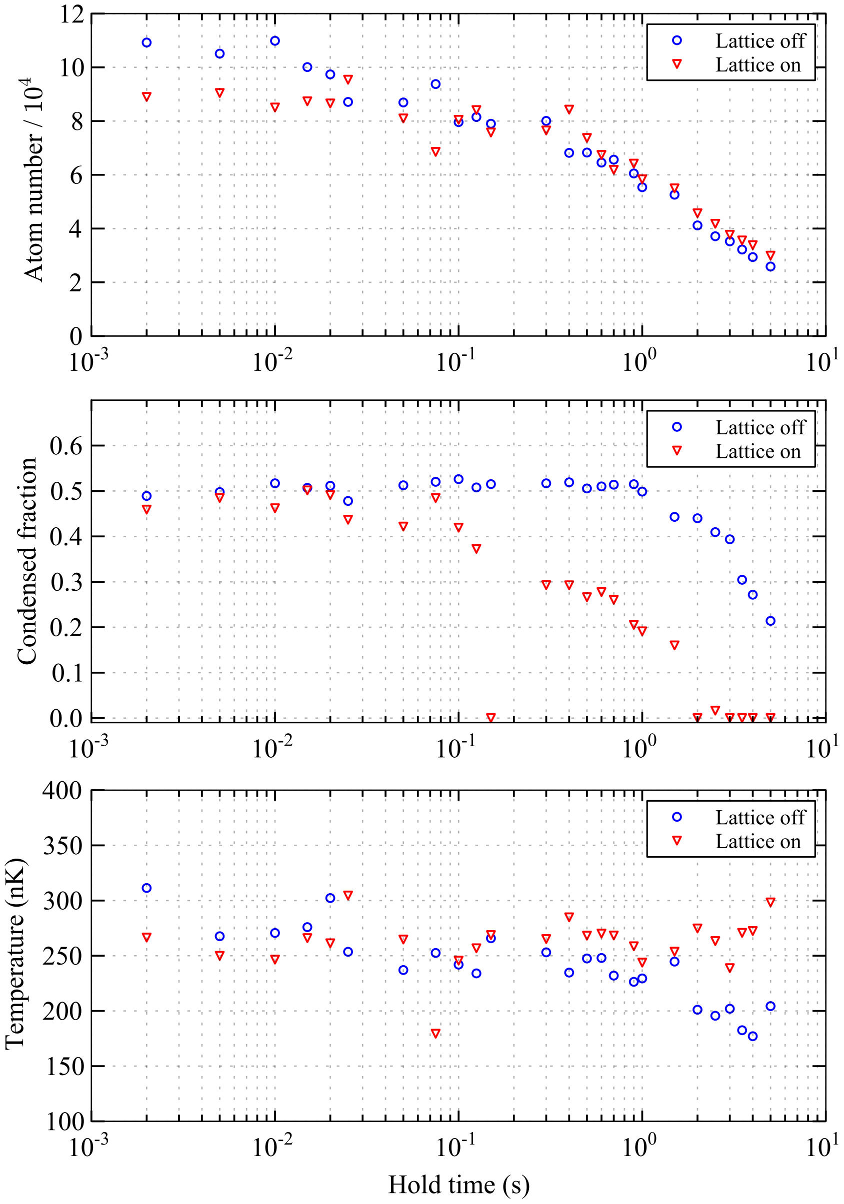

Figure 3.31: Characterization of heating in an optical lattice. The evolution of the atom number, condensed fraction and cloud temperature are shown for a variable hold time of the atoms in the lattice (red triangles). The transfer into and out of the lattice is done in the adiabatic regime. The evolution is compared to the one of equal sequence but with no lattice light applied (blue circles).

second the condensed fraction drops on a time scale of several seconds, probably due to the change in transition temperature according to the observed atom loss, since the temperature of the cloud also drops.

When now looking at the case with lattice loading, it can be seen that the presence of the lattice does not induce supplementary atom loss for the full range of measured hold times. However the fact that the condensed fraction at the same time is reduced on a time scale of hundreds of milliseconds shows that there is definitely heating of the atoms in the optical lattice. This is supported by the fact that the temperature rises slightly as compared to the falling one without lattice. The effect that the temperature rises only marginally, however, is probably influenced by the still ongoing evaporation. The condensed fraction in this sense seems to be much more sensitive to the lattice induced heating. Possible mechanisms that could explain the observed heating could be power fluctuations or pointing instabilities of the lattice beams and/or the crossed dipole trap beams that are kept on during the full sequence of lattice loading and unloading (only the 1070 nm trap beam is actively power stabilized). In particular the pointing stability of the 532 nm dipole trap beam has been observed to be quite poor, which will be solved in a future setup where it will be fiber coupled. Other intrinsic sources of heating could be three-body losses and spontaneous emission, whereas the latter is expected to be on the order of 0.3 nK/s and can therefore be neglected. The presented data shows the nice sensitivity and capability to characterize heating in the lattice using a partially condensed atomic cloud.

3.9.2 Lattice depth calibration

To measure the depth of an optical lattice the technique of Kapitza-Dirac diffraction [110] is used within this thesis. For this a BEC is illuminated with a short pulse of lattice light at a constant power with a variable duration τ. The applied standing wave light field imprints a phase grating onto the BEC wavefunction that transforms after time-of-flight into a diffraction pattern with characteristic peaks at integer multiples of twice the lattice momentum $\pm 2\hbar k_{\mathrm{latt}}$. The momentum transfer of twice the lattice momentum can be understood as the process of photon absorption from one lattice beam and stimulated emission into the other lattice beam. Example data of this effect is shown in Figure 3.32 where a series of TOF absorption images is shown for different pulse durations τ and a lattice depth of about $U_0/E_{\mathrm{R}} \simeq 53$.

The effect can be theoretically described for the case of a one-dimensional lattice in z direction by assuming the initial BEC as a monochromatic plane wave with mean initial momentum $p_z = p_0$. This assumption is reasonable under the condition that the spatial extension of the BEC wavefunction is large compared to the lattice spacing, which is always true in the considered experiments. The

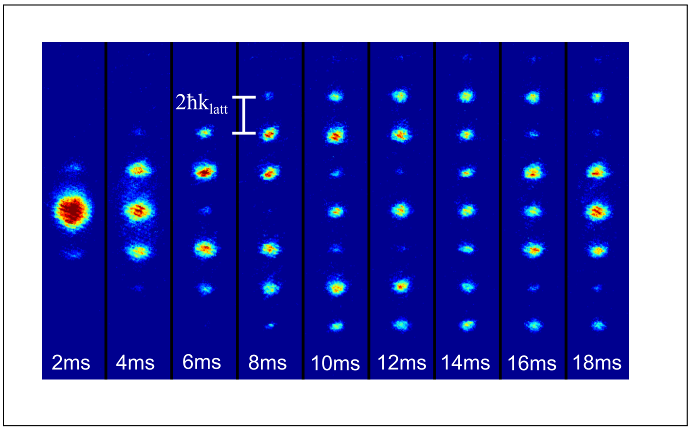

Figure 3.32: Evolution of the Kapitza-Dirac diffraction pattern with the pulse duration τ. Shown is a series of measured density distributions taken after 13 ms time-of-flight. The pulse duration for each measurement is given on the bottom of each image and increases from left to right. The spacing between two neighbouring diffraction peaks corresponds to $2\hbar k_{\mathrm{latt}}$ as indicated in the figure.

Hamiltonian describing the dynamics in the presence of the lattice potential of the form $U(z) = U_0 \cos^2(k_{\mathrm{latt}} z)$ is given by

$$H = \frac{p_z^2}{2m} + \frac{U_0}{2} - \frac{U_0}{4} \cos(2k_{\mathrm{latt}} z)\,, \tag{3.41}$$

where interactions have been neglected. After the pulse time τ the initial monochromatic momentum state $|\psi(0)\rangle = |p_0\rangle$ of the BEC has evolved to

$$|\psi(\tau)\rangle = e^{-iH\tau/\hbar}\,|\psi(0)\rangle\,. \tag{3.42}$$

When τ is short[27], the kinetic energy term $p_z^2/2m$ can be neglected and the final state $|\psi(\tau)\rangle$ can be written as [103]

$$|\psi(\tau)\rangle = \sum_{n\in\mathbb{Z}} i^n J_n\left(\frac{U_0\tau}{2\hbar}\right) |p_0 - 2n\hbar k_{\mathrm{latt}}\rangle\,, \tag{3.43}$$

with $J_n(x)$ the Bessel functions. In this form it becomes clear that the cloud population initially in the monochromatic momentum state gets redistributed over

---

[27] In this approximation we neglect the kinetic energy term in the Hamiltonian (3.41) which is justified if τ is small compared to the harmonic oscillation period in a potential well of the lattice, $\tau \ll \hbar/2\sqrt{V_0 E_{\mathrm{R}}}$ [110].

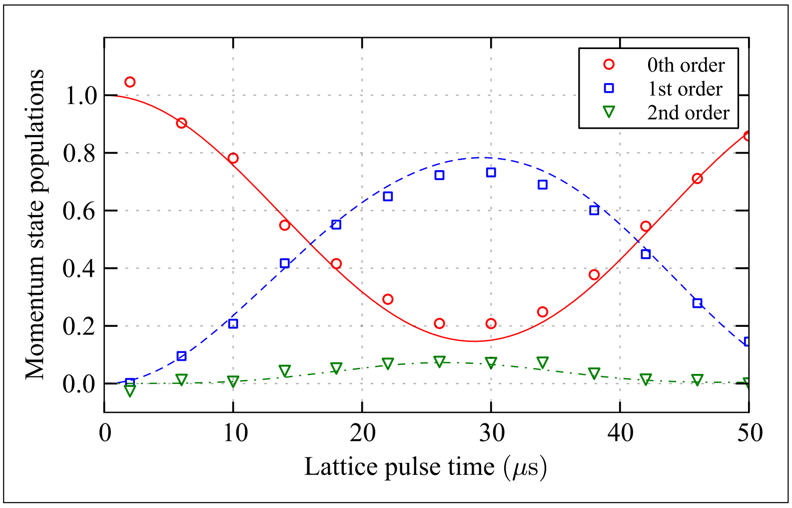

Figure 3.33: Evolution of the momentum state populations in Kapitza-Dirac diffraction of a BEC on a standing wave light field. The populations of the momentum states 0 (0th order), $\pm 2\hbar k_{\mathrm{latt}}$ (1st order) and $\pm 4\hbar k_{\mathrm{latt}}$ (2nd order) are shown as a function of applied lattice pulse duration. The numerically calculated momentum state populations are shown as lines for the 0th (red solid), 1st (blue dashed) and 2nd (green dash-dot) order for a lattice depth of $U_0/E_{\mathrm{R}} = 11.9$.

many momentum states that are spaced in discrete steps of $\pm 2\hbar k_{\mathrm{latt}}$. The population in the different orders is given by the square of the Bessel functions $J_n(x)$. In the case where the internal BEC dynamics cannot be neglected during the pulse duration τ, the time evolution in equation (3.42) can be calculated numerically. This can be done in momentum space by truncating the number of diffraction orders taken into account and diagonalizing the resulting finite dimensional matrix for the state evolution.

An example of experimentally measured populations in the diffraction orders as a function of pulse time τ are shown in Figure 3.33. The measured populations are fitted by a numerically calculated solution of equation 3.42, where the lattice depth U_0 acts as the only free fit parameter. The best fit value allows us to determine the lattice depth which is here found to be $U_0/E_{\mathrm{R}} = 11.9$.

CHAPTER 4

High resolution spectroscopy on a ^{174}Yb Bose-Einstein condensate

One of the central ingredients for the realization of artificial gauge fields with cold ytterbium atoms is the coherent driving of the ultranarrow $^1S_0 \leftrightarrow {}^3P_0$ clock transition at 578 nm (as will be discussed in chapter 5). This is not a trivial task and requires a very stable and narrow linewidth laser system. The laser linewidth should be on the order of tens of Hz (see section 5.2.9) and frequency drifts should not exceed several Hz/s. Such laser systems have been realized in the community of optical clocks, where laser linewidth in the sub-Hz regime with drifts well below 100 mHz/s have been achieved [59] [111]. The basic technique thereby is to lock the laser to an ultralow expansion (ULE) high finesse cavity. Although our requirements are less demanding, the development and handling of such a laser system is complicated and is so far unknown territory for our group. Also in the quantum gases community only very few groups have so far performed experiments with similar laser systems [112, 113].

In this chapter our first spectroscopic results on the clock transition are presented. The main objectives of these spectroscopy experiments are to actually find the atomic resonance and to get some practice in handling the ultranarrow laser system and the techniques involved. Important is thereby to monitor and characterize drifts of the ULE cavity resonances as well as to determine the actual linewidth of our laser. Our short term goal is also to characterize the collisional properties of atoms in the $^3P_0$ state, that are not yet known for ^{174}Yb. The scattering lengths and inelastic collision rates for $^1S_0$-$^3P_0$ and $^3P_0$-$^3P_0$ scattering are in particular relevant for the planned experiments concerning artificial gauge fields (see section 5.2.3).

The chapter starts by explaining the technique to reach a reasonable coupling strength on the clock transition for ^{174}Yb using a static magnetic field. This is followed by the description of the laser system and its stabilization to an ultralow expansion cavity. Afterwards the problem to calibrate the absolute laser and to find the $^1\mathrm{S}_0 \leftrightarrow {}^3\mathrm{P}_0$ resonance is addressed, that we solve using spectroscopy on molecular iodine. Then the results of spectroscopic measurements on a BEC in a crossed dipole trap and during time-of-flight are presented, followed by a discussion of frequency drifts of the ULE cavity. Finally we present spectroscopic measurements on a BEC after hydrodynamic expansion, with the possible application for an absolute laser frequency calibration in a single experimental cycle.

4.1 Magnetically induced clock transition probing

In this section the problem of addressing the highly forbidden $^1\mathrm{S}_0 \leftrightarrow {}^3\mathrm{P}_0$ clock transition in bosonic ytterbium is discussed. We stick here to the usual convention to denote the energy levels of ytterbium by labels as in the Russell-Saunders (also called LS) coupling regime, where the spin-orbit interaction of individual electrons is neglected[1]. In this coupling regime a transition of the type $^1\mathrm{S}_0 \leftrightarrow {}^3\mathrm{P}_0$ ($g \leftrightarrow e$) is forbidden in all multipole orders, since it violates both, the total spin and total angular momentum selection rules $\Delta S = 0$ and $J_g = 0 \not\leftrightarrow J_e = 0$. For the odd (fermionic) isotopes of ytterbium the clock transition is weakly permitted (natural linewidth on the order of 10 mHz [114], [115]) due to hyperfine coupling between the nuclear spin ($\neq 0$) and the total angular momentum of the electrons. However, for the bosonic isotopes, like ^{174}Yb, the nuclear spin is zero and the coupling needs to be permitted by other means.

As proposed in [115] and realized in [116] the coupling for the bosonic isotopes can be provided by an external static magnetic field $\boldsymbol{B}$. This field admixes a small amount of the nearby $|^3\mathrm{P}_1\rangle$ state to the $|^3\mathrm{P}_0\rangle$ state (see Figure 4.1), where the coupling matrix element is given by $\Omega_B = \langle ^3\mathrm{P}_1|\hat{\boldsymbol{\mu}} \cdot \boldsymbol{B}|^3\mathrm{P}_0\rangle/\hbar$, with $\hat{\boldsymbol{\mu}}$ the magnetic dipole operator. In the case where Ω_B is small compared to the energy difference Δ between $|^3\mathrm{P}_0\rangle$ and $|^3\mathrm{P}_1\rangle$, the new energy eigenstate can in first order perturbation theory calculated to be [115]

$$|^3\mathrm{P}'_0\rangle \approx |^3\mathrm{P}_0\rangle + \frac{\Omega_B}{\Delta}|^3\mathrm{P}_1\rangle\,, \tag{4.1}$$

where a small portion of $|^3\mathrm{P}_1\rangle$ is mixed to the bare $|^3\mathrm{P}_0\rangle$ state. This results in the fact that the transition $|^1\mathrm{S}_0\rangle \leftrightarrow |^3\mathrm{P}'_0\rangle$, in the new eigenbasis, is now partially

---

[1] This approximation is in general not true for atoms as heavy as ytterbium and the LS coupling notation does not precisely characterize the properties of the energy eigenstates.

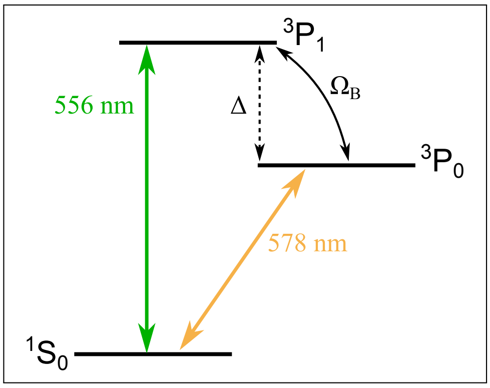

Figure 4.1: Sketch of the relevant energy levels for the technique to magnetically permit the $^1S_0 \leftrightarrow {}^3P_0$ clock transition.

dipole allowed. When applying resonant laser light with an oscillating electric field $\boldsymbol{E}$, the effective Rabi frequency is given by

$$\Omega_{\mathrm{Rabi}} = \frac{1}{\hbar}\langle {}^3\mathrm{P}_0'|\hat{\boldsymbol{d}} \cdot \boldsymbol{E}|{}^1\mathrm{S}_0\rangle \approx \frac{\Omega_{\mathrm{B}}}{\hbar\Delta}\langle {}^3\mathrm{P}_1|\hat{\boldsymbol{d}} \cdot \boldsymbol{E}|{}^1\mathrm{S}_0\rangle\,, \tag{4.2}$$

with $\hat{\boldsymbol{d}}$ being the electric dipole operator. In [115] it has been shown that this Rabi frequency takes the form

$$\boxed{\Omega_{\mathrm{Rabi}} = \alpha\sqrt{I}|\boldsymbol{B}|\cos(\theta)}\,, \tag{4.3}$$

where θ denotes the angle between $\boldsymbol{B}$ and the linearly polarized $\boldsymbol{E}$ field, and I denotes the intensity of the resonant laser light. The $\sqrt{I}$ and $|\boldsymbol{B}|$ dependence can be understood as a result of the linear dependence on the electric field $\boldsymbol{E} \propto \sqrt{I}$ and on the coupling matrix element $\Omega_{\mathrm{B}} \propto \boldsymbol{B}$. The proportionality factor α depends on the specific properties of the considered atomic species. For ytterbium it takes the value [115]

$$\alpha = 2\pi \times 186\frac{\mathrm{Hz}}{\mathrm{T}\sqrt{\mathrm{mW/cm^2}}}\,. \tag{4.4}$$

The application of the magnetic field also shifts the bare resonance frequency due to the quadratic Zeeman effect influencing the energy of the $^3\mathrm{P}_0$ state,

$$\Delta_{\mathrm{Zeeman}} = \beta|\boldsymbol{B}|^2\,, \tag{4.5}$$

with $\beta = -62\,\mathrm{mHz/G^2}$ [115] for ytterbium. The spontaneous emission rate from $|{}^3\mathrm{P}_0'\rangle$ towards the $|{}^1\mathrm{S}_0\rangle$ ground state is given by [115]

$$\Gamma_{\mathrm{sp}} = \left|\frac{\Delta_{\mathrm{Zeeman}}\gamma}{\Delta}\right|\,, \tag{4.6}$$

where γ is the spontaneous emission rate from $|^3\mathrm{P}_1\rangle$ to the ground state.

Experimental realization and typical parameters

We use this technique in our experiment to achieve a reasonable coupling strength on the clock transition of ^{174}Yb. A pair of coils is placed around the science chamber that produces a nearly homogeneous magnetic field of about 150 G in the vertical direction. Typically we use a laser power of about 2 mW that is focussed to a waist on the order of $w_0 \approx 30\,\mu$m. For these parameters the Rabi frequency values to $\Omega_{\mathrm{Rabi}} \approx 2\pi \times 1\,\mathrm{kHz}$ and the quadratic Zeeman shift is about $\Delta_{\mathrm{Zeeman}}/h \approx -1.4\,\mathrm{kHz}$. The spontaneous emission rate towards the ground state calculates to $\Gamma_{\mathrm{sp}} \sim 2\pi \times 10\,\mu\mathrm{Hz}$ and is therefore completely negligible on the experimental time scale.

It is to note that the linear polarization of the coupling light has to be chosen parallel with the magnetic field to achieve the maximum coupling strength [due to $\cos(\theta)$ in equation (4.3)]. Therefore the choice of a vertical magnetic field direction constraints the possible propagation directions of the coupling laser to be in the horizontal plane. In particular when the laser beam propagates parallel to the magnetic field no coupling can be achieved.

4.2 Collisional properties of the $^3\mathrm{P}_0$ state

Collisional properties of atoms in the $^3\mathrm{P}_0$ (e) state play an important role in the high resolution spectroscopy on a BEC and for the planned experiments concerning artificial gauge fields. Relevant processes are thereby scattering of e atoms among each other, as well as with atoms in the $^1\mathrm{S}_0$ (g) ground state. The quantity that characterizes the elastic scattering between the particles is the s-wave scattering length. For interactions between g atoms the scattering length, here labeled a_{gg} has been measured accurately [57]. The scattering lengths a_{ge} and a_{ee}, for g-e and e-e interactions, are not yet measured for ^{174}Yb. However, they are important to know in order to estimate the magnitude of diverse interaction effects. It will therefore be necessary to determine these quantities experimentally.

Beyond the elastic scattering properties, the inelastic scattering of type g-e and e-e also plays an important role in the planned experiments. The fact that the internal energy of the e atoms is released in the inelastic scattering processes, results in enormous kinetic energies of the scattered particles. The associated atom losses can be experimentally problematic.

The inelastic collisions are in general described by a coefficient β that quantifies the collision rate per unit of density. In the case the inelastic collisions lead

Atom	e state	$\beta_{ee}(\mathrm{cm}^3/\mathrm{s})$	$\beta_{ge}(\mathrm{cm}^3/\mathrm{s})$
^{174}Yb	$^3\mathrm{P}_2$	$1.0(3) \times 10^{-11}$	-
^{173}Yb	$^3\mathrm{P}_0$	$2.2(6) \times 10^{-11}$	$3.9(16) \times 10^{-13}$
^{171}Yb	$^3\mathrm{P}_0$	5×10^{-11}	3×10^{-11}
^{88}Sr	$^3\mathrm{P}_0$	$1.9(12) \times 10^{-11}$	-

Table 4.1: Table of measured inelastic collision rate coefficients of metastable states e. The shown values are taken from [112] (^{174}Yb), [118] (^{171}Yb), [113] (^{173}Yb) and [119] (^{88}Sr).

primarily to atom losses, they can be described via a rate equation for the number of remaining atoms N,

$$\dot{N} = -\beta N^2 \,. \tag{4.7}$$

The coefficient β can therefore be experimentally determined by careful loss measurements. The coefficients β_{ge} and β_{ee} for inelastic collisions of type g-e and e-e have not been measured yet for ^{174}Yb. The so far known values for other ytterbium isotopes are summarized in Table 4.1, which allows one to get an idea of the expected orders of magnitude. There, also the measured values for ^{88}Sr and the $^3\mathrm{P}_2$ state in ^{174}Yb are given for comparison. Since our typical condensate densities are on the order of several $10^{14}/\mathrm{cm}^3$, we might well expect decay rates due to inelastic collisions as high as several kHz in the bulk. However the situation is expected to be different when having the atoms in a three-dimensional optical lattice. When working in a regime with less than one atom per lattice site $\bar{n} < 1$, inelastic losses are expected to be strongly reduced. In the case of strong on-site interactions double occupancy will be suppressed, thus further reducing the influence of inelastic losses. For a Mott insulator at unity filling $\bar{n} = 1$, for example, double occupancy is suppressed as $\propto (J/U)^2$ [117], where J and U are the tunneling and interaction energy respectively.

4.3 Ultranarrow laser at 578 nm

The laser system to coherently address the $^1\mathrm{S}_0 \leftrightarrow {}^3\mathrm{P}_0$ clock transition is one of the central components in this experiment. As already mentioned in the introduction of this chapter, the laser linewidth should ideally be much below 100 Hz, which is at least a factor of 1000 lower than the typical linewidths of the lasers used for laser-cooling and trapping. In addition, we would like to limit drifts of the absolute laser frequency to a reasonable level of kHz/hour or below. To achieve these two requirements, we frequency lock the 578 nm laser to a resonance of an ultralow expansion (ULE) high finesse cavity that serves as a passively stable frequency reference. This is an often used technique in the domain of optical clocks, where laser linewidths in the sub-Hz regime and drifts down to 25 mHz/s are reached (see for example [111]).

The typical Rabi frequency we intend to realize (homogeneously over the atomic cloud) is on the order of several kHz. When working with a bosonic ytterbium isotope, like ^{174}Yb, this necessitates typical power levels on the order of ten milliwatts (see section 4.1). The experimental realization of the laser system designated to fulfill these demands is presented in the following.

4.3.1 Getting 578 nm light using sum frequency generation

To create the light at 578 nm we have decided to use a sum frequency generation scheme of an amplified fiber laser system[2] at 1030 nm and a Nd:YAG laser[3] emitting at 1319 nm. The specified free running laser linewidths are $\Delta\nu_{1030} < 10\,\mathrm{kHz}$ (measured over 120 μs) and $\Delta\nu_{1319} < 1\,\mathrm{kHz}$ (measured over 100ms), which is a convenient starting point to reach the desired final linewidth. The available laser powers are $P_{1030} \simeq 500\,\mathrm{mW}$ and $P_{1319} \simeq 200\,\mathrm{mW}$. For the sum frequency generation a non-linear waveguide[4] (length 1 cm) of periodically poled lithium niobate (ppLN) is used. The fact that the mode field diameter in the waveguide is on the order of several micrometers leads to high intensities and therefore reasonable conversion efficiencies in a single pass configuration. The specified conversion coefficient[5] for our waveguide is $\alpha = 2200\,\%\,\mathrm{W/W^2}$.

To estimate the total amount of yellow light that we could expect from the sum frequency generation, the coupling losses for the two fundamental beams into the waveguide have to be taken into account. The transverse mode in the waveguide is specified to be elliptical with a mode field diameter ratio of about 0.6. For an optimal coupling we would need to use elliptically shaped transverse beam profiles, where the waists along the two axes would need to be optimized independently for both incident wavelengths. To keep the optical setup simple (see Figure 4.2), we have decided to keep the circular shape of the incoming beams and to optimize

---

[2] Koheras BoostiK Y10, NKT Photonics.

[3] Mephisto, InnoLight/Coherent.

[4] HC Photonics.

[5] The efficiency of sum frequency generation from waves at frequencies ω_1 and ω_2 to $\omega_1 + \omega_2$ is described by the factor α. It connects the input powers at the fundamental wavelengths with the powers at the sum frequency via $P_{\omega_1+\omega_2} = \alpha\, P_{\omega_1} P_{\omega_2}$ [120]. This holds true when $P_{\omega_1+\omega_2} \ll P_{\omega_1}, P_{\omega_2}$, which is called the non-depleted pump approximation.

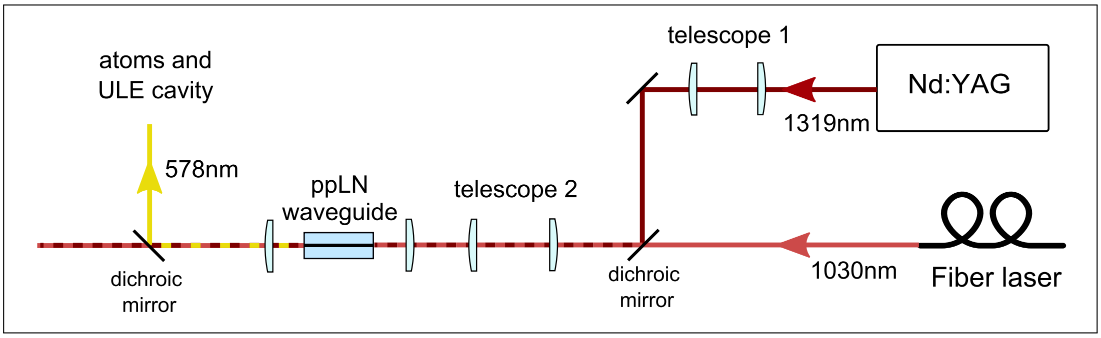

Figure 4.2: Optical setup for sum-frequency generation in a non-linear waveguide. The laser beams at 1319 nm and 1030 nm are overlapped using a dichroic mirror. The mode matching for the two incident beams to the waveguide is achieved using the two telescopes 1 and 2. The sum-frequency generated light at 578 nm is separated from the fundamental wavelengths using a second dichroic mirror.

the waists to have the best overlap with the elliptic mode field[6]. The achieved coupling efficiencies are about 23 % at 1030 nm and 8 % at 1319 nm[7]. The expected overall conversion coefficient for sum-frequency generation would accordingly be on the order of $\alpha_{\mathrm{tot}} \approx 40\,\%\mathrm{W}/\mathrm{W}^2$. Experimentally we have been able to achieve 15 mW at 578 nm with incident powers of $P_{1030} \approx 200\,\mathrm{mW}$ and $P_{1319} \approx 130\,\mathrm{mW}$, corresponding to $\alpha_{\mathrm{tot}}^{\mathrm{meas}} \approx 56\,\%\mathrm{W}/\mathrm{W}^2$. Although we could in principle increase the powers of the two fundamental lasers further, we did not do so to avoid the risk of damaging the waveguide[8]. Instead we continued to work at moderate power levels ($P_{578} < 10\,\mathrm{mW}$), that were found sufficient for the performed experiments.

The mode quality of the exiting yellow beam has been found to be quite poor. Typical fiber coupling efficiencies to a single mode fiber did not exceed 50 % and the beam profile deviated visibly from a fundamental Gaussian mode. All experiments described in this chapter have been carried out with the waveguide setup, but recently we have been able to improve the power of our coupling laser using a slightly different setup.

---

[6] Coupling light into the waveguide in the first place was found to be a tricky task, since most of the light incident on the crystal exits at the end facade, no matter if it passes by the waveguide or not. Some spatial filtering had to be installed to distinguish the coupled light from the non-coupled light.

[7] Theoretically one expects for perfectly circular incoming beams 26 % at 1030 nm and 15 % at 1319 nm in the optimum coupling case. These values are based on the waveguide specifications and a calculation of the overlap between the incoming circular and elliptical waveguide mode.

[8] One of our waveguides got burned on the input surface during an alignment procedure at intermediate power levels. Since we had only one more waveguide left we were cautious with the laser powers and always worked at the lower limit of what was needed for the experiment.

In this second generation setup the waveguide has been replaced with a "regular" magnesium-doped ppLN crystal of 2 cm length. In order to reach reasonably large output powers in a single pass configuration the amplifier of the 1030 nm laser system has been replaced with another amplifier, ten times more powerful (500 mW→5 W). With this system a maximum power of 65 mW at 578 nm has been measured. Compared to the old system, this new setup allows one to work with much larger beam waists, since it does not rely on the coupling of a micron sized waveguide. This makes the system more stable and robust, where furthermore the amount of useful light is increased due to the better output mode quality and the resulting higher fiber coupling efficiency ($> 80\,\%$).

4.3.2 Ultralow expansion cavity

In order to keep the frequency of the 578 nm laser in resonance with the ytterbium $^1\mathrm{S}_0 \leftrightarrow {}^3\mathrm{P}_0$ transition and to further narrow down the laser linewidth, a very stable frequency reference is needed. Obtaining an atomic reference signal in direct spectroscopy of the metastable clock transition is very hard. A common technique is to use the resonances of a high finesse ultralow expansion cavity, acting as a passively stable frequency reference. This method is used in the domain of optical clocks since many years. Very stable high finesse cavities are now commercially available from specialized companies.

The cavity model

The ultralow expansion cavity used in this experiment[9] consists of a spherical spacer with a hole through its center and two optically contacted mirrors with retaining rings on their back (see Figure 4.3). The spacer is made of ultralow expansion (ULE) glass to minimize the effect of thermal drifts on the cavity length, while the mirrors are made of silica to reduce short term thermal noise. The cavity is held at two points and is mounted horizontally. To isolate the system most effectively from acoustic noise and ambient temperature drifts, the cavity is kept under vacuum (pressure of $\sim 10^{-8}$ mbar) within a temperature regulated thermal shield[10]. The vacuum chamber itself is placed on a vibration isolation table[11]. To isolate the cavity from acoustic noise and temperature fluctuations the whole system is placed in a wooden box, covered with acoustic foam[12].

---

[9] Advanced Thin Films, ATF-6300, premium grade ULE ATF-6301-4.

[10] The active temperature stabilization is performed using a Peltier module and commercial control electronics (LFI-3751, Wavelength Electronics).

[11] Nano-K 50 BM-10, Minus K Technology.

[12] It is to note that most of the data presented in this thesis is taken at a time where this wooden box was not yet installed. Instead a cardboard box was used to provide some shielding against currents from the air conditioning and other environmental fluctuations.

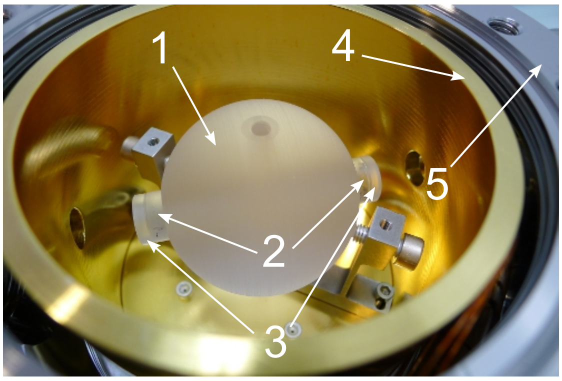

Figure 4.3: Photo of the ultralow expansion cavity before closing the vacuum system. The cavity itself is mounted horizontally and consists of the ULE glass spacer (1) with the cavity mirrors (2) including ULE retaining rings on the back (3). It is placed within a thermal shield (4) inside a vacuum chamber (5).

The cavity itself comes in a plano-concave configuration, where the concave mirror has a radius of curvature of 50 cm and the cavity length is specified to be 47.6 (1) mm.

The temperature zero-crossing point

The ULE glass used for the cavity spacer has the special property that its linear thermal expansion coefficient α_{ULE} has a zero-crossing point (changes sign) close to room temperature. At the so-called zero-crossing temperature the linear expansion coefficient of ULE vanishes and the length of the ULE spacer alone takes a minimum (increases for rising and falling temperature). In practice the mirrors and even the coatings also affect the cavity resonance frequency when changing the temperature. The resonance frequency ω_{res} still shows a zero-crossing, where $\mathrm{d}\omega_{\mathrm{res}}/\mathrm{d}T = 0$, albeit at a lower temperature than the linear expansion coefficient of the ULE spacer. At this temperature it is experimentally most convenient to work, since the cavity resonance frequency is minimally sensitive to temperature fluctuations.

The exact temperature working point is found to be important to reduce drifts of the cavity resonances as will be further discussed in section 4.6. In this section also the precise determination of the temperature zero-crossing point will be presented.

Measurement of the free spectral range

The free spectral range $\delta\nu_{\mathrm{FSR}}$ and the finesse $\mathcal{F}$ are the two basic quantities that characterize the spectral properties of a cavity. The former corresponds to the frequency spacing between adjacent cavity resonances, that is for a Fabry-Pérot cavity of length L given by $\delta\nu_{\mathrm{FSR}} = c/2L$. The latter is defined as the ratio of the free spectral range $\delta\nu_{\mathrm{FSR}}$ and the FWHM[13] of the resonance peaks $\delta\nu_{\mathrm{peak}}$. The experimental determination of those two quantities is briefly presented in the following[14].

The free spectral range of the ULE cavity is measured using an electro-optical modulator (EOM). The EOM is used to add frequency sidebands to the laser light incident on the cavity. These sidebands appear symmetrically around the carrier frequency at integer multiples of the modulation frequency f_{EOM} applied to the EOM. They can be observed as additional cavity transmission resonances as sketched in Figure 4.4. By tuning f_{EOM} such that $\delta\nu_{\mathrm{FSR}} = m f_{\mathrm{EOM}}$, with integer m, the sidebands corresponding to adjacent cavity resonances overlap. Finding this modulation frequency experimentally allows one therefore to measure the free spectral range. The accuracy is thereby only limited by the precision at which one can point the cavity peaks and the absolute knowledge of the EOM modulation frequency, where the latter can be on the order of 1 Hz.

Using this method we have determined the free spectral range of our cavity to be

$$\boxed{\delta\nu_{\mathrm{FSR}} = 3\;144\;366(4)\,\mathrm{kHz}}\,. \tag{4.8}$$

The uncertainty is determined by the accuracy of the fitted cavity peak locations. The relative accuracy of 10^{-6} corresponds to a determination of the cavity length down to several nanometers. The expected value according to the specified cavity length of $L = 47.6\,(1)\,\mathrm{mm}$ would be $\delta\nu_{\mathrm{FSR,spec}} = c/2L = 3.149\,(6)\,\mathrm{GHz}$ and is in accordance with the measured one.

Measurement of the finesse

The finesse $\mathcal{F}$ of a Fabry-Pérot cavity of length L is for high mirror reflectivities R well described [121] by the relation

$$\mathcal{F} = \frac{\delta\nu_{\mathrm{FSR}}}{\delta\nu_{\mathrm{peak}}} \simeq \frac{\pi\sqrt{R}}{1-R}\,. \tag{4.9}$$

One way to determine the finesse experimentally is therefore by measuring the reflectivity of the cavity mirrors R. This can be done using a so-called cavity

---

[13] Full width at half maximum.

[14] More experimental details will be presented in the PhD thesis of Alexandre Dareau.

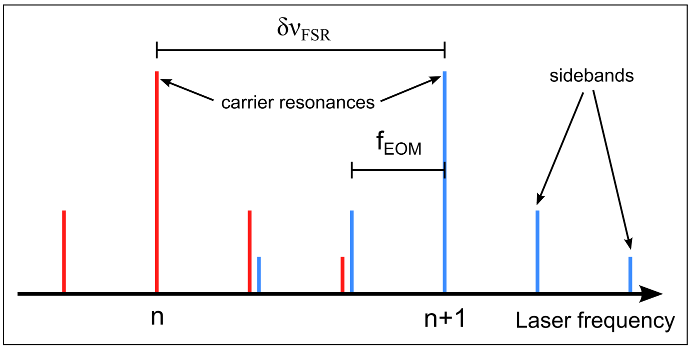

Figure 4.4: Principle of the free spectral range measurement of the ULE cavity. Sketched are the cavity resonances for the carrier frequency of two adjacent cavity peaks indexed by n (red) and $n+1$ (blue), including the additional resonances that appear due to the sidebands on the laser light added using an EOM at modulation frequency f_{EOM}. In the case where the resonances of the sidebands from the adjacent cavity peaks overlap, the free spectral range is an integer multiple of f_{EOM}.

ring-down measurement [122] where the lifetime of the light field in the cavity is determined after switching the incident light to the cavity off. The measured 1/e-lifetime of the light in our cavity has been measured to be 13.0(3) μs, that corresponds to a mirror reflectivity[15] of $R = 1 - 1.22(3) \times 10^{-5}$. From this, the cavity finesse is determined to be

$$\boxed{\mathcal{F} = 2.58(7) \times 10^5}\,. \tag{4.10}$$

This is found to be lower than the specified finesse of $\mathcal{F}_{\mathrm{spec}} = 3.0 \times 10^5$. From the measured finesse and the free spectral range we can determine the FWHM of our cavity peaks to be

$$\boxed{\delta\nu_{\mathrm{peak}} = 12.2(3)\,\mathrm{kHz}}\,. \tag{4.11}$$

4.3.3 Optical setup and frequency lock to the cavity

Frequency lock and linewidth estimation

The optical setup for frequency locking the 578 nm laser to the ULE cavity is shown in Figure 4.5. The electronic error signal required for locking is obtained using the Pound-Drever-Hall technique [123]. For this, the light incident on the cavity is

---

[15] The measured quantity corresponds to the overall transmission losses on a full cavity round-trip, where we describe the combined losses on both mirrors by a single effective reflectivity R.

phase modulated using an EOM at a frequency of 4 MHz. The light reflected on the ULE cavity is measured using a photodiode (PD2) and the signal demodulated in order to obtain the electronic error signal. We use commercially available analog locking electronics[16] to actively stabilize the frequency of the 578 nm light to a given cavity resonance. The lock-box thereby provides two corrective feedback signals for a slow (low-pass filtered) and fast (high-pass filtered) feedback line. The slow output is sent to the piezo input of the 1319 nm laser, whereas the fast output is used to control the RF frequency sent to AOM 1 using a digital synthesizer[17].

When the laser is locked to a cavity peak we can estimate the linewidth of the laser frequency with respect to the cavity resonance from the residual fluctuations of the error signal. The error signal shows peak-peak fluctuations corresponding to a peak-peak frequency excursion of about 100 Hz. A preliminary analysis of the spectral properties of the fluctuations of the error signal with the method given in [124] allowed us to estimate a linewidth with respect to the cavity resonance below 10 Hz (full width at half maximum). Under the assumption that the short term fluctuations of the cavity resonance are negligible, we could also reason to have a laser linewidth on the same order. This, however, has to be verified using ytterbium atoms as a probe. To this end one must operate in a configuration where interactions do not broaden the atomic transition (see section 4.5.1). This probably requires a very dilute gas in an optical lattice (similar configuration as in optical clocks [59]) or possibly a Mott insulator state.

Residual amplitude modulation

The frequency stability of the locked laser depends directly on the offset stability of the electronic error signal. This offset can be influenced by residual amplitude modulation (RAM) of the laser light incident on the cavity. Typical sources of RAM are etaloning effects on optics in the beam path or polarization modulation caused by the Pound-Drever-Hall EOM, that can transform into amplitude modulation on subsequent optics. In the case the amplitude modulation changes in time (e.g. due to temperature variations), also the locking point and therefore the laser frequency will change. It is therefore important to avoid the occurrence of RAM in the first place.

For this, we have placed all optics ($\lambda/2$-plates, photodiodes, lenses, etc.) at a reasonably large angle with respect to the beam propagation axis and have installed an optical isolator close to the cavity. To avoid that the phase modulation on the EOM also leads to a polarization modulation, the linear polarization of the incident light is required to be as pure as possible and well-aligned to the optical axis of the EOM. To ensure this, we use a polarizer to clean the polarization of the light

---

[16] D2-125 Laser Servo, Vescent.

[17] E4400B, Agilent Technologies.

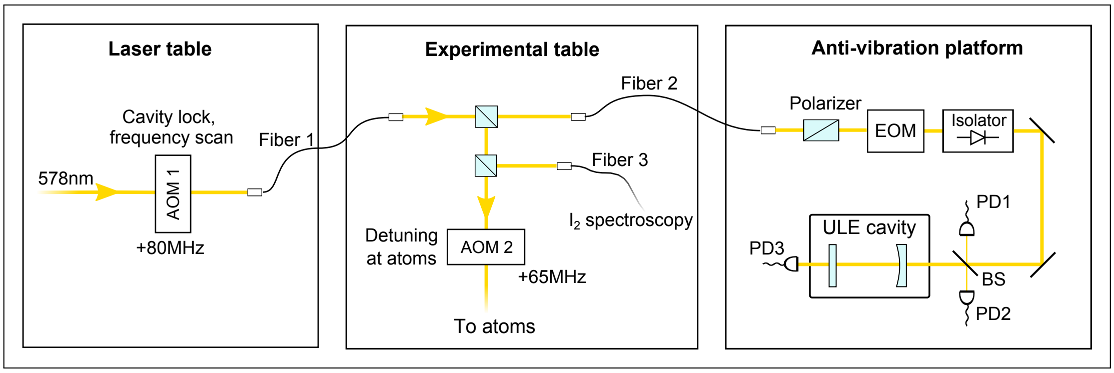

Figure 4.5: Optical setup of the ultranarrow laser at 578 nm. The three shown photodiodes are used for intensity stabilization (PD1), Pound-Drever-Hall detection (PD2) and observation of the cavity transmission (PD3). The beam splitter (BS) has a reflectivity of about $R \approx 90\,\%$. Legend: AOM: Acousto-optical modulator, EOM: Electro-optical modulator.

coming from the fiber. A good alignment of the EOM has been found to be critical to minimize RAM. Moreover, we actively stabilize the light power incident on the cavity that is monitored with a photodiode (PD1). The feedback for this is realized on the RF amplitude of AOM 1. With these precautions we were able to reduce the variations of the locking point to an amplitude of about 0.5 % of the peak-peak size of the error signal. The according maximum offset variations correspond to changes of the laser frequency of a few tens of Hz. For the experiments performed so far these fluctuations were not limiting since a frequency resolution on the kHz level was sufficient. In future experiments, however, it might be necessary to further reduce the variations of the error signal offset, that might also have origins different than RAM.

AOM frequency sources

The choice of RF sources used for the AOMs and EOMs in the setup is important. The usually used voltage controlled oscillators (VCO), for example, have a typical frequency sensitivity to temperature fluctuations on the order of several kHz/K. Accordingly standard VCOs are not a good choice as RF sources when a stability on the sub-kHz level is required. Furthermore standard VCOs with a central frequency on the order of 100 MHz are usually not controllable in frequency down to the sub-kHz level. Therefore mostly direct digital synthesizers (DDS) are used as frequency sources for the relevant AOMs and EOMs. They offer frequency sensitivities on the order of Hz/K and better. To reduce drifts between the different frequency sources, the driving clocks are planned to be phase locked to a 10 MHz quartz oscillator[18].

4.4 Finding the $^1S_0 \leftrightarrow {}^3P_0$ resonance using an iodine spectroscopy

One challenge when performing spectroscopy on an ultranarrow transition is to actually find the atomic resonance in the first place. Even though the resonance frequency of the ^{174}Yb clock transition is well known these days [53], one has to be able to calibrate the initial probe laser frequency with a sufficient accuracy.

In our case we perform spectroscopy on a BEC, where we expect a spectroscopic feature on the kHz level, determined by the Rabi frequency and a possible mean field broadening on the same order. With a good wavelength meter we could be able to determine the laser frequency with an accuracy down to several tens of MHz. To search a kHz feature within this range of uncertainty may take, in a naive point per point search, a total of tens of thousands of experimental cycles. For a typical experimental cycle time on the order of 10 s, a successful search may therefore take many days. When using frequency sweeps in each run, the scanning range per point can be realistically enlarged by a factor on the order of 100 (leaving some safety margins), which may still require hours of measurement time. Searching for the resonance in this way may be acceptable once, but will be impractical in the case it has to be repeated due to a change of the cavity resonance frequency after an intentional change of the parameters or uncontrolled drifts of the experiment.

This shows the need for an absolute frequency reference that allows one to determine the clock laser frequency ideally with an accuracy better than about 1 MHz. One possible way to realize this is to use a frequency comb as a reference. These devices, however, are very expensive and not yet standard equipment in cold atom laboratories. Another possibility is to use previously calibrated resonance frequencies of other atoms or molecules, that are reasonably close to the ytterbium resonance. This is the path we have chosen. We thereby use a hyperfine resonance in molecular iodine as a frequency reference, that has been calibrated by a research team in Japan [125] with an absolute accuracy of about 2 kHz using a frequency comb. This line is about 10 GHz detuned from the ^{174}Yb clock transition[19]. Using this absolute frequency reference, we were able to limit the initial search space for the resonance to a range smaller than about 500 kHz, allowing us to find the

---

[18] Stanford Research Systems, SRS SC10-15-3-J-A-A-J-SMA.

[19] The concerned resonance line in iodine is called R(37)16-1. It belongs to a series of transitions that are insensitive to the first order Zeeman shift and therefore well suited as frequency references.

resonance line within the very first scan of about 10 min duration. This technique is in particular interesting as a low cost and easy to set up solution since it is only based on a simple Doppler-free spectroscopy on an iodine vapor cell. After gaining some better understanding of systematic frequency shifts in our iodine spectroscopy setup[20], we are finally able to predict the ytterbium resonance with an absolute accuracy of better than 50 kHz.

In the following we present the main steps for the frequency calibration of our laser system and show the first search scans for the atomic resonance.

4.4.1 Calibration of the ULE cavity resonances using iodine

We observe the considered iodine transition in a standard saturated absorption spectroscopy setup, where a linewidth of the concerned transition of about 2 MHz has been measured. To calibrate the laser frequency close to the ytterbium line we use the ULE cavity resonances as a periodic frequency reference. The frequency configuration is sketched in Figure 4.6. First the absolute frequency of the $n + 3$ peak is calibrated with respect to the iodine transition by measuring the frequency difference $\delta\nu_{\mathrm{I}_2}$. This is achieved with the help of a frequency tunable EOM (not shown in the setup in Figure 4.5) that allows one to create sidebands on the laser light with a well known frequency spacing. Tuning the laser light in resonance with the considered iodine transition and the EOM frequency such that the sideband of order -1 is resonant with the $n + 3$ cavity peak allows to determine $\delta\nu_{\mathrm{I}_2}$ from the EOM modulation frequency. Due to our good knowledge of the free spectral range of the cavity we are then able to determine the frequency of the cavity peak n, onto which the laser is subsequently locked. The remaining frequency shift $\delta\nu_{\mathrm{Yb}}$ towards the ytterbium resonance is in our case about 65 MHz and is bridged using an AOM (AOM 2 in Figure 4.5). This AOM is also used to scan the laser frequency with respect to the atomic resonance for all spectroscopy measurements that will be presented in the following.

This technique to calibrate the frequencies of the cavity resonances has the very practical advantage that it is independent of the main ytterbium machine to be operational. This allows one to track and calibrate drifts of the cavity resonances in real time with an accuracy better than 50 kHz. This is for example used to determine the temperature zero-crossing point of the ULE cavity, as will be shown in section 4.6.

---

[20] Details will be presented in the PhD thesis of Alexandre Dareau.

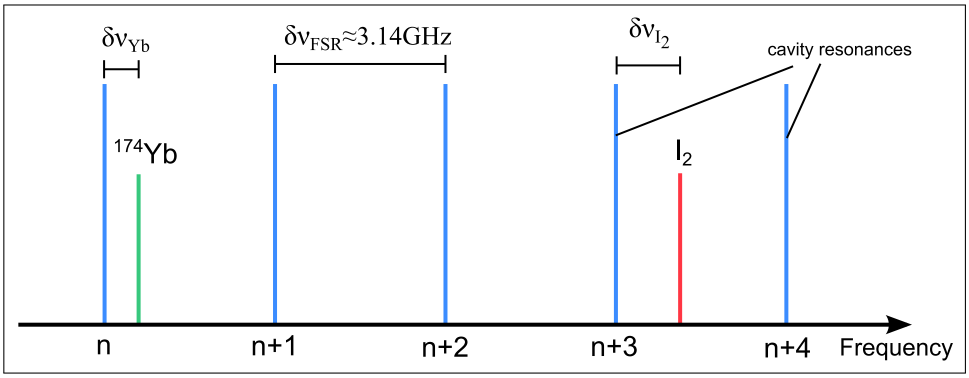

Figure 4.6: Sketch of the frequency relation between the ULE cavity resonances (blue), the ^{174}Yb clock transition (green) and the iodine transition (red) used for frequency calibration.

4.4.2 The first search scans

We have decided to perform the first spectroscopy measurements directly on a BEC, which was the simplest for us to set up[21]. The expected experimental signature when searching the resonance is a drop in observed atom number when imaging the atoms in the $^1S_0$ state. This drop is expected due to the excitation of atoms into the metastable $^3P_0$ state, where they are either not visible in the imaging or lost from the trap due to inelastic collisions with other atoms in the $^3P_0$ or $^1S_0$ state. Since the inelastic collision rates for e-e and g-e scattering are not known yet for ^{174}Yb, it is not clear which part will dominate. Since we performed our first experiments on a pure BEC, it is however likely that due to our central densities on the order of $10^{15}/\text{cm}^3$, inelastic losses might play a major role. Additionally, in our crossed dipole trap configuration atoms in the e state are slightly anti-trapped.

In Figure 4.7 our very first scan for the ytterbium resonance is shown. For this, we have sent the clock laser with a power of $260\,\mu$W and waist of about $25\,\mu$m (resulting in $\Omega_{\text{Rabi}}\approx 400\,$Hz) onto the BEC in the crossed dipole trap. The laser frequency is thereby tuned using an AOM. Within this first scan we could find a tiny signature, that we could confirm with a second, finer scan to be truly the desired resonance feature (see right-hand side of Figure 4.7).

---

[21] Another possible technique to find the resonance frequency is to illuminate the MOT with the clock light and to look for atom loss caused by the depumping from the cooling cycle (see for example [126] and [127]).

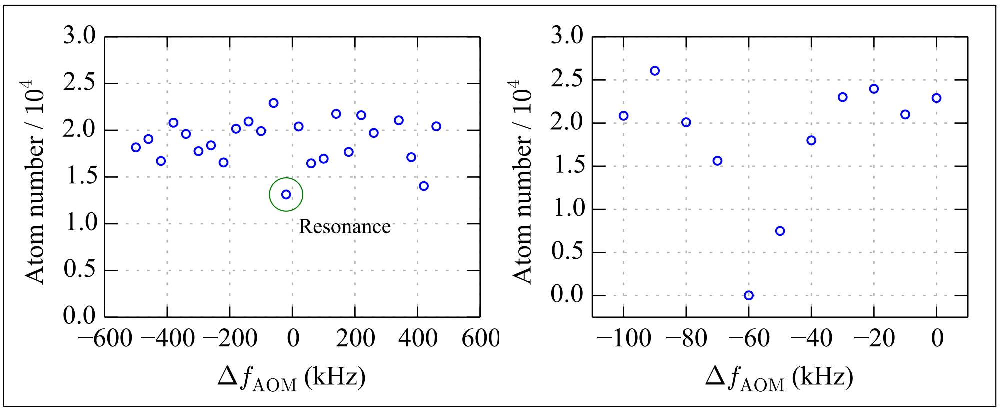

Figure 4.7: Search for the ^{174}Yb clock resonance. Shown is the number of atoms in the $^1S_0$ state of a BEC after an excitation pulse of the clock laser. On the left hand side the very first scan is shown, where for each data point the laser frequency is scanned in steps of 0.2 kHz with 10 ms dwell time resulting in a total span of 40 kHz per shot and 2 s interaction time. A second, finer scan is shown on the right-hand side, where a step size of 100 Hz with 10 ms dwell time over a total span of 10 kHz is used for each data point.

4.5 Results of spectroscopic measurements

In this section we report on the so far executed spectroscopy experiments on the $^1S_0 \leftrightarrow {}^3P_0$ transition, that were intended to characterize and understand the behaviour of our laser system and the basic physical effects associated with a spectroscopy on the kHz level. On the search of the narrowest spectrum that we could achieve with our system, we passed improvements in several steps that are presented in the following. This covers spectroscopy on a BEC in a crossed dipole trap and on an expanding cloud during time-of-flight. For both types of spectroscopic measurements we try to estimate the limiting physical or technical effects for the observed resonance width. The focus thereby lies more on the qualitative understanding of the observed spectra since a rigorous quantitative description is not possible due to the unknown scattering properties of the $^3P_0$ state. We try to estimate these properties from the observed spectra.

Before we go into the discussion of the observed spectra we would like to clarify a subtle point concerning the tuning of the probe laser frequency. Experimentally we perform frequency scans by tuning the RF frequency sent to an AOM. However, in addition to this controlled shift, the reference cavity is drifting and the laser frequency which is locked to it also changes in time. The frequency control using the AOM therefore does not necessarily map to the instantaneous real laser frequency. The cavity drifts can be observed as the effect that the AOM frequency required to hit the atomic resonance varies in time (see for example on the right-hand side of Figure 4.8). Since the frequency drifts are mostly found to be linear, we were able to correct the data points in post processing, provided that multiple spectra were measured close in time. The origin and further characterizations of these drifts will be discussed in section 4.6. Here we would like to concentrate on the physics associated with the spectroscopy methods. We will use the convention throughout this chapter that drift corrected frequency scales are denoted by Δf and non-drift-corrected ones by the bare AOM frequency scale Δf_{AOM}. The offset of the frequency scales are thereby chosen to match a characteristic point and have mostly no relation between different graphs.

4.5.1 In-situ spectroscopy

The first spectroscopy measurements have been performed on a BEC in the crossed dipole trap, created by two intersecting beams at 532 nm and 1070 nm (see section 3.8.1). The fact that the atomic cloud is trapped enables reasonably long interaction times with the probe beam, such that the Fourier broadening of the resonance due to the finite pulse length can be kept sufficiently small.

The typical sequence is to produce a pure BEC ($> 80\,\%$ condensed fraction) that is subsequently illuminated with the clock laser for a square pulse duration of $\tau_{\mathrm{pulse}} = 10\,\mathrm{ms}$. Then the atoms in the $^1\mathrm{S}_0$ state are imaged on the 399 nm transition after some time-of-flight. A typical spectrum obtained with a Rabi frequency of $\Omega_{\mathrm{Rabi}}/2\pi \approx 350\,\mathrm{Hz}$ is shown in Figure 4.8. The data points are corrected for the linear variation on the order of -1.9 Hz/s of the basic laser frequency during the measurement, as shown on the right-hand side of Figure 4.8.

The typical resonance width we could achieve was on the order of 10 kHz, where an asymmetric line shape is observed. Understanding the origin of the line shape and the width limitation is not easy since many effects are likely to contribute in this configuration, as will be discussed in the following. Two effects that play an important role are the differential light shift induced by the dipole trap beams and possibly the broadening due to mean field interactions of the condensate. Those two points are further explained in the next sections. The mean field broadening has been observed in other experiments to become an important effect for high resolution spectroscopy on BECs [126]. The associated broadening and line shift has in particular been used to observe the occurrence of a hydrogen BEC [128]. It is to note that a broadening due to the Doppler effect can in our case be neglected, since the momentum spread of the BEC wave function corresponds to a Doppler width on the order of $\Delta\omega_{\mathrm{Doppler}}/2\pi \sim \hbar/m\lambda\Delta x \sim 100\,\mathrm{Hz}$, for $\lambda = 578\,\mathrm{nm}$ and the typical spatial extension of the BEC wavefunction of $\Delta x \sim 3\,\mu\mathrm{m}$.

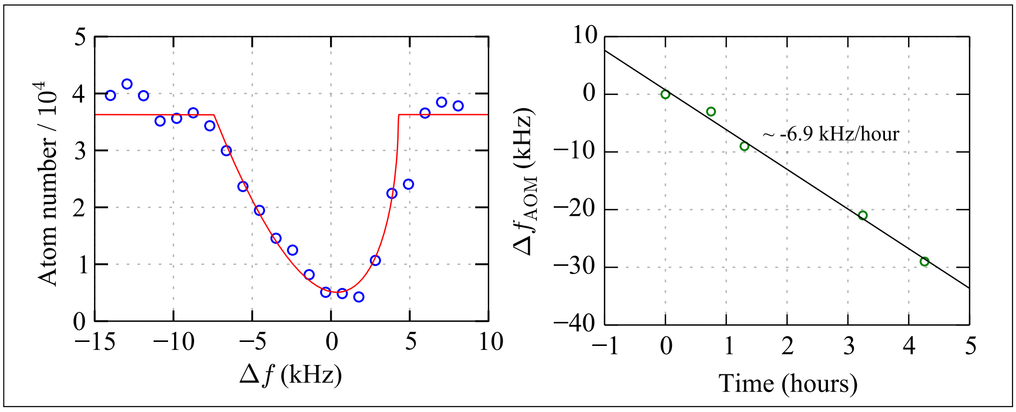

Figure 4.8: Clock resonance of a BEC in a crossed dipole trap. On the left-hand side the atom number in state g is shown as a function of the probe light frequency. The red curve corresponds to a fit to the data points with the line shape function from equation (4.18). The drift of the basic laser frequency on the same day is shown on the right-hand side, where the required AOM frequency to be at resonance is shown as a function of time. The frequency scale on the left-hand side has been corrected by this drift.

Thomas-Fermi profile and mean field interactions of a BEC

To describe the influence of the mean field interactions on the observed spectrum we treat the condensate of g state atoms within the external trapping potential $V^g_{\mathrm{ext}}(\boldsymbol{r})$ in the Thomas-Fermi approximation, where the density profile is given by [105]

$$n_g(\boldsymbol{r}) = \begin{cases} \frac{\mu - V^g_{\mathrm{ext}}(\boldsymbol{r})}{g_{gg}} & \text{for } \mu \geq V^g_{\mathrm{ext}}(\boldsymbol{r}) \\ 0 & \text{for } \mu < V^g_{\mathrm{ext}}(\boldsymbol{r}) \end{cases}, \tag{4.12}$$

with $g_{gg} = 4\pi\hbar^2 a_{\mathrm{gg}}/m$ being the interaction parameter for atoms in g and μ being the chemical potential in the center of the cloud. We assume in the following the external trapping potential to be harmonic, $V^g_{\mathrm{ext}}(\boldsymbol{r}) = m(\omega_x^2 x^2 + \omega_y^2 y^2 + \omega_z^2 z^2)/2$, with angular trapping frequencies ω_x, ω_y and ω_z along the main axes. The density distribution takes the form of an inverted parabola that goes to zero at the so-called Thomas-Fermi radii R_i given by [105]

$$R_i = \sqrt{\frac{2\mu}{m\omega_i^2}}, \tag{4.13}$$

with $i = (x, y, z)$. The chemical potential μ is fixed by the normalization condition for the total number of atoms to be $N = \int n_g(\boldsymbol{r})\,\mathrm{d}^3\boldsymbol{r}$, resulting in [105]

$$\mu = \frac{\hbar\omega_{\mathrm{ho}}}{2}\left(\frac{15Na_{gg}}{a_{\mathrm{ho}}}\right)^{2/5}, \tag{4.14}$$

where $\omega_{\mathrm{ho}} = (\omega_x\omega_y\omega_z)^{1/3}$ is the geometrical mean of the angular trapping frequencies and $a_{\mathrm{ho}} = \sqrt{\hbar/(m\omega_{\mathrm{ho}})}$ the associated mean oscillator length. The local energy of a condensate atom in state g within the mean field potential of the other condensate atoms is given by

$$U_g(\boldsymbol{r}) = g_{gg}n_g(\boldsymbol{r}) = \frac{4\pi\hbar^2 a_{gg}}{m}n_g(\boldsymbol{r})\,. \tag{4.15}$$

Resonance condition and mean field effects

We consider in the following the resonance condition for a condensate atom initially in g to be excited to state e. To simplify the formalism we assume the fraction of e atoms to be small, such that mean field interactions between e atoms can be neglected. Furthermore we restrict the discussion to energy contributions related to the mean field energy and the external trapping potentials. The trapping potentials in our case are not the same for g and e atoms since the atomic polarizabilities at the trapping wavelengths are not equal for both states[22].

In a semi-classical description we can write the resonance condition in terms of energy conservation as

$$\hbar\omega_{\mathrm{res}}(\boldsymbol{r}) = \hbar\omega_0 + (g_{ge} - g_{gg})\,n_g(\boldsymbol{r}) + V^e_{\mathrm{ext}}(\boldsymbol{r}) - V^g_{\mathrm{ext}}(\boldsymbol{r})\,, \tag{4.16}$$

where the term $g_{ge}n_g(\boldsymbol{r})$ denotes the interaction energy of an e atom in the mean field potential created by the condensate atoms in g and $\hbar\omega_0$ denotes the unperturbed transition energy between the internal atomic states. $V^e_{\mathrm{ext}}(\boldsymbol{r})$ and $V^g_{\mathrm{ext}}(\boldsymbol{r})$ correspond to the external potentials felt by g and e atoms respectively. Since the mean field and the differential external trapping potential are spatially dependent, also the laser frequency required to drive the transition, $\omega_{\mathrm{res}}(\boldsymbol{r})$, depends on the position of the atoms in the cloud.

In order to qualitatively understand the resulting line shape and broadening, let us first consider the case without differential light shift, $V^e_{\mathrm{ext}}(\boldsymbol{r}) = V^g_{\mathrm{ext}}(\boldsymbol{r})$. Here the situation depends on whether g_{ge} is larger or smaller than g_{gg}. The effective trapping potentials for g and e atoms are sketched in Figure 4.9 for both cases. For $g_{ge} > g_{gg}$, ($g_{ge} < g_{gg}$), the potential for e atoms is more repulsive (less repulsive)

---

[22] For the wavelengths used for the crossed dipole trap the atomic polarizabilities differ by a factor of $\alpha'_g/\alpha'_e \approx 2.5$ for 532 nm and $\alpha'_g/\alpha'_e \approx -1.8$ for 1070 nm (see Appendix A).

with respect to the one for g atoms. Accordingly the possible resonance frequencies are shifted to the blue (red). In the case $g_{ge} = g_{gg}$, the resonance condition would be independent of the position of the atoms and the line shape would not be affected by mean field interactions. The possible range of resonance frequencies is restricted between $\omega_{\text{res}}(0) = \omega_0 + (g_{ge} - g_{gg})\, n_g(0)/\hbar$ in the center of the cloud and $\omega_{\text{res}}(R_{\text{TF}}) = \omega_0$ at the edge of the BEC.

The form of the resulting spectrum is determined by the amount of atoms that contribute at a given resonance frequency. For a spherically symmetric trap, atoms with the same resonance frequencies are located in spherical shells around the trap center. The fact that the shell volume and therefore the number of contributing atoms increases with larger distances results in general in an asymmetric line shape. This however has to be combined with the decreasing parabolic density distribution towards the edge of the cloud. The expected line shape, taking both effects into account, has been calculated in [129] and has the form

$$S(\omega) \propto \frac{\hbar(\omega - \omega_0)}{n_g(0)(g_{ge} - g_{gg})} \sqrt{1 - \frac{\hbar(\omega - \omega_0)}{n_g(0)(g_{ge} - g_{gg})}}\,, \tag{4.17}$$

where ω is the angular frequency of the applied laser light.

The effect of the differential light shift on the spectrum can qualitatively be understood in a similar way. It also leads to a position dependent resonance frequency and an in general asymmetric line shape due to the mentioned shell effect. The possible range of resonance frequencies is thereby bounded between the maximum and minimum light shift that occur between the center and the edge of the cloud.

Interpretation of the observed spectrum

To understand the broadening of the spectrum in Figure 4.8, we estimate the effect of the differential light shift first. For the trap parameters used, the central differential light shift is expected to be about $V^e_{\text{ext}}(0) - V^g_{\text{ext}}(0) \approx h \times 150\,\text{kHz}$, resulting in an overall shift of the resonance frequency of the same amount. The trapping potential for e atoms in the center of the trap is in our configuration slightly repulsive ($V^e_{\text{ext}}(0) \approx +2\,\text{kHz}$). Using the estimated trapping frequencies of $(\omega_x, \omega_y, \omega_z)/2\pi \approx (240, 110, 264)\,\text{Hz}$ for the atoms in the ground state[23], we can calculate the Thomas-Fermi radii to be $(R_x, R_y, R_z) = (2.5, 5.5, 2.3)\,\mu\text{m}$. With these cloud radii we can estimate the full range of possible resonance frequencies due to the differential light shift to be about 5 kHz, dominated by the light shift variation along y direction. The sign of the shift is thereby such that the resonance

---

[23] Here x corresponds to the propagation direction of the 1070 nm trapping beam, y to the propagation direction of the 532 nm trapping beam and z to the vertical direction.

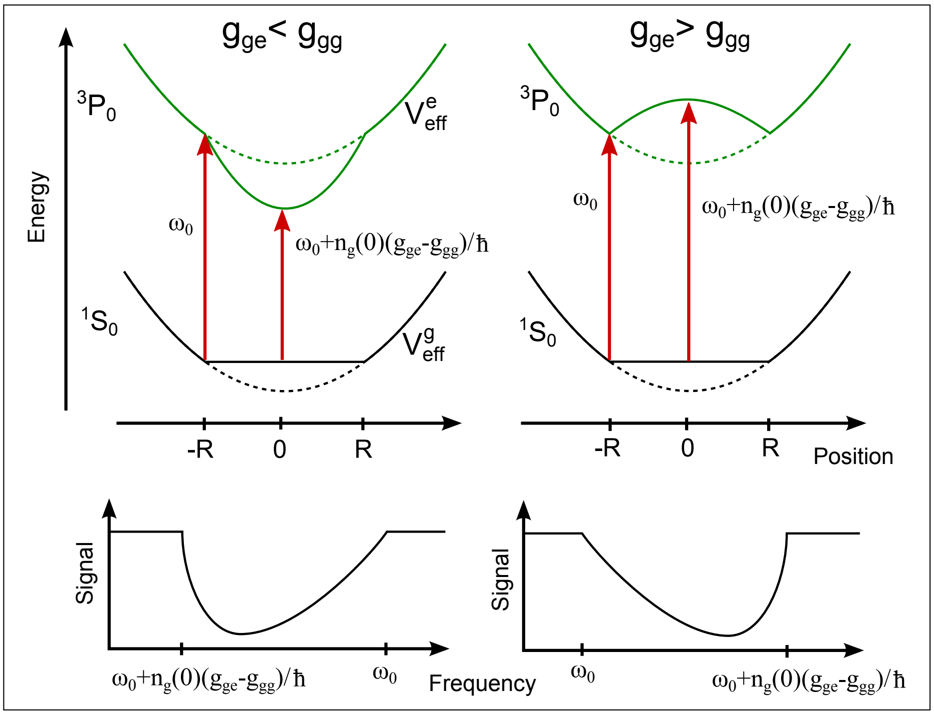

Figure 4.9: Illustration of the mean field interactions on the spectrum for the case of $g_{ge} < g_{gg}$ (left) and $g_{ge} > g_{gg}$ (right). In the upper part the spatially dependent potential energies are sketched. Shown are the external potentials $V^g_{\text{ext}}(\boldsymbol{r}) = V^e_{\text{ext}}(\boldsymbol{r})$ (dashed) and the effective potentials $V^{g/e}_{\text{eff}} = V^{g/e}_{\text{ext}}(\boldsymbol{r}) + g_{gg/ge}n_g(\boldsymbol{r})$ (solid), taking the local mean field interactions with the BEC of g atoms into account. The resonance frequencies in the center and the edge of the cloud are indicated by the red arrows. The corresponding spectroscopic line shapes are sketched in the lower part.

frequency from the center of the cloud towards the edge decreases. This is in accordance with the observed asymmetry in the spectrum, but the magnitude is not large enough to explain the full range of observed resonance frequencies of more than 10 kHz. Accordingly mean field interactions might also have an important contribution on the observed spectral line shape.

Since a_{ge} is not known yet for ^{174}Yb, we cannot directly estimate the influence of the mean field effects on the spectrum. However using the model equation (4.17) we might be able to get a first estimate for a_{ge} from the spectrum in Figure 4.8. When we assume that the influence of the differential light shift does not change the form of the line shape as given in equation (4.17), but only enlarges the range of possible resonance frequencies by about $\Delta_{\text{diff}} \approx h \times 5\,\text{kHz}$, we might model the expected line shape by a curve of the form

$$S(\omega) \propto \frac{\hbar(\omega-\omega_0)}{[n_g(0)(g_{ge}-g_{gg})+\Delta_{\text{diff}}]}\sqrt{1-\frac{\hbar(\omega-\omega_0)}{[n_g(0)(g_{ge}-g_{gg})+\Delta_{\text{diff}}]}}\,, \tag{4.18}$$

This model function has been fitted to the data in Figure 4.8, where the peak mean field shift $n_g(0)(g_{ge}-g_{gg})$ is determined to be on the order of 7 kHz. For the estimated central density of about $n_g(0) \approx 8 \times 10^{14}/\text{cm}^3$ and the scattering length $a_{gg} = 5.55\,\text{nm}$ [57], we then obtain $a_{ge} \approx 18\,\text{nm} \approx 3\,a_{gg}$.

This is a very rough first estimate of the scattering length between g and e atoms that is obtained under very strict assumptions. In particular we have assumed no other broadening mechanism to be present and that the population in e stays small. However, given the Rabi frequency of $\Omega_{\text{Rabi}}/2\pi \approx 350\,\text{Hz}$ and the interaction time of $\tau_{\text{pulse}} = 10\,\text{ms}$, this might not be a good approximation. Furthermore inelastic collisions between g and e have so far been neglected in the description. Those deplete the sample during the interaction time, also leading to a broadening of the resonance. However this broadening mechanism alone could not explain the asymmetry in the spectrum since it does not result in a position dependent resonance frequency. Since the inelastic scattering properties are not known for ^{174}Yb, we can only speculate about the magnitude of this effect. When assuming the loss coefficient to be similar to the one in ^{171}Yb of $\beta_{ge} = 3 \times 10^{-11}\,\text{cm}^3/\text{s}$ (see Table 4.1), the resulting instantaneous loss rate $\beta_{ge}\bar{n}_g$ for our mean density [130] $\bar{n}_g = 2n_g(0)/7 \approx 2 \times 10^{14}/\text{cm}^3$ would be on the order of 6 kHz. The resulting line broadening on the same order could then also well explain the observed width of the spectrum. The asymmetric line shape could then be a result of a combination with the differential light shift, rather than a consequence of the mean field shift.

In summary we can estimate from these preliminary measurements that the broadening effects other than the differential light shift are determined to be on the order of 7 kHz. This could be explained by mean field interactions as well as by losses due to inelastic collisions. A more precise estimation of these effects would require more careful measurements with better controlled experimental conditions, in particular in a trap without differential light shifts. The results of the discussion suggest that we are not limited at the kHz level by other technical effects or the laser linewidth.

4.5.2 Time-of-flight spectroscopy

In the second type of spectroscopy measurements the BEC is released from the crossed dipole trap and the interaction with the probe light takes place during free fall. With this time-of-flight method the limitation due to the differential light shift is eliminated. Furthermore density related effects like mean field interactions and inelastic scattering can be reduced due to the expansion of the atomic cloud during free fall. One drawback of this method is that the atomic cloud moves out of the probe beam during time-of-flight, limiting the possible interaction duration. In our case the probe beam has a waist of about 25 μm, where this limit is about 2.5 ms. Accordingly the Fourier limitation for the observable resonance width is expected to be on the order of 500 Hz.

The typical sequence for the time-of-flight measurements is to switch off the crossed dipole trap and to illuminate the atoms with a square pulse of the probe light of 3 ms duration. To ensure that no residual trapping light is present during the pulse, a waiting time of 200 μs is added after the dipole trap is switched off. Similar as for the measurements in the crossed dipole trap, the laser frequency has been subject to drifts during the resonance scans. Since these drifts were found to be mostly linear (see Figure 4.10) we could remove the additional change in laser frequency during the measurements in post-processing. The resulting drift corrected and averaged spectrum over a series of about 40 measurements is shown in Figure 4.10. As already mentioned, the origin of these drifts is further investigated in section 4.6. The characteristic width of the spectrum is about 3 kHz and therefore about a factor of 3 smaller than in the in-situ measurements. The possible limitations for this observed width are discussed in the following.

Interaction versus kinetic energy during time-of-flight

The main process to understand for the time-of-flight spectroscopy measurements is the transformation of the mean field energy to kinetic energy during the free fall due to the repulsive interactions. This effect is modeled in the following, where we assume as previously that the cloud is initially trapped in a harmonic confinement with angular trapping frequencies $\omega_j(t=0)$, with $j = x, y, z$. It has been shown in [131] that in a harmonic trapping potential with time-dependent angular trapping frequencies $\omega_j(t)$, the initial Thomas-Fermi wave function $\Phi(\boldsymbol{r}, t=0)$ evolves according to a scaling solution that reads

$$\Phi(\boldsymbol{r}, t) = \frac{1}{\sqrt{b_x(t)b_y(t)b_z(t)}}\,\Phi(\{r_j/b_j(t)\}_{j=x,y,z}, 0)\,e^{i[\beta(t)+\theta(\boldsymbol{r},t)]}\,, \tag{4.19}$$

with the phase of the wave function given by $\theta(\boldsymbol{r}, t) = m\sum_j r_j^2\dot{b}_j(t)/2\hbar b_j(t)$ and $\hbar\dot{\beta} = \mu/\lambda_x(t)\lambda_y(t)\lambda_z(t)$. The b_j (with $j = (x, y, z)$) are the scaling factors that are determined by the coupled differential equations

$$\ddot{b}_j = \frac{\omega_j(0)^2}{b_j b_x b_y b_z} - \omega_j^2(t>0)\,b_j\,, \tag{4.20}$$

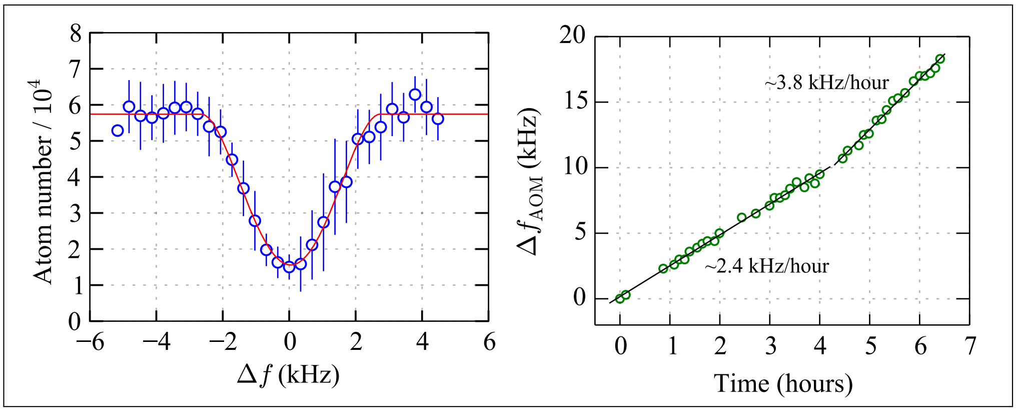

Figure 4.10: Spectroscopy during time-of-flight. Left: The atom number in state g is shown as a function of the probe laser frequency. The shown data is binned and represents the average over about 40 single resonance scans. The frequency scale of each individual spectrum has been corrected for the observed drifts during the measurements. The red curve corresponds to a fit using equation (4.24). Right: Drift of the laser frequency during the measurements. The solid lines represent linear fits to the data in the two drift regimes.

where $\omega_j(t > 0)$ are the time-dependent angular trapping frequencies. The case of a free expansion during time-of-flight is realized by $\omega_j(t > 0) = 0$.

In this scaling solution the density distribution $N|\Phi(\boldsymbol{r}, t)|^2$ keeps its initial form of a Thomas-Fermi profile (inverted parabola) during free fall and the coordinates are rescaled by the scaling factors b_j. The Thomas-Fermi radii for example then evolve like $R_j(t) = R_j(0)b_j(t)$. The fact that the density is scaled by $1/b_x(t)b_y(t)b_z(t)$ during free fall leads to a reduction of the interaction energy with the same factor. This energy is transformed into kinetic energy which is described by the fact that a velocity field develops given by

$$\boldsymbol{v}(\boldsymbol{r}) = \frac{\hbar\nabla\theta(\boldsymbol{r}, t)}{m} = \sum_j \frac{\dot{b}_j(t)}{b_j(t)} r_j \boldsymbol{e}_j \, . \tag{4.21}$$

The local velocity varies linearly over the size of the cloud and the peak velocity at the edges is given by $v[R_j(t)] = \pm\dot{b}_j R_j(0)$. Accordingly the Doppler shift at the cloud edges with respect to the center is given by $\Delta\omega_j = \pm\dot{b}_j R_j(0)\boldsymbol{k}\cdot\boldsymbol{e}_j$, for probe light with wave vector $\boldsymbol{k}$.

The differential equations (4.20) determining the scaling factors can in general not be analytically solved. The numerically calculated solutions for the scaling factors b_j for our trap parameters are shown in Figure 4.11. The ballistic expansion

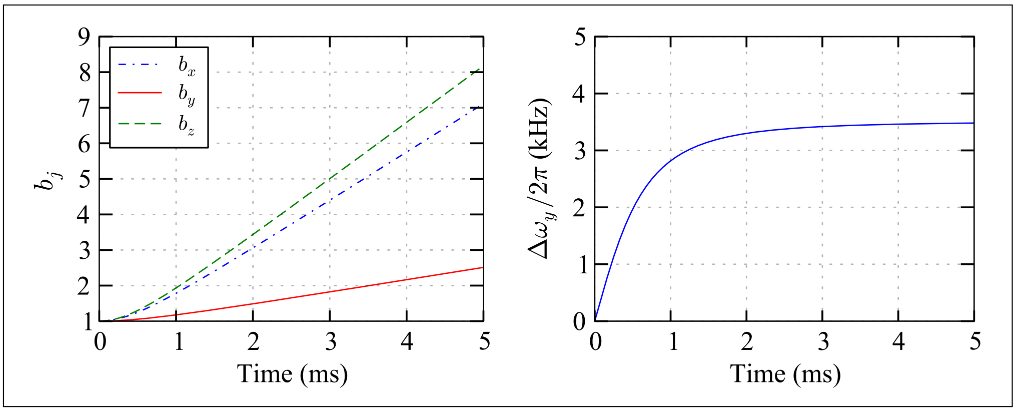

Figure 4.11: Left: Evolution of the scaling factors b_j during time-of-flight. The initial trapping frequencies used for the numerical calculations are $(\omega_x, \omega_y, \omega_z)/2\pi = (240, 110, 264)$ Hz. Right: Evolution of the Doppler shift at the edge of the cloud along the probe light propagation direction y.

regime, characterized by a linear dependence of the scaling factors, is reached after about 2 ms. In this regime the kinetic energy dominates. For shorter times the energy in the system is split between interaction and kinetic energy.

Interpretation of the spectrum and line shape

In our performed time-of-flight measurements, the effective interaction time of the atoms with the probe light is about 2.5 ms after the release from the trap. We have therefore the situation that in the beginning of the probe pulse the interaction energy still dominates, whereas towards the end of the pulse the kinetic energy and therefore the Doppler shift yields the more important energy scale. A quantitative description of the expected line shape of the spectroscopy signal is therefore not simple.

To get an estimation of the expected width of the resonance we might look at the "mean" configuration in the middle of the interaction time, after about 1.5 ms. To estimate the broadening due to interactions and inelastic collisions we can use the observations from the in-situ measurements that the full range of resonance frequencies due to these effects spans about 7 kHz. Since mean field interactions as well as the inelastic collision rate scale with the cloud density we can estimate the remaining broadening to be reduced by the scaling factor $1/b_x b_y b_z \approx 1/10$, leading to a full span of less than 1 kHz after 1.5 ms. We can therefore to a good approximation neglect effects of interactions and calculate the expected line shape due to the kinetic energy and the related Doppler effect.

For this we need to calculate the number of atoms being resonant with the probe light at a given angular frequency ω_{L}. When taking the Doppler effect into account, the resonance frequency for the atoms in the expanding cloud depends on the position and is given by

$$\omega_{\mathrm{res}}(\boldsymbol{r}) = \omega_0 + \boldsymbol{k} \cdot \boldsymbol{v}(\boldsymbol{r}) = \omega_0 + k\dot{b}_y \frac{y}{b_y} \,, \tag{4.22}$$

where $\omega_0 = \omega_{ge} + \omega_{\mathrm{R}}$ is resonance frequency without Doppler effect, consisting of the sum of the bare atomic resonance frequency ω_{ge} and the recoil frequency $\omega_{\mathrm{R}} = \hbar k^2/2m$. The wave vector of the probe beam $\boldsymbol{k} = k\,\boldsymbol{e}_y$ is assumed to be propagating along the y direction. The number of atoms being resonant with a given laser frequency at time $t \geq 0$ can then be calculated via

$$N_{\mathrm{res}}(\omega_{\mathrm{L}}, t) = N \int \delta[\omega_{\mathrm{L}} - \omega_{\mathrm{res}}(\boldsymbol{r})]\, |\Phi(\boldsymbol{r}, t)|^2 \, \mathrm{d}^3\boldsymbol{r} \,, \tag{4.23}$$

where $\delta(x)$ is the Dirac delta function. This can be evaluated to be proportional to

$$N_{\mathrm{res}}(\omega_{\mathrm{L}}) \propto \begin{cases} \left(1 - \frac{(\omega_{\mathrm{L}}-\omega_0)^2}{\Delta\omega_y^2}\right)^2 & \text{for } |\omega_{\mathrm{L}} - \omega_0| \leq \Delta\omega_y \\ 0 & \text{for } |\omega_{\mathrm{L}} - \omega_0| > \Delta\omega_y \end{cases} \,, \tag{4.24}$$

with $\Delta\omega_y = k\dot{b}_y R_y$ being the instantaneous Doppler shift at the edge of the cloud.

The experimental data in Figure 4.10 has been fitted[24] with this model function for the line shape, where we could derive $\Delta\omega_y^{\mathrm{fit}}/2\pi = 2.7(1)\,\mathrm{kHz}$. This is in reasonable agreement with the expected Doppler broadening after the "mean" duration of 1.5 ms, calculated to be $\Delta\omega_y^{\mathrm{calc}}/2\pi \approx 3.1\,\mathrm{kHz}$. This suggests that we can to some extent understand the observed line shape as a result of the Doppler broadening along the axis of the probe light. The fact that the observed spectrum is symmetric supports that we are not limited by interaction effects.

An additional effect that might play a role for the observed spectrum is the differential light shift induced by the coupling laser itself. This has been measured in [78] to be on the order[25] of $\kappa \approx 15\,\mathrm{mHz}/(\mathrm{mW}/\mathrm{cm}^2)$. We typically used beam powers on the order of 0.5 mW, where the central differential light shift is expected to be about 0.5 kHz. The fact that the cloud moves out of the probe beam during time-of-flight leads to a time dependent variation of this differential light shift.

---

[24] Open fit parameters are a global amplitude and offset as well as ω_0 and $\Delta\omega$.

[25] The measured value presented in [78] should be taken as an order of magnitude. Effects of an inhomogeneous intensity of the clock laser beam over the cloud were not well calibrated, as mentioned in [78]. However, this value is on the same order as the one expected according to the polarizability calculations in Appendix A, of $\kappa_{\mathrm{calc}} \approx 13\,\mathrm{mHz}/(\mathrm{mW}/\mathrm{cm}^2)$. For the following estimations we use the "measured" value of $\kappa \approx 15\,\mathrm{mHz}/(\mathrm{mW}/\mathrm{cm}^2)$.

The same holds true for the Rabi frequency which becomes also effectively time dependent during time-of-flight. These effects are complicated to model but the associated broadening of several hundreds of Hz can in our case be neglected.

In summary the time-of-flight technique allowed us to achieve a smaller resonance width as compared to the in-situ case. It has been argued that the observed linewidth matches the estimated limitation by the Doppler effect within about 15 %. This suggests that we have not yet reached the level where technical limitations of our laser system become important.

4.6 Frequency drifts and the temperature zero-crossing point

It has been seen during the so far performed spectroscopy measurements, that drifts of the laser frequency on the order of several kHz/hour were present. These frequency variations are caused by drifts of the ULE cavity resonances on which the laser system is locked to. Under the influence of drifts on this order of magnitude it will become difficult to observe resonance widths in the range of hundreds of Hz and below. The main problem is thereby that the repetition rate of our experiment is about 3 shots/minute and the laser frequency will drift faster than we are able to sample the atomic resonance. Additionally, frequency drifts on this level will be disturbing when we need to keep the laser frequency constantly at resonance, as planned in the experiments concerning artificial gauge fields (see chapter 5) or when trying to see Rabi oscillations. Accordingly we focused as a next step on understanding the origin of the frequency drifts. The obtained results are presented in this section.

4.6.1 Characterization of the typical drift behaviour

To further characterize the cavity drifts, the atomic resonance frequency has been tracked in time-of-flight measurements during several days. The resulting appearance of the atomic resonance as a function of time is shown in Figure 4.12. It can be seen that from one day to another the initial resonance frequency changes only by a few kHz. However during the day the resonance frequency is subject to a much stronger, mostly linear drift, opposite to the one observed from one day to another. We could identify the drift of the cavity resonances during the day to be of thermal nature and suspected that the temperature working point of the cavity might not exactly be at the temperature-zero crossing point. The initial working temperature at $T = 5.0\,^{\circ}\mathrm{C}$ of the cavity had been chosen according to a previous determination of the temperature zero-crossing point with an accuracy of about

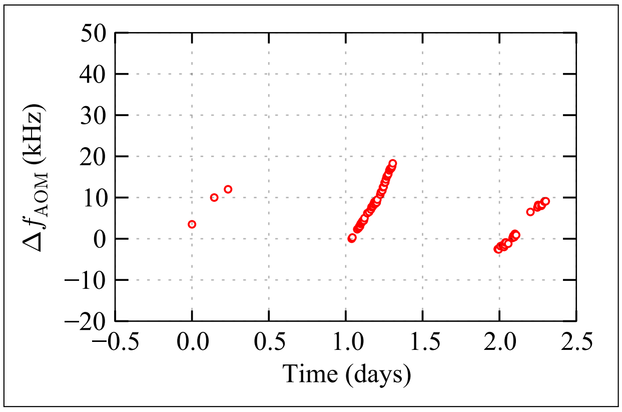

Figure 4.12: Characterization of the frequency drifts over a period of three days. Shown is the AOM frequency at which the atomic resonance is observed in time-of-flight spectroscopy measurements as a function of time. The zero of the AOM frequency scale is chosen arbitrarily.

±1 °C. A new, more precise determination of the zero-crossing temperature has subsequently been performed.

4.6.2 Determination of the temperature zero-crossing point

To experimentally determine the temperature zero-crossing point, one can monitor the frequency change of the cavity resonances as a function of the cavity temperature. The required absolute frequency reference to compare the cavity resonances to, was in our case realized by a hyperfine resonance in iodine molecules. This molecular transition is observed in a saturated absorption spectroscopy setup (see section 4.4.1) simultaneously with the considered cavity resonance. This allows to monitor the absolute cavity resonance frequencies with an accuracy of about 50 kHz, limited by the precision at which we can determine the iodine resonance. The cavity temperature is tuned via the set point of the temperature regulation for the thermal shield. In Figure 4.13 the measured resonance frequency of one cavity peak is shown for different cavity temperatures.

The temperature zero-crossing point is located where the maximum of the cavity frequency is reached and determined to be at $T_0 = 4.31\,(4)\,^\circ\mathrm{C}$. At this point the cavity length is minimally sensitive to temperature fluctuations. The curvature of the quadratic variation around this point has been fitted to be $383\,\mathrm{kHz/K^2}$. It is to note that due to the low thermal coupling of the ULE cavity to its environment, the time to reach a new thermal equilibrium of the cavity after a change in thermal

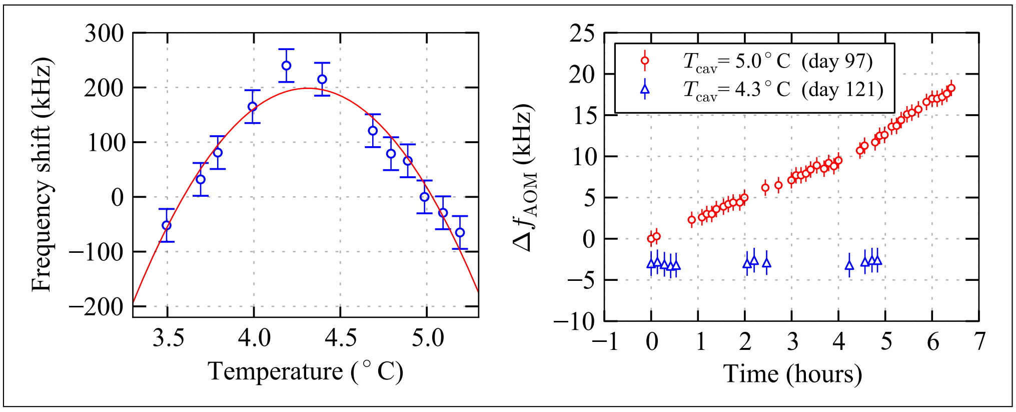

Figure 4.13: Left: Measurement of the temperature zero-crossing point. The frequency change of a cavity resonance is monitored with respect to an iodine transition that is observed in parallel using a saturated absorption spectroscopy. The zero-crossing point is determined to be at $T_0 = 4.31\,(4)\,°\mathrm{C}$ using a parabolic fit. Right: Comparison of the drift behaviour during the day between the old working temperature $T = 5.0\,°\mathrm{C}$ and the new working temperature $T = 4.3\,°\mathrm{C}$ of the cavity. The day reference given with respect to data in Figure 4.14.

shield temperature is quite long. For a sudden change in temperature from 3.5 °C to 4.3 °C, for example, the thermalization time until the signal is stable within 50 kHz is on the order of 8 hours. Accordingly the measurement of the temperature zero-crossing point is a rather lengthy procedure.

After setting the new working temperature of the ULE cavity to $T = 4.3\,°\mathrm{C}$ we could observe a drastically reduced amplitude of frequency drifts during the day. An example measurement is shown on the right-hand side in Figure 4.13, where we compare the typical drifts between the new and the old working temperature. At $T = 5.0\,°\mathrm{C}$, drifts on the order of 3 kHz/hour were observed. At the new working point no significant drift within the measurement precision of the resonance frequency could be observed for a duration of about 5 hours. Within the errorbars we can therefore restrict the residual drifts to be less than 0.6 kHz/hour ≈ 200 mHz/s.

The local thermal sensitivity at the old working temperature of $T = 5\,°\mathrm{C}$ is according to the parabolic fit found to be about $\Delta\nu/\Delta T \approx 270\,\mathrm{kHz/K}$. The observed frequency drifts on the order of 20 kHz during the day, therefore correspond to temperature variations of the cavity of about 0.07 °C. We attribute this change in cavity temperature to an increase of the ambient temperature in the laboratory during the day, which is in accordance with the observed drift direction. It is to note that for all measurements shown so far, the vacuum chamber hosting the ULE cavity was only protected by a temporary cardboard box, providing a lim-

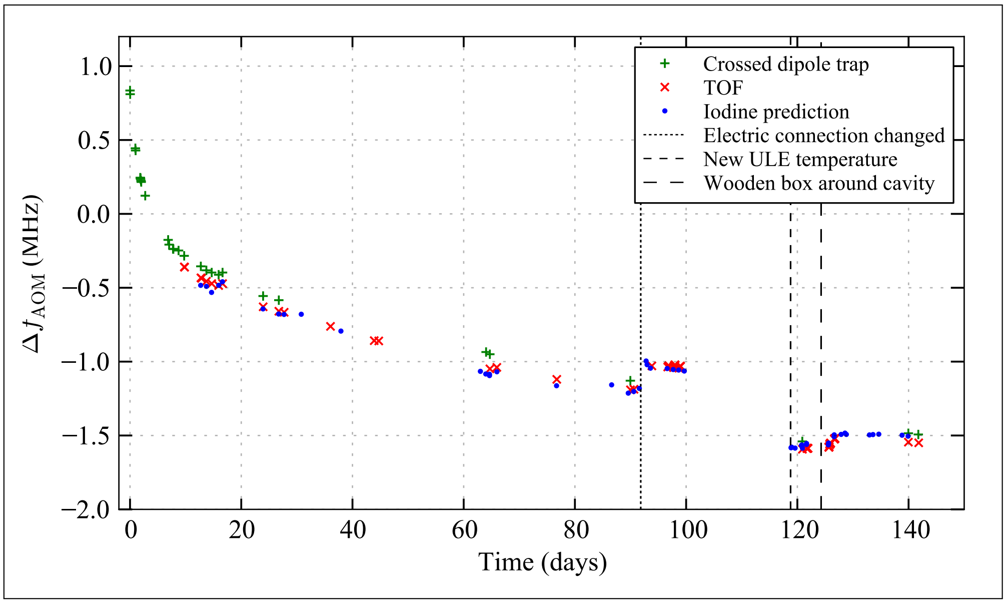

Figure 4.14: Long term monitoring of cavity frequency drifts. Shown is the AOM frequency at which the resonances in the crossed dipole and time-of-flight (TOF) measurements are observed. The frequency offset is arbitrarily set. Special events are marked by the vertical lines and further explained in the text.

ited thermal isolation from changes of the ambient laboratory temperature. This box has been replaced at a later point by a fully closed wooden box with acoustic isolation foam, where a much better thermal isolation is achieved.

4.6.3 Long term monitoring of cavity drifts

Apart from characterizing the drifts during the day we have been able to also monitor the frequency variations of the ULE cavity on the long term during a period of about 140 days. The ensemble of spectroscopic measurements on ytterbium (time-of-flight and in-situ) and the prediction using the iodine spectroscopy method (see section 4.4.1) in this time period are shown in Figure 4.14.

The time $t = 0$ corresponds roughly to the point where the temperature stabilization of the cavity base plate was switched on. In the following first two weeks a strong drift of the cavity resonances on the order of several tens of kHz/hour is observed, which can be explained by the very slow thermalization of the cavity to the new equilibrium temperature around 5 °C. In the following 60 days the cavity drifts slow down and are on the order of about 10 kHz/day. The small "jump" in resonance frequency at about day 90 correlates with a change of an

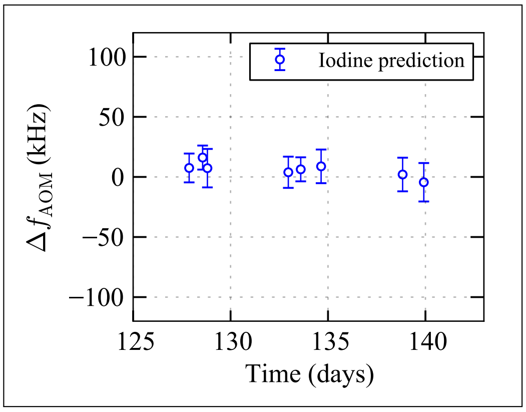

Figure 4.15: Long term monitoring of cavity drifts using the iodine spectroscopy

electronic connection of the temperature regulation that slightly shifted the temperature working point. After that the typical drifts from one day to another value to about 3 kHz/day, whereas the drifts during the day, as already discussed, were observed to be much larger than that.

At about day 119, the new temperature working point at the more precisely determined temperature zero-crossing point has been set. Shortly after, the wooden box around the vacuum system has been added, which slightly changed the temperature equilibrium of the system and therefore the resonance frequency. Afterwards the day to day drifts are monitored during a period of about 14 days using the iodine spectroscopy (for a zoom see Figure 4.15). In this period no significant long term drift has been observed within the errorbars of the iodine spectroscopy reference. When excluding systematic drifts of the iodine resonance during this period, we can restrict residual drifts within the errorbars to below about $\lesssim 40\,\mathrm{kHz}/14\,\mathrm{days} \approx 3\,\mathrm{kHz/day}$. This would correspond to a long term stability of better than 35 mHz/s. However, this has to be further characterized in future experiments[26] using the more precise spectroscopic measurements on a BEC.

As a last point we would like to point out that the prediction of the resonance frequency for the time-of-flight measurements using the iodine method (see section 4.4.1) is reliable within a range of about ±50 kHz throughout the full time period shown in Figure 4.14.

---

[26] Unfortunately the experiment had to be partially disassembled at this point since it had to move from École Normale Supérieure to Collège de France.

4.7 Single shot calibration of the laser frequency

It has been seen in the previous section that we managed to reduce drifts of the ULE cavity during the day to a level on the order of 100 mHz/s or below. However, even at this level of drifts it might become necessary to perform an active drift correction when one is interested in keeping the laser constantly in resonance with the atomic transition within 100 Hz or less. The main problem is thereby that in principle one would like to perform the intended experiments while simultaneously verifying the laser frequency with respect to the resonance. Accordingly spectroscopic calibration measurements of the laser frequency need to be performed between the actual measurements one is interested in. Measuring a full spectrum, however, takes many experimental cycles and is therefore impractical. The laser frequency calibration should be done with the least amount of shots possible.

One method to estimate the laser frequency with respect to the atomic resonance is to measure two consecutive points on the expected left and right wing of the spectroscopy signal. The difference signal between the two shots can then be used to evaluate the current resonance frequency. This method requires in principle at least two shots and the resonance frequency to be stable within the resonance width between two calibration measurements. Here we present a different method that allows one to determine the laser frequency with a single shot over a range much larger than the atomic resonance width, based on a spatially resolved Doppler sensitive spectroscopy in time-of-flight.

The basic idea is to perform a quasi one-dimensional hydrodynamic expansion of a BEC. The cloud thereby develops a velocity profile along the expansion axis with a linear velocity-position mapping, according to equation (4.21). For an excitation with the probe light propagating along the expansion axis, the atoms are sensitive to the Doppler shift. Resonant atoms are located in a well defined slice of the cloud, that can be observed as a dip in the density profile when performing absorption imaging of the atoms in g. Due to position-velocity mapping, the position of the slice changes as a function of the probe laser frequency. This effect can be seen in Figure 4.16, where a series of absorption images of the axial density profile is shown as a function of the applied probe laser frequency.

Changes in the relative laser frequency can in such a configuration be observed as a change of the dip position. In the case one is able to calibrate the absolute position-frequency mapping, it becomes even possible to determine the absolute laser frequency in a single shot. In the following we present the experimental sequence used to obtain these images and further analyze this method and the physical processes behind it.

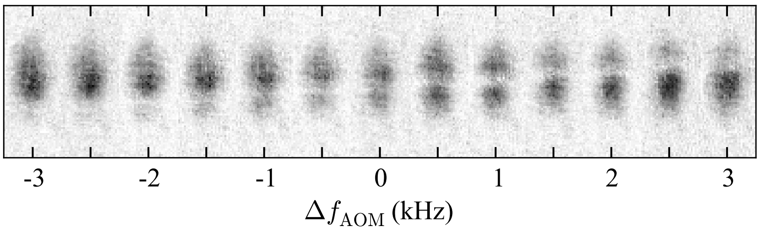

Figure 4.16: Spatially resolved velocity selective excitation of the clock transition. Shown is the density distribution after the interaction with the probe light for different laser frequencies. The absorption imaging is performed along an axis perpendicular to the probe light propagation direction.

4.7.1 Experimental sequence

The one-dimensional hydrodynamic expansion is realized by performing a "1D guided" time-of-flight in one of the horizontal dipole trap arms. For this, we first produce a pure BEC of about 5×10^4 atoms ($> 80\,\%$ condensed fraction) in the crossed dipole trap and subsequently switch off the trapping beam at 1070 nm propagating along the x axis. The BEC then expands along the axis of the remaining dipole trap beam (y axis). During this expansion the interaction energy of the BEC transforms into kinetic energy, mainly along the y axis. The duration of the expansion is chosen to be $\tau_{\mathrm{exp}} = 10\,\mathrm{ms}$, which is short compared to the axial oscillation period in the remaining dipole trap beam of about 400 ms, but sufficiently long such that the interaction energy is reasonably lowered and a sufficient velocity spread has developed.

The next step consist in probing the atomic cloud with the clock laser along the y axis, where the atoms are Doppler sensitive. In practice we have performed the excitation pulse of the probe light 200 μs after switching the remaining dipole trap beam off. This is required to avoid an influence of the differential light shift of the 532 nm light. The probe light pulse has a duration of 3 ms and is followed by an additional time-of-flight of 19 ms and subsequent imaging of the cloud along the vertical z direction. The total time starting from the guided expansion to the final imaging is 32 ms.

4.7.2 Theory modeling

From the theory point of view the dynamics of the BEC during this sequence can be described by the previously introduced scaling solution for the Thomas-Fermi

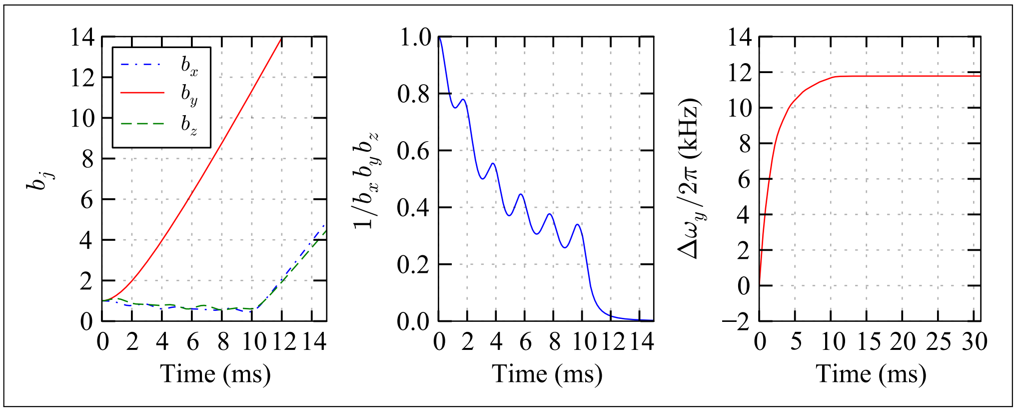

Figure 4.17: Left: Evolution of the scaling factors b_j during the guided time-of-flight. Middle: Evolution of the inverse product of the scaling factors, corresponding to the time-dependent reduction factor for the cloud density. Right: Evolution of the Doppler shift at the edge of the cloud along y direction $\Delta\omega_y/2\pi = k\dot{b}_y R_y/2\pi$.

profile. The developing velocity field across the cloud is, as already presented in section 4.5.2, of the form

$$\boldsymbol{v}(\boldsymbol{r}) = \sum_j \frac{\dot{b}_j(t)}{b_j(t)} r_j \boldsymbol{e}_j \,, \tag{4.25}$$

with the previously introduced scaling factors b_j with $j = (x, y, z)$. The local mean velocity is therefore expected to vary linearly over the size of the cloud.

The numerically calculated solutions of the differential equations (4.20) for the scaling factors b_j are shown in Figure 4.17, where the following evolution of the trap frequencies during the sequence is used

$$(\omega_x, \omega_y, \omega_z)/2\pi = \begin{cases} (256, 128, 286)\,\text{Hz} & \text{for } t = 0 \\ (256, 2.3, 256)\,\text{Hz} & \text{for } 0 < t \leq 10\,\text{ms} \\ (0, 0, 0)\,\text{Hz} & \text{for } 10\,\text{ms} < t \end{cases} . \tag{4.26}$$

During the guided expansion in the first 10 ms it can be seen that the cloud mostly expands along the y direction and that the scaling factors along x and z stay on the order of unity. The cloud is therefore expected to stay well confined in the transverse directions. The interaction energy after 10 ms guided time-of-flight is reduced by about a factor of $b_x b_y b_z \approx 3$. The fact that the cloud mainly expands along the y axis leads to a quite large range of velocities with a total expected Doppler spread of about 23 kHz from $-R_y$ to R_y. The evolution during the free expansion for $t > 10$ ms is found to be completely ballistic along the y

axis, indicated by the constant Doppler width $\Delta\omega_y$. The additional time-of-flight therefore does not affect the axial velocity distribution that is present after the hydrodynamic expansion.

4.7.3 Analysis of experimental data

Dip position versus laser frequency

We have fitted the measured density profiles from Figure 4.16 with a Thomas-Fermi profile multiplied with a heuristic "hole" function to extract the positions of the cloud center as well as the dip. Example curves of the double integrated density and the according fits are shown on the left-hand side of Figure 4.18. The dependence of the dip position on the probe light frequency is shown on the right-hand side of Figure 4.18. It is found to be linear with a slope of about $\xi^{\mathrm{meas}} = \mathrm{d}y/\mathrm{d}f \approx -20.6\,\mu\mathrm{m/kHz}$. From the scaling model we would expect the slope after 32 ms to be $\xi^{\mathrm{theo}} = -\lambda\, b_y(t)/\dot{b}_y(t)|_{t=32\,\mathrm{ms}} \approx -17.7\,\mu\mathrm{m/kHz}$, which agrees within 15 % with the measured value.

However, it has been found that the Doppler shift between the edges of the cloud spans only about 13 kHz instead of the expected range of 23 kHz. This is connected to the fact that the measured Thomas-Fermi radius along y is about a factor of 1.6 smaller than the expected from the scaling model. One explanation for this difference could be that our knowledge of the initial trapping conditions might not be very precise, leading to errors in the modelling of the cloud expansion. Possible uncertainties could be in the trapping frequencies used for the calculations that are scaled down from the measured ones at full trap beam powers. This would influence the initial cloud size as well as the behaviour during the one-dimensional expansion. Other possible effects could result from an imperfect experimental sequence, for example that the 1070 nm dipole trap beam is not fully switched off and some remaining light might slow down the expansion. However, these systematic errors concern only the quantitative understanding of the cloud expansion but do not influence the principle spectroscopic results of the method.

On the right-hand side of Figure 4.18 also the center of the cloud as a function of the applied probe light frequency is shown. It is found to stay nearly constant, as expected, although a small residual linear variation with the laser frequency is observed. A possible origin could be a systematic error in the fitting of the data caused by the fact that the size of the dip is not small compared to the extension of the cloud. This could lead to an artificial "line pulling" effect for the center of the Thomas-Fermi fit.

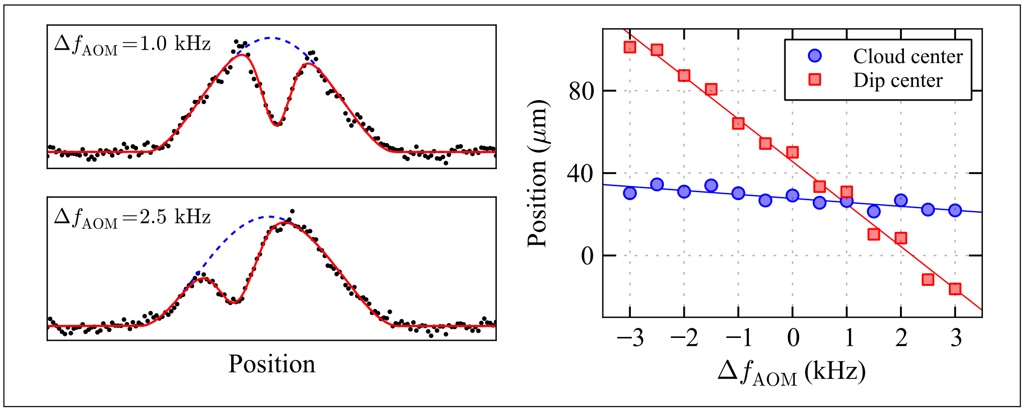

Figure 4.18: Left: Double integrated density (black dots) of two example absorption images from Figure 4.16. The blue curve corresponds to a fit using a double integrated Thomas-Fermi profile multiplied with a Gaussian shaped hole function. The contribution of the Thomas-Fermi profile is shown as the red dashed line. Right: Fitted position along the y axis of the cloud center (blue circles) and the hole center (red squares) as a function of the frequency of the probe laser.

Absolute calibration of the laser frequency

Due to the linearity between the dip position and the laser frequency this method is well adapted to monitor changes of the laser frequency with a single shot. In the ideal case one would expect that the dip should appear in the middle of the cloud when the laser is in resonance with an atom in free space. This fact could in principle be used to obtain even an absolute frequency calibration of the laser with a single shot. Important for this is that the center of mass motion of the cloud with respect to the probe laser direction is negligible. In our case we could observe that when the dip position is in the middle of the cloud, the laser frequency did not coincide with the expected resonance frequency from regular time-of-flight spectra.

By changing the duration of the hydrodynamic expansion we could in fact observe an accelerated motion of the cloud center, as shown in the data on the left-hand side of Figure 4.19. It is to note that the position variable reflects the velocity along y, due to the additional time-of-flight before absorption imaging. We presume this acceleration to be caused by a misalignment of the trap focus. Assuming this to be true, we can deduce the center of mass velocity after the hydrodynamic expansion $v(\tau_{\mathrm{exp}})$ from the data in Figure 4.19. For this, we consider the cloud to be accelerated in a displaced harmonic potential during τ_{exp} and make the approximation that the expansion duration is small compared to the axial trap

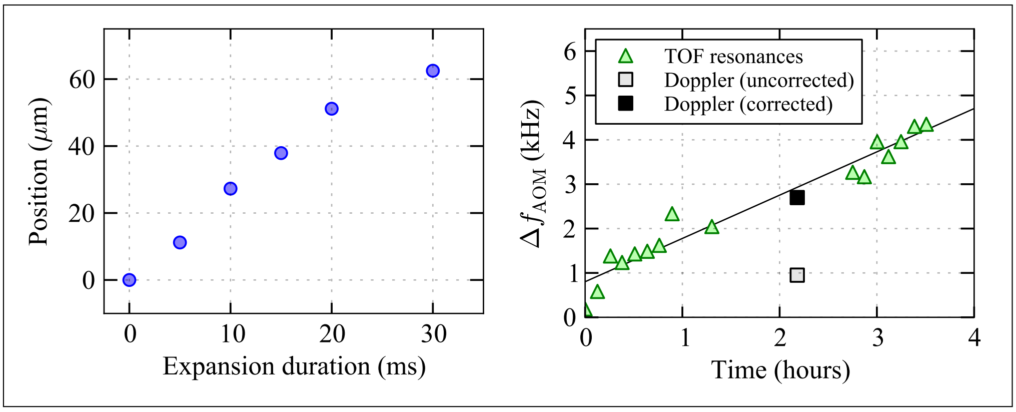

Figure 4.19: Left: Axial position of the fitted cloud center measured after time-of-flight as a function of the guided expansion duration. Right: The resonance frequencies measured with regular time-of-flight spectra (green triangles) are shown as a function of time, as well as the resonance frequency obtained using the Doppler method, with (black square) and without (gray square) correction of the center of mass Doppler shift.

period, expected to be on the order of 400 ms. Taking the subsequent ballistic motion in free fall during $t_{\mathrm{TOF}} = 22$ ms into account, the velocity after the guided expansion $v(\tau_{\mathrm{exp}})$ can be calculated as function of the cloud position Δy after both, expansion and free fall, via

$$v(\tau_{\mathrm{exp}}) = \frac{\Delta y}{t_{\mathrm{TOF}} + \tau_{\mathrm{exp}}/2} \, . \tag{4.27}$$

For the data point at $\tau_{\mathrm{exp}} = 10$ ms this results in $v(10\,\mathrm{ms}) \approx 1.0$ mm/s and therefore an additional Doppler shift due to the center of mass motion of $\Delta\omega_{\mathrm{com}}/2\pi \approx$ 1.7 kHz.

Knowing the additional Doppler shift due to the center of mass motion we can correct the frequency measurement of the hydrodynamic expansion method. The obtained result is shown on the right-hand side of Figure 4.19, where it is compared to the observed resonance frequencies in regular time-of-flight spectra that were measured in a time window of about ±2 hours around the hydrodynamic expansion measurements. By extrapolating the observed drift in the time-of-flight data with a linear slope we can see that the center of mass velocity corrected value indeed matches the extrapolated absolute frequency within half a kHz.

This shows the capability of this method to determine the absolute laser frequency within a single shot. The resulting accuracy in the presented example configuration is on the order of 0.5 kHz, but should in principle be adaptable to a large variety of frequency ranges using different trapping configurations.

4.8 Future improvements

In future experiments we plan to perform spectroscopy measurements in an optical lattice at a magic wavelength[27], where we are no longer limited by the differential light shift. In optical lattices it also possible to profit from the Lamb-Dicke effect, where the spectroscopic lines are not affected by the first-order Doppler effect. In this regime resonance widths in the sub-Hz regime can be observed, as realized in optical clocks [59]. In some preliminary measurements we could observe resonance widths in the sub-kHz regime, but were limited by technical issues leading to a jitter of the resonance frequency on the minute time scale with an amplitude of several hundreds of Hz.

Future technical improvements will be the addition of a second box around the vacuum chamber of the ULE cavity, that is specially designed to isolate from acoustic vibrations and to further improve the thermal isolation of the cavity. Moreover to avoid an influence of the Doppler phase noise caused in optical fibers transporting the light to the cavity we have already installed an active fiber noise cancellation. This effect typically leads to a time varying probe light frequency with an amplitude up to the order of hundreds of Hz, for typical fiber length of several meters.

---

[27] Such a wavelength is characterized by the fact that the atomic polarizabilities for g and e are equal.

Chapter 5

Towards artificial gauge fields in optical lattices

The results described so far showed the realization of a BEC of ^{174}Yb, the loading of an optical lattice and the spectroscopy on the ultranarrow $^1\mathrm{S}_0 \leftrightarrow {}^3\mathrm{P}_0$ clock transition. These are important steps towards the realization of artificial gauge fields in optical lattices. The understanding and experimental practice (especially in handling the clock laser) are crucial for the long term success of the experiment. In this chapter, the remaining steps towards the realization of artificial gauge fields will be presented. The experimental scheme follows the proposal of [39] whose work is based on the idea presented by Jaksch and Zoller in [38].

In the first section, the main ideas behind the experimental scheme are reviewed. This is followed by a detailed discussion of the required experimental conditions for an actual implementation using ytterbium. Afterwards we present several possible ways to implement the needed optical superlattice potential.

5.1 Proposal to simulate gauge fields in optical lattices

As discussed in section 2.2, the key to simulate orbital magnetism using cold atoms consists in the emulation of the Aharonov-Bohm phase. For atoms moving on a lattice, this falls back to the engineering of complex tunneling matrix elements. In the case of non-interacting particles on a 2D lattice in the tight-binding regime, subject to a perpendicular homogeneous magnetic field, the physics is described by the Harper Hamiltonian

$$\hat{H}_{\text{Harper}} = -J \sum_{m,n,\pm} \left[e^{\pm i 2\pi\alpha n} \hat{c}^{\dagger}_{m\pm1,n} \hat{c}_{m,n} + \hat{c}^{\dagger}_{m,n\pm1} \hat{c}_{m,n} \right] , \tag{5.1}$$

as motivated in section 2.2, where for the case of an electron $\alpha = \Phi/\Phi_0$ denotes the magnetic flux on an elementary cell in units of the flux quantum $\Phi_0 = h/e$. In this description the Landau gauge is chosen, where the complex tunneling elements appear only for hopping along the x axis. The experimental implementation of this Hamiltonian (or similar) using cold atoms as proposed in [39] will be presented in the following as well as its intended implementation using ytterbium.

The plan for the presentation is to first discuss the basic idea to implement the complex tunneling matrix elements $Je^{i2\pi\alpha n}$ in a two-dimensional state-dependent square lattice using laser-assisted tunneling. The most basic version of this will lead to a staggered effective magnetic flux that changes sign from one elementary cell to another. In a second part, the general principle to rectify the magnetic flux is presented as well as one possible implementation using an optical superlattice. Both discussions will be held on a qualitative level to allow the reader to familiarize with the basics concepts. An exhaustive discussion of the possible experimental implementation using ytterbium and required experimental conditions then follows in the sections afterwards.

5.1.1 The basic scheme - staggered flux

At the heart of the scheme proposed in [38] and [39] is the presence of two separate atomic ground or long-lived excited states, labelled g and e in the following, that can be coherently coupled by laser light. Important in the proposal [39] is furthermore the existence of a so-called "magic" wavelength λ_m at which the real parts of the atomic polarizabilities α' of the two states g and e are equal, $\alpha'_g(\lambda_\mathrm{m}) = \alpha'_e(\lambda_\mathrm{m})$, as well as an "anti-magic" wavelength λ_am where the polarizabilities are equal in magnitude but have opposite signs, $\alpha'_g(\lambda_\mathrm{am}) = -\alpha'_e(\lambda_\mathrm{am})$.

The lattice configuration

The atomic cloud is in the following considered to be strongly confined along the z direction by laser light at a magic wavelength, such that the resulting dynamics is in an effective 2D regime for both states g and e. For this, the atoms are assumed to be in the the ground state of an harmonic oscillator potential with wave function $\zeta(z)$. The remaining two-dimensional dynamics is governed by the presence of two optical lattices giving rise to a state dependent lattice configuration as sketched in Figure 5.1 (a). Along the y-axis an optical lattice at a magic wavelength λ_m is assumed with a period of $d_y = \lambda_\mathrm{m}/2$ and a lattice potential of the form

$$V_\mathrm{M}(y) = -V_\mathrm{m}\cos^2(k_\mathrm{m} y)\,, \tag{5.2}$$

where $k_\mathrm{m} = \pi/d_y$ denotes the lattice wave vector and $V_\mathrm{m} \geq 0$ the lattice depth. In this lattice the two states g and e see the same trapping potential and are trapped at the same positions along the y axis. In x-direction a lattice near an anti-magic wavelength λ_{am} is considered leading to periodic potentials that depend on the internal atomic state and will be written as

$$V_{\mathrm{am,g}}(x) = -V_{\mathrm{g}} \cos^2(k_x x)\,, \tag{5.3}$$

$$V_{\mathrm{am,e}}(x) = V_{\mathrm{e}} \cos^2(k_x x)\,, \tag{5.4}$$

with lattice wave vector $k_x = \pi/d_x = 2\pi/\lambda_{\mathrm{am}}$ and the potential depths $V_{\mathrm{g,e}} \geq 0$. The perfectly anti-magic case would be realized for $V_{\mathrm{g}} = V_{\mathrm{e}}$. In the chosen sign convention[1] of these lattice potentials, atoms in g are trapped at the intensity maxima of the standing wave light field, whereas atoms in e are trapped at the intensity minima. Accordingly atoms in the two states arrange in two distinct sublattices each of period $d_x = \lambda_{\mathrm{am}}/2$, that are spatially separated by $d_x/2$. The unit cell[2] of this lattice geometry is indicated as gray shaded in Figure 5.1 (a) and has a size of $d_x \times d_y$, containing one g and one e atom. The position of the atoms in the full 2D lattice will be labeled by integer indices (m, n) such that atoms in g and e are located at positions

$$\boldsymbol{r}^g_{\mathrm{m,n}} = n\boldsymbol{d}_y + m\boldsymbol{d}_x\,, \tag{5.5}$$

$$\boldsymbol{r}^e_{\mathrm{m,n}} = n\boldsymbol{d}_y + (m + 1/2)\boldsymbol{d}_x\,, \tag{5.6}$$

where $\boldsymbol{d}_x$ and $\boldsymbol{d}_y$ are the lattice vectors along x and y respectively. In the upcoming discussions we will also use the term "plaquette" that will denote the lattice cells of size $d_x/2 \times d_y$, containing half an atom of g and e and correspond to the unit cell cut in half along the x axis.

Furthermore all applied lattices are assumed to be in the tight-binding regime and the dynamics will be restricted to the fundamental Bloch band. In addition we assume for simplicity $V_{\mathrm{g/e}} \gg V_{\mathrm{m}}$, such that the regular tunneling amplitudes J_{gg} and J_{ee} along x (within each of the two sublattices) are small compared to the tunneling energy J_y along y. The Wannier functions in each state will be written as $\langle \boldsymbol{r} | w_0^g \rangle = w_0^g(x)\, w_0(y)\, \zeta(z)$ and $\langle \boldsymbol{r} | w_0^e \rangle = w_0^e(x)\, w_0(y)\, \zeta(z)$ respectively.

Laser-assisted tunneling and magnetic flux

The key ingredient in simulating a magnetic flux for the atoms on the lattice now lies in the emulation of the complex tunneling matrix elements. This can be realized by coherently coupling the two internal atomic states with resonant laser light of wave vector $\boldsymbol{k}$ and wavelength λ_{c}. This gives rise to so-called laser-assisted tunneling processes (for details see section 2.1.5) that are characterized

---

[1] The sign convention is chosen in anticipation of the potentials that we plan to use.

[2] The unit cell is the pattern that allows to construct the lattice geometry through periodic repetition.

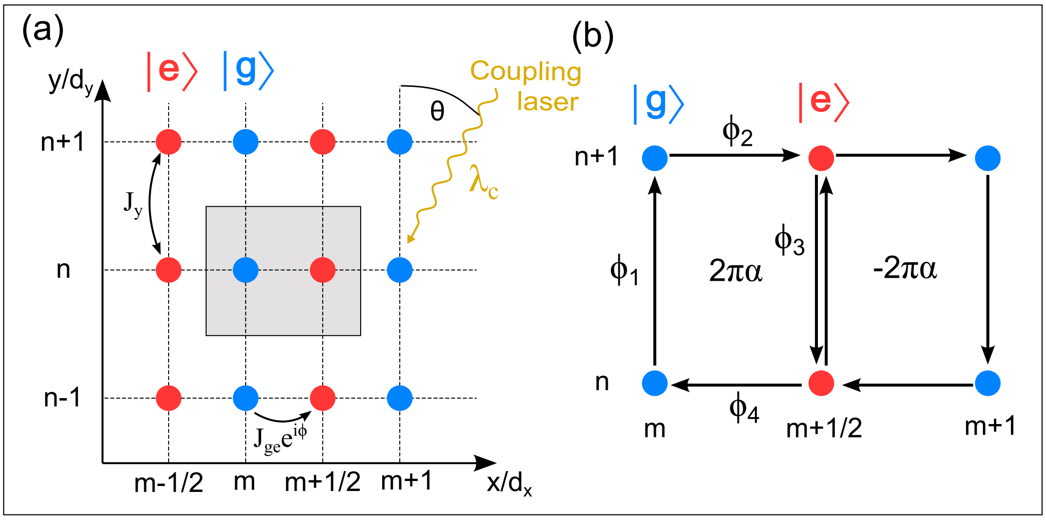

Figure 5.1: (a): Sketch of the two dimensional state-dependent optical lattice to realize artificial gauge fields. The unit cell is shown as gray shaded. (b): Illustration of the simulated staggered magnetic flux configuration on a unit cell of the lattice.

by a simultaneous change of internal atomic state and lattice site in the state dependent lattice. When considering only laser-assisted tunneling between nearest neighbours, it has been shown in section 2.1.5 that the tunneling amplitude for a transition between the sublattices from g to e is determined by[3]

$$J_{\text{eff}} = \frac{\hbar\Omega_{\text{Rabi}}}{2}\, e^{i\boldsymbol{k}\cdot(\boldsymbol{r}^{g}_{\text{m,n}} \pm \boldsymbol{d}_x/4)}\, \eta_x\, \eta_y\, \eta_z \,, \tag{5.7}$$

with Ω_{Rabi} the free space Rabi frequency and the integration factors $\eta_{x,y,z}$ given by equations (2.36) to (2.38). For simplicity in the following we will make the

---

[3] The fact that two different signs can appear is connected to the fact that for a given starting site $\boldsymbol{r}^{g}_{m,n}$ transitions to the left-hand and right-hand side neighbour can occur. In the chosen notation the upper sign corresponds to transitions of type $\boldsymbol{r}^{g}_{m,n} \rightarrow \boldsymbol{r}^{e}_{m,n}$ and the lower sign for transitions of type $\boldsymbol{r}^{g}_{m,n} \rightarrow \boldsymbol{r}^{e}_{m-1,n}$.

approximation[4] $\eta_y, \eta_z \approx 1$, as motivated in section 2.1.5. The remaining integration factor η_x reads

$$\eta_x = \int w_0^{e*}(x \mp d_x/4)\, e^{ik_x x}\, w_0^{g}(x \pm d_x/4)\, \mathrm{d}x\,, \tag{5.8}$$

where in the following the potential depths V_g and V_e are assumed to be equal, such that the Wannier functions for g and e become identical. In this case η_x is a real quantity and the tunneling energy J_{eff} can be decomposed in an amplitude and a phase like

$$J_{\text{eff}} = J_{\text{ge}} e^{i\phi}\,, \tag{5.9}$$

with $J_{\text{ge}} \approx \hbar\Omega_{\text{Rabi}}\eta_x/2$ and $\phi = \boldsymbol{k} \cdot (\boldsymbol{r}^g_{\text{m,n}} \pm \boldsymbol{d}_x/4)$. From this it can be seen that, compared to regular hopping on a lattice with real valued tunneling amplitudes, the laser-induced tunneling results in complex tunneling matrix elements, where the laser phase ϕ gets imprinted onto the atomic wave function.

It is to note that ϕ is only defined up to a global constant that depends on the choice of origin for the integration variables in $\eta_{x,y,z}$. The free choice of the absolute value of this phase corresponds to a gauge freedom[5]. Furthermore it is to note that the realized gauge depends on the orientation of $\boldsymbol{k}$. The specific choice of $\boldsymbol{k} = \pm|\boldsymbol{k}|\boldsymbol{e}_y$ realizes the Landau gauge, but other orientations of the coupling laser can be chosen as well. Therefore the so obtained phases in the tunneling matrix elements J_{eff} do not directly map to the ones defined in the Harper Hamiltonian in equation (5.1), written in the Landau gauge.

In order to find the right mapping one has to compare the two models using a gauge-independent quantity. Here we use the total geometrical phase the particle acquires on a semi-classical round-trip trajectory on a plaquette. This quantity corresponds to the encircled magnetic flux piercing through the plaquette and is therefore gauge-independent. To calculate the total phase on a plaquette round-trip, as sketched in Figure 5.1, one has to note that for an inverse laser-assisted transition from e to g the complex conjugate J^*_{eff} applies and the acquired phase

---

[4] The approximation is valid when the spatial extensions of $w_0(y)$ and $\zeta(z)$ are smaller than $1/k_y$ and $1/k_z$ respectively, which are bound in our case below the possible maximum value of $1/|\boldsymbol{k}| \simeq 90\,\text{nm}$, for the coupling wavelength of $\lambda_{\text{c}} = 578\,\text{nm}$. The extension of $\zeta(z)$ will be similar to the one of a Wannier function in a $30\,E_{\text{R}}$ deep lattice as described in section 5.2.4, where the approximation $\eta_z \approx 1$ has been found to be reasonable in section 2.1.5.

[5] The one chosen here is convenient due to its symmetry.

is inverted. Using this, the round trip phase on the left-hand side plaquette in Figure 5.1 (b) is determined to

$$\begin{aligned}\phi_{\text{round-trip}} &= \phi_1 + \phi_2 + \phi_3 + \phi_4 \\ &= 0 + \boldsymbol{k} \cdot (\boldsymbol{r}^g_{m,n+1} + \boldsymbol{d}_x/4) + 0 - \boldsymbol{k} \cdot (\boldsymbol{r}^g_{m,n} + \boldsymbol{d}_x/4) \\ &= \boldsymbol{k} \cdot (\boldsymbol{r}^g_{m,n+1} - \boldsymbol{r}^g_{m,n}) \\ &= k_y d_y = 2\pi \frac{\lambda_\text{m}}{2\lambda_\text{c}} \cos(\theta)\,, \end{aligned} \tag{5.10}$$

where θ denotes the angle between $\boldsymbol{k}$ and the y axis. From this the simulated magnetic flux can be identified to be

$$\alpha = \frac{\lambda_\text{m}}{2\lambda_\text{c}} \cos(\theta)\,. \tag{5.11}$$

It is to note that this acquired total phase depends only on geometrical parameters, such as the lattice spacing of the magic lattice and the projection of the coupling laser wave vector $\boldsymbol{k}$ onto the magic lattice axis in y direction[6]. Furthermore the acquired total phase does not depend on the time the particle needs to perform the round trip and is therefore of purely geometrical origin. This is of course the desired feature, that allows one to identify it as analog to the Aharonov-Bohm phase.

We now want to see what the realized magnetic flux on a plaquette neighbouring to the previously considered one (see Figure 5.1) values to. For this we have to calculate the round-trip phase on the right-hand side plaquette in Figure 5.1 (b) in the same sense of orientation. Taking the sign change in acquired phase for J_{ge} with respect to J_{eg} into account, one finds

$$\begin{aligned}\phi^{\text{neighbour}}_{\text{round-trip}} &= 0 - \boldsymbol{k} \cdot (\boldsymbol{r}^g_{m+1,n+1} - \boldsymbol{d}_x/4) + 0 + \boldsymbol{k} \cdot (\boldsymbol{r}^g_{m+1,n} - \boldsymbol{d}_x/4) \\ &= -\, \boldsymbol{k} \cdot (\boldsymbol{r}^g_{m+1,n+1} - \boldsymbol{r}^g_{m+1,n}) \\ &= -\, \phi_{\text{round-trip}}\,, \end{aligned} \tag{5.12}$$

corresponding to the opposite magnetic flux $-\alpha$. This pattern continues along x and leads to a staggered magnetic flux having an alternating sign from one plaquette to another along the x direction. Along y it can be verified that the flux between neighbouring plaquettes stays the identical. The realized flux pattern is sketched in Figure 5.2.

---

[6] Moreover any supplementary phases that do not depend on the y coordinate have no influence on the total round-trip phase. This is in particular true for the case when the Wannier functions for the two internal states in expression (5.8) are not equal and η_x therefore not purely real.

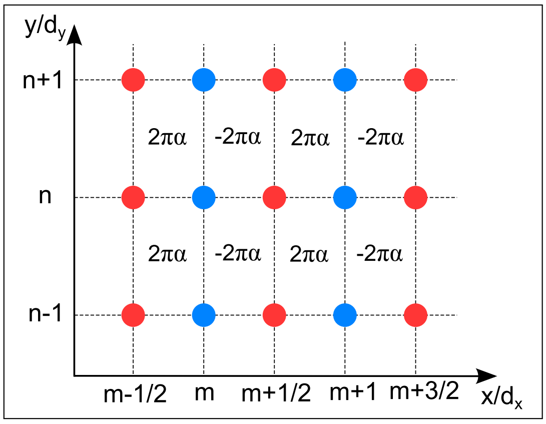

Figure 5.2: Illustration of the staggered magnetic flux pattern that is realized with the so far presented scheme.

This scheme therefore cannot exactly emulate the Harper Hamiltonian except for the case of $\alpha = 1/2$. The physics associated with this value of flux is interesting but the realization of a homogeneous flux and with equal sign over the whole lattice is desirable to access the full physics of the Harper Hamiltonian. How this can be realized is discussed in the next section.

5.1.2 Flux rectification

The main idea - rectification on the two plaquettes unit cell

To realize a homogeneous flux with equal signs in all plaquettes one has to find a mean to invert the flux on every other plaquette along x direction (rectification). It turns out that this is equivalent to inverting the imprinted laser phase on every other link for laser-assisted tunneling along x, which can be achieved by using two coupling lasers with opposite propagation directions ($\boldsymbol{k} \rightarrow -\boldsymbol{k}$ corresponds to $\alpha \rightarrow -\alpha$). Making each of them only resonant with every other plaquette, results in a rectification of the simulated flux, as sketched in Figure 5.3 (a). To achieve this experimentally, the degeneracy of neighbouring link resonances has to be lifted and the frequencies of the two counter propagating laser beams be slightly detuned with respect to each other, such that each laser addresses only one of the two classes of transition links[7].

A simple way to realize a link-dependent resonance frequency is to add a linear potential to the state-dependent lattice potential along x, as sketched in Figure

---

[7] For this, the two resonance frequencies need to have a detuning large compared to the tunneling energy J_{ge}, which will in our case not be larger than about a kHz.

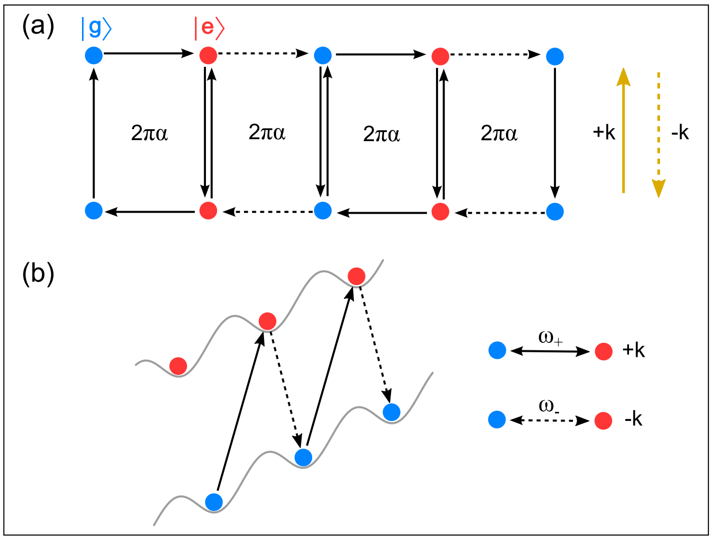

Figure 5.3: (a): Sketch to illustrate the idea of flux rectification. Two coupling lasers for laser-assisted tunneling propagate in opposite directions (yellow arrows) and are only resonant with every other plaquette. (b): Sketch of a possible rectification implementation in a tilted optical lattice, created by superposing a linear potential along x. This results in two alternating resonance frequencies for laser-assisted tunneling, that can be addressed by counter propagating coupling beams.

5.3 (b). In such a "tilted" state-dependent lattice configuration two resonance frequencies appear that alternate between neighbouring links. For magnetically sensitive atoms this could be realized using a constant magnetic field gradient along x. However with bosonic ytterbium this solution is not possible since it is magnetically not sensitive. An optical realization using a laser-induced differential light shift gradient could in principle be possible when placing the atomic cloud in the wing of a Gaussian laser beam at a "non-magic" wavelength. However it is found to be challenging to ensure the needed homogeneity of the gradient over the full cloud, while getting a large enough energy difference between neighbouring sites. Using static electric fields has been estimated in [39] to be also technically challenging.

Superlattice solution - rectification on the four plaquettes unit cell

Another possible solution for rectification has been proposed in [39] and implies the addition of a second optical lattice along x direction having twice the period of the anti-magic lattice. This double period lattice is intended to modulate the on-site energies along x for atoms in states g and e differently, such that neighbouring

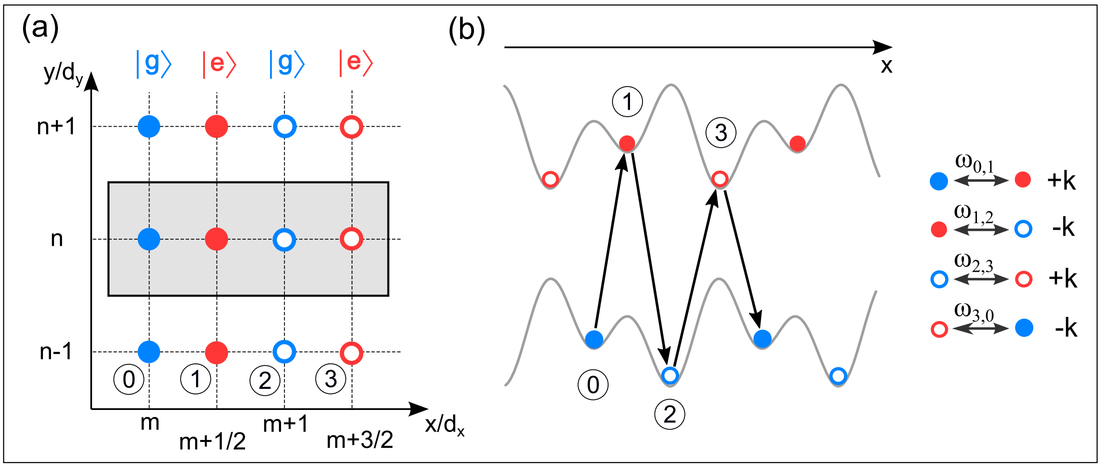

Figure 5.4: Illustration of the rectification scheme using a superlattice potential. (a): The lattice geometry with four distinguishable types of lattice sites within one unit cell (gray shaded) is shown. (b): The complementary superlattice potentials for atoms in g and e are sketched as well as the according transitions between neighbouring sites with unequal resonance frequencies on a given line (fixed n). The four sites corresponding to one unit cell are labeled with numbers from 0 to 3. The four link types are summarized on the right-hand side with an example configuration for the coupling laser propagation directions $\pm\boldsymbol{k}$, that would be required for flux rectification.

links have unequal resonance frequencies. This superlattice potential has twice the periodicity of the anti-magic lattice and therefore four non-equivalent links (transition frequencies) can in general be distinguished (as sketched in Figure 5.4), requiring four coupling laser frequencies to address all possible links. In the following the transition frequencies of these four link types are calculated as a function of the applied double period lattice properties. It will turn out that there is a special configuration where two of the four frequencies are degenerate and only three coupling frequencies are needed.

The potential created by the double period lattice for the states g and e can be considered in the form

$$W_{\mathrm{sup,g}}(x) = -W_{\mathrm{g}} \cos^2(k_x x/2 + \phi_{\mathrm{rel}})\,, \tag{5.13}$$

$$W_{\mathrm{sup,e}}(x) = W_{\mathrm{e}} \cos^2(k_x x/2 + \phi_{\mathrm{rel}})\,, \tag{5.14}$$

with $W_{\mathrm{g,e}} \geq 0$ the lattice depths[8] for g and e and ϕ_{rel} the relative phase between the applied double period lattice and the anti-magic lattice. The double period lattice is assumed to be a small perturbation to the anti-magic lattice, $W_{\mathrm{g/e}} \ll V_{\mathrm{g/e}}$, such that the general structure of the potential landscape stays[9] as sketched in Figure 5.4.

The unit cell in this superlattice configuration spans four plaquettes along x, due to the periodicity over a distance $2d_x$. Accordingly four distinguishable types of sites with different on-site energies can be identified that will be labeled in the following with integers from 0 to 3 (see Figure 5.4). Their positions are chosen to be given by

$$0: \quad \boldsymbol{r}^g_{m,n}\,, \quad \text{for } m \text{ even}\,, \tag{5.15}$$
$$1: \quad \boldsymbol{r}^e_{m,n}\,, \quad \text{for } m \text{ even}\,, \tag{5.16}$$
$$2: \quad \boldsymbol{r}^g_{m,n}\,, \quad \text{for } m \text{ odd}\,, \tag{5.17}$$
$$3: \quad \boldsymbol{r}^e_{m,n}\,, \quad \text{for } m \text{ odd}\,, \tag{5.18}$$

with $\boldsymbol{r}^g_{m,n}$ and $\boldsymbol{r}^e_{m,n}$ as defined in equations (5.5) and (5.6). The on-site energies are determined as the sum of the internal energy and the energy shifts caused by the anti-magic and the double period lattices and read

$$E_0 = E_g - V_g + \hbar\omega_g/2 - W_g \cos^2(\phi_{\mathrm{rel}})\,, \tag{5.19}$$
$$E_1 = E_e \qquad + \hbar\omega_e/2 + W_e \cos^2(\phi_{\mathrm{rel}} + \pi/4)\,, \tag{5.20}$$
$$E_2 = E_g - V_g + \hbar\omega_g/2 - W_g \cos^2(\phi_{\mathrm{rel}} + 2\pi/4)\,, \tag{5.21}$$
$$E_3 = E_e \qquad + \hbar\omega_e/2 + W_e \cos^2(\phi_{\mathrm{rel}} + 3\pi/4)\,, \tag{5.22}$$

where $E_g - E_e$ is the energy difference between the internal atomic states in free space, and $\hbar\omega_{g,e}/2 = \sqrt{V_{g,e}\, E_{\mathrm{R,am}}}$ the zero point energy of g and e atoms at the bottom of each lattice site[10], with $E_{\mathrm{R,am}}$ the recoil energy of the anti-magic lattice. Here we have used that neighbouring g and e sites are displaced by $d_x/2$, which can be expressed as a phase shift of $\pi/4$ for our chosen phase convention, as defined in equations (5.13) and (5.14). From these on-site energies the transition frequencies

---

[8] The sign convention for the potentials is chosen according to the potentials that we plan to realize using ytterbium as explained in the next section.

[9] If the double period potential dominates over the anti-magic lattice, the general lattice geometry will change and half of the lattice sites will disappear since they are no longer minima of the potential.

[10] The zero point energy due to the magic lattice along y direction is omitted since it shifts all sites by the same quantity and is therefore irrelevant for the discussion.

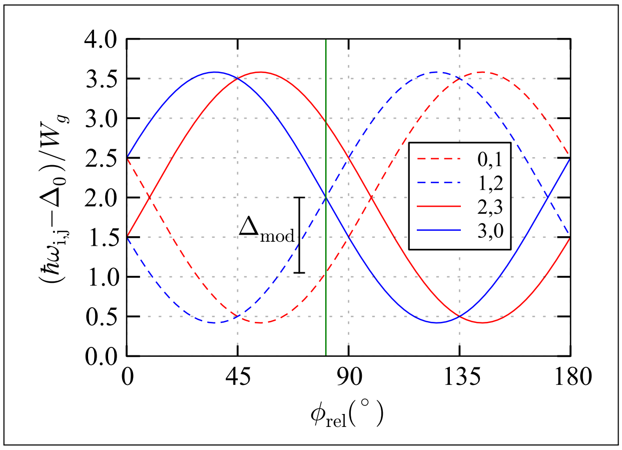

Figure 5.5: Dependence of the resonance frequencies $\omega_{0,1}$ (red dashed), $\omega_{1,2}$ (blue dashed), $\omega_{2,3}$ (red solid) and $\omega_{3,0}$ (blue solid) on the relative lattice phase $\phi_{\rm rel}$, for the case of $W_e = 3W_g$. The vertical green line indicates one of the special phases, $\phi_{\rm rel} = \phi_{\rm rel,3f}$, where two of the four frequencies, corresponding to the same propagation direction of the coupling laser, are degenerate. The energy difference $\Delta_{\rm mod}$ between the resonances at this point is also indicated in the figure.

$\omega_{i,j}$, between neighbouring sites i and j, for the four link types can be calculated as

$$\hbar\omega_{0,1} = E_1 - E_0 = \Delta_0 + W_e\cos^2(\phi_{\rm rel}+\pi/4) + W_g\cos^2(\phi_{\rm rel})\,, \tag{5.23}$$

$$\hbar\omega_{1,2} = E_1 - E_2 = \Delta_0 + W_e\cos^2(\phi_{\rm rel}+\pi/4) + W_g\sin^2(\phi_{\rm rel})\,, \tag{5.24}$$

$$\hbar\omega_{2,3} = E_3 - E_2 = \Delta_0 + W_e\sin^2(\phi_{\rm rel}+\pi/4) + W_g\sin^2(\phi_{\rm rel})\,, \tag{5.25}$$

$$\hbar\omega_{3,0} = E_3 - E_0 = \Delta_0 + W_e\sin^2(\phi_{\rm rel}+\pi/4) + W_g\cos^2(\phi_{\rm rel})\,, \tag{5.26}$$

with $\Delta_0 = E_e - E_g + V_g + \hbar(\omega_e - \omega_g)/2$, summarizing all energy shifts that are independent of $\phi_{\rm rel}$. The presence of these four coupling frequencies is illustrated in Figure 5.4 (b) where the unequal superlattice potentials for g and e are sketched. For flux rectification it is necessary that the direction of the coupling laser alternates between neighbouring links, meaning to have $+\boldsymbol{k}$ for $\omega_{0,1}$ and $\omega_{2,3}$ and $-\boldsymbol{k}$ for $\omega_{1,2}$ and $\omega_{3,0}$, or vice versa.

Reduction to three coupling frequencies

In Figure 5.5 the dependence of the link resonances on the relative lattice phase is shown for a potential depth ratio of $W_e/W_g = 3$ (in anticipation of our case for ytterbium). From there it can be seen that there are particular values for the relative lattice phase ϕ_{rel}, where the two transition frequencies corresponding to the same coupling direction can be chosen to be equal. In this case only three laser frequencies are needed to address all link types while having the full flux rectification. By imposing for example $\omega_{0,1} = \omega_{2,3}$, the "three-frequency" relative phase $\phi_{\text{rel,3f}}$, is determined by

$$\boxed{\tan(2\phi_{\text{rel,3f}}) = \frac{W_g}{W_e}}\,. \tag{5.27}$$

With this choice of phase the on-site energies are given by

$$E_0 = E_g - V_g + \hbar\omega_g/2 - W_g/2 - \Delta_{\text{mod}}/2\,, \tag{5.28}$$
$$E_1 = E_e + \hbar\omega_e/2 \qquad + W_e/2 - \Delta_{\text{mod}}/2\,, \tag{5.29}$$
$$E_2 = E_g - V_g + \hbar\omega_g/2 - W_g/2 + \Delta_{\text{mod}}/2\,, \tag{5.30}$$
$$E_3 = E_e + \hbar\omega_e/2 \qquad + W_e/2 + \Delta_{\text{mod}}/2\,, \tag{5.31}$$

and the transition energies read

$$\hbar\omega_{0,1} = \Delta_0 + \frac{W_e + W_g}{2}\,, \tag{5.32}$$
$$\hbar\omega_{1,2} = \Delta_0 + \frac{W_e + W_g}{2} - \Delta_{\text{mod}}\,, \tag{5.33}$$
$$\hbar\omega_{2,3} = \Delta_0 + \frac{W_e + W_g}{2}\,, \tag{5.34}$$
$$\hbar\omega_{3,0} = \Delta_0 + \frac{W_e + W_g}{2} + \Delta_{\text{mod}}\,, \tag{5.35}$$

with $\Delta_{\text{mod}} = W_g\, W_e / \sqrt{{W_g}^2 + {W_e}^2}$ being the energy modulation between the three resonance frequencies.

In Figure 5.5 it can be seen that this choice of phase maximizes the energy splitting between the three resonance frequencies. In the considered case of $W_e/W_g = 3$, the special "three-frequency" phases occur periodically at $\phi_{\text{rel,3f}} \approx n \times 90\,^\circ \pm 9\,^\circ$, with integer valued n, where the plus sign corresponds to cases with $\omega_{0,1} = \omega_{2,3}$ and the minus sign to $\omega_{1,2} = \omega_{3,0}$. Both cases can be equivalently used for flux rectification[11]. The experimentally needed tuning range to reach one of these cases needs therefore in the worst case to be about $72\,^\circ$.

---

[11] In the case where the coupling laser frequencies and propagation directions are fixed, the two situations correspond to the simulation of homogeneous fluxes of opposite signs α or $-\alpha$. The basic physics in both cases is identical.

5.2 Analysis of practical requirements and experimental conditions

The scheme as presented in the previous sections can be favourably implemented using ytterbium atoms. The $^1\mathrm{S}_0$ and $^3\mathrm{P}_0$ states offer an ideal two-level system with negligible spontaneous emission on the experimentally relevant time scales, as needed for the states g and e. The coherent coupling between the two states can be achieved with laser light at an experimentally accessible wavelength of $\lambda_\mathrm{c} = 578\,\mathrm{nm}$ (details see chapter 4). The fact that the two states couple differently to excited states in the presence of far-off-resonant light gives rise to the required magic and anti-magic wavelengths (details see Appendix A). We will use the magic wavelength at $\lambda_\mathrm{m} \approx 760\,\mathrm{nm}$, where powerful and robust laser sources are available[12] and spontaneous emission is negligible. For the anti-magic wavelength we have chosen to work at about 612 nm[13], which is close to an anti-magic wavelength that is expected around $\lambda_\mathrm{am} \approx 617\,\mathrm{nm}$ (according to the calculations in Appendix A). The double period lattice will then be realized at about $\lambda_\mathrm{sup} = 1224\,\mathrm{nm}$. For both wavelengths reasonably small spontaneous emission rates are expected (∼nK/s or smaller for $10\,E_\mathrm{R}$ lattice depth).

Before proceeding further I would like to summarize the full potential landscape that is needed to be realized for the intended scheme, in order to clarify the notations for the following discussions:

$$V_\mathrm{am,g}(x) = -V_\mathrm{g}\cos^2(k_x x)\,, \tag{5.36}$$

$$V_\mathrm{am,e}(x) = V_\mathrm{e}\cos^2(k_x x)\,, \tag{5.37}$$

$$W_\mathrm{sup,g}(x) = -W_\mathrm{g}\cos^2(k_x x/2 + \phi)\,, \tag{5.38}$$

$$W_\mathrm{sup,e}(x) = W_\mathrm{e}\cos^2(k_x x/2 + \phi)\,, \tag{5.39}$$

$$V_\mathrm{M}(y) = -V_\mathrm{m}\cos^2(k_\mathrm{m} y)\,, \tag{5.40}$$

$$V_\mathrm{Z}(z) = \frac{1}{2}m\omega_z^2 z^2\,. \tag{5.41}$$

The strong 2D confinement along z is chosen as a generic harmonic potential with trapping frequency ω_z. The z direction in our implementation will be parallel to the direction of gravity. For stability reasons all optical lattices are planed to be realized in retro-reflected configuration.

---

[12] We use a titanium-sapphire laser system providing 5.5 W at 760 nm (SolsTiS, from M Squared Lasers).

[13] A second anti-magic wavelength with reasonably low spontaneous emission is at about 1.12 μm (see Appendix A) where the double period lattice would be at 2.23 μm. However especially for 2.23 μm it was difficult to get appropriate anti-reflection coatings for the viewports, that work also well for the rest of our "wavelength zoo" down to 400 nm. Additionally there is the inconvenience that the transmission of usually used glasses like fused silica starts to drop for wavelengths above about 2 μm.

In the now upcoming discussions, the previously described scheme to realize the Harper Hamiltonian is regarded from a closer point of view and a detailed analysis of the required and achievable experimental conditions is given. It is to note that some of the given conditions are formally necessary to realize the exact form of the Harper Hamiltonian, although they might not be necessary to see the physics associated with the artificial magnetic field, that should in general be connected to the presence of the geometrical phase. For the discussion it is assumed that the superlattice rectification in the "three-frequency" configuration is applied.

5.2.1 Range of effective magnetic flux

When using the magic wavelength at 760 nm in a retro-reflected lattice configuration the maximum reachable value of flux is $\alpha_{\mathrm{max}} = 759.4\,\mathrm{nm}/2\times 578.4\,\mathrm{nm} \simeq 0.656$ and therefore in principle magnetic fluxes in the range of

$$0 \leq \alpha \leq 0.656\,, \tag{5.42}$$

accessible. This includes in principle all important values for magnetic fluxes since the spectrum of the Harper Hamiltonian is symmetric with respect to $\alpha = 0.5$ (values between 0.5 and unity correspond to negative magnetic fluxes but show the same basic physics as the values between 0 and 0.5). To tune the value of α, the angle of the coupling beams with respect to the y axis can be used (in plane as well as out of plane). However the reachable values depend on the optical access provided by the vacuum chamber design. In case a desired flux value is not attainable due to geometrical constraints, one could create the magic lattice using two 760 nm beams intersecting at an angle. This allows to tune the lattice spacing along y and therefore the simulated flux, probably at the cost of increased pointing instabilities of the lattice beams.

5.2.2 Tunneling energies and bandgap - lattice benchmark values

Important in the considerations of laser-assisted tunneling is to avoid the coupling to higher-lying Bloch bands. This is needed to keep the dynamics within the theory description in the tight-binding regime and to avoid the associated heating of the atoms in the lattice[14]. To ensure this, the necessary condition is that the laser-assisted tunneling energy J_{ge} stays small compared to the bandgap from the

---

[14] As seen before (section 2.1.3), higher bands have larger bandwidth J and therefore atoms transferred to a higher band are typically more energetic than in the ground band. Redistribution of this energy via collisions will lead to heating of the atoms in the ground band, which is thus to be avoided.

$E_{\mathrm{R,am}}/h$	$V_{\mathrm{g}}/E_{\mathrm{R,am}}$	$V_{\mathrm{e}}/E_{\mathrm{R,am}}$	$\Delta_{\mathrm{gap,e}}/h$	J_{ee}/h	η_x	J_{ge}/h
3.0 kHz	13.6	10	13.9 kHz	0.06 kHz	0.2	0.2 kHz

Table 5.1: Anti-magic lattice benchmark parameters at $\lambda_{\mathrm{am}} = 612\,\mathrm{nm}$. The value for J_{ge} is calculated for a vacuum Rabi frequency of $\Omega_{\mathrm{Rabi}} \approx 2\pi \times 2\,\mathrm{kHz}$ and assuming $\eta_{y,z} \approx 1$. J_{ee} is the tunneling amplitude without taking the modulation of the superlattice potential into account.

fundamental to the first excited Bloch band Δ_{gap}. In addition, in the case of the rectification scheme in the superlattice three resonance frequencies are present with spacings of Δ_{mod}. It has to be avoided that one of the coupling lasers becomes resonant with a "wrong" transition in the rectification scheme (for example the laser at frequency $\omega_{0,1}$ being resonant with the $1 \leftrightarrow 2$ transition), which is ensured by keeping $J_{ge} \ll \Delta_{\mathrm{mod}}$. We also impose that $\Delta_{\mathrm{mod}} \ll \Delta_{\mathrm{gap}}$, which leaves the "main" band structure of the lattice intact. In summary these conditions read

$$\boxed{J_{ge} \ll \Delta_{\mathrm{mod}} \ll \Delta_{\mathrm{gap}}}\,. \tag{5.43}$$

A reasonable choice is for example $J_{ge} \approx \Delta_{\mathrm{mod}}/7 \approx \Delta_{\mathrm{gap}}/70$ which will be used in the following to estimate the orders of magnitudes involved.

To realize the exact form of the Harper Hamiltonian the laser-assisted tunneling energy J_{ge} has to dominate over the regular tunneling along x, determined by J_{gg} and J_{ee}. When considering the superlattice configuration, however, neighbouring sites in the g and e sublattices are shifted in energy by Δ_{mod} [see equations (5.28) to (5.31)]. As soon as this shift becomes large compared to $J_{gg/ee}$, normal tunneling will be strongly suppressed. Therefore we can impose the condition

$$\boxed{J_{gg}, J_{ee} \ll \Delta_{\mathrm{mod}}}\,. \tag{5.44}$$

In tables 5.1 and 5.2 some typical numerical values for the anti-magic and double period lattice properties are shown that fulfill the two conditions in equations (5.43) and (5.44). These values will serve in the following considerations as benchmark values to be attained, to help find numerical estimates for other effects within a coherent framework. For completeness also benchmark values for the magic lattice along y direction are given in Table 5.3, that correspond to typical values we plan to implement. It is to note, that the chosen parameters do not implement an identical tunneling rate along x and y as in the exact form of the Harper Hamiltonian, but this is not expected to change the main physics associated with the artificial magnetic field, provided the difference is not too large.

$E_{\mathrm{R,sup}}/h$	$W_{\mathrm{g}}/E_{\mathrm{R,sup}}$	$W_{\mathrm{e}}/E_{\mathrm{R,sup}}$	Δ_{mod}
0.76 kHz	2.7	8.0	$2.6\,E_{\mathrm{R}} \approx h \times 2\,\mathrm{kHz}$

Table 5.2: Double period lattice benchmark parameters at $\lambda_{\mathrm{sup}} = 1224\,\mathrm{nm}$.

$E_{\mathrm{R,m}}/h$	$V_{\mathrm{m}}/E_{\mathrm{R,m}}$	J_y/h
2.0 kHz	8	0.06 kHz

Table 5.3: Magic lattice benchmark parameters at $\lambda_{\mathrm{m}} = 760\,\mathrm{nm}$.

5.2.3 The problem of inelastic collisions

One of the problematic points in the experimental realization of the described scheme could be strong atom loss due to inelastic collisions between atoms in the metastable $^3\mathrm{P}_0$ excited state. As already mentioned in section 4.2, the expected collisions rate coefficients for $^3\mathrm{P}_0$-$^3\mathrm{P}_0$ (e-e) and $^1\mathrm{S}_0$-$^3\mathrm{P}_0$ (g-e) collisions are not known yet for ^{174}Yb but are expected to be similar as for other ytterbium isotopes where $\beta_{ge}, \beta_{ee} \sim 10^{-11}\mathrm{cm}^3/\mathrm{s}$ has been measured [118, 113]. In the proposed scheme g-e collisions are strongly suppressed due to the spatial separation of the two states in the state-dependent lattice. On-site collisions between atoms in the e states can be avoided by working in a regime of low density with much less than one atom per site. Then the probability to find two e atoms at the same site could be small enough to ensure reasonably small atom loss on the time scale of the performed experiments. Alternatively, working at a density near one atom per site, one expects a large suppression of double occupancy in the regime of large on-site interactions. In a Mott-insulator state, for instance, double occupancy will be suppressed as $\sim (J_{ge}/U_{ee})^2$ [117], where U_{ee} is the on-site energy for e atoms. Finally, detuning the coupling laser from resonance will reduce the population on e sites at the expense of a reduced J_{ge}. These options will need to be tested experimentally.

5.2.4 Realizing a 2D quantum gas

As assumed in the described scheme, the dynamics of the atomic cloud should be restricted to two dimensions (x-y plane). This can be realized by "freezing" out the motion in the z direction, where the necessary condition to achieve effective 2D dynamics of a Bose-Einstein condensate is to have [16]

$$k_{\mathrm{B}}T, \mu \ll \hbar\omega_z\,, \tag{5.45}$$

where $k_\mathrm{B}T$ and μ are the thermal energy and the chemical potential. This condition basically states that the interaction energy scale of the condensate should be small compared to the level spacing of the harmonic oscillator potential in z direction. Then the atoms will populate the harmonic oscillator ground state and motional excitations along z are negligible.

Scheme for single plane preparation in an optical lattice

Experimentally we plan to realize the 2D confinement using a retro-reflected optical lattice in the z direction at the magic wavelength $\lambda_\mathrm{m} = 760\,\mathrm{nm}$. This lattice creates disc shaped atomic clouds in each site, where the on-site confinement along z can be very strong. Choosing a deep enough lattice, tunneling between neighbouring sites can be strongly suppressed such that the atomic clouds in each plane can be regarded as independent two-dimensional systems. For a lattice depth of about $30\,E_\mathrm{R,m}$, for instance, the on-site trapping frequency along z values to about $\omega_z/2\pi \approx 22\,\mathrm{kHz}$, which is about a factor of ten larger than the typical chemical potential of a BEC (see also the calculation further down). The tunneling energy in this case values to $J/h \approx 1\,\mathrm{Hz}$, which determines the time scale for the coupling between the different planes.

Since the initial size of the condensate is usually larger than the lattice spacing of $\lambda_\mathrm{m}/2 \approx 380\,\mathrm{nm}$ (retro-reflected configuration), several lattice sites will be occupied after loading. Since we would like to work with atoms in a single plane only[15] we will need a mean to remove the atoms from all planes except one. One way this can be achieved has been shown in [132] for rubidium atoms. There a magnetic field gradient is used to create a spatially dependent resonance frequency for microwave transitions between magnetic sublevels of the two hyperfine ground states of rubidium. When the gradient is strong enough, the considered transition can be site selectively addressed. Then the population in the two hyperfine ground states can be controlled for each site independently and the atoms in all planes except one are transferred into one of the hyperfine states. These atoms are then removed with light that is only resonant with atoms in this certain hyperfine states.

For our case this technique is not directly applicable since bosonic ytterbium is not magnetically sensitive and does not show a hyperfine structure in the ground state. The idea instead is to use a laser to create a differential light shift gradient[16]

---

[15] For imaging reasons it is advantageous to have only a single plane of atoms. If many planes are populated, averaging effects for an imaging along z direction could wash out important features.

[16] This can be realized with laser light at a wavelength with a reasonably high differential polarizability. By placing the atoms in the wing of the transverse Gaussian beam envelope, a spatial gradient for the differential light shift can be achieved.

for the states g and e along z. In the case where the differential light shift between neighbouring planes becomes on the order of several kHz, the clock transition can be site selectively addressed. Then the atoms in all but one plane can be transferred to the e state, where they will suffer strong atom loss due to the beforehand mentioned inelastic collisions (see section 5.2.3). Since the inelastic loss rate will also decrease when the density is reduced, it is to verify experimentally to what extend the atoms can be effectively removed from the unwanted planes using this method. Alternatively the atoms can be blast away using light that is only resonant for e atoms (like for example light at 649 nm, being resonant with the $^3\mathrm{P}_0$ (6s6p) to $^3\mathrm{S}_1$ (6s7s) transition).

Typical atom number and cloud size

The size of the 2D confined atomic cloud in the x-y plane (within the two-dimensional lattice system) will become important when considering inhomogeneities of the lattice beams. The typical atom number to be attained will be set by the condition that the expected strong inelastic losses are likely to force us to work around unity density or below (see section 5.2.3). To get an estimation of the atom number and cloud radius in the unity density regime, the results from section 2.1.6 are used, where the case of atoms in a two-dimensional lattice in the superfluid regime is considered.

For simplicity we restrict the discussion to g atoms only and we neglect the influence of the double period potential. The maximum atom number and cloud radius as given in equations (2.47) depend on the on-site interaction energy in the 2D lattice U_{gg} [equation (2.43)], here taken for the g atoms only. This interaction energy is, apart from the lattice depth, mainly determined by the ratio of s-wave scattering length a_s to harmonic oscillator length a_z, associated with the strong confinement along the z axis.

In order to get some numerical estimates we will use the above mentioned example value of $\omega_z/2\pi \approx 22\,\mathrm{kHz}$, which leads to an harmonic oscillator length of about $a_z \approx 50\,\mathrm{nm}$. Furthermore we use a mean lattice spacing along x and y of $\bar{d} = (d_x + d_y)/2 \approx 340\,\mathrm{nm}$ as well as a mean lattice depth $10\,\bar{E}_\mathrm{R}$ in both axis, with $\bar{E}_\mathrm{R} = (E_\mathrm{R,m} + E_\mathrm{R,am})/2 \approx h \times 2.5\,\mathrm{kHz}$. Then the on-site interaction energy calculates to about $U_{gg}/h \approx 1.4\,\mathrm{kHz}$, which is under the assumption of unity central density equal to the central chemical potential $\mu_{gg} \approx U_{gg}$. When considering an isotropic harmonic confinement in the x-y plane with a trapping frequency of $\Omega \approx 2\pi \times 25\,\mathrm{Hz}$ the cloud radius to obtain a unity central density is determined to be $R_\mathrm{max} \approx 15\,\mu\mathrm{m}$. The according atom number would be $N_\mathrm{max} \approx 3500$. These numbers will in the following be used as typical values for other estimations. In the case of a Mott-insulator similar values are expected[17].

It is to note that this calculation can only be done for g atoms so far. The interaction energy between e states U_{ee} for example cannot be calculated since the scattering length for e atoms is not known.

5.2.5 Inhomogeneities due to Gaussian beam envelopes

The so far considered lattice potentials, as summarized in equations (5.36) to (5.41), are assumed to be created by ideal plane waves. However in the experiment the optical lattices will be generated by Gaussian laser beams having a finite transverse envelope[18], leading to spatially dependent lattice potentials of the (general) form

$$V(\boldsymbol{r}) = -V_0 \cos^2(kx) e^{-2(y^2+z^2)/w^2}\,, \tag{5.46}$$

where w denotes the waist of the circular Gaussian beam, V_0 the lattice depth and π/k the lattice spacing. In the case where the cloud size is small compared to the waist of the Gaussian beam, the transverse variation of the potential can be treated in harmonic approximation. For atoms in the lowest Bloch band, the potential in equation (5.46) can then be approximated as the sum of the bare lattice potential and the smooth harmonic confinement, $V(\boldsymbol{r}) \approx -V_0\cos^2(kx) + \delta V(\boldsymbol{r})$, with $\delta V(\boldsymbol{r}) = \frac{1}{2}m\omega^2(y^2+z^2)$ and the trapping frequency $\omega = \sqrt{4V_0/mw^2}$.

When considering now the potential landscape from equations (5.36) to (5.41), the supplementary harmonic confinements for the states g and e in the x-y plane can be denoted in the form

$$\delta V_g(\boldsymbol{r}) = \frac{1}{2}m(\Omega^2 + \omega_x^2)x^2 + \frac{1}{2}m(\Omega^2 + \omega_{y,g}^2)y^2\,, \tag{5.47}$$

$$\delta V_e(\boldsymbol{r}) = \frac{1}{2}m(\Omega^2 + \omega_x^2)x^2 + \frac{1}{2}m(\Omega^2 - \omega_{y,e}^2)y^2\,, \tag{5.48}$$

where Ω corresponds to the contribution of the z magic 2D confinement, ω_x to the contribution from the y magic lattice and $\omega_{y,g/e}$ to the combined contribution from the x anti-magic and double period lattice. The minus sign in equation (5.48) takes the repulsive nature of the anti-magic and double period potentials for atoms in the e state into account (which is true for our choice of wavelengths). Several effects resulting from these harmonic confinements are important and are discussed now.

---

[17] In fact we are likely to work close to the Mott-insulator transition that would for an interaction energy of $U_{gg}/h = 1.4\,\mathrm{kHz}$, for the g atoms at unity filling, be at a mean lattice depth of about $8\,\bar{E}_\mathrm{R}$.

[18] The longitudinal contributions are much smaller than the transverse ones and can safely be neglected in the following.

Spatially dependent differential light shift

The first effect arises from the fact that the transverse potentials lead to a spatially dependent differential light shift between g and e states. This light shift is given by

$$\delta V_g(\boldsymbol{r}) - \delta V_e(\boldsymbol{r}) = \frac{1}{2} m(\omega_{y,g}^2 + \omega_{y,e}^2) y^2 \,, \tag{5.49}$$

and results in an inhomogeneous resonance frequency for laser-assisted tunneling along the y direction. In order to keep the tunneling energy homogeneous over the size of the cloud, we have to impose the condition

$$\boxed{\frac{1}{2} m(\omega_{y,g}^2 + \omega_{y,e}^2) R^2 \ll J_{ge}} \,, \tag{5.50}$$

with R being the radius of the atomic cloud. This sets an upper limit on the combined trapping frequencies of the anti-magic and double period lattice. When assuming $R = 15\,\mu\text{m}$ and $J_{ge}/h = 0.2\,\text{kHz}$, this yields $\sqrt{\omega_{y,g}^2 + \omega_{y,e}^2}/2\pi \lesssim 10\,\text{Hz}$, which is a quite strong condition on the transverse confinements. For the benchmark lattice parameters from tables 5.1 and 5.2, for example, this would imply to work with lattice beam waists on the order of $300\,\mu\text{m}$ or larger. Accordingly the amount of required laser power for the lattice beams is relatively high ($\sim 1\,\text{W}$ at 612 nm) which causes some complications in the experimental implementation (see section 5.3.4).

A more relaxed condition might be to impose that we want to avoid that one of the coupling lasers becomes resonant with the "wrong" link type in the rectification scheme at the edge of the cloud. Then the resulting condition would lead to $\sqrt{\omega_{y,g}^2 + \omega_{y,e}^2}/2\pi \lesssim 30\,\text{Hz}$, when assuming $\Delta_{\text{mod}} = h \times 2\,\text{kHz}$. In this case beam waists larger than about $150\,\mu\text{m}$ would be sufficient.

Overall attractive potential

The second effect related to the external harmonic confinements is that the overall confinement should be attractive for both states since otherwise atoms would be lost after a certain time. This risk is present for atoms in state e where both the anti-magic and double period lattice create repulsive transverse potentials. To ensure an overall attractive potential, the confinement defined by the 2D trapping in z direction should dominate, leading to the condition

$$\boxed{\Omega^2 \gtrsim \omega_{y,e}^2} \,. \tag{5.51}$$

Assuming that the condition (5.50) is satisfied, this would be fulfilled by the already above used example value of $\Omega/2\pi \approx 25\,\text{Hz}$.

Suppression of regular tunneling

The third effect arising from the residual harmonic confinements concerns the general energy shift between neighbouring lattice sites. This energy shift can influence the regular tunneling along y, when becoming comparable to J_y. This problem has already been discussed in section 2.1.6 and leads to the condition in equation (2.49), that reads

$$\boxed{m(\Omega^2 - \omega_{y,e}^2) R d_y \lesssim J_y}\,. \tag{5.52}$$

Using $J_y \simeq 60\,\mathrm{Hz}$ as in the benchmark table 5.3, results in $\sqrt{\Omega^2 - \omega_{y,e}^2}/2\pi \lesssim 150\,\mathrm{Hz}$, which is automatically fulfilled when the conditions (5.50) and (5.51) are satisfied.

5.2.6 Relative lattice phase tuning range and fluctuations

In the discussion in section 5.1.2 it has been seen that "three-frequency" relative lattice phases for our choice of lattice wavelengths appear periodically at $\phi_{\mathrm{rel,3f}} \approx n \times 90\,^\circ \pm 9\,^\circ$, with integer valued n. It has been equally argued that the all experimentally relevant cases are covered by a tuning range of a bit less than $90\,^\circ$.

Fluctuations of the relative phase ϕ_{rel} between the anti-magic and double period lattice can lead to changes of the different resonance frequencies for laser-assisted tunneling within the rectification scheme. The shift of the resonance frequencies should ideally be kept small compared to J_{ge}. This condition can be quantified by evaluating the derivative of the transition frequencies in equations (5.23) to (5.26) with respect to the relative phase ϕ_{rel}. Assuming to work at a phase corresponding to the three-frequency reduction scheme, the strongest dependence is given by

$$\left| \frac{d\hbar\omega_{01}}{d\phi_{\mathrm{rel}}} \right|_{\phi_{\mathrm{rel}} = \phi_{\mathrm{rel,3f}}} = \sqrt{W_g^2 + W_e^2}\,, \tag{5.53}$$

leading to the condition for fluctuations of the relative phase of

$$\boxed{\delta\phi_{\mathrm{rel}} \ll J_{ge}/\sqrt{W_g^2 + W_e^2}}\,. \tag{5.54}$$

For the benchmark values in tables 5.1 and 5.2 this yields $\delta\phi_{\mathrm{rel}} \ll 0.02 \approx 1^\circ$, which is well within the technically realizable (see section 5.3.2).

5.2.7 Power fluctuations of lattice beams

The exact energy of the coupling resonances $\hbar\omega_{i,j}$ also depends on the potential depths $V_{g/e}$ and $W_{g/e}$ as can be seen in equations (5.32) to (5.35). Fluctuations on these lattice depths directly influence the transition energies and their effect should be kept small compared to the laser-assisted tunneling energy J_{ge}. The strongest dependences of equations (5.32) to (5.35) on the lattice depths determine the dominant sensitivity to relative power fluctuations $\delta P/P$ and lead to the conditions for the anti-magic and double period lattice power fluctuations of

$$\delta P_{\mathrm{am}}/P_{\mathrm{am}} \ll J_{ge}/V_g\,, \tag{5.55}$$

$$\delta P_{\mathrm{sup}}/P_{\mathrm{sup}} \ll 2J_{ge}/(W_g + W_e)\,. \tag{5.56}$$

For the values in the benchmark tables 5.1 and 5.2, the typical restrictions become $\delta P_{\mathrm{am}}/P_{\mathrm{am}} \ll 0.005$ and $\delta P_{\mathrm{sup}}/P_{\mathrm{sup}} \ll 0.04$. Both conditions lie within the experimentally feasible, provided the laser intensities are actively stabilized.

5.2.8 Accuracy of magic and anti-magic wavelengths

The influence of deviations of the lattice laser wavelengths away from the ideal magic and anti-magic case are considered next. For the potentials created at the magic wavelength (lattice in y direction and strong confinement along the z axis) a small deviation $\delta\lambda = \lambda_{\mathrm{laser}} - \lambda_{\mathrm{m}}$ leads to a differential light shift for the states g and e that depends on the local potential depth. The fact that the potentials vary spatially due to the Gaussian envelopes of the applied laser beams then gives rise to position-dependent laser-assisted tunneling resonance frequency, similar to the above discussed cases of inhomogeneities. Ideally, the differential light shift variation over the whole cloud should stay small compared to the laser-induced tunneling energy to ensure the same resonance frequencies all over the cloud. When applying the harmonic approximation to the generic Gaussian transverse potential dependence for the two states g and e as given by $U_{g/e}(r) = U_{0,g/e}\exp(-2r^2/w_0^2) \approx U_{0,g/e} - 2U_{0,g/e}r^2/w_0^2$, this condition becomes

$$\frac{2(U_{0,g} - U_{0,e})R^2}{w_0^2} \ll J_{ge}\,, \tag{5.57}$$

with the cloud radius R. The quantity that determines $U_{0,g}(\lambda) - U_{0,e}(\lambda)$ as a function of applied laser wavelength is the differential polarizability $\alpha'_{\mathrm{diff}} = \alpha'_g(\lambda) - \alpha'_e(\lambda)$. The dependence of this quantity on the laser frequency close to the magic wavelength can be linearized, where the slope has been measured in [78] to be $\mathrm{d}\alpha'_{\mathrm{diff}}/\mathrm{d}\nu = -22\,\mathrm{mHz}/(E_{\mathrm{R,m}}\cdot\mathrm{GHz})$, given in frequency units. When considering an upper limit on the experimentally used potential depths of $50\,E_{\mathrm{R,m}}$ and the smallest used beam waist of about $100\,\mu$m and generous $R = 30\,\mu$m, the amplitude of the differential light shift over the full cloud size (left-hand side of equation (5.57)) values to 0.2 Hz/GHz. When this should stay small compared to $J_{ge}/h \simeq 0.2\,$kHz, the magic wavelength does not need to be more accurately set than about 100 GHz, corresponding to about $\delta\lambda \lesssim 0.2\,\mathrm{nm}$. This can be easily fulfilled using a standard wavemeter and the known value of the magic wavelength $\lambda_{\mathrm{magic}}^{\mathrm{meas}} = 759.3537\,\mathrm{nm}$ that has been measured in [133].

The situation is different when considering deviations from the ideal anti-magic wavelength for the state-dependent lattice along x direction. There the differential light shift is by construction on the order of twice the potential depth for each of the two states g and e due to the opposite signs in polarizability. As a result, a mismatch from the exact anti-magic value only reduces this shift without changing its order of magnitude. It is thus not necessary to precisely set the lattice laser at the anti-magic wavelength. To be more quantitative, the homogeneity condition on this much larger differential light shift has already been discussed above and is found to be ensured by transverse trapping frequencies on the order of $2\pi \times 10\,\mathrm{Hz}$.

For the lattice scheme itself, the main consequence would be that the potential depths V_g and V_e would not be equal. This would influence the overlap integral η_x, that determines the magnitude of J_{ge}, where the two Wannier functions would not be identical. However the value of η_x does not strongly depend on a difference in lattice depth ($\eta_x \approx 0.23$ for $V_g = V_e = 10\,E_{\mathrm{R,am}}$, whereas $\eta_x \approx 0.17$ for $V_g = V_e/2 = 10\,E_{\mathrm{R,am}}$, when using the approximated form 2.40). Therefore in principle even a factor of two difference in the polarizability magnitudes for g and e would not be problematic. For the anti-magic wavelength at about 617.5 nm, this would mean that the lattice wavelength does not need to be set more accurately than about ±10 nm.

5.2.9 Coupling laser: light shift and power stability

The fact that the coupling laser at 578 nm itself creates a differential light shift[19] between the g and e states also imposes constraints on the acceptable power fluctuations and transverse size of the coupling beams. This differential light shift has been measured in [78] to be on the order of $\kappa \approx 15\,\mathrm{mHz}/(\mathrm{mW/cm^2})$, as already pointed out in section 4.5.2. To achieve $J_{ge}/h \approx 0.2\,\mathrm{kHz}$ with the values as given in the benchmark table 5.1, a vacuum Rabi frequency of $\Omega_{\mathrm{Rabi}} \approx 2\,\mathrm{kHz}$ is needed. For this, a peak intensity of about $I_0 \approx 3 \times 10^5\,\mathrm{mW/cm^2}$ is required, when assuming a coupling magnetic field of $B = 200\,\mathrm{G}$ (see section 4.1). This corresponds to a central differential light shift (per coupling beam) of about 4.7 kHz, which constraints the acceptable amplitude of power fluctuations to below about 4 %.

Furthermore the inhomogeneity of the differential light shift due to the transverse envelope of the coupling beam needs to be limited to below J_{ge} over the size of

---

[19] In fact the experienced differential light shift at resonance is mainly due to the $^1\mathrm{S}_0$ state. The polarizability for the $^3\mathrm{P}_0$ state happens to have a zero crossing around 578 nm (see Appendix A).

the cloud. To ensure a variation smaller than 4 % over the cloud radius $R \approx 15\,\mu$m, the waist w_y of the coupling beam along y direction has to be chosen such that $w_y \gtrsim 7R \approx 110\,\mu$m. A reasonable choice would be for example $w_y \approx 150\,\mu$m, where the differential light shift change from the center of the cloud to the edge values to about 80 Hz per coupling beam. To achieve the intended peak intensity with a laser power of about ~ 10 mW per beam would then require to work with elliptically shaped beams, where the waist in z direction would need to be on the order of $w_z \approx 15\,\mu$m (meaning to have an aspect ratio of $w_y/w_x \approx 10$). This can be experimentally implemented using cylindrical optics.

One additional requirement on the coupling laser is that its linewidth needs to be small compared to J_{ge}. For the benchmark value of $J_{ge}/h = 0.2$ kHz, the laser linewidth would need to be reasonably well below 100 Hz. Achieving this, is one of the main challenges in the construction of the experiment as already discussed in chapter 4.

5.3 Anti-magic lattice and superlattice

In this section the possible experimental realization of the anti-magic and superposed double period lattice for flux rectification is discussed. It had been seen in section 5.1.2 that the relative phase between these two lattices needs to be tunable. The possible mechanisms to achieve this are explored from a theoretical point of view, followed by a discussion of possible experimental implementations. Afterwards the laser system for the two wavelengths at 612 nm and 1224 nm is briefly presented. With the achieved power levels it is found that some of the validity conditions presented in the previous section might be hard to be satisfied. Two possible ways to "boost" the reachable potentials depths are proposed to circumvent this problem. Finally a concrete scheme that combines the relative lattice phase tuning and power boosting is presented.

5.3.1 Theory of relative phase tuning between two lattices in retro-reflected configuration

It has been shown in section 5.1.2 that one way to rectify the simulated flux consists in using a superlattice configuration where a double period lattice is added to the state dependent lattice such that the intensities of the two lattices have the form

$$I_{\text{sup}} \propto \cos^2(k_{\text{am}}x/2 + \phi_{\text{rel}}), \quad I_{\text{am}} \propto \cos^2(k_{\text{am}}x)\,. \tag{5.58}$$

Important thereby is the relative phase ϕ_{rel} between the two lattices that determines the precise modulation of the on-site energies as described in section 5.1.2.

This phase needs to be experimentally tunable over a total range on the order of $\pi/2$, where in principle a static tunability (tuning from on run to another) is sufficient. The goal of the discussion in this section is to identify the possible ways to realize the control of this phase. For the discussion we will keep the notation using labels "am" for the "short period" and "sup" for the "long period" lattice, but this discussion has a very general character (valid outside the special case of an anti-magic wavelength).

In the following two superposed optical lattices are considered that are created by two retro-reflected plane waves with frequencies $\nu'_{\text{sup}} = c/\lambda'_{\text{sup}}$ and $\nu'_{\text{am}} = c/\lambda'_{\text{am}}$. The two frequencies ν'_{sup} and ν'_{am} are assumed to be the double of each other up to a small individual detuning of $\delta\nu_{\text{sup}} \ll \nu'_{\text{sup}}$ and $\delta\nu_{\text{am}} \ll \nu'_{\text{am}}$ away from the frequency doubled case, such that

$$\nu'_{\text{sup}} = \nu_{\text{sup}} + \delta\nu_{\text{sup}}\,, \quad \nu'_{\text{am}} = \nu_{\text{am}} + \delta\nu_{\text{am}}\,, \tag{5.59}$$

$$\nu_{\text{am}} = 2\,\nu_{\text{sup}}\,. \tag{5.60}$$

Both plane waves are considered to be retro-reflected by the same mirror which fixes a node for both lattices at the mirror position[20].

The quantity to consider in the following is the resulting intensity profile of the two lattice waves at a physical distance d from the retro-reflecting mirror. However, due to dispersive materials (glass) on the beam path, the optical distances d_{sup} and d_{am} seen by the two wavelengths might differ from d. This effect will be expressed as

$$d_{\text{sup}} = d + \delta d_{\text{sup}}, \quad d_{\text{am}} = d + \delta d_{\text{am}}\,, \tag{5.61}$$

where $\delta d_{\text{sup}}, \delta d_{\text{am}} \ll d$ denote the small corrections due to possible dispersion.

The resulting light intensity consists of the sum of two independent standing waves $I_{\text{total}} \simeq I_1 + I_2$, since interference effects between the two lattices can be neglected due to the large frequency difference $\nu'_{\text{am}} - \nu'_{\text{sup}} \simeq \nu'_{\text{sup}}$. The standing wave intensities at a physical distance d, using equations (5.61), then read

$$I_{\text{sup}} \propto \cos^2\left[k'_{\text{sup}}(d + \delta d_{\text{sup}})\right]\,, \quad I_{\text{am}} \propto \cos^2\left[k'_{\text{am}}(d + \delta d_{\text{am}})\right]\,, \tag{5.62}$$

with the wave vectors $k'_{\text{sup}} = 2\pi\nu'_{\text{sup}}/c$ and $k'_{\text{am}} = 2\pi\nu'_{\text{am}}/c$. The arguments of the $\cos^2$ functions can be developed using equation (5.59) to

$$k'_{\text{sup}}(d + \delta d_{\text{sup}}) \approx k_{\text{sup}} d + \frac{2\pi}{c}(\nu_{\text{sup}}\delta d_{\text{sup}} + \delta\nu_{\text{sup}} d)\,, \tag{5.63}$$

$$k'_{\text{am}}(d + \delta d_{\text{am}}) \approx k_{\text{am}} d + \frac{2\pi}{c}(\nu_{\text{am}}\delta d_{\text{am}} + \delta\nu_{\text{am}} d)\,, \tag{5.64}$$

---

[20] In the case of an ideal mirror the node positions are equal. For a dielectric mirror, however, the effective node positions might slightly differ, due to the multilayer structure of the reflection coating. This can lead to an additional static phase shift between the lattices. For the phase tuning considerations in this section, this static phase shift is irrelevant since it can be compensated once and for all and will be silently omitted in the following.

where we neglect small terms $\delta\nu_{\mathrm{sup}}\delta d_{\mathrm{sup}}$ and $\delta\nu_{\mathrm{am}}\delta d_{\mathrm{am}}$. The intensities then can be rewritten as

$$I_{\mathrm{sup}} \propto \cos^2(k_{\mathrm{am}}d/2 + \phi_{\mathrm{sup}}), \quad I_{\mathrm{am}} \propto \cos^2(k_{\mathrm{am}}d + \phi_{\mathrm{am}})\,, \tag{5.65}$$

with $\phi_{\mathrm{sup}} \equiv 2\pi(\nu_{\mathrm{sup}}\delta d_{\mathrm{sup}} + \delta\nu_{\mathrm{sup}}d)/c$ and $\phi_{\mathrm{am}} \equiv 2\pi(\nu_{\mathrm{am}}\delta d_{\mathrm{am}} + \delta\nu_{\mathrm{am}}d)/c$ the phases for each lattice part. In this form we basically treat the two standing waves as if they were in the ideal frequency doubled case and where we have absorbed effects due to dispersion and a "detuning" away from the frequency doubled case into the (position dependent) phases ϕ_{sup} and ϕ_{am}.

To be able to compare these expressions with the desired ones from equations (5.58), we have to transform these relations such that the phase appears only on the double period lattice part. To achieve this, ϕ_{am} can be eliminated from the anti-magic lattice by a local coordinate recentering to the closest node of the anti-magic lattice[21] that yields

$$I_{\mathrm{sup}} \propto \cos^2(k_{\mathrm{sup}}d + \phi_{\mathrm{sup}} - \phi_{\mathrm{am}}/2), \quad I_{\mathrm{am}} \propto \cos^2(k_{\mathrm{am}}d)\,. \tag{5.66}$$

This now has the intended form and allows one to identify the relative lattice phase as defined in equation (5.58) as $\phi_{\mathrm{rel}} = \phi_{\mathrm{sup}} - \phi_{\mathrm{am}}/2$ and therefore

$$\boxed{\phi_{\mathrm{rel}}(d) = \frac{2\pi}{c}\Big[\nu_{\mathrm{sup}}\,(\delta d_{\mathrm{sup}} - \delta d_{\mathrm{am}}) + d\,(\delta\nu_{\mathrm{sup}} - \delta\nu_{\mathrm{am}}/2)\Big]}\,. \tag{5.67}$$

Here the first term describes the effect that the relative phase is changed when tuning the differential optical path length of $\delta d_{\mathrm{sup}} - \delta d_{\mathrm{am}}$. The second term describes the effect that a non-zero detuning from the frequency doubled case of $\delta\nu_{\mathrm{sup}} - \delta\nu_{\mathrm{am}}/2$ leads to a change in relative phase that depends linearly on the propagation distance d of the two standing waves from the retro-reflecting mirror.

From this, the possible ways to control the relative lattice phase can be identified:

- **Propagation phase:** Controlling the relative phase due to propagation that appears in the case of a non-zero "detuning" $\delta\nu_{\mathrm{sup}} - \delta\nu_{\mathrm{am}}/2$ away from the frequency doubled situation (see Figure 5.6). One way to tune this is by changing the frequency "detunings" of the two lasers, where the effect of $\delta\nu_{\mathrm{sup}}$ and $\delta\nu_{\mathrm{am}}$ differ by a factor of two. The other way is to vary the distance d_{atoms} between retro-reflecting mirror and atoms, while having a fixed non-zero "detuning" $\delta\nu_{\mathrm{sup}} - \delta\nu_{\mathrm{am}}/2$.

---

[21] This transformation corresponds to $k_{\mathrm{am}}d \to k_{\mathrm{am}}d - \phi_{\mathrm{am}}$ and therefore $k_{\mathrm{am}}d/2 \to k_{\mathrm{am}}d/2 - \phi_{\mathrm{am}}/2$. This is equivalent to a coordinate recentering to a node of the anti-magic lattice, where it is to note that in the case of position dependent phases $\phi_{\mathrm{am}}(d)$ and $\phi_{\mathrm{sup}}(d)$, this transformation is only locally possible.

- **Discrete phase shifts using optical elements:** Introducing an optical element between retro-reflecting mirror and atoms that allows to change the differential optical path length $\delta d_{\rm sup} - \delta d_{\rm am}$ (see Figure 5.7). This is independent of the frequency detunings within the approximations done.

It is worth mentioning that in the case where the light for the short period lattice is generated in a frequency doubling scheme from the long period lattice, the effect of a frequency shift of the long period light before frequency doubling ($\nu_{\rm sup} \to \nu_{\rm sup} + \delta\nu_{\rm sup}$ and therefore $\nu_{\rm am} \to \nu_{\rm am} + 2\delta\nu_{\rm sup}$) has no effect on $\phi_{\rm rel}$.

5.3.2 Implementing relative phase tuning experimentally

In this section the possible experimental implementations for the relative lattice phase tuning are discussed based on the results on possible tuning mechanisms obtained in the previous section. For this, both lattices are assumed to be retro-reflected by the same mirror. The most important parameters to compare the different methods are the total available tuning range of phase (static and dynamic), the effort for the experimental implementation and power loss for the lattice beams. Furthermore the sensitivity of the phase to external perturbations like vibrations and changes in the ambient temperature are additional measures for comparison. It is to note that the relative phase tuning range need not to be larger than $\pi/2$ for the phase as defined in equations (5.13) and (5.14). Phase fluctuations $\delta\phi_{\rm rel}$ should stay smaller than about 1°, as motivated in section 5.2.6.

Detuning-controlled lattice phase

The first way to change the relative lattice phase $\phi_{\rm rel}$ consists in changing the frequency detunings $\delta\nu_{\rm sup}$ and $\delta\nu_{\rm am}$ away from the ideal frequency doubled case on the two lattice parts (see illustration in Figure 5.6). The dependence of the relative lattice phase on these detunings is given by [see equation (5.67)]

$$\Delta\phi_{\rm rel} = \frac{2\pi}{c}(\delta\nu_{\rm sup} - \delta\nu_{\rm am}/2)\, d\,. \tag{5.68}$$

Important for this way of tuning is the distance $d_{\rm atoms}$ of the atomic cloud from the retro-reflecting mirror which is typically on the order of tens of centimeters. Assuming $d_{\rm atoms} = 20\,\rm cm$ the detuning changes needed to achieve a phase shift of $\pi/2$ are about $\delta\nu_{\rm sup} - \delta\nu_{\rm am}/2 \approx 400\,\rm MHz$.

When working with two independent laser systems for the two lattices, this can be achieved using a frequency offset lock for the two lasers with tunable offset frequency[22]. This technique is for example used in [134]. Like this, usually detun-

---

[22] For this the double period lattice light has to be frequency doubled and the beatnote frequency with the anti-magic lattice electronically stabilized.

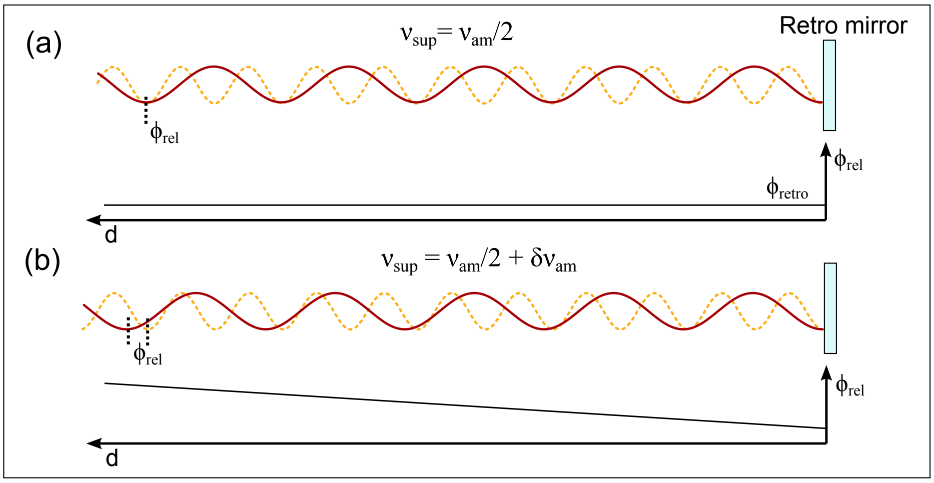

Figure 5.6: Illustration of the relative phase tuning between the short (yellow dashed) and long period lattice (red solid) using a frequency detuning away from the frequency doubled case. In the case without detuning (a) the relative phase stays constant in space. In the case of a small detuning (b), the spatially varying phase slip leads to a change of relative phase at a given distance from the retro-reflecting mirror.

ing scanning ranges on the order of a GHz can be achieved. The relative lattice phase stability then relies on the quality of the offset lock.

In the case where the two lattice laser frequencies are not independent (like for example in a frequency doubling scheme that is used in our experiment), the needed tuning range could be realized using large bandwidth acousto-optical modulators. Typical AOMs on the market can have single pass bandwidths of about 100 MHz with a central frequency on the order of 350 MHz to 500 MHz. When using double pass configurations on both lattice arms, a total detuning of $\delta\nu_{\mathrm{sup}} - \delta\nu_{\mathrm{am}}/2 \approx$ 300 MHz could be reached. The convenience of this method would be that ϕ_{rel} can be fully controlled by electrical means without changing the actual optical lattice setup. However the large AOM bandwidth is normally at the cost of a reduced diffraction efficiency and the specified single pass efficiencies are typically on the order of 70 % at 612 nm, but only 30 % for about 1224 nm. Accordingly this would be a quite power costly method, which is problematic in our setup where the available power is limited (as will be seen in section 5.3.4).

Distance-controlled lattice phase

A second option is to have a fixed non-zero detuning $\delta\nu_{\mathrm{sup}} - \delta\nu_{\mathrm{am}}/2$ and to tune the distance d_{atoms} between atoms and retro-reflecting mirror. For this case the phase slip $\Delta\phi$ per distance change Δd is given by

$$\frac{\Delta\phi_{\mathrm{rel}}}{\Delta d} = \frac{2\pi}{c}(\delta\nu_{\mathrm{sup}} - \delta\nu_{\mathrm{am}}/2)\,. \tag{5.69}$$

Assuming a combined detuning of $\delta\nu_{\mathrm{sup}} - \delta\nu_{\mathrm{am}}/2 \approx 500\,\mathrm{MHz}$, the phase gradient calculates to

$$\frac{\Delta\phi_{\mathrm{rel}}}{\Delta d} \approx 6\,^\circ/\mathrm{cm}\,. \tag{5.70}$$

A phase change of $\pi/2$ would be realized by a distance change of about 15 cm. Displacing the retro-mirror over such a long distance is experimentally quite inconvenient since it would require a realignment of the reflected lattice beams every time the phase is changed. Although this method could be useful for coarse tuning, we rejected it as a sole control of ϕ_{rel}.

Differential path length controlled lattice phase

The third possibility is to place a transmissive optical element between retro-reflecting mirror and atoms that allows to tune the differential optical path length $\delta d = \delta d_{\mathrm{sup}} - \delta d_{\mathrm{am}}$ between the two lattice wavelengths. The amount of phase change induced by this is given by [see equation (5.67)]

$$\Delta\phi_{\mathrm{rel}} = \frac{2\pi\nu_{\mathrm{sup}}}{c}\delta d\,. \tag{5.71}$$

In general the optical path length for light passing a transmissive optical element is determined by the product of the index of refraction $n(\lambda)$ and the physical length L the light passes within the optical element. The differential optical path length between two beams at different wavelengths is therefore determined by the differential index of refraction $\Delta n_{\lambda_{\mathrm{am}},\lambda_{\mathrm{sup}}} = n(\lambda_{\mathrm{am}}) - n(\lambda_{\mathrm{sup}})$ and reads

$$\delta d = L\,\Delta n_{\lambda_{\mathrm{am}},\lambda_{\mathrm{sup}}}\,. \tag{5.72}$$

From this it becomes apparent that δd can be tuned by either changing the physical path length L while having $\Delta n_{\lambda_{\mathrm{am}},\lambda_{\mathrm{sup}}} \neq 0$, or by changing $\Delta n_{\lambda_{\mathrm{am}},\lambda_{\mathrm{sup}}}$ with fixed physical path length L. Two possible ways to achieve this are presented next.

Etalon tuning: One way where only the physical length of the optical element is changed is by placing an AR[23]-coated etalon between the retro-reflecting mirror and the atoms (see Figure 5.7). When changing the angle α of the etalon

---

[23] AR = anti-reflection.

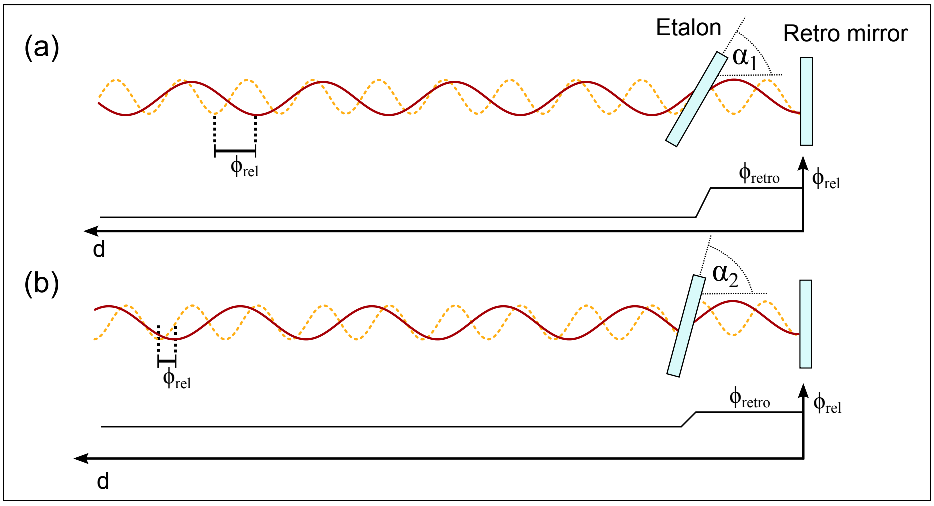

Figure 5.7: Illustration of the relative phase tuning between the short (yellow dashed) and long period lattice (red solid) using the tilting angle of an etalon within the beam path.

with respect to the beam propagation axis, the path length within the glass substrate changes. In the case of a non-zero differential refractive index $\Delta n_{\lambda_{\mathrm{am}},\lambda_{\mathrm{sup}}} = n(\lambda_{\mathrm{am}}) - n(\lambda_{\mathrm{sup}})$, also δd and therefore the relative lattice phase is changed. The physical path length for passing the etalon L_{eff} as a function of the angle of incidence α is given by

$$L_{\mathrm{eff}}(\alpha, \lambda) = \frac{t_0}{\sqrt{1 - \frac{\sin^2(\alpha)}{n(\lambda)^2}}}\,, \tag{5.73}$$

where t_0 is the physical thickness of the etalon. Some typical results for the relative lattice phase tuning capabilities in the case of a fused silica etalon are shown in Figure 5.8, for the considered lattice beam wavelengths of 612 nm and 1224 nm.

The sensitivity of the phase tuning depends on the thickness of the etalon, where for $t_0 = 2\,\mathrm{mm}$ a $\pi/2$ phase tuning range is realized by changing the etalon angle from 0 ° to about 15 °, whereas for $t_0 = 1\,\mathrm{mm}$ angles up to about 20 ° would be needed. The needed range in etalon angle tuning seems to be reasonable to realize experimentally and corresponds roughly to the acceptance angle of typical AR-coatings. The needed precision for the positioning of the etalon angle would be typically on the order of 0.1 ° to achieve a relative phase tuning accuracy of 1°, in the case of $t_0 = 2\,\mathrm{mm}$. This is well within the specifications of commercially available rotation stages (manual and motorized).

The main advantage of this method with respect to the previously presented one, using a propagation phase, is that the power loss on the lattice beams is

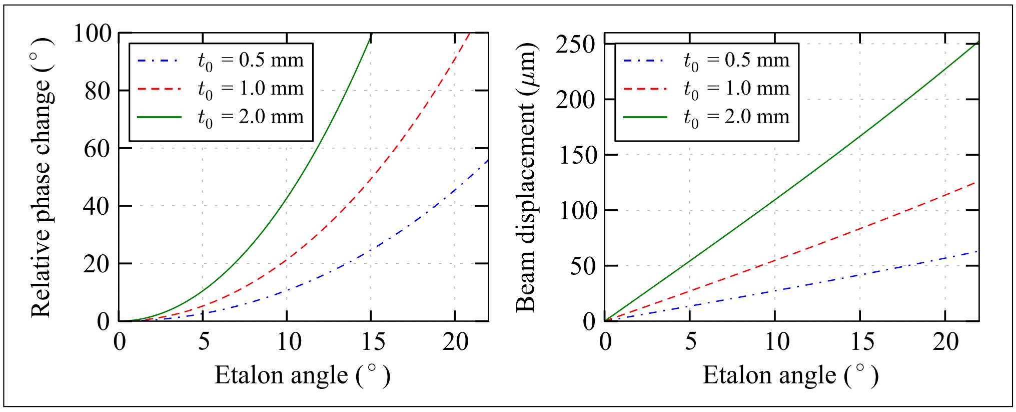

Figure 5.8: On the left-hand side the change of the relative lattice phase as a function of the angle of incidence on a fused silica etalon of thickness t_0 is shown. The considered lattice wavelengths are 612 nm and 1224 nm, where the differential refractive index for fused silica at room temperature is $\Delta n_{612,1224} = 0.98 \times 10^{-2}$ (see Table 5.4). On the right-hand side the transverse beam displacement for the beam when passing a fused silica etalon (for 1224 nm) is shown.

only determined by the residual reflectivity of the AR-coating which can be well below 1 %. Concerning the relative phase tuning, in principle no AOMs would be necessary and the full available laser power could be used. However a disadvantage of this method is that the etalon introduces a transverse displacement $\Delta_\perp(\alpha, \lambda)$ of the lattice beam that depends on the etalon angle via

$$\Delta_\perp(\alpha, \lambda) = t_0 \sin(\alpha) \left[1 - \frac{\cos(\alpha)}{\sqrt{n(\lambda)^2 - \sin^2(\alpha)}} \right] . \tag{5.74}$$

Typical displacements as a function of the angle are also shown in Figure 5.8. It can be seen that depending on the thickness of the etalon the displacements[24] might not be negligible compared to the lattice beam sizes that will typically have a waist on the order of 300 μm in our case. However, in the case where a flat mirror is used for retro-reflection this effect is in principle cancelled out since the retro-reflected beam has passed the etalon twice before arriving again at the atoms. Nevertheless this effect will become important in the discussions in section 5.3.5.

Temperature tuning: One way to change $\Delta n_{\lambda_{\mathrm{am}},\lambda_{\mathrm{sup}}}$ is to make use of the different temperature dependence of the refractive indices for the two lattice wave-

---

[24] The differential displacement between the two lattice beams at 612 nm and 1224 nm is typically found to be less than 10 μm and therefore negligible.

Material	$\Delta n_{612,1224}$ $\times 10^{-2}$	$\frac{\mathrm{d}}{\mathrm{d}T}\Delta n_{612,1224}$ $\times 10^{-7}/^\circ\mathrm{C}$	$\alpha_{\mathrm{thermExp}}$ $\times 10^{-6}$	$\frac{\mathrm{d}}{\mathrm{d}T}\phi_{\mathrm{rel}}$ $^\circ/\mathrm{cm}^\circ\mathrm{C}$
Fused Silica	0.98	4.6	0.55	1.4
BK7	1.1	3.9	7.1	1.4
Air	0.0003	0.1(3)	-	$0.03(9)^*$

Table 5.4: Table of typical values connected to the temperature tuning of the relative lattice phase. The differential refractive indices $\Delta n_{612,1224}$ and their temperature derivative around room temperature are determined using [135] (fused silica) and [136] (BK7). For air the computations are done for a pressure of 101.325 kPa and a relative humidity of 50% using [137]. The temperature derivatives $\frac{\mathrm{d}}{\mathrm{d}T}\Delta n_{612,1224}$ are verified to not vary by more than a factor of two in the range of 20°C to 50°C. The thermal expansion coefficients are taken from [138] and [139]. *Not taking pressure changes into account.

lengths. By changing the temperature of an optical element, placed between the retro-reflecting mirror and the atoms, the differential optical path length and therefore the relative lattice phase can be changed. In Table 5.4 some numerical values for the temperature dependence of the differential refractive index for typical materials are given. However, when changing the temperature of the optical element, not only the refractive indices are influenced but also the physical size of the element, which is described by the thermal expansion coefficient $\alpha_{\mathrm{thermExp}} = \Delta L/L$. Both effects lead to a change in relative lattice phase, though the temperature dependence of the refractive indices is the dominant effect for the two considered glasses. The typical sensitivity of the relative lattice phase on the temperature and physical thickness of the optical element is given in the last column of Table 5.4. It can be seen that for a 1 cm thick fused silica etalon, for example, temperature changes on the order of 60 °C would be necessary to achieve a $\pi/2$ phase shift.

The obtained results in temperature sensitivity are also important to estimate the achievable relative phase stability. It can be seen that each transmissive optical element that is placed between the atoms and the retro-reflecting mirror contributes to a higher phase sensitivity to ambient temperature fluctuations. The temperature stability in our laboratory over a full day is typically on the order of 1 °C. When relative phase changes should be kept below 1 °, as motivated in section 5.2, the accumulated thickness of all optical elements between atoms and retro-reflecting mirror should be ideally below 1 cm (viewports, lenses, etc..). From the values in Table 5.4 it can also be seen that for large distances between retro-reflecting mirror and atoms ($\sim$ 1 m) even the free propagation in air might have considerable influence on the temperature sensitivity of the relative phase.

5.3.3 Laser system at 612 nm and 1224 nm

In order to create the needed lattice depths for the anti-magic and double period lattice, powerful laser sources at 612 nm and 1224 nm are necessary. In general one has the choice to either use two independent laser sources at 612 nm and 1224 nm or to create the 612 nm by frequency doubling starting from a laser at 1224 nm. In the former case the frequency difference of the two lasers needs to be electronically stabilized in order to guarantee a well-defined and controlled phase relation in the superlattice[25] (like used in [134]). In the latter case the two wavelengths automatically have a fixed phase relation and frequency or phase fluctuations are mostly common mode.

The solution chosen[26] for this experiment is to use a laser system consisting of a commercial laser diode with tapered amplifier system[27] at 1224 nm that delivers about 600 mW of output power. The 612 nm light is created in a second harmonic generation scheme in a non-linear ppLN[28] crystal of $L = 2\,\mathrm{cm}$ length as sketched in Figure 5.9. The crystal is placed within a bow-tie type enhancement cavity in order to increase the doubling efficiency. When using the full 600 mW of infrared light, a frequency doubled power of 430 mW is reached. The non-doubled infrared light is mainly reflected/lost on the cavity incoupling mirror ($\sim 100\,\mathrm{mW}$) and can be reused for the creation of the double period lattice, like sketched in Figure 5.9, where the power requirements are more relaxed. However with these power levels it is not straightforward to reach the desired lattice parameters as will be discussed in the next section.

5.3.4 Overcoming power issues

The discussion in section 5.2.5 has shown that the needed lattice depths for the anti-magic and double period lattice are on the order of $V_e \sim 10\,E_{\mathrm{R,am}}$ and $W_g \sim 3\,E_{\mathrm{R,sup}}$ respectively. At the same time the transverse confinements should stay small to avoid effects of inhomogeneity. It has been found that for both lattices $1/e^2$ beam radii on the order of $300\,\mu\mathrm{m}$ (or larger) at the position of the atoms would be necessary. The accordingly needed beam powers for these waists are about 1.3 W for 612 nm and about 100 mW for 1224 nm.

---

[25] This requires frequency doubling of the 1224 nm light in order to get a beat note signal with the 612 nm light. This beat note frequency can then be electronically stabilized by feeding back to one of the two laser frequencies. The stability of the relative lattice phase in this case might be limited by the quality of this frequency offset lock.

[26] Other options were available based on an optical parametric oscillator (OPO) or a Raman laser system but which were quite pricey compared to the chosen solution, without providing significantly higher power levels.

[27] TA-Pro, Toptica.

[28] Periodically poled lithium niobate.

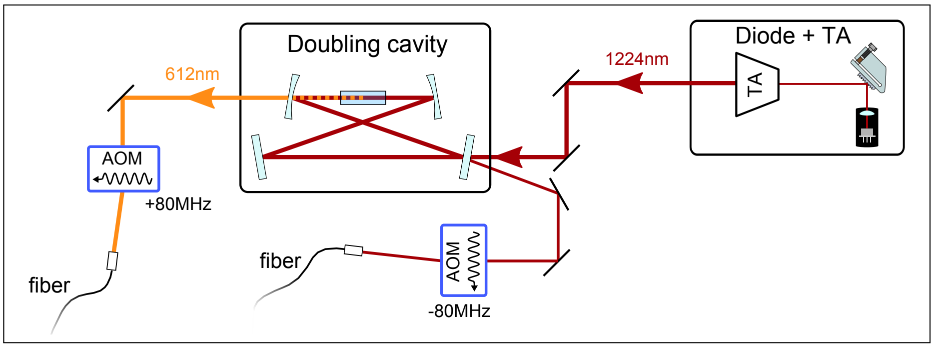

Figure 5.9: Sketch of the laser setup for the 612 nm and 1224 nm light for the anti-magic and double period lattice. The light source at 1224 nm is a laser diode plus tapered amplifier (TA) system.

The currently available power with the laser system as described in the previous section, however is more on the order of 200 mW for 612 nm and on the order of 50 mW for 1224 nm (including losses on fiber couplings, AOMs and dynamic range for power stabilization). This means that we need to find a mean in order to "boost" the light power or the achievable lattice depths by a factor on the order of 10 (including some safety margin). In principle there are two main solutions, namely to use elliptically shaped beams or to enhance the power in a resonance cavity. Both options are discussed in the following.

Elliptic beams

The fact that the atomic cloud will be strongly confined along the vertical z-direction allows to work with highly anisotropic lattice beams, since the constraints on the transverse harmonic confinements are primarily important along the y axis. In order to gain the needed power enhancement factor while keeping the waist along the y direction constant, an aspect ratio of about 10 for the lattice waists needs to be realized. This can for example be implemented using cylindrical optics. In Table 5.5 typical configurations are shown that would lead to the benchmark parameters in tables 5.1 and 5.2. The found values lie within the experimentally feasible.

However, for reasons of stability of the relative lattice phase, the lattice beams of the two wavelengths have to be reflected by the same retro-reflecting mirror and have to partially pass the same optics. For the waists as given in Table 5.5, the Rayleigh lengths for the z component will be on the order of several millimetres only. Under these circumstances the alignment and mode matching of the forth and back going lattice beams in the retro-reflected configuration might be trou-

$\lambda\,(\mathrm{nm})$	$P\,(\mathrm{mW})$	$w_y\,(\mu\mathrm{m})$	$w_z\,(\mu\mathrm{m})$	$\omega_y/2\pi\,(\mathrm{Hz})$	$z_\mathrm{R}^z\,(\mathrm{mm})$
612	130	300	30	10	4.6
1224	20	400	40	3	4.1

Table 5.5: Typical parameters for elliptic beams with aspect ratios of w_y/w_z =10, to reach the benchmark values from tables 5.1 and 5.2. The beam waists at the atoms position along y and z are denoted by w_y and w_z respectively. The values for ω_y correspond to the trap frequencies along y direction for each laser individually, where the stronger one with respect to the states g and e is shown. The quantity z_R^z denotes the Rayleigh length corresponding to w_z.

blesome since they cannot be performed fully independently for both wavelengths. Furthermore one has to take care that the ellipticity axis needs to be well aligned with the 2D plane of the atomic cloud. Possible tilts could result in an increase of the trapping frequency along y due to the mixing with the stronger confined z component. In spite of these experimental complications, this method should work for large enough aspect ratios of the waists w_y/w_z.

Enhancement cavity

A second option to overcome the mentioned power issues would be to create the lattice within an optical cavity, where the intracavity power build-up could be used to achieve the needed lattice depths. In its simplest form this cavity would consist of two mirrors that are placed on two opposite sides of the vacuum chamber as sketched in Figure 5.10. When the incoming light is in resonance with a cavity mode, a power build-up of the circulating intracavity power P_cav is achieved. The enhancement is characterized by the so-called build-up factor, defined as the ratio of P_cav to the power incident on the cavity P_in, that is given by

$$\frac{P_\mathrm{cav}}{P_\mathrm{in}} = \frac{\gamma\,(1-R_\mathrm{in})}{\left[1-\sqrt{R_\mathrm{in}(1-Q)}\right]^2}\,, \tag{5.75}$$

where R_in denotes the reflectivity of the incoupling mirror and Q summarizes all other passive intra-cavity losses experienced on a full cavity round trip (including the retro-reflecting mirror). The factor $\gamma \leq 1$ takes an imperfect coupling of the incident beam to the transverse cavity eigenmode into account. The maximum achievable build-up factor is mainly determined by the intracavity losses Q.

Some typical achievable build-up factors are shown in Figure 5.11 for a variety of intracavity losses Q. It can be seen that the needed build-up factor on the order of 10 can be attained when having intracavity losses on the order of 10 % or below.

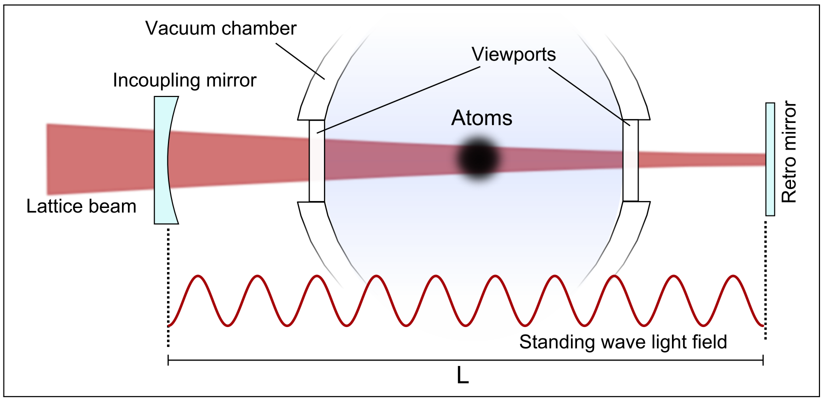

Figure 5.10: Sketch of a setup to realize an enhancement cavity for an optical lattice. In this example a plano-concave cavity design is shown as considered in the discussion in the text.

Typically the only elements that can cause intracavity losses are the viewports attached to the vacuum chamber and other optical elements within the cavity. Assuming to have reasonably good anti-reflection (AR) coatings for all intracavity optics, values of $Q < 10\,\%$ could be achievable. For example for two intracavity viewports with AR-coatings of $R = 0.5\,\%$ per surface, the corresponding full round trip losses would be $Q \approx 4\,\%$, when assuming a perfect retro-reflecting mirror with unity reflectivity. With this, a build-up factor up to 25 could be reached (assuming $\gamma = 1$).

The cavity itself could be realized in a biconvex or plano-convex design. Using a plano-concave cavity, the resonator stability criterion is $|m| < 1$ with $m = 1-2L/\rho$ [121], where L is the distance between the two cavity mirrors and ρ the radius of curvature of the concave mirror. The beam waist in a plano-concave cavity is situated on the plane mirror and values to [121]

$$w_0^2 = \frac{\lambda L}{\pi}\sqrt{\frac{\rho}{L} - 1}\,. \tag{5.76}$$

In Table 5.6 typical cavity parameters are shown, for an example cavity length of $L = 35\,\text{cm}$, that would lead to reasonable beam sizes for 612 nm and 1224 nm. Due to the very long Rayleigh length z_R the increase in beam size between retro-reflecting mirror and atoms would be small, when having the atoms in the center of the cavity.

The estimated values suggest that also this solution might be reasonable to implement. However, since the enhancement of only one of the wavelengths within the cavity might not be sufficient, one might think of having a cavity that is

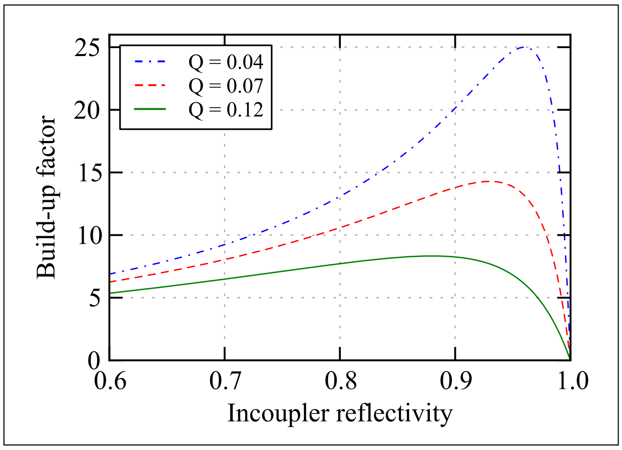

Figure 5.11: Cavity build-up factor as a function of incoupler reflectivity for different values for intracavity losses Q. For the calculations a perfect cavity coupling, $\gamma = 1$, is assumed.

L(m)	ρ(m)	w_0^{612}(μm)	w_0^{1224}(μm)	z_{R}(m)	m
0.35	0.75	270	382	0.37	0.1
0.35	1.0	305	431	0.48	0.3
0.35	2.0	384	544	0.71	0.7

Table 5.6: Typical beam parameters for a stable plano-concave resonance cavity.

resonant for both wavelengths. This case is considered in the next section, where also the problem of locking the light to a cavity resonance is addressed.

5.3.5 Scheme for power enhancement and relative lattice phase tuning in a doubly-resonant cavity

As discussed in the previous section, we can boost the achievable lattice depths to the desired values by either using elliptically shaped lattice beams or by placing a resonance cavity around the vacuum chamber. In the resonance cavity case it had been seen, that the cavity build-up should be achieved for both wavelengths creating the superlattice (612 nm and 1224 nm) at the same time. In addition the relative phase between the two lattices needs to be tunable at the atoms position. Although the implementation of a doubly-resonant enhancement cavity seems to be the more complicated solution, we will concentrate on its possible implementation in this section. As we will see, the doubly-resonant cavity offers a main conceptual advantage over the elliptical beam solution: One can directly monitor changes in the relative phase of the two lattices when scanning the cavity resonances.

In the following the setup we plan to implement is presented that allows to achieve the doubly-resonant case and relative phase tuning at the atoms position, using an optical cavity with intracavity etalons.

Having two wavelengths resonating in the same cavity

The first point that needs to be clarified is the condition to have two different wavelengths λ_{am} and λ_{sup} resonating in the same cavity. The general condition for resonance is that the optical distance of the cavity mirrors L_{opt} is a multiple of half the considered light wavelength, $L_{\mathrm{opt}} = m\lambda/2$, with positive integer m. Since the optical length of the cavity can be different for the two considered wavelengths (due to dispersive intracavity optics) the condition is a priori not fulfilled for both wavelengths at the same time, even in the frequency doubled case. To be able to bring two arbitrary wavelengths into resonance for a given physical cavity length, one needs a way to tune the differential optical path length seen by the two laser beams.

Alternatively one can also think in terms of the relative phase ϕ_{rel} between the two created standing waves. The retro-reflecting cavity mirror fixes a certain phase relation ϕ_{retro} for the two standing waves at its position. Along the propagation in the cavity, back to the incoupling mirror, the two standing waves get dephased due to propagation or dispersion (see section 5.3.1). In order to bring both waves in resonance with the cavity, one simply has to set the "right" relative phase ϕ_{cav} at the incoupling mirror position, corresponding to setting a node for both waves at the mirror position. In this picture it becomes clear, that to bring both waves into simultaneous resonance one simply has to find a mean to tune the relative phase between the two standing waves. Therefore all the methods for relative phase tuning as presented in section 5.3.2 can be applied to achieve the doubly-resonant case (etalon angle, etalon temperature, frequency detuning, etc.).

To illustrate this point of view further, the transmission peaks of the cavity when changing the cavity length L are sketched in Figure 5.12, for the particular case of having 612 nm light and 1224 nm light injected into the cavity. Resonances appear twice as often for the 612 nm light at lengths L_n as compared to the 1224 nm light at lengths L_m. The distance change between neighbouring peaks $L_m - L_{m-1} = \lambda_{\mathrm{sup}}/2$ and $L_n - L_{n-1} = \lambda_{\mathrm{am}}/2$ correspond to the free spectral range of the cavity with respect to each wavelength. Tuning the relative phase between the two standing waves in this picture is exactly the same as moving the cavity resonances with respect to each other. In fact the distance $L_m - L_n$ between neighbouring peaks of the two wavelengths can be directly mapped to the relative phase between the two standing waves. In the phase definition as given in equa-

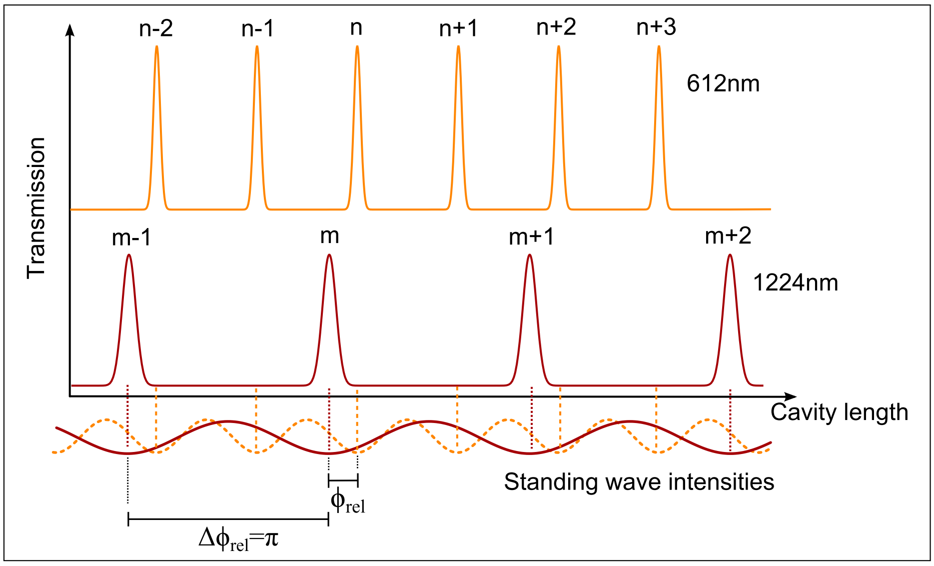

Figure 5.12: Sketch of the transmission peaks for two lattice wavelengths when changing the cavity length for a generic relative phase between the two at the cavity entrance mirror. Peaks at 612 nm appear twice as often as the ones for the 1224 nm light. The free spectral range for the 1224 nm part can be mapped to a relative phase change of $\Delta\phi_{\text{rel}} = \pi$.

tions (5.13) and (5.14) the distance between neighbouring peaks of the 1224 nm wave $L_m - L_{m-1}$ corresponds to a relative phase shift of π. Achieving the doubly-resonant case requires thus to tune the relative phase between the two standing waves such that the resonance peaks appear at the same position (e.g. $L_m = L_n$). The needed tuning range for the relative phase in the worst case would be $\pi/2$.

The optical setup

Knowing the principle how both wavelengths can be brought to simultaneous resonance in the cavity, we can now extend the idea to the supplementary freedom to set an arbitrary relative lattice phase at the position of the atoms, that will be denoted by ϕ_{atoms} in the following. For this the setup as sketched in Figure 5.13 can be used, where two intracavity etalons are present. The first one (etalon 1) allows us to set the intended relative lattice phase at the atoms position ϕ_{atoms}. The second etalon (etalon 2), placed between incoupling mirror and atoms, enables us to independently set the relative phase at the incoupling mirror ϕ_{cav} to achieve simultaneous resonance for both wavelengths.

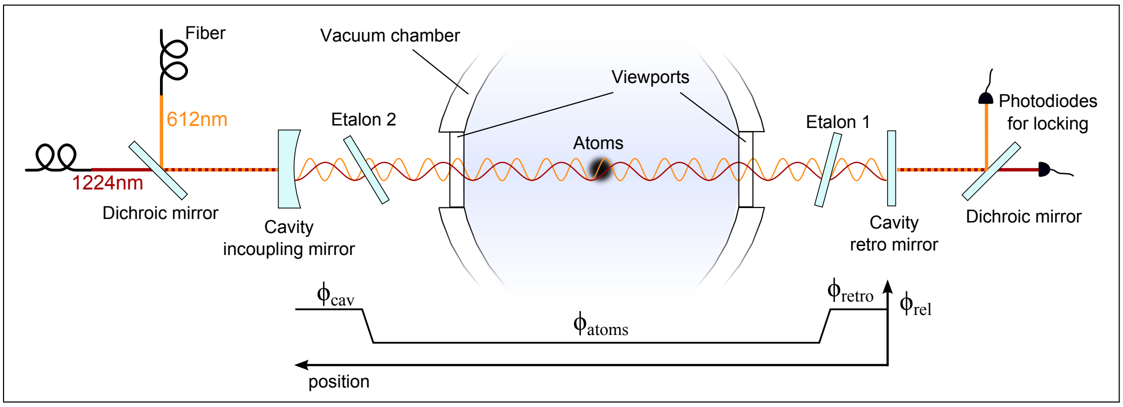

Figure 5.13: Sketch of the setup for a superlattice in a doubly-resonant cavity including relative lattice phase tuning. In the lower part of the image the spatial variation of the relative lattice phase is illustrated in the case of $\nu_{\mathrm{am}} = 2\nu_{\mathrm{sup}}$, not accounting for the effect of the viewports on ϕ_{rel}.

In terms of cavity build-up factor, the intracavity losses Q would be determined by reflection losses on two viewports and two etalons. For the etalons and viewports that we plan to use, the total reflection losses on a full round trip are measured to be $Q_{1224} \approx 12\,\%$ and $Q_{612} \approx 8\,\%$ and build-up factors of about 8 and 12 are expected.

The fact to have both wavelengths resonating in the same cavity setup fixes the size of the transverse mode of one lattice beam with respect to the other to $w_0^{1224} = \sqrt{2}\, w_0^{612}$. Some realistic example parameters that would lead to the desired lattice depths from tables 5.1 and 5.2 are shown in Table 5.7 for the expected build-up factors.

A possible drawback of this setup is that when tuning the angle of "etalon 2", the lattice beams experience a small displacement that changes the beam alignment with respect to the atoms position. The angle sensitivity of the displacement depends on the etalon thickness and values for a 2 mm thick fused silica etalon to about $11\,\mu\mathrm{m}/^\circ$ (see Figure 5.8). This effect should in principle not influence the cavity alignment since it is compensated when passing the etalon twice in opposite directions.

One of the big advantages of the doubly-resonant cavity setup is that the relative phase between the two lattices can directly be observed when scanning the cavity resonances via the cavity length (or the frequency of the 1224 nm light before frequency doubling), as illustrated in Figure 5.12. Although this will not directly yield the absolute value of the relative phase at the atoms position, it will nevertheless enable one to monitor drifts and changes in the relative phase.

λ (nm)	ρ (m)	P_{in} (mW)	Build-up	w_0 (μm)	w_{atoms} (μm)	$\omega/2\pi$
612	1	160	12	305	357	8.7 Hz
1224	1	35	8	431	504	2.3 Hz
612	0.75	135	12	270	327	9.6 Hz
1224	0.75	30	8	382	463	2.5 Hz

Table 5.7: Typical parameters of the cavity enhancement setup to achieve the desired lattice parameters at the atoms position for different radii of curvature ρ of the incoupling mirror. The cavity length is assumed to be $L = 35$ cm and the atomic cloud considered to be in the middle. The quantity w_0 corresponds to the waist on the flat retro-reflecting mirror and w_{atoms} to the $1/e^2$ radius at the atoms position. The values for ω correspond to the trap frequencies at the atoms position for each laser individually, where the stronger one with respect to the states g and e is shown.

This information would otherwise only be accessible by performing rather involved experiments with cold atoms in the superlattice potentials, whose interpretation can be complex and possibly misleading.

Locking scheme

To lock the lattice light to a cavity resonance one can either use a piezoelectric actuator on one of the cavity mirrors to feed back on the cavity length or to directly feed back to the frequency of the lasers (as we plan to do[29]). Since in our case the 612 nm light is created in a frequency doubling scheme, it is in principle sufficient to realize cavity locking with a feedback on the frequency of 1224 nm laser, before frequency doubling. Since this feedback will influence both wavelengths in common mode, in principle the lock needs to be performed only for either the 612 nm or the 1224 nm light, as long the cavity is simultaneously resonant with both. The other will in principle be automatically locked. In practice it may be necessary to react on "etalon 2" to maintain this conditions.

Sensitivity to perturbations

The sensitivity to external perturbations and drifts of the simultaneous resonance is determined by the criterion that changes in the relative phase of the two waves

---

[29] The achievable locking bandwidth for feedback on a piezo would be limited to the order of kHz. For the feedback on the laser frequency, using an AOM or the modulation input of the diode current of the 1224 nm laser, the typical bandwidth limitation is on the order of a MHz.

should stay small compared to the width of the cavity peaks. This width is characterized by the finesse of the cavity that is defined as the ratio of free spectral range to width of the cavity peak. For the planned build-up factors of ~ 10, typically the cavity finesse is on the order of $F \sim 20$, where the width of a cavity peak would correspond to a relative phase shift on the order of several degrees. Therefore the tolerable fluctuations of the relative phase have similar constraints as has been found for the one at the atoms position, as discussed in section 5.2.6. Except from thermal effects on the dispersive elements within the cavity, there are no major effects expected that could influence the relative phase between the two waves. For the setup as sketched in Figure 5.13, two viewports and two etalons would be within the cavity that will have an accumulated thickness on the order of 1 cm. When assuming them to be made of fused silica, the typical thermal sensitivity of the relative phase at the incoupling mirror position is expected to be on the order of $1\,^\circ/^\circ$C (see Table 5.4). A temperature stability of the intracavity elements of better than one degree is within the experimentally manageable.

Chapter 6

Summary and outlook

In the context of this thesis the construction of an experiment to produce quantum degenerate gases of ytterbium for the study of artificial gauge fields in optical lattices and the high resolution spectroscopy on a BEC has been presented.

In chapter 2 the basic theory of optical lattices has been reviewed with a focus on the physics in the tight-binding regime. The process of laser-assisted tunneling in a state-dependent lattice configuration has been introduced and an expression for the complex tunneling matrix element is derived. Useful approximations of this expression are verified with the help of numerical calculations of Wannier functions in the fundamental band. Furthermore the basic concepts of orbital magnetism in quantum mechanics have been reviewed and the Harper Hamiltonian is introduced.

The successful implementation of laser cooling and trapping for the production of a Bose-Einstein condensate (BEC) of ^{174}Yb has been described in chapter 3. We have reported on Zeeman slowing on the $^1S_0 \leftrightarrow {}^1P_1$ transition and subsequent direct loading of a magneto-optical trap, operating on the $^1S_0 \leftrightarrow {}^3P_1$ intercombination line. Laser cooling has lead to temperatures as low as $10\,\mu$K and the efficient transfer to a single beam dipole trap has been shown. A subsequent transport of the atomic cloud in a mechanically displaced optical dipole trap is carried out over a distance of 22 cm with a transport efficiency above 60 %. The possible loss mechanisms during transport have been investigated, where acceleration induced losses are found to yield a dominate contribution for fast transport times. The subsequent evaporative cooling in a crossed dipole trap has been characterized and the production of pure BECs of about 6×10^4 atoms is reported, where an atom number reproducibility better than 5% is reached. After that the adiabatic loading of a BEC into a one-dimensional optical lattice has been characterized by a sensitive heating measurement using a partially condensed cloud. We have successfully applied the method of Kapitza-Dirac diffraction to determine the depth of optical lattices.

In chapter 4 we have described the ultranarrow linewidth laser system to address the ${}^1\mathrm{S}_0 \leftrightarrow {}^3\mathrm{P}_0$ clock transition and have presented the method to calibrate its frequency with an absolute accuracy better than 50 kHz using spectroscopy on molecular iodine. Furthermore we have discussed the results of high resolution spectroscopic measurements on a BEC in a crossed dipole trap. Possible mechanisms to explain the observed features of the resonance are described. Spectroscopy measurements on a BEC during time-of-flight have been also presented. The resonance width of about 3 kHz was found in accordance with the Doppler broadening of a BEC in free expansion. Frequency drifts of the ULE cavity resonances have been characterized and could be reduced from typically 1 Hz/s to below about 100 mHz/s. The key for this has been found to be a precise determination of the temperature zero-crossing point, carried out using molecular iodine as a frequency reference. Moreover we could demonstrate the spatially resolved Doppler sensitive addressing of the clock transition in a BEC after a one-dimensional hydrodynamic expansion. This technique has been shown to be capable of measuring the absolute frequency of the clock laser in a single shot with a precision of about 0.5 kHz.

The main goal of the experiment is the realization of artificial gauge fields in optical lattices. The scheme we plan to implement has been presented in chapter 5, followed by a detailed analysis of the experimentally required conditions. Possible ways to achieve relative phase tuning of the two lattices building the required state-dependent superlattice potential have been studied. We have discussed possible methods to boost the intensity of the lattce light and have proposed a scheme using a doubly-resonant cavity where, power boosting and relative phase tuning can both be achieved. Implementing and testing this setup using the laser system at 612 nm and 1224 nm is under way.

Further upcoming steps in the development of the experiment are technical improvements on the clock laser system, like the addition of fiber noise cancellation and a better thermal and vibrational isolation of the cavity. Performing spectroscopy in the Lamb-Dicke regime in an optical lattice at a magic wavelength will allow us to reach smaller resonance widths and to investigate the technical limitations of our laser system.

Another short term objective is the measurement of the scattering properties of atoms in the ${}^3\mathrm{P}_0$ state. This could be achieved in a controlled way using dipole traps or lattices at a magic wavelength, where an influence of the differential light shift can be eliminated. Performing careful loss measurements after controlled excitation should allow to determine the inelastic loss coefficients β_{ge} and β_{ee}.

Moreover a possible future step could be to switch to one of the fermionic isotopes of ytterbium. Interesting is in particular ${}^{173}\mathrm{Yb}$ with a nuclear spin of 5/2. Convenient is the fact that quantum degeneracy can be achieved without sympathetic cooling as has been shown in several experiments [56, 140, 113] (typically

$T/T_\mathrm{F} \approx 0.3$ is achieved, with T_F the Fermi temperature). The fermionic isotopes have the advantage that the clock transition is naturally stronger permitted than for the bosonic isotopes due to the additional hyperfine coupling. This allows for much higher Rabi frequencies, thus reducing the timescales involved.

In the mid-term we plan to test the scheme for single plane selection of atoms in a vertical optical lattice presented in section 5.2.4. We intend to achieve this by applying a strong differential light shift gradient that allows to site selectively address the clock transition. Performing a transfer of the atoms to the metastable e state in all but one plane will allow to either blast the atoms away with resonant light or the unwanted sites will be depleted due to inelastic collisions. Preparing atoms in a single plane in combination with an artificial magnetic field in a two-dimensional lattice is a novel system, where particle interactions become important as well. In most of the so far performed experiments the gauge fields are realized in arrays of one-dimensional tubes [41, 45], where interaction effects between the particles are small and only single particle properties can be probed. However particle interactions are for example important to realize fractional quantum Hall states.

Appendix A

Dipole potential and polarizability

The fact that far-off-resonant light allows to create repulsive and attractive forces on neutral atoms is an important effect in ultracold atom physics. The working principle of optical dipole traps and lattices is based on this effect. The quantity that characterizes the light-atom interaction is the so-called atomic polarizability. It depends on the wavelength of the applied light field and on the accessible atomic transitions and is therefore different for each atomic species.

The goal of this section is to set the theoretical basics to describe the dipole potentials used within this thesis. For this the framework of considered atomic transitions of ytterbium is set and used to calculate the polarizabilities. From this basic knowledge, the trap parameters (trap depths, trapping frequencies, etc.) can be calculated. The theory presentation is based on [62].

A.1 Semi-classical theory of atom-light interaction

In the following we consider an atom placed into a monochromatic laser field of angular frequency ω and intensity profile $I(\boldsymbol{r})$. The oscillating electric field $\boldsymbol{E}$, associated with the laser light, will induce an oscillating electric dipole moment $\boldsymbol{p}$ in the atom given by

$$\boldsymbol{p} = \alpha(\omega)\boldsymbol{E}\,. \tag{A.1}$$

Here $\alpha(\omega)$ is the complex atomic polarizability, describing the linear response to the electric field. The induced dipole moment interacts itself with the electric field $\boldsymbol{E}$, shifting the potential energy of the atom. For simplicity we treat the electric field classically (see [141] for a more detailed description). This interaction energy gives rise to a time averaged dipole potential that reads [62]

$$\boxed{V_{\mathrm{dip}}(\boldsymbol{r}) = -\frac{1}{2}\langle \boldsymbol{p}\cdot\boldsymbol{E}\rangle_t = -\frac{1}{2\epsilon_0 c}\mathrm{Re}[\alpha(\omega)]I(\boldsymbol{r})}\,, \tag{A.2}$$

with c the speed of light, ϵ_0 the vacuum permittivity and $\mathrm{Re}[\alpha]$ the real part of the polarizability.

The fact that the induced dipole oscillator also absorbs power from the light field can be understood in terms of cycles of absorption of photons from the applied light field and spontaneous reemission into vacuum modes. The scattering rate corresponding to this process is determined by [62]

$$\Gamma_{\mathrm{sc}}(\boldsymbol{r}) = \frac{1}{\hbar\epsilon_0 c}\mathrm{Im}[\alpha(\omega)]I(\boldsymbol{r})\,, \tag{A.3}$$

where $\mathrm{Im}[\alpha]$ denotes the imaginary part of the polarizability. For a trapped atomic ensemble this scattering process will lead to a time averaged heating rate of [62]

$$\Gamma_{\mathrm{heat}} = 2E_{\mathrm{R}}\Gamma_{\mathrm{sc}}\,. \tag{A.4}$$

Here $E_{\mathrm{R}} = h^2/2m\lambda^2$ is the so called recoil energy, associated with the absorption of a photon from the light field at wavelength $\lambda = 2\pi c/\omega$.

An analytic expression for the atomic polarizability can be derived when considering a two-level atom coupled to far-off resonant light in a semi-classical oscillator model. Considering the atomic transition at energy $\hbar\omega_0$ with a natural linewidth Γ, the complex polarizability takes the form [62]

$$\alpha(\omega) = 6\pi\epsilon_0 c^3 \frac{\Gamma/\omega_0^2}{\omega_0^2 - \omega^2 - i\,\Gamma\omega^3/\omega_0^2}\,, \tag{A.5}$$

where ω is the angular frequency of the far-off resonant light and i the imaginary unit. In this model the real and imaginary parts of the polarizability calculate to

$$\boxed{\mathrm{Re}[\alpha(\omega)] = \frac{3\pi\epsilon_0 c^3}{\omega_0^3}\left(\frac{\Gamma}{\omega_0-\omega} + \frac{\Gamma}{\omega_0+\omega}\right)}\,, \tag{A.6}$$

and

$$\boxed{\mathrm{Im}[\alpha(\omega)] = \frac{3\pi\epsilon_0 c^3}{2\omega_0^3}\left(\frac{\omega}{\omega_0}\right)^3\left(\frac{\Gamma}{\omega_0-\omega} + \frac{\Gamma}{\omega_0+\omega}\right)^2}\,. \tag{A.7}$$

When considering an atom with multiple internal resonances, the resulting polarizability can be calculated by summing over the contributions of all considered atomic transitions

$$\alpha_{\mathrm{tot}}(\omega) = 6\pi\epsilon_0 c^3 \sum_j \frac{\Gamma_j/\omega_{0,j}^2}{\omega_{0,j}^2 - \omega^2 - i\,\Gamma_j\,\omega^3/\omega_{0,j}^2}\,. \tag{A.8}$$

This however is only valid for weak saturation and under the approximation that each transition is closed and that a decay to states other than the considered starting state of the atom are negligible. Furthermore

A.2 Transition data used for polarizability calculations

To calculate the dipole trap and lattice potentials for ytterbium within this thesis, the formulas presented in the preceding section are used. Of particular importance are the polarizabilities for an atom in the $^1\mathrm{S}_0$ ground state and the $^3\mathrm{P}_0$ metastable excited state in the range of wavelengths from about 500 nm to 1400 nm. The atomic resonances with the dominant contribution in this wavelength range are listed in Table A.1 which form the basis for the calculations done within this thesis.

The data presented in Table A.1 is based on multiple sources. The transition wavelengths are measured values taken from [87] and the linewidths of the $^1\mathrm{P}_1$ ($6s6p$) and $^3\mathrm{P}_1$ ($6s6p$) states are taken from [77] and [142]. The linewidths of the remaining transitions are less well known experimentally and are extracted from the data shown in [143]. In this article the polarizabilities of the $^1\mathrm{S}_0$ and $^3\mathrm{P}_0$ states are calculated for a broad range of wavelengths based on a relativistic many body calculation taking experimental data for one magic wavelength at $\lambda_{\mathrm{magic}} = 759.3537\,\mathrm{nm}$ [133] into account. To extract the needed linewidth parameters, the polarizability data presented in this article has been exported "by hand" and the obtained data points fitted using the model equations (A.6) and (A.8), with the missing linewidth values as open fit parameters. It is to note that the fitted linewidth values Γ might not directly be used as the real transition linewidths since the used fitting model neglects effects of branching to other excited state. In this sense the presented values for Γ are just best fit values to reproduce the data behavior presented in [143]. The resulting polarizability curves are shown in Figure A.1.

A.3 Magic and anti-magic wavelengths

Important for the discussions in this thesis are so-called magic and anti-magic wavelengths λ_{m} and λ_{am} for the $^1\mathrm{S}_0$ and $^3\mathrm{P}_0$ states. These wavelength are characterized by the fact that the real part of the polarizabilities for the two states are equal at a magic wavelength and opposite in sign but equal in magnitude at an anti-magic wavelength. According to the obtained model data, magic wavelengths are located at about $\lambda_{\mathrm{m}} = (761.5,\ 552.5,\ 458.0)\,\mathrm{nm}$. However the one at

initial state	final state	$\Gamma/2\pi$ (MHz)	λ (nm)
$^1\mathrm{S}_0$ $(6s^2)$	$^1\mathrm{P}_1$ $(6s6p)$	29.13	398.91
	$^3\mathrm{P}_1$ $(6s6p)$	0.183	555.80
	$(7/2, 5/2)_{J=1}$	16.07	346.54
$^3\mathrm{P}_0$ $(6s6p)$	$^3\mathrm{D}_1$ $(6s5d)$	0.3371	1388.8
	$^3\mathrm{S}_1$ $(6s7s)$	1.491	649.1
	$^3\mathrm{D}_1$ $(6s6d)$	3.601	444.05
	$^3\mathrm{P}_1$ $(6p^2)$	26.320	377.1

Table A.1: List of states used to calculate the polarizability for the $^1\mathrm{S}_0$ and $^3\mathrm{P}_0$ states. The final state labeled $(7/2, 5/2)_{J=1}$ corresponds to an excitation of an electron from the inner $4f$-shell to the $5d$-shell where the two $6s^2$ electrons are left unchanged.

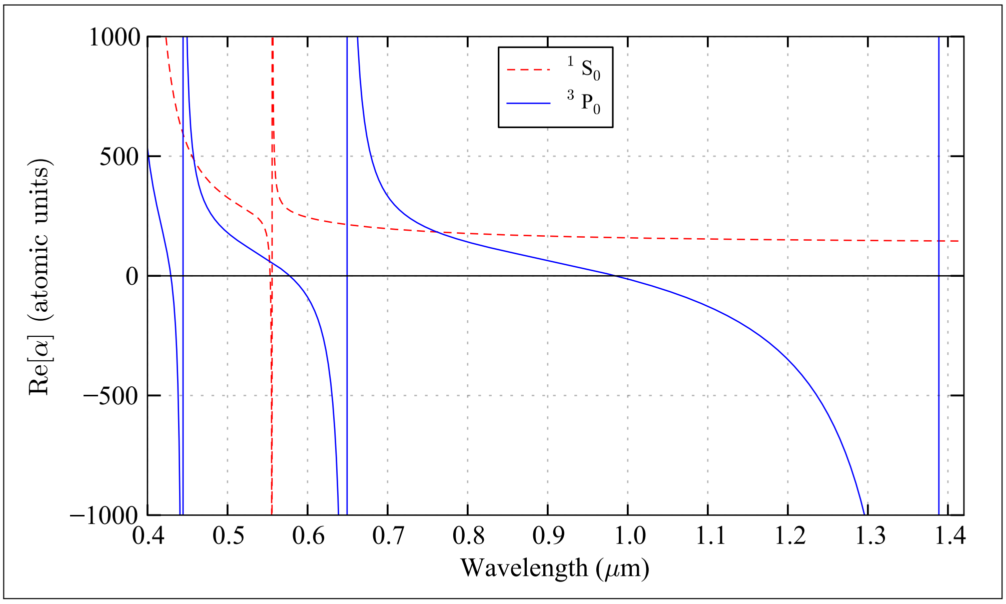

Figure A.1: Dynamic polarizability of the $^1\mathrm{S}_0$ (red dashed line) and $^3\mathrm{P}_0$ (blue solid line) states of ytterbium, calculated based on the transition data in Table A.1. Attractive atom-light interaction is realized for $\mathrm{Re}[\alpha] > 0$, repulsive interaction for $\mathrm{Re}[\alpha] < 0$. The values are given in atomic units, $\hbar = e = m_e = 1$, where m_e and e are the mass and the charge of an electron, respectively. Conversion to SI units is achieved by multiplication with $e^2 m_e a_0^4/\hbar^2$.

about 760 nm is probably the most useful one, since the others are quite close to resonances, where the spontaneous emission rates and according cloud heating are expected to be higher. Anti-magic wavelengths are according to the model data located at $\lambda_{\mathrm{am}} = (1117,\ 617.5,\ 553.7,\ 439.3,\ 386.6,\ 352.6)\,\mathrm{nm}$. Here the most useful ones are at 1117 nm and 617.5 nm where reasonably low spontaneous emission rates are expected.

Appendix B

A microcontroller based digital feedback loop

Electronic feedback loops are a key component in modern experiments. They serve to stabilize erratic experimental parameters that would otherwise exceed the acceptable margins for fluctuations and drifts. Common applications in the field of ultracold atoms are the locking of laser frequencies to an atomic resonance, the active stabilization of laser powers or of the temperature of laser diodes.

The traditional way of implementing electronic feedback loops is by using operational amplifiers within some analog electronic circuit. In a more advanced approach the feedback loop is realized using a control algorithm that is evaluated by a digital processing unit. This alternative path was followed within this thesis by the development of a digital proportional-integral-derivative (PID) controller using an Arduino DUE microcontroller, that is presented in the following. This controller is applied to dynamically control the position of a motorized rotation stage, where typical performance results are shown. In principle this controller could be used for practically every purpose.

B.1 Digital versus analog feedback loop

Analog PID circuits are usually based on operational amplifiers and can have bandwidths in the MHz region. Their resolution is in principle only limited by electronic noise of the control signals and the components within the electronic PID circuit. However, one of the main disadvantages of an analog implementation is its lack of flexibility. Implementing important features like integrator clamping, auto-relock, adaptive loop constants or 'sample and hold'[1] functionality can be very challenging. Furthermore, major changes in the control behaviour mostly necessitate a redesign of the printed circuit board.

Digital PID loops, on the contrary, are based on an algorithm implemented in software that can be changed by the programmer at any time via a computer interface. Including or changing custom functionalities like the above mentioned ones become easy tasks. The possibility of interfacing the digital control unit with a PC allows for real time changing and monitoring of all system variables. In this way also command signals like ramps can be directly sent via a digital communication channel to the control unit. This can reduce the susceptibility to pickup noise as compared to using analog command signals. The fact that all data processing is digital also allows to use many algorithms and operations from the domain of digital signal processing. This includes amongst others high order low-, high- and bandpass filters as well as fast Fourier transform (FFT) [144], [145].

The main disadvantage of digital control loops is that, depending on the algorithm and additional features, the bandwidth might be well below analog equivalents. However, these days the computation speed of microcontrollers, FPGA's [2] and DSP's [3] is sufficient to reach equivalent bandwidths on the order of tens of kHz and above[4]. This is sufficient for many applications like motion control systems, temperature locks and systems where perturbations in the acoustic frequency regime need to be eliminated.

B.2 Digital PID working principle

At the heart of the implementation of a digital PID is the algorithm that is supposed to emulate the ideal PID behaviour described by

$$\mathrm{O}(t) = K_\mathrm{p} e(t) + K_\mathrm{i} \int_0^t e(t')\mathrm{d}t' + K_\mathrm{d} \frac{\mathrm{d}}{\mathrm{d}t} e(t)\,, \tag{B.1}$$

where $e(t) = \mathrm{setpoint}(t) - \mathrm{input}(t)$ is the instantaneous following error, O the PID output and $K_\mathrm{p,i,d}$ are the loop constants used to tune the system behaviour. Due to the sequential nature of a digital processing unit and the finite evaluation time of the algorithm, it is necessary to calculate new output states in a periodic

---

[1] When the servo loop needs to be deactivated on purpose for a certain time interval, ideally the lock circuit should keeps its output constant and memorize its internal integrator and differentiator values, to ensure a smooth transition when the lock is turned back on.

[2] Field-programmable gate array

[3] Digital signal processor

[4] Commercial systems typically offer down to the microsecond level PID calculation delay times (e.g. Digital LaseLock, TEM Messtechnik).

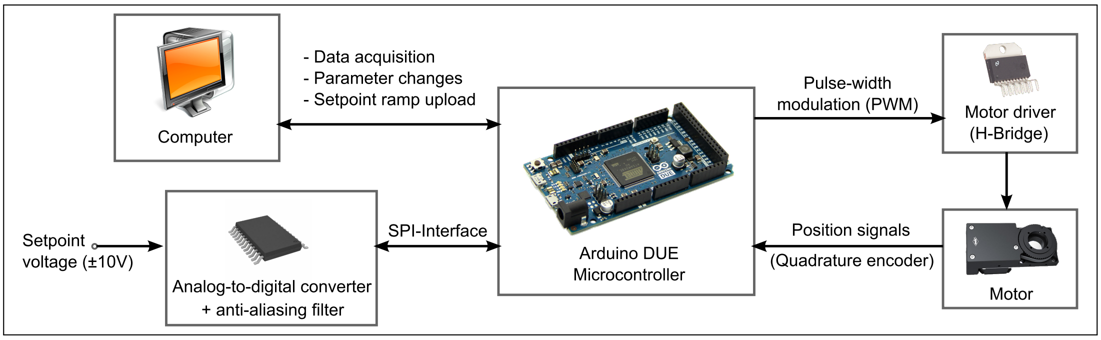

Figure B.1: Building blocks of the Ardunio DUE based motion control system.

manner. In practice this means that a discretized version of the ideal behaviour is implemented described by

$$O(t_j) = K_\mathrm{p} e(t_j) + K_\mathrm{i}\, \tau \sum_{n=0}^{j} e(t_n) + K_\mathrm{d} \frac{e(t_j) - e(t_{j-1})}{\tau}\,, \tag{B.2}$$

where τ is the time interval between two algorithm evaluations and $t_j = j\tau$ the time after j evaluations. On top of this basic formula the programmer can choose to add all sorts of custom design functionalities. A nice tutorial on useful additional functionalities can be found in [146]. Since the maximum possible loop bandwidth depends on the evaluation time of the algorithm it is important to adapt the programming "style" to the hardware capabilities in order to minimize the computation time.

B.3 Application to a motion control system

An implementation of a digital PID using an Arduino DUE microcontroller has been developed and applied within this thesis to actively control the position of a motorized rotation stage[5]. This serves to ramp the optical power of a laser beam for evaporative cooling (see section 3.8.1). The principle parts of the full control system are illustrated as a block diagram in Figure B.1.

Motor control using pulse-width modulation

The DC motor of the rotation stage is controlled by an H-bride module[6] that allows to send a variable current through the motor coil in a desired direction. The

---

[5] Motor model: DRTM40, OWIS.

[6] LMD18200.

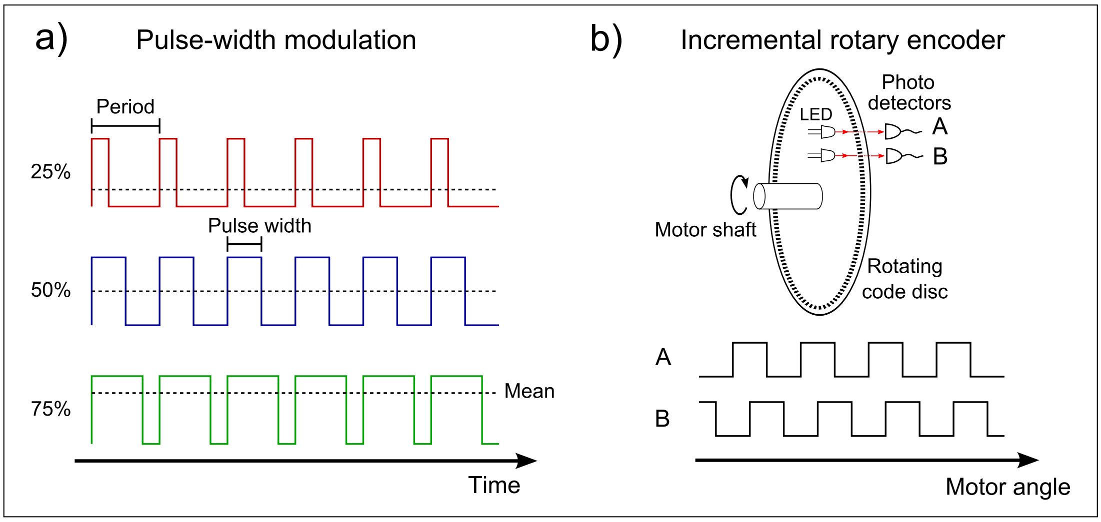

Figure B.2: (a): Illustration of the pulse-width modulation technique to control the motor current. The voltage applied to the motor is periodically switched at a rate much faster than the motor response time. The pulse length during one period, called duty cycle, thereby determines its average value and therefore the rotation speed of the motor. Here the signal for duty cycles of 25 %, 50 % and 75 % is shown. (b): Principle of an incremental rotary encoder. Sketched is the code wheel that rotates with the motor shaft, having equally spaced transparent and opaque areas. The two LEDs and photo detectors are arranged such that two 90° out-of-phase signals are acquired during rotation. They are provided as quadrature signals, called A and B, that allow to track changes of the motor angle.

amount of current is controlled by pulse-width modulation (PWM) of a digital input of the H-bridge (see Figure B.2). The way this works is that the digital input controls the voltage across the coil which is switched on and off periodically at a frequency much faster than the response time of the motor. The duty cycle (amount of "on" time during one period) then determines the amount of average current flowing trough the motor and therefore its rotation speed. A second digital input of the H-bridge controls the direction of the voltage applied to the motor and therefore its sense of rotation.

Motor position tracking

The position of the motor is tracked using its build-in incremental rotary encoder with a step resolution of 0.06 °. The rotary encoder typically consists of a disc connected to the motor shaft that has equally spaced opaque and transparent areas (see Figure B.2). Using a light source on one side of the disc and a photo detector on the other, an optical pattern is acquired during rotation that allows to track changes in the motor rotation angle. The optical signal is thereby converted to a quadrature type electronic signal, where two 90 ° out-of-phase signals (called A and B) are provided to extract information about the rotation direction. Those two out-of-phase quadrature signals are evaluated using the Arduino DUE's internal hardware quadrature decoder[7]. For absolute position referencing the motor is equipped with a magnetic reference (Hall) sensor and a so-called index signal, that pulses at one particular rotation angle per revolution.

Typical PID cycle and system performance

The desired position of the motor is controlled by an analog voltage that is sampled at each servo cycle by an ADC[8]. Alternatively the command position can also be predefined in a look-up table that is sent via USB[9] to the microcontroller and can subsequently be started by a digital trigger signal. The typically performed steps on the microcontroller in one full PID evaluation cycle are as follows:

1. Analog-to-digital conversion of command position voltage (or values taken from look-up table) and reading of current motor position.
2. Calculation of PID output using predefined algorithm (based on equation (B.2), plus free choice of including other features).
3. Updating the PWM duty cycle and motor current direction according to the new PID output.
4. Save current values of important variables for monitoring.

The evaluation time for one such cycle depends on the complexity of the algorithm used and is in the present[10] configuration about 10 μs, allowing for up to 100 kHz update rate. Important is to start the evaluation cycles with a well-controlled temporal delay which is ensured by using so-called timer interrupts. They allow to execute a program routine periodically at a predefined time interval, which happens deterministically in the sense that all other processor tasks with lower priority are interrupted. The time jitter between successive routine executions is usually on the order of the inverse processor clock frequency (here $\lesssim$ 100 ns). All important

---

[7] The fact that it is evaluated in hardware liberates the processor quite a bit. Especially at high rotation speeds a software solution might heavily occupy the microprocessor.

[8] Analog-to-digital converter, the model used is: AD7367-5 from Analog Devices.

[9] USB = Universal Serial Bus.

[10] The algorithm includes proportional, integral and derivative feedback, integrator and output clamping as well as four variable live monitoring and is based on 64 bit fixed point math.

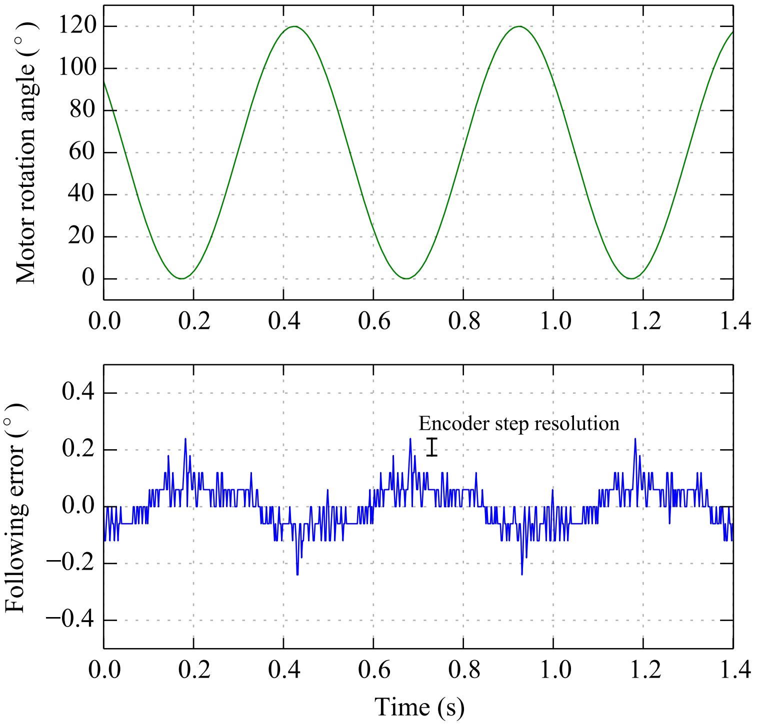

Figure B.3: Typical closed-loop performance of the digital PID motor controller. The desired trajectory of rotation angle of the motor is a sine function with a total amplitude of 120 ° and a period of $T = 500\,\text{ms}$ (upper graph). The motor following error, defined as the difference between desired and actual position, is shown in the lower graph. The motor follows the commanded trajectory within a total accuracy of better than ±0.25 °, which corresponds to deviations of less than about four times the discrete encoder resolution of 0.06 °.

system parameters can be monitored with an external PC using a developed control software that is written in Python. The system data is transferred via USB from the microcontroller with up to 100 kSamples/s in parallel with the PID algorithm.

A typical example of the closed loop position control performance of the motor is shown in Figure B.3. It can be seen that dynamic position control down to the measurement resolution limitation of the motor is achieved. For the chosen example trajectory, a 90 ° rotation is performed in about 200 ms, where the peak deviation from the desired motor position stays below 0.25 ° throughout the full nonlinear trajectory.

It is to note that this controller can be modified to a "standard" analog PID (having only analog inputs and an analog output instead of PWM control), by simply replacing the H-bridge part with a digital-to-analog converter (DAC) of appropriate performance[11].

---

[11] In practice a bandwidth limiting reconstruction filter [145] needs to be added to attenuate image frequencies (inverse effect of aliasing, that is known from analog-to-digital conversions).

Appendix C

A corner cube reflector for the transport of cold atoms

To transport the atomic cloud the focus of a single beam dipole trap beam is moved using a mechanical translation stage[1]. Due to manufacturing imperfections and mechanical play the translation stage will undergo off-axis motion and vibrations during transport. The optical element that is placed on the stage will couple these movements to the dipole trap position, that can lead to issues of heating and atom loss during transport. With a proper choice of the optical element this coupling of mechanical vibrations to the dipole trap position can be minimized.

In the following the effect of parasitic stage motions on the transverse[2] dipole trap position is estimated for different mirror configurations. The important types of off-axis movements to consider are horizontal and vertical shifts (displacements) as well as angular tilts. For the description of angular tilts the language of mechanical engineering will be used where three tilt orientations are distinguished called pitch, yaw and roll (see Figure C.1). Those terms are here defined with respect to the geometrical center of the stage and the direction of travel. The specifications for the translation stage used in this experiment are as follows:

- Pitch, Yaw: $50\,\mu$rad (maximum tilting angle during motion, Roll is not specified)

- Straightness, Flatness: $1.5\,\mu$m (maximum vertical and horizontal displacement during motion)

---

[1] Model: XMS160, Newport

[2] The effect on the longitudinal position (along propagation axis) of the dipole trap can be neglected due to the high anisotropy of $\omega_\perp/\omega_{\text{long}} \approx 100$ of the trap frequencies, making the atoms primarily sensitive to heating in transverse direction.

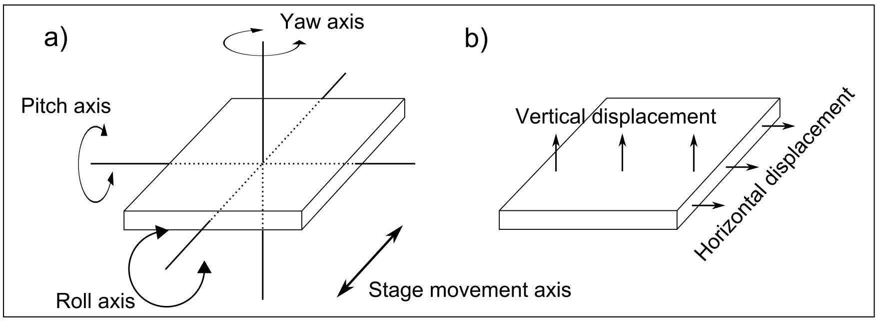

Figure C.1: Sketch of the considered types of off-axis stage motion. On the left hand side (a) rotations of type pitch, yaw and roll are shown, defined with respect to the axis of motion. On the right hand side (b) the terms vertical displacement and horizontal displacement are illustrated.

To simplify the formalism, the discussion will be restricted to tilts and displacements in one dimension only but the results can be generalized to two dimensions straightforwardly.

Furthermore it is assumed that the last focusing lens for the dipole trap beam is located before the translation stage (like in our transport setup as shown in Figure 3.15). Thereby an effect of the reflecting device on the outgoing beam is directly converted to the dipole trap position.

C.1 Single mirror versus two-mirror retroreflector

Single mirror

The simplest way to reflect the incoming dipole trap beam consists in using a single mirror mounted on the stage with an angle of incidence of 0 ° (this necessitates using a polarizer and a $\lambda/4$-waveplate to separate the incoming from the outgoing beam). Considering a small tilt of angle α (see Figure C.2, a), the dipole trap gets transversely shifted by

$$\Delta_{\text{tilt}}^{\text{single}} = d_{\text{trap}} \tan(2\alpha) \simeq 2\, d_{\text{trap}}\, \alpha\,, \tag{C.1}$$

where d_{trap} is the distance from the mirror to the dipole trap focus position. On the contrary, a transverse shift of the translation stage does not change the position and the angle of the reflected beam.

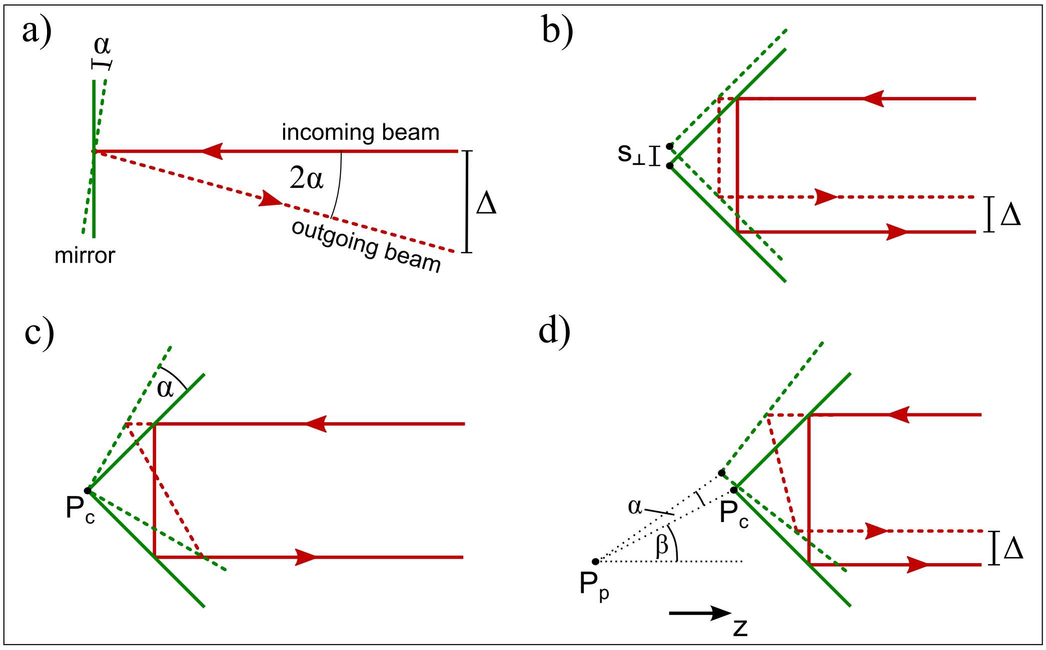

Figure C.2: Illustration of the effect of parasitic stage motion on the transverse dipole trap position for a single mirror and a two-mirror retroreflector configuration. The four considered situations are a tilt of a single mirror (a), a transverse shift of a retroreflector (b), a tilt of a retroreflector with respect to its corner point P_c (c) and a tilt of a retroreflector with respect to an arbitrary pivot point P_p (d).

Two-mirror retroreflector

A more sophisticated approach is to use two mirrors in a retroreflector configuration (90 ° to each other) to reflect the dipole trap beam at the translation stage. The fact that the reflected and ingoing beam are naturally displaced from each other allows to use this configuration without an additional polarizer and $\lambda/4$-waveplate.

In this configuration the dipole trap position is sensitive to transverse stage displacements. A stage shift of $s_\perp$ leads to a beam displacement of

$$\Delta_{\text{shift}}^{\text{retro}} = 2\, s_\perp \,. \tag{C.2}$$

Note that this is independent of the distance d_{trap} from the mirrors to the focus position (see Figure C.2, b).

The big advantage of the retroreflector is that the angle of the reflected beam is independent of the orientation of the retroreflector. This means that any tilt with respect to the retroreflector corner point P_c leave the reflected dipole trap beam unchanged, in angle as well as in displacement (see Figure C.2, c). This however holds only true for tilts with respect to an axis going through P_c. In the more general case a tilt with respect to an arbitrary pivot point P_p needs to be considered. Then the resulting motion can be expressed as a combination of a tilt around the corner point P_c and a shift of the retroreflector position (see Figure C.2, d). The displacement of the dipole trap position then takes the form

$$\Delta^{\mathrm{retro}}_{\mathrm{tilt},\vec{P}_\mathrm{p}} = \cancelto{0}{\Delta^{\mathrm{retro}}_{\mathrm{tilt},\vec{P}_\mathrm{c}}} + \Delta^{\mathrm{retro}}_{\mathrm{shift},\vec{P}_\mathrm{c}} \,, \tag{C.3}$$

where the residual shift component for small tilting angles α is given by

$$\Delta^{\mathrm{retro}}_{\mathrm{shift},\vec{P}_\mathrm{c}} \simeq 2\,\alpha\,\overrightarrow{P_\mathrm{c}P_\mathrm{p}} \cdot \hat{z} \;= 2\,\alpha\, d^z_{\mathrm{c,p}} \tag{C.4}$$

Here $\hat{z}$ denotes the unit vector along the stage transport movement axis, $\overrightarrow{P_\mathrm{c}P_\mathrm{p}}$ the distance vector between P_c and P_p and $d^z_{\mathrm{c,p}} = |\overrightarrow{P_\mathrm{c}P_\mathrm{p}}| \cos\beta$ its projection onto the z-axis. This result shows that the important quantity that determines the coupling to the transverse dipole trap position is the distance between the pivot point and the corner point, projected onto the transport axis, $d^z_{\mathrm{c,a}}$. An optimum positioning of the two-mirror configuration would be achieved for $d^z_{\mathrm{c,a}} = 0$, where the coupling is minimized. The placing in the transverse directions is not as important[3], leading to trap displacements of higher orders in α. This is in particular true for the height of the optical arrangement above the stage.

To find the best positioning for the two-mirror configuration experimentally, the difficulty lies in knowing where exactly the pivot point is. This is not trivial since in general the stage will undergo motions that will be complicated combinations of displacements and tilts with respect to variable pivot points. However, due to symmetry reasons one can assume that the pivot point will in average be located in the vicinity of the center of the stage.

In the next section the expected magnitude of trap displacements will be estimated, based on the specifications for pitch, yaw and transverse displacements of the stage. For these estimations it is in principle also necessary to know where the pivot points are located during motion in order to know $d^z_{\mathrm{c,a}}$. However here it is to note that the stage specifications for pitch and yaw are defined with respect to a pivot point in the center of the stage. All rotations with respect to a different pivot point can be decomposed into a rotation around the center and a transverse displacement. The combined specifications of pitch, yaw and the transverse displacements therefore covers the full spectrum of possible pivot points.

---

[3] This is only true when not considering roll type rotations, which are not specified for the XMS160 stage.

Comparison

The quantity to compare the single mirror to the retroreflector configuration is the sensitivity ratio which is in the most general case given by

$$R = \frac{\Delta^{\text{single}}}{\Delta^{\text{retro}}} = \frac{\Delta^{\text{single}}_{\text{tilt}}}{\Delta^{\text{retro}}_{\text{shift}} + \Delta^{\text{retro}}_{\text{tilt},\vec{P}_{\text{p}}}} \simeq \frac{2\, d_{\text{trap}}\, \alpha}{2\, d^{z}_{\text{c,p}}\, \alpha + 2\, s_{\perp}} \, . \tag{C.5}$$

Important to note already is the difference in scaling for the tilt sensitivity. For the single mirror the important scale is d_{trap} whereas for the retroreflector $d^{z}_{\text{c,p}}$ is the relevant scale, which is in general much smaller than d_{trap}. This however has to be compared to the added influence to transverse shifts $s_{\perp}$.

To determine the more favourable configuration, the real experimental parameters have to be considered. For the specified translation stage values ($s_{\perp,\max} = 1.5\,\mu$m, $\alpha_{\max} = 50\,\mu$rad) and the present typical experimental parameters ($d_{\text{trap}} \simeq 600\,$mm and $d^{z}_{\text{c,a}} \simeq 50\,$mm) R calculates to

$$R = \frac{\Delta^{\text{single}}}{\Delta^{\text{retro}}} = \frac{60\,\mu\text{m}}{5\,\mu\text{m} + 3\,\mu\text{m}} = 7.5 \, . \tag{C.6}$$

Thus the sensitivity to off-axis stage movements is expected to be lowered by about a factor of 7 using the retroreflector configuration. Note that the single mirror case is expected to produce transverse movements with up to $60\,\mu$m amplitude. This corresponds to about four times the FWHM[4] transverse size of a thermal cloud at $T \simeq 80\,\mu$K for the current trap configuration.

However experimentally the total amplitude is not the most relevant quantity, rather its spectral contribution around the trapping frequencies and their harmonics will determine the heating rate [99]. The specifications for the translation stage are maximum amplitudes without indication of their spectral distribution. Nevertheless, the reduction in sensitivity is an effect that is independent of the perturbation frequency and will therefore be in any case beneficial.

C.2 Corner cube and experimental test

The two-mirror retroreflector generates the reduced sensitivity only for transverse movements in the plane of incidence and acts like a single mirror in the perpendicular direction. However, the retroreflector effect can be generalized to two dimensions by using a so called corner cube that mimics the incidence of the beam in the corner of a cube (see Figure 3.15 (b)).

---

[4] Full width at half maximum.

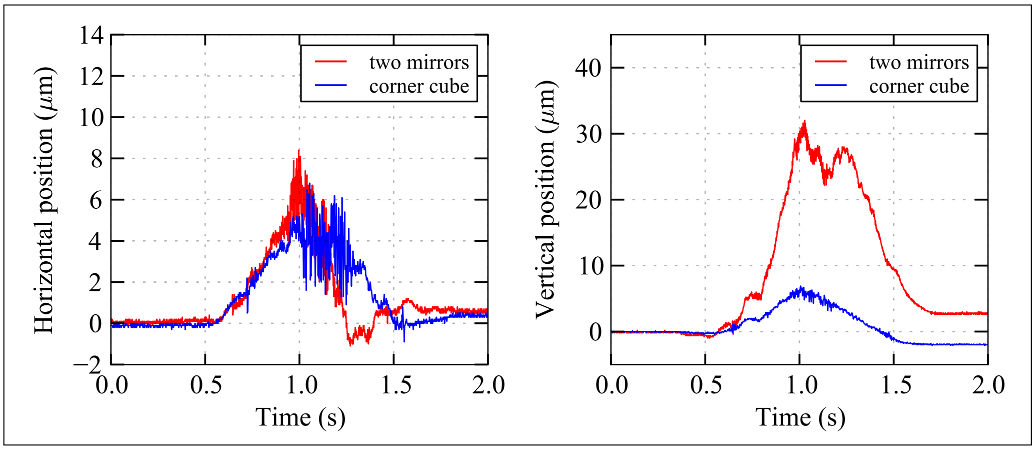

Figure C.3: Transverse beam pointing measurements when simulating a transport for $d_{\text{trap}} \simeq 25\,\text{cm}$. The translation stage is moved over 15 cm (93 % of the travel range) using the motion profile as described in section 3.7.3 with a duration of 1.5 s. The absolute position scale calibration is not better than about 30 %.

To experimentally verify the reduced sensitivity to parasitic stage motion, the corner cube is compared to the two-mirror retroreflector configuration. For this a collimated laser beam is sent onto the reflecting device which is placed on the translation stage. Using a quadrant photodiode the transverse beam position of the reflected beam is monitored during stage movement. The resulting transverse beam trajectories are shown in Figure C.3.

The two devices show a similar sensitivity in the horizontal direction, where both of them are expected to yield a reduced sensitivity. In the vertical direction the sensitivity of the two-mirror configuration is clearly enhanced with respect to the corner cube. This is due to the fact that the two-mirror configuration has no sensitivity reduction in the vertical direction and is supposed to act like a single mirror. Theoretically a reduction factor of about 5 is expected, for the test conditions of $d_{\text{trap}} \simeq 25\,\text{cm}$ and $d^{z}_{\text{c,p}} \simeq 2\,\text{cm}$. This is in accordance with the experimental result.

Bibliography

[1] Steven Chu, L. Hollberg, J. E. Bjorkholm, Alex Cable, and A. Ashkin. Three-dimensional viscous confinement and cooling of atoms by resonance radiation pressure. *Phys. Rev. Lett.*, 55:48–51, 1985.

[2] E. L. Raab, M. Prentiss, Alex Cable, Steven Chu, and D. E. Pritchard. Trapping of Neutral Sodium Atoms with Radiation Pressure. *Phys. Rev. Lett.*, 59:2631–2634, Dec 1987.

[3] P. D. Lett, R. N. Watts, C. I. Westbrook, W. D. Phillips, P. L. Gould, and H. J. Metcalf. Observation of Atoms Laser Cooled below the Doppler Limit. *Phys. Rev. Lett.*, 61(2), 1988.

[4] J. Dalibard and C. Cohen-Tannoudji. Laser cooling below the Doppler limit by polarization gradients: simple theoretical models. *J. Opt. Soc. Am. B*, 6(2023-2045), 1989.

[5] M. Anderson, J. Ensher, M. Matthews, C. Wieman, and E. Cornell. Observation of Bose-Einstein Condensation in a Dilute Atomic Vapor. *Science*, 269:198–201, 1995.

[6] K. B. Davis, M. O. Mewes, M. R. Andrews, N. J. van Druten, D. S. Durfee, D. M. Kurn, and W. Ketterle. Bose-Einstein Condensation in a Gas of Sodium Atoms. *Phys. Rev. Lett.*, 75:3969–3973, 1995.

[7] C. C. Bradley, C. A. Sackett, J. J. Tollett, and R. G. Hulet. Evidence of Bose-Einstein Condensation in an Atomic Gas with Attractive Interactions. *Phys. Rev. Lett.*, 75:1687–1690, 1995.

[8] M. R. Andrews, C. G. Townsend, H.-J. Miesner, D. S. Durfee, D. M. Kurn, and W. Ketterle. Observation of Interference Between Two Bose Condensates. *Science*, 275:637–641, 1997.

[9] S. Burger, K. Bongs, S. Dettmer, W. Ertmer, K. Sengstock, A. Sanpera, G. V. Shlyapnikov, and M. Lewenstein. Dark Solitons in Bose-Einstein Condensates. *Phys. Rev. Lett.*, 83:5198–5201, 1999.

[10] J. Denschlag, J. E. Simsarian, D. L. Feder, Charles W. Clark, L. A. Collins, J. Cubizolles, L. Deng, E. W. Hagley, K. Helmerson, W. P. Reinhardt, S. L. Rolston, B. I. Schneider, and W. D. Phillips. Generating Solitons by Phase Engineering of a Bose-Einstein Condensate. *Science*, 287(5450):97–101, 2000.

[11] L. Khaykovich, F. Schreck, G. Ferrari, T. Bourdel, J. Cubizolles, L. D. Carr, Y. Castin, and C. Salomon. Formation of a Matter-Wave Bright Soliton. *Science*, 296(5571):1290–1293, 2002.

[12] K. E. Strecker, G. B. Partridge, A. G. Truscott, and R. G. Hulet. Formation and propagation of matter-wave soliton trains. *Nature*, 417:150–153, 2002.

[13] M. R. Matthews, B. P. Anderson, P. C. Haljan, D. S. Hall, C. E. Wieman, and E. A. Cornell. Vortices in a Bose-Einstein Condensate. *Phys. Rev. Lett.*, 83:2498–2501, 1999.

[14] M.-O. Mewes, M. R. Andrews, D. M. Kurn, D. S. Durfee, C. G. Townsend, and W. Ketterle. Output Coupler for Bose-Einstein Condensed Atoms. *Phys. Rev. Lett.*, 78:582–585, 1997.

[15] B. DeMarco and D. S. Jin. Onset of Fermi Degeneracy in a Trapped Atomic Gas. *Science*, 285:1703–1706, 1999.

[16] I. Bloch, J. Dalibard, and W. Zwerger. Many-body physics with ultracold gases. *Rev. Mod. Phys.*, 80:885, 2008.

[17] S. Inouye, M. R. Andrews, J. Stenger, H.-J. Miesner, D. M. Stamper-Kurn, and W. Ketterle. Observation of Feshbach resonances in a Bose-Einstein condensate. *Nature*, 392:151–154, 1998.

[18] W. Ketterle and M. W. Zwierlein. "Making, probing and understanding ultracold Fermi gases" in "Ultracold Fermi Gases",. *Proceedings of the International School of Physics "Enrico Fermi", Course CLXIV, Varenna, 20 - 30 June 2006.* edited by M. Inguscio, W. Ketterle, and C. Salomon (IOS Press, Amsterdam) 2008.

[19] O. Morsch and M. Oberthaler. Dynamics of Bose-Einstein condensates in optical lattices. *Rev. Mod. Phys.*, 78:179–215, 2006.

[20] M. Greiner, I. Bloch, O. Mandel, T. W. Hänsch, and T. Esslinger. Exploring Phase Coherence in a 2D Lattice of Bose-Einstein Condensates. *Phys. Rev. Lett.*, 87:160405, 2001.

[21] Michael Köhl, Henning Moritz, Thilo Stöferle, Kenneth Günter, and Tilman Esslinger. Fermionic Atoms in a Three Dimensional Optical Lattice: Observing Fermi Surfaces, Dynamics, and Interactions. *Phys. Rev. Lett.*, 94:080403, 2005.

[22] T. Gericke, P. Würtz, D. Reitz, T. Langen, and H. Ott. High-resolution scanning electron microscopy of an ultracold quantum gas. *Nature Physics*, 4:949–953, 2008.

[23] W. S. Bakr, J. I. Gillen, A. Peng, S. Fölling, and Markus Greiner. A quantum gas microscope for detecting single atoms in a Hubbard-regime optical lattice. *Nature*, 462:74–77, 2009.

[24] J. F. Sherson, C. Weitenberg, M. Endres, M. Cheneau, I. Bloch, and S. Kuhr. Single-atom-resolved fluorescence imaging of an atomic Mott insulator. *Nature*, 467:68–72, 2010.

[25] R. Jördens, N. Strohmaier, K. Günter, Henning Moritz, and Tilman Esslinger. A Mott insulator of fermionic atoms in an optical lattice. *Nature*, 455:204–207, 2008.

[26] M. Greiner, O. Mandel, T. Esslinger, T. W. Hänsch, and I. Bloch. Quantum phase transition from a superfluid to a Mott insulator in a gas of ultracold atoms. *Nature*, 415:39–44, 2002.

[27] K. Winkler, G. Thalhammer, F. Lang, R. Grimm, J. Hecker Denschlag, A. J. Daley, A. Kantian, H. P. Büchler, and P. Zoller. Repulsively bound atom pairs in an optical lattice. *Nature*, 441:853–856, 2006.

[28] K. v. Klitzing, G. Dorda, and M. Pepper. New Method for High-Accuracy Determination of the Fine-Structure Constant Based on Quantized Hall Resistance. *Phys. Rev. Lett.*, 45:494–497, 1980.

[29] D. C. Tsui, H. L. Stormer, and A. C. Gossard. Two-Dimensional Magnetotransport in the Extreme Quantum Limit. *Phys. Rev. Lett.*, 48:1559–1562, 1982.

[30] R. B. Laughlin. Anomalous Quantum Hall Effect: An Incompressible Quantum Fluid with Fractionally Charged Excitations. *Phys. Rev. Lett.*, 50:1395–1398, 1983.

[31] Jean Dalibard, Fabrice Gerbier, Gediminas Juzeliūnas, and Patrik Öhberg. Colloquium: Artificial gauge potentials for neutral atoms. *Rev. Mod. Phys.*, 83(1523), 2011.

[32] K. W. Madison, F. Chevy, W. Wohlleben, and J. Dalibard. Vortex Formation in a Stirred Bose-Einstein Condensate. *Phys. Rev. Lett.*, 84:806–809, 2000.

[33] P. Rosenbusch, D. S. Petrov, S. Sinha, F. Chevy, V. Bretin, Y. Castin, G. Shlyapnikov, and J. Dalibard. Critical Rotation of a Harmonically Trapped Bose Gas. *Phys. Rev. Lett.*, 88:250403, 2002.

[34] V. Schweikhard, I. Coddington, P. Engels, V. P. Mogendorff, and E. A. Cornell. Rapidly Rotating Bose-Einstein Condensates in and near the Lowest Landau Level. *Phys. Rev. Lett.*, 92:040404, 2004.

[35] Y.-J. Lin, R. L. Compton, K. Jiménez-García, J. V. Porto, and I. B. Spielman. Synthetic magnetic fields for ultracold neutral atoms. *Nature*, 462:628–632, 2009.

[36] Y.-J. Lin, K. Jiménez-García, and I. B. Spielman. Spinorbit-coupled BoseEinstein condensates. *Nature*, 471:83–86, 2011.

[37] M. C. Beeler, R. A. Williams, K. Jiménez-García, L. J. LeBlanc, A. R. Perry, and I. B. Spielman. The spin Hall effect in a quantum gas. *Nature*, 498:201–204, 2013.

[38] D. Jaksch and P. Zoller. Creation of effective magnetic fields in optical lattices: the Hofstadter butterfly for cold neutral atoms. *New J. Phys.*, 5(56), 2003.

[39] F. Gerbier and J. Dalibard. Gauge fields for ultracold atoms in optical superlattices. *New J. Phys.*, 12(033007), 2010.

[40] A. R. Kolovsky. Creating artificial magnetic fields for cold atoms by photon-assisted tunneling. *Europhys. Lett.*, 93(20003), 2011.

[41] J. Struck, C. Ölschläger, M. Weinberg, P. Hauke, J. Simonet, A. Eckardt, M. Lewenstein, K. Sengstock, and P. Windpassinger. Tunable Gauge Potential for Neutral and Spinless Particles in Driven Optical Lattices. *Phys. Rev. Lett.*, 108(225304), 2012.

[42] J. Struck, M.Weinberg, C. Ölschläger, P.Windpassinger, J. Simonet, K. Sengstock, R. Höppner, P. Hauke, A. Eckardt, M. Lewenstein, and L. Mathey. Engineering Ising-XY spin-models in a triangular lattice using tunable artificial gauge fields. *Nature Phys.*, 9:738–743, 2013.

[43] G. Jotzu, M. Messer, R. Desbuquois, M. Lebrat, T. Uehlinger, D. Greif, and T. Esslinger. Experimental realisation of the topological Haldane model. arXiv:1406.7874v1, 2014.

[44] F. D. M. Haldane. Model for a Quantum Hall Effect without Landau Levels: Condensed-Matter Realization of the "Parity Anomaly". *Phys. Rev. Lett.*, 61(2015), 1988.

[45] M. Aidelsburger, M. Atala, S. Nascimbène, S. Trotzky, Y.-A. Chen, and I. Bloch. Experimental Realization of Strong Effective Magnetic Fields in an Optical Lattice. *Phys. Rev. Lett.*, 107(255301), 2011.

[46] M. Aidelsburger, M. Atala, S. Nascimbène, S. Trotzky, Y.-A. Chen, and I. Bloch. Experimental realization of strong effective magnetic fields in optical superlattice potentials. *Appl. Phys. B*, 113(1), 2013.

[47] M. Aidelsburger, M. Atala, M. Lohse, J. T. Barreiro, B. Paredes, and I. Bloch. Realization of the Hofstadter Hamiltonian with Ultracold Atoms in Optical Lattices. *Phys. Rev. Lett.*, 111(185301), 2013.

[48] H. Miyake, G. A. Siviloglou, C. J. Kennedy, W. Cody Burton, and W. Ketterle. Realizing the Harper Hamiltonian with Laser-Assisted Tunneling in Optical Lattices. *Phys. Rev. Lett.*, 111(185302), 2013.

[49] M. Atala, M. Aidelsburger, M. Lohse, J. T. Barreiro, B. Paredes, and I. Bloch. Observation of chiral currents with ultracold atoms in bosonic ladders. *Nature Physics*, 10:588–593, 2014.

[50] M. Aidelsburger, M. Lohse, C. Schweizer, M. Atala, J. T. Barreiro, S. Nascimbène, N. R. Cooper, I. Bloch, and N. Goldman. Measuring the Chern number of Hofstadter bands with ultracold bosonic atoms. arXiv:1407.4205v2, 2014.

[51] D. A. Church and H. G. Dehmelt. Radiative Cooling of an Electrodynamically Contained Proton Gas. *J. Appl. Phys.*, 40(3421), 1969.

[52] T. Bilitewski and N. R. Cooper. Scattering Theory for Floquet-Bloch States. arXiv:1410.5364v1, 2014.

[53] N. Poli, Z. W. Barber, N. D. Lemke, C. W. Oates, L. S. Ma, J. E. Stalnaker, T. M. Fortier, S. A. Diddams, L. Hollberg, J. C. Bergquist, A. Brusch, S. Jefferts, T. Heavner, and T. Parker. Frequency evaluation of the doubly forbidden $^1S_0 \rightarrow {}^3P_0$ transition in bosonic ^{174}Yb. *Phys. Rev. A*, 77(5):050501, 2008.

[54] T. Kohno, M. Yasuda, K. Hosaka, H. Inaba, Y. Nakajima, and F.-L. Hong. One-Dimensional Optical Lattice Clock with a Fermionic ^{171}Yb Isotope. *Appl. Phys. Express*, 2(7):072501, 2009.

[55] Y. Takasu, K. Maki, K. Komori, T. Takano, K. Honda, M. Kumakura, T. Yabuzaki, and Y. Takahashi. Spin-Singlet Bose-Einstein Condensation of Two-Electron Atoms. *Phys. Rev. Lett.*, 91(4), 2004.

[56] T. Fukuhara, Y. Takasu, M. Kumakura, and Y. Takahashi. Degenerate Fermi Gases of Ytterbium. *Phys. Rev. Lett.*, 98(030401), 2007.

[57] T. Fukuhara, S. Sugawa, Y. Takasu, and Y. Takahashi. All-optical formation of quantum degenerate mixtures. *Phys. Rev. A*, 79(021601(R)), 2009.

[58] S. Taie, Y. Takasu, S. Sugawa, R. Yamazaki, T. Tsujimoto, R. Murakami, and Y. Takahashi. Realization of a SU(2)×SU(6) System of Fermions in a Cold Atomic Gas. *Phys. Rev. Lett.*, 105(190401), 2010.

[59] N. Poli, C. W. Oates, P. Gill, and G. M. Tino. Optical atomic clocks. *Rivista del Nuovo Cimento*, 36(12):555–624, 2013.

[60] J. Dalibard. Des cages de lumière pour les atomes: la physique des pièges et des réseaux optiques. Lecture series at Collège de France, 2013.

[61] J. Dalibard. Le magnétisme artificiel pour les gaz d'atomes froids. Lecture series at Collège de France, 2014.

[62] R. Grimm, M. Weidemüller, and Y. B. Ovchinnikov. Optical dipole traps for neutral atoms. *Advances in Atomic, Molecular and Optical Physics*, 42:95–170, 2000.

[63] N. W. Ashcroft and N. D. Mermin. *Solid state physics.* Brooks Cole, 1976.

[64] W. Kohn. Analytic Properties of Bloch Waves and Wannier Functions. *Phys. Rev.*, 115(809), 1959.

[65] M. Krämer, L. Pitaevskii, and S. Stringari. Macroscopic dynamics of a trapped Bose-Einstein condensate in the presence of 1D and 2D optical lattices. *Phys. Rev. Lett.*, 88(18):180404, 2002.

[66] K. Sheshadri, H. R. Krishnamurthy, R. Pandit, and T. V. Ramakrishnan. Superfluid and Insulating Phases in an Interacting-Boson Model: Mean-Field Theory and the RPA. *Europhys. Lett.*, 22(4), 1993.

[67] Q. Beaufils, G. Tackmann, X. Wang, B. Pelle, S. Pelisson, P. Wolf, and F. Pereira dos Santos. Laser Controlled Tunneling in a Vertical Optical Lattice. *Phys. Rev. Lett.*, 106(213002), 2011.

[68] B. Capogrosso-Sansone, Ş. G. Söyler, N. Prokofev, and B. Svistunov. Monte Carlo study of the two-dimensional Bose-Hubbard model. *Phys. Rev. A*, 77(015602), 2008.

[69] Y. Aharonov and D. Bohm. Significance of Electromagnetic Potentials in the Quantum Theory. *Physical Review*, 115(3), 1959.

[70] A. Tonomura, T. Matsuda, R. Suzuki, A. Fukuhara, N. Osakabe, H. Umezaki, J. Endo, K. Shinagawa, Y. Sugita, and H. Fujiwara. Observation of Aharonov-Bohm Effect by Electron Holography. *Phys. Rev. Lett.*, 48:1443, 1982.

[71] R. G. Chambers. Shift of an Electron Interference Pattern by Enclosed Magnetic Flux. *Phys. Rev. Lett.*, 5:3, 1960.

[72] J. M. Luttinger. The Effect of a Magnetic Field on Electrons in a Periodic Potential. *Phys. Rev.*, 84:814, 1951.

[73] W. Kohn. Theory of Bloch Electrons in a Magnetic Field: The Effective Hamiltonian. *Phys. Rev.*, 115:1460, 1959.

[74] G. Nenciu. Dynamics of band electrons in electric and magnetic fields: rigorous justification of the effective Hamiltonians. *Rev. Mod. Phys.*, 63:91, 1991.

[75] D. R. Hofstadter. Energy levels and wave functions of Bloch electrons in rational and irrational magnetic fields. *Phys. Rev. B*, 14(6), 1976.

[76] W. D. Phillips and H. Metcalf. Laser Deceleration of an Atomic Beam. *Phys. Rev. Lett.*, 48(9), 1982.

[77] Y. Takasu, K. Komori, K. Honda, M. Kumakura, T. Yabuzaki, and Y. Takahashi. Photoassociation Spectroscopy of Laser-Cooled Ytterbium Atoms. *Phys. Rev. Lett.*, 93(12), 2004.

[78] Zeb Barber. *Ytterbium Optical Lattice Clock.* PhD thesis, Montana State University, 2007.

[79] R. Maruyama. *Optical Trapping of Ytterbium Atoms.* PhD thesis, University of Washington, 2003.

[80] C. J. Foot. *Atomic Physics.* Oxford University Press, 2009.

[81] K. Honda, Y. Takahashi, T. Kuwamoto, M. Fujimoto, K. Toyoda, K. Ishikawa, and T. Yabuzaki. Magneto-optical trapping of Yb atoms and a limit on the branching ratio of the $^1P_1$ state. *Phys. Rev. A*, (R934), 1999.

[82] N. Kostylev, E. Ivanov, M. E. Tobar, and J. J. McFerran. Sub-Doppler cooling of ytterbium with the $^1S_0 - {}^1P_1$ transition including ^{171}Yb (I=1/2). *JOSA B*, 31(7):1614–1620, 2014.

[83] E. Mimoun. *Condensat de Bose-Einstein de sodium dans un piège mésoscopique.* PhD thesis, Université Paris 6, 2010.

[84] A. Keshet and W. Ketterle. A distributed, graphical user interface based, computer control system for atomic physics experiments. *Rev. Sci. Instrum.*, 84(015105), 2013.

[85] T. Kuwamotoa, K. Honda, Y. Takahashi, and T. Yabuzaki. Magneto-optical trapping of Yb atoms using an intercombination transition. *Phys. Rev. A*, 60(2), 1999.

[86] H.J. Metcalf and P. van der Straten. *Laser Cooling and Trapping.* Springer, 1999.

[87] W.C. Martin, R. Zalubas, and L. Hagan. Atomic Energy Levels - The Rare-Earth Elements. *National Bureau of Standards*, 1978.

[88] J.H. Lundeman, O.B. Jensen, P.E. Andersen, and P.M. Petersen. Threshold for strong thermal dephasing in periodically poled KTP in external cavity frequency doubling. *Appl Phys B*, 96:827831, 2009.

[89] J. Weiner, V. S. Bagnato, S. Zilio, and P. S. Julienne. Experiments and theory in cold and ultracold collisions. *Rev. Mod. Phys.*, 71(1), 1999.

[90] D. A. Steck. `http://steck.us/alkalidata`, 2010.

[91] G. E. Marti, R. Olf, E. Vogt, A. Öttl, and D. M. Stamper-Kurn. Two-element Zeeman slower for rubidium and lithium. *Phys. Rev. A.*, 81(043424), 2010.

[92] W. Ketterle, D.S. Durfee, and D.M. Stamper-Kurn. Making, probing and understanding Bose-Einstein condensates, In M. Inguscio, S. Stringari and C. E. Wieman, eds., Proceedings of the International School of Physics ”Enrico Fermi”. *IOS Press, Amsterdam*, 1999.

[93] A. Couvert, T. Kawalec, G. Reinaudi, and D. Guéry-Odelin. Optimal transport of ultracold atoms in the non-adiabatic regime. *EPL*, 83(13001), 2008.

[94] T. L. Gustavson, A. P. Chikkatur, A. E. Leanhardt, A. Görlitz, S. Gupta, D. E. Pritchard, and W. Ketterle. Transport of Bose-Einstein Condensates with Optical Tweezers. *Phys. Rev. Lett.*, 88(2), 2002.

[95] S. Schmid, G. Thalhammer, K. Winkler, F. Lang, and J. Hecker Denschlag. Long distance transport of ultracold atoms using a 1D optical lattice. *New J. Phys.*, 8(159), 2006.

[96] J. Leonard, M. Lee, A. Morales, T. M. Karg, T. Esslinger, and T. Donner. Optical transport of ultracold atoms using focus-tunable lenses. arXiv:1406.2336, 2014.

[97] J. Petersen. Optischer Transport ultrakalter Atome. Master's thesis, Johannes Gutenberg-Universität Mainz, 2009.

[98] K.B. Davis, M.-O. Mewes, and W. Ketterle. An analytical model for evaporative cooling of atoms. *Appl. Phys. B*, 60:155–159, 1995.

[99] T. A. Savard, K. M. O'Hara, and J. E. Thomas. Laser-noise-induced heating in far-off resonance optical traps. *Phys. Rev. A*, 56(2), 1997.

[100] S. Friebel, C. D'Andrea, J. Walz, M. Weitz, and T. W. Hänsch. CO_2-laser optical lattice with cold rubidium atoms. *Phys. Rev. A.*, 57(1 (R20)), 1998.

[101] S. J. M. Kuppens, K. L. Corwin, K. W. Miller, T. E. Chupp, and C. E. Wieman. Loading an optical dipole trap. *Phys. Rev. A*, 62(013406), 2000.

[102] B. Fröhlich, T. Lahaye, B. Kaltenhäuser, H. Kübler, S. Müller, T. Koch, M. Fattori, and T. Pfau. A two-frequency acousto-optic modulator driver to improve the beam pointing stability during intensity ramps. *Rev. Sci. Instrum.*, 78:043101, 2007.

[103] J. Dalibard. Atomes ultra-froids. Lecture notes from course at Ecole normale supérieure, 2006.

[104] E. A. Burt, R. W. Ghrist, C. J. Myatt, M. J. Holland, E. A. Cornell, and C. E. Wieman. Coherence, Correlations, and Collisions: What One Learns about Bose-Einstein Condensates from Their Decay. *Phys. Rev. Lett.*, 79(3):337, 1997.

[105] F. Dalfovo, S. Giorgini, L. P. Pitaevskii, and S. Stringari. Theory of Bose-Einstein condensation in trapped gases. *Rev. Mod. Phys.*, 71(3), 1999.

[106] F. Gerbier. *Condensats de Bose-Einstein dans un piège anisotrope.* PhD thesis, Université Paris VI, 2003.

[107] M. B. Dahan, E. Peik, J. Reichel, Y. Castin, and Christophe Salomon. Bloch Oscillations of Atoms in an Optical Potential. *Phys. Rev. Lett.*, 76(24), 1996.

[108] J. Hecker Denschlag, J. E. Simsarian, H. Häffner, C. McKenzie, A. Browaeys, D. Cho, K. Helmerson, S. L. Rolston, and W. D. Phillips. A Bose-Einstein condensate in an optical lattice. *J. Phys. B: At. Mol. Opt. Phys.*, 35:3095–3110, 2002.

[109] T. Gericke, F. Gerbier, A. Widera, S. Fölling, O. Mandel, and I. Bloch. Adiabatic loading of a Bose-Einstein condensate in a 3D optical lattice. *J. Mod. Opt.*, 54:735, 2007.

[110] B. Gadway, D. Pertot, R. Reimann, M. G. Cohen, and D. Schneble. Analysis of Kapitza-Dirac diffraction patterns beyond the Raman-Nath regime. *Optics Express*, 17(21):19173–19180, 2009.

[111] S. Hirata, T. Akatsuka, Y. Ohtake, and A. Morinaga. Sub-hertz-linewidth diode laser stabilized to an ultralow-drift high-finesse optical cavity. *Appl. Phys. Express*, 7(2), 2014.

[112] A. Yamaguchi, S. Uetake, D. Hashimoto, J.M. Doyle, and Y. Takahashi. Inelastic Collisions in Optically Trapped Ultracold Metastable Ytterbium. *Phys. Rev. Lett.*, 101:233002, 2008.

[113] F. Scazza, C. Hofrichter, M. Höfer, P. C. De Groot, I. Bloch, and S. Fölling. Observation of two-orbital spin-exchange interactions with ultracold SU(N)-symmetric fermions. *Nature Physics*, 10:779–784, 2014.

[114] S. G. Porsev, A. Derevianko, and E. N. Fortson. Possibility of an optical clock using the $6\,{}^1\mathrm{S}_0 \rightarrow 6\,{}^3\mathrm{P}_0^0$ transition in ^{171,173}Yb atoms held in an optical lattice. *Phys. Rev. A*, 69(021403(R)), 2004.

[115] A. V. Taichenachev, V. I. Yudin, C. W. Oates, C. W. Hoyt, Z. W. Barber, and L. Hollberg. Magnetic Field-Induced Spectroscopy of Forbidden Optical Transitions with Application to Lattice-Based Optical Atomic Clocks. *Phys. Rev. Lett.*, 96(083001), 2006.

[116] Z. W. Barber, C. W. Hoyt, C. W. Oates, L. Hollberg, A. V. Taichenachev, and V. I. Yudin. Direct Excitation of the Forbidden Clock Transition in Neutral ^{174}Yb Atoms Confined to an Optical Lattice. *Phys. Rev. Lett.*, 96(8):083002, 2006.

[117] F. Gerbier, A. Widera, S. Fölling, O. Mandel, T. Gericke, and I. Bloch. Phase Coherence of an Atomic Mott Insulator. *Phys. Rev. Lett.*, 95(050404), 2005.

[118] A. D. Ludlow, N. D. Lemke, J. A. Sherman, C. W. Oates, G. Quéméner, J. von Stecher, and A. M. Rey. Cold-collision-shift cancellation and inelastic scattering in a Yb optical lattice clock. *Phys. Rev. A*, 84:052724, 2011.

[119] A. Traverso, R. Chakraborty, Y. N. Martinez de Escobar, P. G. Mickelson, S. B. Nagel, M. Yan, and T. C. Killian. Inelastic and elastic collision rates for triplet states of ultracold strontium. *Phys. Rev. A*, 79:060702(R), 2009.

[120] W.P. Risk, T.R. Gosnell, and A.V. Nurmikko. *Compact Blue-Green Lasers.* Cambridge University Press, 2003.

[121] A. E. Siegman. *Lasers.* University Science Books, 20 Edgehill Road, Mill Valley, California 94941, 1986.

[122] G. Rempe, R. J. Thompson, H. J. Kimble, and R. Lalezari. Measurement of ultralow losses in an optical interferometer. *Optics Letters*, 17(5), 1992.

[123] R. W. P. Drever, J. L. Hall, F. V. Kowalski, J. Hough, G. M. Ford, A. J. Munley, and H. Ward. Laser Phase and Frequency Stabilization Using an Optical Resonator. *Appl. Phys. B*, 31(2), 1983.

[124] G. Di Domenico, S. Schilt, and P. Thomann. Simple approach to the relation between laser frequency noise and laser line shape. *Applied Optics*, 49(25):4801–4807, 2010.

[125] F. Hong, H. Inaba, K. Hosaka, M. Yasuda, and A. Onae. Doppler-free spectroscopy of molecular iodine using a frequency-stable light source at 578 nm. *Optics Express*, 17(3), 2009.

[126] A. Yamaguchi. *Metastable State of Ultracold and Quantum Degenerate Ytterbium Atoms: High-Resolution Spectroscopy and Cold Collisions.* PhD thesis, Kyoto University, 2008.

[127] C.W. Hoyt, Z.W. Barber, C.W. Oates, T. M. Fortier, S. A. Diddams, and L. Hollberg. Observation and Absolute Frequency Measurements of the $^1S_0$-$^3P_0$ Optical Clock Transition in Neutral Ytterbium. *Phys. Rev. Lett.*, 95(083003), 2005.

[128] D. G. Fried, T. C. Killian, L. Willmann, D. Landhuis, S. C. Moss, D. Kleppner, and T. J. Greytak. Bose-Einstein Condensation of Atomic Hydrogen. *Phys. Rev. Lett.*, 81(18), 1998.

[129] T. C. Killian. 1S-2S spectrum of a hydrogen Bose-Einstein condensate. *Phys. Rev. A*, 61(033611), 2000.

[130] L. Pitaevskii and S. Stringari. *Bose-Einstein Condensation.* Clarendon Press - Oxford, 2003.

[131] Y. Castin and R. Dum. Bose-Einstein Condensates in Time Dependent Traps. *Phys. Rev. Lett.*, 77(27), 2014.

[132] C. Weitenberg. *Single-Atom Resolved Imaging and Manipulation in an Atomic Mott Insulator.* PhD thesis, LMU München, 2011.

[133] Z. W. Barber, J. E. Stalnaker, N. D. Lemke, N. Poli, C. W. Oates, T. M. Fortier, S. A. Diddams, L. Hollberg, C. W. Hoyt, A. V. Taichenachev, and V. I. Yudin. Optical Lattice Induced Light Shifts in an Yb Atomic Clock. *Phys. Rev. Lett.*, 100(103002), 2008.

[134] S. Fölling, S. Trotzky, P. Cheinet, M. Feld, R. Saers, A. Widera, T. Müller, and I. Bloch. Direct observation of second-order atom tunnelling. *Nature*, 448:1029–1032, 2007.

[135] G. Ghosh, M. Endo, and T. Iwasaki. Temperature-dependent Sellmeier coefficients and chromatic dispersions for some optical fiber glasses. *Lightwave Technology*, 12(8), 1994.

[136] B. J. Frey, D. B. Leviton, T. J. Madison, Q. Gong, and M. Tecza. Cryogenic temperature-dependent refractive index measurements of N-BK7, BaLKN3, SF15, and E-SF03. *SPIE Proceedings: Cryogenic Optical Systems and Instruments XII*, 6692, 2007.

[137] National Institute of Standards and Technology (NIST). `http://emtoolbox.nist.gov/Wavelength/Edlen.asp`, 2004.

[138] Accuratus Corporation. Fused Silica, SiO_2 Glass Properties. `http://accuratus.com/fused.html`, 2013.

[139] Schott AG. Optical Glass - Data Sheets. `http://www.schott.com/advanced_optics/us/abbe_datasheets/schott_datasheet_all_us.pdf`, 2013.

[140] S. Dörscher, A. Thobe, B. Hundt, A. Kochanke, R. Le Targat, P. Windpassinger, C. Becker, and K. Sengstock. Creation of quantum-degenerate gases of ytterbium in a compact 2D-/3D-magneto-optical trap setup. *Rev. Sci. Instrum*, 84(043109), 2013.

[141] C. Cohen-Tannoudji, J. Dupont-Roc, and G. Grynberg. *Atom - Photon Interactions: Basic Process and Appilcations.* WILEY-VCH Verlag, 2004.

[142] J. E. Sansonetti and W. C. Martin. Handbook of Basic Atomic Spectroscopic Data. `http://www.nist.gov/pml/data/handbook/index.cfm`, 2014.

[143] V. A. Dzuba and A. Derevianko. Dynamic polarizabilities and related properties of clock states of ytterbium atom. *J. Phys. B: Atomic, Molecular and Optical Physics*, 43(074011), 2010.

[144] E. C. Ifeachor and B. W. Jervis. *Digital Signal Processing: A Practical Approach.* Addison-Wesley, 2nd edition, 1993.

[145] S. M. Kuo and B. H. Lee. *Real-Time Digital Signal Processing.* John Wiley and Sons, Ltd, 2001.

[146] B. Beauregard. Improving the Beginner's PID Introduction. `http://brettbeauregard.com/blog/2011/04/improving-the-beginners-pid-introduction/`.